

Protein Cages for the Encapsulation of Nanoparticles with Various Geometries

Dissertation

zur Erlangung der Würde des Doktors der Naturwissenschaften der
Fakultät für Mathematik, Informatik und Naturwissenschaften,
Fachbereich Chemie der Universität Hamburg

vorgelegt von

Varnika Yadav

Hamburg 2025

Gutachter der Dissertation Prof. Dr. Tobias Beck
Prof. Dr. Volker Abetz

Gutachter der Disputation Prof. Dr. Tobias Beck
Prof. Dr. Wolfgang Maison
Dr. Tobias Vossmeier

Tag der Disputation 21.11.2025

The work presented in this thesis was carried out at the Institute of Physical Chemistry of the University Hamburg in the work group of Prof. Dr. Tobias Beck between September 2021 and June 2025.

The author has contributed to the following related publications:

Ngoi, K.H.; Lang, L.; Kim, Y.Y.; Mucke, N.; Hinsley, G.N.; Kim, D.; Rütten, M.; Klemeyer, L.; Ruffer, M.; Yadav, V.; Wagler, H.; Katenkamp, T.; Perbandt, M.; Khadiev, A.; Novikov, D.; Beck, T.; Vartanyants, I.A.; Structure of Protein Cage Supercrystals Revealed by Angular X-ray Cross Correlation Analysis. *Small Structures* **2025**, 6: 2400684. DOI: 10.1002/sstr.202400684

Conference contributions:

- Talk: “Establish protein containers as building blocks for the assembly of anisotropic nanorods into optical hybrid nanomaterials” *NanoTage*, Hamburg, Germany, **2022**.
- Poster: “Establish protein containers as building blocks for the assembly of anisotropic nanorods into optical hybrid nanomaterials” *NANOHYBRID - Hamburg Conference on Complex Nanostructures*, Hamburg, Germany, **2022**.
- Talk: “Establish protein containers as building blocks for the assembly of anisotropic nanorods into optical hybrid nanomaterials” *NanoTage*, Dresden, Germany, **2023**.
- Talk: “Establish protein containers as building blocks for the assembly of anisotropic nanorods into optical hybrid nanomaterials” *NANOHYBRID - Hamburg Conference on Complex Nanostructures*, Lübeck, Germany, **2023**.
- Poster: “Establish protein containers as building blocks for the assembly of anisotropic nanorods into optical hybrid nanomaterials” *Bunsen-Tagung*, Aachen, Germany, **2024**.
- Talk: “Establish protein containers as building blocks for the assembly of anisotropic nanorods into optical hybrid nanomaterials” *NanoTage*, Karlsruhe, Germany, **2024**.
- Talk: “Establish protein containers as building blocks for the assembly of anisotropic nanorods into optical hybrid nanomaterials” *NANOHYBRID - Hamburg Conference on Complex Nanostructures*, Potsdam, Germany, **2024**.
- Poster: “Establish protein containers as building blocks for the assembly of anisotropic nanorods into optical hybrid nanomaterials” *ACS Spring*, San Diego, USA, **2025**.

Epigraph

Look at your wrist – see the bluish veins? The blood flowing through them contains hemoglobin, a protein with four iron atoms incorporated into its structure. Iron can only be forged in the core of dying stars. The same goes for calcium strengthening your bones and teeth, and the carbon forming the very backbone of your DNA. Every time you move, breathe or simply exist, remember that you're built from, and kept alive by the remnants of ancient stars. Remember – you are stardust, made conscious.

- *Varnika Yadav*

Zusammenfassung

Die bottom-up Konstruktion geordneter Supergitterstrukturen aus nanoskaligen Bausteinen stellt weiterhin eine zentrale Herausforderung in der Nanotechnologie dar. Sie hat jedoch das Potenzial, Materialien mit neuartigen optischen und elektronischen Eigenschaften herzustellen. Protein cages (Proteinkäfige) wie Viruskapside und Encapsuline bieten eine biologische, atomar präzise Matrix, um anorganische Nanomaterialien strukturiert anzuordnen. Die vorliegende Arbeit untersucht die Einkapselung von Nanopartikeln unterschiedlicher Formen und Größen durch protein cages – mit einem besonderen Fokus auf plasmonischen Goldnanopartikel (AuNPs), Goldnanorods (AuNRs) sowie fluoreszierenden CdSe/CdS-Dot-in-Rods (DiRs) – mit dem Ziel, hybride Nanomaterialien herzustellen.

Die Forschung wurde dabei von drei Zielen geleitet: (1) Oberflächenfunktionalisierung von Nanopartikeln um biologische Kompatibilität zu gewährleisten, (2) Entwicklung einer anpassbaren Proteinhülle, die als Plattform dienen kann, und (3) effiziente Einkapselung und Koassemblierung der Komponenten. Zu diesem Zweck wurden CdSe/CdS-DiRs und AuNRs synthetisiert und mithilfe verschiedener Liganden sowie eines cargo loading peptides (CLP) funktionalisiert, um ihre Löslichkeit zu steuern und die Einkapselung zu ermöglichen. Erste Versuche zur Einkapselung dieser anisotropen Nanopartikel wurden mit dem Encapsulin aus *Thermotoga maritima* durchgeführt. Dabei wurden Parameter wie die Ligandenchemie, das Partikel-zu-Protein-Verhältnis, Pufferzusammensetzung und Salzkonzentration systematisch variiert, um Faktoren für eine erfolgreiche Einkapselung zu identifizieren. Im Verlauf der Arbeit wurde die Proteinplattform jedoch gewechselt. Dieser Wechsel erfolgte von *T. maritima*-Encapsulin zu einer größeren und strukturell flexibleren Plattform aufgrund räumlicher und struktureller Limitation, insbesondere dessen starrer T = 1-Architektur.

Zur Überwindung dieser Einschränkungen wurde eine alternative Encapsulin-Plattform basierend auf *Myxococcus xanthus* etabliert. Es wurden Protokolle zur rekombinanten Expression und Reinigung entwickelt, sowie das Dis- und Reassembly-verhalten detailliert untersucht. Parallel dazu wurden AuNPs synthetisiert und mit geeigneten Liganden und CLP funktionalisiert, um diese als Modellcargo für die Einkapselung in *M. xanthus*-Encapsulin zu verwenden. Diese Einkapselung konnte zwar prinzipiell demonstriert werden, jedoch blieb die Effizienz begrenzt. Allerdings konnte im Rahmen dieser Arbeit gezeigt werden, dass Pufferzusammensetzung, Ionenstärke und Redoxbedingungen die Ausbildung definierter ikosaedrischer Architekturen (T = 1 und T = 3) beeinflussen und somit eine gezielte Kontrolle der Proteinmorphologie ermöglichen.

Zusammenfassend präsentiert diese Arbeit eine umfassende Strategie zur Konstruktion von Protein-Nanopartikel-Hybridsystemen mit Fokus auf der Einkapselung anisotroper Nanomaterialien. Das M. xanthus-Encapsulin wird dabei als vielseitige und steuerbare Matrix positioniert. Gleichzeitig wurde ein methodisches Fundament geschaffen, das für zukünftige layer-by-layer Assembly-prozesse herangezogen werden kann. Diese Erkenntnisse ebnen den Weg zur Entwicklung biohybrider Materialien der nächsten Generation mit maßgeschneiderten optischen Eigenschaften für Anwendungen in Sensorik, Nanophotonik und Quantentechnologien.

Abstract

The bottom-up assembly of nanoscale building blocks into ordered superlattices remains a central challenge in nanotechnology, with the potential to unlock materials with novel optical and electronic properties. Protein cages, such as virus capsids and encapsulins, offer an atomically precise, biologically derived scaffold for organizing inorganic nanomaterials with high fidelity. This thesis explores the use of protein cages to encapsulate cargo of different geometries, focusing on plasmonic gold nanoparticles (AuNPs), gold nanorods (AuNRs) and fluorescent CdSe/CdS dot-in-rods (DiRs) to create hybrid materials.

Three core objectives shaped the research: (1) engineer nanoparticle surfaces for biological compatibility, (2) develop a tunable protein container platform, and (3) achieve efficient encapsulation and co-assembly of these components. In this work, CdSe/CdS DiRs and AuNRs were synthesized and functionalized with a series of ligands and a cargo-loading peptide (CLP) to modulate solubility and enable encapsulation. Initial encapsulation with these anisotropic nanoparticles trials were carried out using *Thermotoga Maritima* encapsulin. Encapsulation trials systematically varied ligand chemistry, particle-to-protein ratios, buffer composition and salt concentration to define the key parameters influencing successful loading. However, the spatial and structural limitations of *T. maritima* encapsulin, particularly its rigid $T = 1$ architecture, motivated the transition to a larger and more adaptable scaffold.

To overcome these constraints, a new encapsulin platform based on *Myxococcus Xanthus* was established. High-yield recombinant expression and purification protocols were developed, followed by a detailed study of disassembly and reassembly pathways. In parallel, AuNPs were synthesized and functionalized with a ligand shell and CLP to use as model cargo for encapsulation into *M. xanthus* encapsulin. Although the encapsulation was achieved, the efficiency remained low. Crucially, the work identified how buffer composition, ionic strength, and redox conditions influence the formation of distinct $T = 1$ and $T = 3$ icosahedral architectures and hence enabling precise control over cage morphology.

In summary, this thesis presents a comprehensive strategy for constructing protein-nanoparticle hybrid systems, with a particular focus on encapsulation of anisotropic materials into protein cages. It positions *M. xanthus* encapsulin as a flexible and controllable scaffold, and establishes a toolkit necessary for guiding future layer-by-layer assembly. These findings pave the way for the development of next-generation biohybrid materials with customizable optical properties suited for applications in sensing, nanophotonics, and quantum technologies.

Table of Contents

1. Introduction.....	1
2. Theoretical Background.....	2
2.1 Introduction to Nanomaterials	2
2.1.1 CdSe/CdS dot-in-rods	6
2.1.2 Gold Nanorods.....	10
2.1.3 Gold Nanoparticles.....	16
2.2 Protein Cages	19
2.2.1 Anisotropic Protein Containers in Nature.....	20
2.2.2 Common Symmetric Protein Cages	21
2.2.3 Encapsulins.....	23
2.3 Biohybrid Nanostructures.....	31
2.3.1 Protein Nanoparticle Interaction	32
2.3.2 Biohybrid Assemblies	34
3. Basis of the present work	37
3.1 Supercharging of the <i>T. maritima</i> encapsulin.....	37
3.2 Encapsulation of spherical gold nanoparticles via CLP.....	38
4. Concept and aim of this thesis.....	40
5. Results and Discussion	42
5.1 Synthesis of Nanomaterials	42
5.1.1 Synthesis of CdSe/CdS DiRs	42
5.1.2 Synthesis of Gold Nanorods.....	45
5.1.3 Synthesis of Spherical Gold Nanoparticles.....	51
5.2 Ligand Exchange Strategies	54
5.2.1 Functionalization of CdSe/CdS DiRs	54

5.2.2 Gold Nanorods.....	67
5.2.3 Functionalization of Gold Nanoparticles	77
5.3 Production and Purification of Encapsulins	86
5.3.1 Production and Purification of <i>T. maritima</i> Encapsulin.....	86
5.3.2 Production and Purification of <i>M. xanthus</i> Encapsulin	87
5.4 Encapsulation of Cargo into <i>T. maritima</i> encapsulin	101
5.4.1 Encapsulation of CdSe/CdS DiRs in <i>T. maritima</i> encapsulin	101
5.4.2 Encapsulation of Gold Nanorods in <i>T. maritima</i> Encapsulin	113
5.5 Encapsulation of Cargo into <i>M. xanthus</i> Encapsulin	116
5.5.1 <i>M. xanthus</i> Encapsulin Dis- and Reassembly.....	116
5.5.2 Comparison of T1 vs. T3 behavior	124
5.5.3 Encapsulation of Cargo	125
5.5.4 Mechanistic Insights into <i>M. xanthus</i> Encapsulin Reassembly	134
6. Summary and Outlook	146
7. Experimental Part	149
7.1 General	149
7.2 E. coli strains.....	149
7.3 Chemicals	150
7.4 Analytical Methods.....	150
7.4.1 UV-Vis Spectroscopy	150
7.4.2 Transmission Electron Microscopy	150
7.4.3 Dynamic Light Scattering	150
7.4.4 Zeta Potential.....	151
7.4.5 Fluorescence Spectroscopy	151
7.4.6 SDS Page	151
7.5 Gold Nanorod Synthesis	152
7.5.1. H ₂ O ₂ Method	152

7.5.2 CTAB-Decanol Method	153
7.5.3 Calculation of Gold Nanorod Concentration	154
7.6 CdSe/CdS DiR synthesis	154
7.7 AuNPs synthesis:	155
7.9 Ligand Exchange	155
7.9.1 MUA Stabilized AuNRs	155
7.9.2 MUTAB stabilized AuNRs	156
7.9.3 CdSe/CdS DiRs	157
7.9.4 Gold Nanoparticles.....	158
7.10 Protein Related Protocols	159
7.10.1 Protein Production and Purification	159
7.10.2 Dis and Reassembly	161
7.10.3 Nanomaterial encapsulation	161
7.11 Surface Deposition.....	162
8. Appendix	163
9. Bibliography.....	174
10. Abbreviations	193
11. List of Figures	196
12. List of Tables	204
13. List of Chemicals	205
Acknowledgement.....	208
Statutory Declaration	210
Curriculum Vitae.....	211

1. Introduction

The integration of inorganic nanomaterials with biological molecules to form functional biohybrid structures is a key strategy in advancing nanotechnology.^[1-2] This approach merges the unique optical, electronic, and magnetic properties of nanoparticles with the precise organizational capabilities and biocompatibility of biomolecular scaffolds, opening pathways for applications in sensing, catalysis, and nanomedicine.^[3-6]

Among biological templates, protein cages offer an ideal platform for creating well-defined biohybrid materials due to their monodisperse size, atomic-level precision, and programmability.^[7-9] In particular, encapsulins are highly attractive scaffolds. Their architecture, based on icosahedral symmetry with defined triangulation numbers (e.g., $T = 1$, $T = 3$, $T = 4$), provides a range of sizes and porosities suited for diverse cargo.^[10-11] Encapsulins have been successfully engineered to encapsulate a variety of cargo, including gold nanoparticles, organometallic catalysts, and fluorescent proteins.^[12-15] This versatile loading capability makes them promising platforms for applications in targeted drug delivery, vaccine development, and protected bionanoreactors.^[12, 16-20]

However, moving from the encapsulation of isotropic nanoparticles to anisotropic nanoparticles represents a significant materials challenge and an opportunity to access novel functionalities. Anisotropic nanoparticles, such as gold nanorods and CdSe/CdS dot-in-rods, exhibit properties that are not available in their spherical counterparts, including shape-dependent plasmonic resonances, polarized emission, and large transition dipole moments.^[21-24] Their integration into a protein shell could enable the construction of building blocks with directional optical properties for advanced metamaterials. Despite this potential, the encapsulation of such non-spherical cargo remains largely unexplored and poses fundamental questions regarding structural compatibility and loading mechanisms.

In this work, we investigate the encapsulation of anisotropic gold nanorods and CdSe/CdS dot-in-rods into the *Thermotoga maritima* encapsulin. Our goal is to probe the fundamental challenges associated with incorporating large, non-spherical cargo into a defined protein cavity. We focus on understanding how nanoparticle anisotropy influences and potentially challenges the structural integrity of the cage and whether the protein geometry can adapt to accommodate the shape. By exploring strategies such as surface functionalization and solution condition modulation, this study establishes the critical parameters and outlines a roadmap for transforming encapsulins into versatile hosts for the next generation of anisotropic nanohybrids.

2. Theoretical Background

In this section, the theoretical principles relevant to the presented work are summarized. The focus lies on gold-based nanostructures, including gold nanoparticles, and nanorods, highlighting their synthesis, size-dependent optical properties, and potential applications. Semiconductor heterostructures such as CdSe/CdS dot-in-rods are introduced as fluorescent probes with tunable emission characteristics. Furthermore, protein-based nanocages, particularly encapsulins from *Thermotoga maritima* and *Myxococcus Xanthus*, are discussed as biological scaffolds capable of encapsulating inorganic nanoparticles. Finally, strategies for integrating these components into nanoscale assemblies, including superlattices and surface-deposited biohybrid materials, are outlined.

2.1 Introduction to Nanomaterials

The concept that matter is composed of atoms has been foundational in materials science for over a century. From this understanding emerged the long-standing goal to manipulate matter at the atomic scale, an idea that remained largely theoretical until the late 20th century. It was hypothesized that if just 100 atoms were required to store one bit of data, all the books ever written could be stored in a cube measuring only 0.02 inches on each side.^[25] While this estimate was once aspirational, advances in nanotechnology have now brought such levels of control within reach.^[26]

Nanomaterials are typically defined as materials with at least one structural dimension below 100 nanometers.^[27-29] At this scale, materials begin to exhibit size-dependent properties that differ significantly from their bulk counterparts. These effects arise primarily from an increased surface-to-volume ratio, reduced atomic coordination, and quantum confinement, which together influence physical, chemical, optical, and electronic properties.^[30-34] The field of nanomaterials draws from various foundational discoveries across physics, chemistry, and engineering. Early studies of colloidal systems laid the groundwork for particle synthesis and stabilization.^[35] The development of techniques such as the scanning tunneling microscope (STM) and atomic force microscope (AFM) in the 1980s enabled direct imaging and manipulation at the atomic level.^[36-37] As a result, nanoscience quickly evolved from theory to an experimental discipline.

The exceptional properties of nanomaterials including enhanced catalytic activity, tunable optical behavior, improved mechanical strength, and quantum effects make them highly desirable in a wide range of sectors.^[38-40] In medicine, they are applied in targeted drug delivery, contrast agents and biosensors.^[40-42] Their small size also allows them to penetrate

cells and biological barriers, expanding their utility in therapeutic applications. In the field of energy related research, they are central to photovoltaics, fuel cells, and supercapacitors.^[43-45] In environmental engineering, they are used for water purification, air filtration, and pollutant degradation.^[46-48]

Nanomaterials can be broadly classified based on their composition into metallic, semiconductor, carbon-based, etc.^[30, 49-52] Metallic nanomaterials, such as those composed of gold, silver, or platinum, exhibit strong surface plasmon resonance effects, which make them useful in biomedical imaging, photothermal therapy, and catalysis.^[53-58] Semiconductor nanomaterials, including CdSe, ZnO, or PbS, exhibit quantum size effects that result in tunable optical and electronic properties, and have found extensive use in optoelectronics, light harvesting, and bioimaging.^[59-61] Carbon-based nanomaterials such as fullerenes, carbon nanotubes, and graphene derivatives offer exceptional mechanical strength and electrical conductivity, lending themselves to applications in nanoelectronics and structural materials.^[62-64]

The synthesis of nanomaterials is based on 'bottom-up' or 'top-down' strategies.^[65-66] In the 'top-down' approach, physical methods like laser or thermal ablation, sputtering, or mechanical milling are used.^[65] For example, through mechanical milling, bulk material is broken down into smaller particles.^[67] However, drawbacks such as erosion, impurity formation, and broad size distributions are common. Still, this route is advantageous for large-scale production.^[68-69] Conversely, the 'bottom-up' approach builds nanoparticles from atoms or molecules in liquid phase via chemical reduction.^[65-66] This method allows for precise control over particle size and shape.^[70-72]

The liquid-phase formation of nanoparticles was first described by LaMer and Dinegar in the 1950s.^[73] Their model remains the standard framework for explaining nucleation and growth in colloidal systems.^[74-75] It divides the process into three phases (Figure 2.1). First, the concentration of free monomers rises rapidly until it exceeds the minimum concentration for nucleation (C_{min}), eventually reaching the critical supersaturation threshold (C_s)(I). Once the C_s is exceeded, a burst of nucleation occurs (II), sharply reducing the monomer concentration. With monomer levels back below C_s , no new nuclei form, and existing particles grow instead (III). Growth continues as monomers are consumed until equilibrium concentration is reached again.^[73-75]

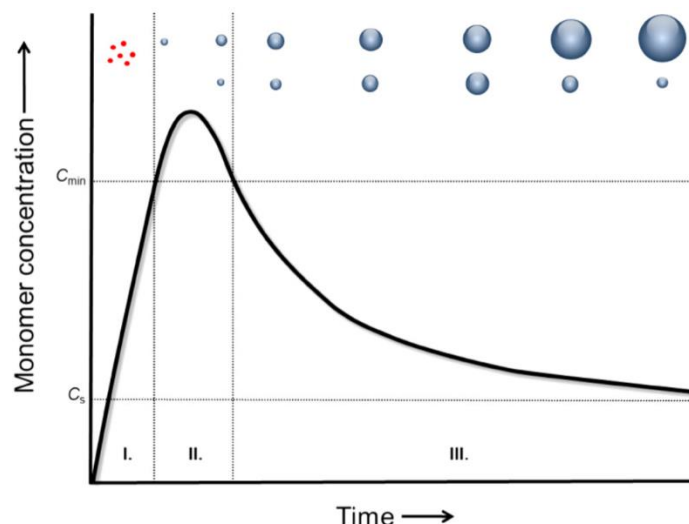


Figure 2.1: Lamer model for nanoparticle growth. Diagram of the three phases of nanoparticle growth and dependence of monomer concentration over time. Figure adopted from reference Vreeland et. al^[74], under a Creative Commons CC BY license (<https://creativecommons.org/licenses/by/4.0/>)

Following nucleation and growth, particles undergo Ostwald ripening, a process first described by Wilhelm Ostwald in 1900.^[76] Because smaller particles have higher solubility and surface energy, they tend to dissolve, with the dissolved material redepositing onto larger, more stable particles.^[77-78] According to the Lifshitz–Slyozov–Wagner (LSW) theory, this process leads to a predictable size distribution that narrows over time under diffusion-controlled conditions. However, in real systems, deviations from ideal behavior, such as secondary nucleation, aggregation, or insufficient kinetic control can lead to broader size distribution. Without stabilization, nanoparticles aggregate or oxidize easily due to their high surface energy and reactivity, and they remain stable only under extreme conditions such as ultra-high vacuum.^[79]

Size control is not the only feature that is influenced during nucleation and growth. Monomer concentration also plays a decisive role in shaping nanocrystals.^[75] At low concentrations or after prolonged growth, the system favors thermodynamic equilibrium, producing stable spherical dots.^[80] At intermediate concentrations, isotropic growth yields spindle-shaped structures, while high concentrations can give rise to metastable anisotropic morphologies such as rods, driven by the stabilization of “magic-sized” clusters. Under conditions of extreme supersaturation, tetrahedral seeds can extend arms along their (111) facets, forming tetrapods.^[80-83] Over time, however, depletion of monomer supply shifts the system back towards equilibrium. Without replenishment, anisotropic structures revert toward spheres either through Ostwald ripening or intraparticle mass transfer. In practice, kinetic arrest combined with ligand stabilization enables the persistence of these otherwise metastable shapes.^[80]

Surface chemistry is equally critical to nanoparticle stability and function. The outer interface dictates solubility, reactivity, melting point, stability, and even electronic structure.^[30] It also governs how nanoparticles interact with their surroundings, controlling assembly into superlattices for device fabrication and conjugation with biomolecules in drug delivery.^[33, 84-87] During synthesis, stabilizing agents are introduced to prevent aggregation and precipitation. Electrostatic stabilization relies on charged ligands at the surface, creating repulsion between like-charged particles.^[79, 88-91] Both organic and inorganic capping materials can be used, typically binding through covalent or ionic interactions.^[33, 87] Steric stabilization uses bulky ligands, such as long alkyl chains in nonpolar solvents or amphiphilic polyethylene glycol (PEG) derivatives in polar systems, to physically prevent close contact.^[79, 92-94] Electrosteric stabilization combines both strategies, often using polymers.^[95-99] Functional ligands further influence nanoparticle solubility, morphology, and binding specificity,^[100-102] often attaching via thiols or amines.^[93, 103-105] These groups improve colloidal stability, passivate surface electronic traps, and in semiconductor QDs, dramatically enhance photoluminescence quantum yields.^[86, 106-107] Beyond stabilization, ligands define interparticle spacing in ordered assemblies and provide molecular handles for bioconjugation.^[33, 84-85]

Ligand chemistry can also be modified post-synthesis. Ligand exchange enables systematic replacement of native capping groups with competitors, tuning solubility, phase transfer, stability, and interfacial functionality.^[108-112] For organic ligands, both head and tail groups can be engineered independently through substitution chemistry, offering a versatile strategy to tailor nanoparticle interfaces for diverse applications.^[100]

Nanoparticles can be synthesized in a wide array of morphologies, each offering unique physical and chemical characteristics determined by their dimensionality and symmetry.^[113-114] Spherical nanoparticles, commonly formed via colloidal methods that promote isotropic growth, exhibit high symmetry and are widely used for studying size-dependent quantum confinement and surface plasmon resonance phenomena.^[38, 115] Anisotropic morphologies, in contrast, arise when growth is directionally dependent, leading to structures such as nanorods, nanowires, nanoplates, and branched architectures.^[116-118]

For instance, nanorods and nanowires typically result from anisotropic growth mechanisms like the vapor-liquid-solid (VLS) process or surfactant-directed solution-phase synthesis.^[70, 119-120] These elongated structures often exhibit direction-dependent properties, such as polarized photoluminescence and tunable longitudinal plasmon modes, making them useful in optoelectronics and photothermal therapy.^[117, 121-123] Nanodisks and nanoplates, achievable through micelle-assisted or photochemical methods, show distinctive optical signatures due to their planar symmetry.^[124-125] Branched nanostructures such as tetrapods, bipods, and star-shaped crystals, often arise from seed-mediated growth under surfactant control and exhibit

enhanced charge separation and field enhancement effects.^[126-127] Core/shell nanocrystals, where one material is epitaxially grown around another, allow fine-tuning of electronic structure, surface passivation, and stability.^[106, 128-129]

Beyond these examples, nanomaterials have also been engineered into nanostars, nanocubes, etc., each providing tailored optical, catalytic, or electronic behaviors based on their anisotropic geometries.^[127, 130-132] These morphologies are not merely aesthetic variants; rather, their asymmetry induces direction-dependent properties, commonly referred to as anisotropy. Anisotropic nanomaterials differ from their isotropic counterparts in that their physical, chemical, and optical behaviors vary with direction making them uniquely suited for applications that exploit polarization, directional transport, or enhanced local fields.^[117, 133-134] Anisotropy can influence multiple phenomena including surface plasmon resonance (SPR), photoluminescence, charge mobility, and catalysis. For example, gold nanorods exhibit dual SPR modes (transverse and longitudinal) depending on their aspect ratio.^[22, 134] CdSe/CdS dot-in-rods (DiRs) show polarized emission and suppressed blinking due to shape-induced electronic confinement.^[23, 135] As such, anisotropic nanostructures play a crucial role in modern nanotechnology, enabling advanced applications in theranostics, waveguiding, and bioimaging.

In the following sections, selected anisotropic nanomaterials relevant to this work, including CdSe/CdS DiRs and AuNRs, along with isotropic species such as gold nanoparticles will be introduced. Their synthesis, properties, and relevance in hybrid assemblies with biological scaffolds will be discussed in detail.

2.1.1 CdSe/CdS dot-in-rods

In semiconductors, electronic behavior is dictated by the energy band structure. Insulators have large band gaps (>4 eV) that prevent electron excitation under typical conditions, while conductors have overlapping valence and conduction bands that allow for free charge movement. Semiconductors sit between these extremes, with band gaps ranging from ~0.1 to 4.0 eV.^[136-137] Upon absorption of sufficient energy, electrons in a semiconductor can be excited from the valence band into the conduction band, leaving behind holes. The Coulombically bound electron-hole pair is referred to as an exciton.^[138-139] Radiative recombination of this exciton gives rise to fluorescence, with the photon energy corresponding to the material's band gap.^[140] When semiconductor materials are reduced to nanometer-scale dimensions, they exhibit a phenomenon known as the quantum size effect.^[141-142] As the particle size approaches the exciton Bohr radius, quantum confinement leads to discrete energy levels and an increase in the effective band gap. This alters the optical and electronic

properties dramatically compared to bulk materials. Materials exhibiting these effects are known as quantum dots (QDs).^[30, 38] One of the most distinctive features of QDs is their size-dependent fluorescence: Smaller QDs emit at shorter (blue) wavelengths, while larger QDs fluoresce at longer (red) wavelengths (Figure 2.2).^[142-143]

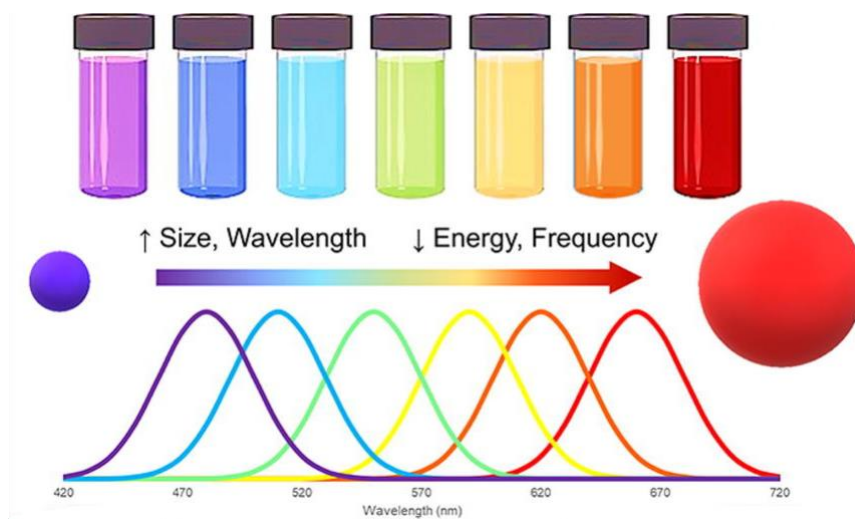


Figure 2.2: Illustration of the size-dependent optical properties of QDs. With increasing size, the emission wavelength increases, while the energy and frequency drop. Figure adopted from reference Wagner et. al^[144] with permission from Elsevier, copyright 2019.

These tunable optical properties, along with narrow emission spectra and high brightness, make QDs ideal candidates for applications in bioimaging, sensing, optoelectronics, and photovoltaics.^[143, 145-147] However, traditional spherical QDs have limitations, particularly regarding photostability, blinking behavior, and emission polarization.^[148-151] To overcome these challenges, anisotropic nanostructures have been developed that offer direction-dependent electronic and optical behavior.^[24, 118]

The synthesis of CdSe/CdS DiRs is most commonly achieved through a seeded-growth mechanism, in which pre-formed CdSe QDs act as nucleation centers for the anisotropic overgrowth of CdS (Figure 2.3) Unlike isotropic core-shell growth, anisotropy arises because surface ligands selectively passivate certain crystallographic facets of CdS while leaving others more reactive.^[152] Phosphonic acids such as hexylphosphonic acid (HPA) and octadecylphosphonic acid (ODPA) preferentially bind to lateral facets, restricting growth, while the c-axis remains less passivated, enabling elongation into a rod-like geometry.^[153] Reaction parameters including precursor concentration, injection rate, and surfactant chemistry dictate whether the resulting heterostructure forms rods, tetrapods, or isotropic shells.^[70] Advances in synthetic control, particularly slow-injection protocols, minimize lattice mismatch defects and trap states at the CdSe/CdS interface, yielding nanorods with near-unity photoluminescence quantum yields.^[154] By tuning shell thickness and aspect ratio, charge-carrier distribution can

be engineered: thicker shells passivate surface traps and promote electron delocalization along the rod, which in turn extends exciton lifetime and reduces nonradiative Auger recombination.^[155] This facet-selective, ligand-mediated growth mechanism is therefore central to the unique optical properties and stability of CdSe/CdS DiRs.

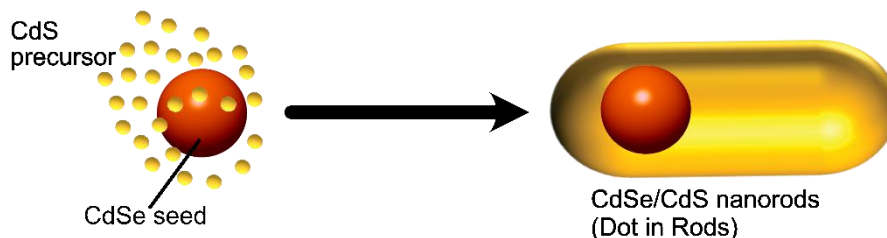


Figure 2.3: Schematic of seeded growth mechanism for CdSe/CdS DiRs. CdSe nanocrystals serve as seeds for anisotropic CdS shell growth. Selective ligand passivation of lateral facets promotes elongation along the c-axis, yielding a rod-like heterostructure

The electronic structure of CdSe/CdS DiRs is defined by a quasi-type-II band alignment. The large valence band offset confines holes within the CdSe core, while electrons are partially delocalized along the CdS shell.^[156] This spatial separation of carriers reduces nonradiative Auger recombination, which is one of the dominant mechanisms limiting fluorescence efficiency in spherical QDs. As a result, DiRs display bright, stable fluorescence with reduced blinking behavior compared to isotropic QDs.^[24] The longer exciton lifetimes that arise from spatial separation also enable more efficient radiative recombination, thereby enhancing overall emission brightness.^[24, 156]

One of the most important performance metrics for fluorescent nanocrystals is the photoluminescence quantum yield (PLQY), defined as the ratio of photons emitted to photons absorbed.^[157] High PLQY indicates efficient suppression of trap-assisted nonradiative decay pathways. In CdSe/CdS DiRs, thick CdS shells play a central role by passivating surface states and minimizing carrier recombination at defects, which often results in PLQYs exceeding 80-90% under optimized conditions.^[118] Methods such as slow-injection shell growth have been shown to produce DiRs with near-unity PLQY, controlled crystallinity, and minimized surface defects, all of which are essential for achieving optimal fluorescence.^[154] Conversely, thinner shells or poorly controlled growth conditions can introduce interface traps, lowering PLQY and broadening emission spectra. Beyond efficiency, the elongated shell geometry also imparts polarized emission along the long axis of the nanorod. The degree of emission anisotropy depends not simply on rod length but on the ratio of CdSe core size to CdS shell diameter, as well as shell thickness.^[118] Such polarized fluorescence is advantageous in applications that rely on directional emission, including display technologies and optical circuitry. Furthermore, anisotropic geometries suppress fluorescence intermittency

(“blinking”) by spatially separating carriers and reducing electron-hole overlap, ensuring more consistent emission compared to spherical QDs.^[24]

Despite their excellent intrinsic fluorescence, the surface chemistry of as-synthesized CdSe/CdS DiRs often limits their applicability.^[158-159] Native ligands such as trioctylphosphine oxide (TOPO) and octadecylphosphonic acid (ODPA) can only stabilize nanocrystals in organic solvents.^[70, 158] These hydrophobic coatings are incompatible with aqueous media and biological systems, making post-synthetic ligand exchange essential.^[54, 160-161] For biomedical applications such as biosensing, bioimaging, and diagnostics, the ability to transfer DiRs into water while maintaining their fluorescence properties is critical. Ligand exchange strategies replace the long hydrophobic ligands with shorter, hydrophilic ones that introduce functional groups on the surface. Hydrophilic thiols such as mercaptopropionic acid (MPA) and aminoethanethiol (AET) can efficiently displace native ligands, producing water-dispersible DiRs with reactive terminal groups (-COOH, -NH₂, -SH) that facilitate covalent coupling to biomolecules.^[160-162] Similarly, biogenic ligands such as cysteine and glutathione improve biocompatibility and aqueous stability while preserving relatively high PLQY.^[159] The chemical identity of the ligand is crucial: carboxylates enhance dispersibility, amines provide reactive sites for conjugation, and zwitterionic ligands suppress nonspecific protein adsorption in biological fluids.^[163]

A persistent challenge in ligand exchange is the trade-off between water solubility and retention of optical quality. Short-chain monodentate ligands provide efficient phase transfer but can compromise surface passivation, introducing trap states that quench fluorescence.^[160, 164] Quantitative studies of ligand exchange dynamics confirm that thiols, carboxylates, and phosphonates compete differently for surface binding, and incomplete coverage can lower quantum yield.^[160] To address this, multidentate and polymer-based ligands have been designed to provide stronger, more stable passivation. Dihydrolipoic acid (DHLLA) derivatives, especially when conjugated to polyethylene glycol (PEG), have emerged as particularly effective coatings. These ligands provide multivalent anchoring to the CdS shell, maintain compact and stable hydration shells, and reduce nonspecific interactions.^[110] Importantly, DHLLA-PEG coatings suppress surface trap states and preserve high PLQY even after transfer into polar solvents. They also extend colloidal stability under physiological conditions and enhance circulation times *in vivo*, making them highly attractive for bioimaging and diagnostic use.^[54, 100] NMR-based analyses further demonstrate that multidentate ligands displace native oleates more effectively than monodentate thiols, leading to more complete passivation and more reproducible fluorescence.^[164]

Beyond simple solubility, ligand engineering enables modular functionalization of DiRs. PEGylated ligands with terminal carboxyl or amine groups allow straightforward conjugation to proteins, peptides, or antibodies, while zwitterionic coatings improve stability against aggregation in high-salt or protein-rich environments.^[101] Such advances transform CdSe/CdS and CdSe/CdTe DiRs from hydrophobic, synthesis-limited nanocrystals into versatile, biocompatible probes. Their narrow emission spectra, high brightness, suppressed blinking, and retained PLQY make them particularly promising for biomedical applications.

In the context of this work, ligand-exchanged DiRs will serve as the foundation for further biocompatibility enhancement through encapsulation into protein nanocages. Protein encapsulation offers several benefits: It shields the inorganic core from direct interaction with the biological environment, reduces cytotoxicity, and allows precise spatial organization through the protein scaffold. This strategy builds on the advantages of ligand exchange: Aqueous solubility, surface functionality, and fluorescence retention; while adding an additional level of biological stability and modularity. As such, encapsulated DiRs have strong potential as multifunctional platforms for biosensing, fluorescence imaging, and diagnostic applications.

2.1.2 Gold Nanorods

Gold nanostructures represent one of the most extensively studied classes of nanomaterials owing to their remarkable optical, electronic, and chemical properties.^[165] Depending on morphology, gold nanostructures can exist as spheres, rods, cubes, stars, or atomically precise clusters, each exhibiting distinctive physicochemical behavior.^[22, 115, 166] Among these, gold nanorods (AuNRs) are particularly attractive because of their strong shape-dependent localized surface plasmon resonance (LSPR), high photostability, and ease of surface modification.^[21-22, 167] This section focuses on AuNRs, which form one of the primary components of this work, while subsequent sections address gold nanoclusters and spherical nanoparticles that were also explored as part of the study. The inclusion of these additional morphologies highlights the broader versatility of gold nanostructures in nanobiotechnology, but AuNRs remain central due to their tunable optical properties in the visible-near-infrared (NIR) range and compatibility with biofunctionalization strategies.^[168-170]

The unique properties of AuNRs derive from the excitation of collective oscillations of conduction band electrons when illuminated with light, known as localized surface plasmon resonance (LSPR). Unlike spherical nanoparticles, which exhibit a single resonance band, AuNRs display two distinct plasmon modes (Figure 2.4) The transverse mode corresponding to oscillations along the short axis (~520 nm, nearly size-invariant) and the longitudinal mode

corresponding to oscillations along the long axis, tunable from the visible to the NIR region by varying aspect ratio.^[21-22] This tunability is critical because the NIR “biological window” (650-900 nm) allows deeper tissue penetration with reduced scattering and absorption, making AuNRs highly suitable for bioimaging and photothermal therapy.^[167, 170-173]

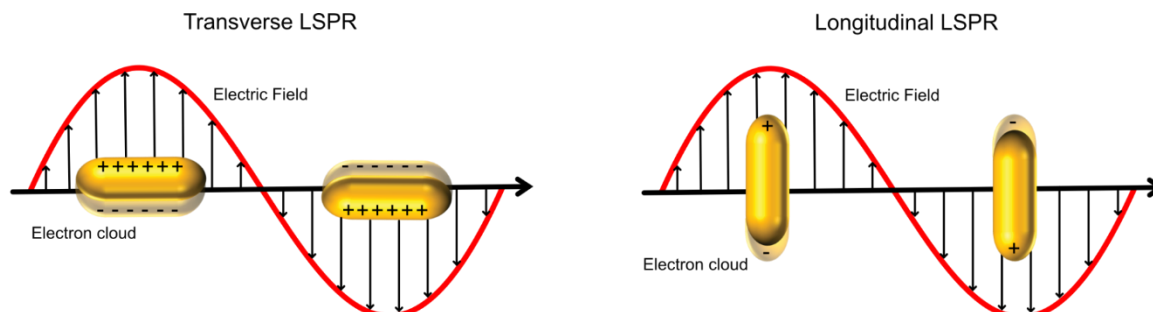


Figure 2.4: Schematics of localized plasmon resonance in AuNRs. Electron clouds oscillating along (left) the width and (right) the length of AuNRs, leading to transverse and longitudinal localized surface plasmon resonances (LSPRs), respectively.

Electromagnetic theory provides a framework for this anisotropy. According to Gans’ extension of Mie theory, the longitudinal plasmon peak position is strongly dependent on the aspect ratio, while peak intensity and width are influenced by dielectric environment and surface chemistry.^[174] (Figure 2.5) Quadrupolar modes can emerge in rods with larger diameters, further enriching their spectral behavior.^[175] Importantly, the high absorption cross-section of AuNRs, orders of magnitude higher than that of organic dyes, renders them efficient photothermal transducers. Upon NIR irradiation, the non-radiative relaxation of plasmons leads to localized heat generation that can ablate cells or trigger drug release.^[176]

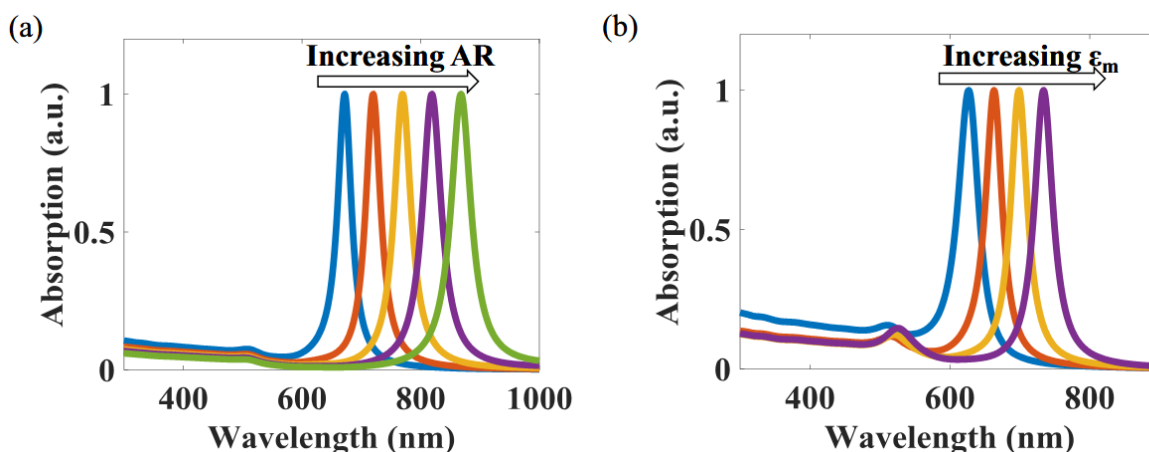


Figure 2.5: Self-normalized modelled absorption spectra showing the red shift in the Longitudinal Plasmon Resonance due to an increase in (a) the Aspect Ratio (AR) and (b) the Permittivity of the surrounding medium (ϵ_m). Figured adopted from Kumar et. al^[177] with permission from Springer Nature, copyright 2019.

Beyond linear optical effects, AuNRs also exhibit nonlinear phenomena, including multiphoton luminescence and enhanced Raman scattering. Their plasmonic “hot spots” can amplify local electromagnetic fields, enabling surface-enhanced Raman spectroscopy (SERS) at single-molecule sensitivity.^[178] Furthermore, AuNRs demonstrate photostability superior to organic fluorophores and QDs, resisting photobleaching under prolonged illumination.^[121] Collectively, broad spectral tunability, strong light-matter interactions, and high stability make AuNRs versatile tools across photonics, sensing, and biomedicine.^[21, 167, 170, 179]

The most widely employed method for AuNR synthesis is the seed-mediated growth strategy, originally refined by the groups of Murphy and El-Sayed.^[119, 180] In this approach, small gold seeds (1-3 nm) are first generated by reducing tetrachloroauric(III) acid (HAuCl_4) with a strong reductant (e.g., sodium borohydride, NaBH_4) in the presence of surfactants such as hexadecyltrimethylammonium bromide (CTAB). These seeds are then introduced into a growth solution containing additional HAuCl_4 , a mild reductant (ascorbic acid), CTAB, and often silver nitrate (AgNO_3). Under these conditions, anisotropic growth occurs preferentially along the crystallographic [001] direction, leading to rod-shaped nanocrystals.^[181]

Several factors influence rod morphology but the role of CTAB is central. It forms a bilayer around the growing nanocrystals, stabilizing specific crystal facets and directing anisotropic elongation. Silver ions introduced as AgNO_3 deposit on [110] side facets via underpotential deposition, selectively blocking lateral growth and promoting elongation along the rod axis.^[182] This synergistic effect of surfactant micelles and silver ions is widely accepted as the main driving force behind rod formation. Molecular dynamics simulations further support this view, showing that anisotropic growth is facilitated by the epitaxial adsorption of CTAB onto developing facets.^[183] The differing adsorption energies induce passivation at the (110) and (100) surfaces, while reduction proceeds preferentially on the (111) facet, thereby driving anisotropic elongation. In addition, the micellar morphology and surface chemistry of CTAB, governed by ionic strength and counterion population, play a decisive role in enabling facet-selective passivation and stabilizing the epitaxial gold surfaces.^[119, 181, 184] Alternative mechanistic models have also been proposed, emphasizing either electrostatic stabilization of facets or micellar templating effects.^[185]

Aspect ratio is tuned by varying seed concentration, silver ion content, ascorbic acid concentration, CTAB concentration and several secondary growth parameters.^[186-189] Increasing seed concentration leaves less precursor for more particles, producing shorter AuNRs with lower aspect ratios, while fewer seeds promote longer AuNRs but at the expense of monodispersity.^[185, 190] Silver ions are central to anisotropic growth by depositing on side facets to suppress lateral expansion; higher Ag^+ levels push AuNRs to higher aspect ratios, but excessive concentrations or halide impurities promote polydispersity and irregular

morphologies.^[119, 191-192] Ascorbic acid, acting as a mild reductant, tunes the growth rate: low concentrations favor controlled anisotropy, while high concentrations accelerate reduction, compromise facet selectivity, and may initiate secondary nucleation.^[193] CTAB provides both bromide and a micellar environment that stabilizes rod sidewalls; concentrations below the critical micelle concentration (CMC) lead to spherical particles, while excess CTAB alters silver availability through silver bromide (AgBr) formation and complicates growth kinetics.^[188] The choice of halide counterion further determines morphology, with bromide strongly favoring anisotropy by selectively binding to the side facets while chloride shifting the system toward spherical growth.^[194-196] Temperature also plays a key role by accelerating growth kinetics and shifting the balance between end and side deposition, which alters the aspect ratio distribution.^[197] Finally, pH modulates the activity of ascorbic acid; acidic conditions suppress unseeded nucleation and help maintain controlled growth, whereas higher pH accelerates reduction and broadens size and shape distributions.^[198]

Beyond the classical ascorbic acid-based protocol, alternative reductant and cosurfactant systems have been explored to improve reproducibility and yield. One such strategy employs hydrogen peroxide (H₂O₂) in place of ascorbic acid.^[199] H₂O₂ provides a milder and more controllable redox environment, slowing the reduction of Au³⁺ to Au⁰ and thereby suppressing uncontrolled secondary nucleation. This moderated reduction process allows for more precise control over rod aspect ratios while maintaining the facet-selective stabilization by CTAB and Ag⁺ ions. The use of H₂O₂ is particularly advantageous when reproducibility across batches is critical, as the slower electron transfer kinetics reduce sensitivity to small variations in reaction conditions.

Another refinement involves the use of CTAB-decanol mixed surfactant systems in a symmetry-disconnected growth strategy.^[200] While 1-decanol alone can act as a weak reductant and modify the micellar packing environment, its combination with CTAB enhances the stability of micellar templates and provides stronger directional control over anisotropic growth. Decanol molecules intercalate into the CTAB bilayer, altering micelle curvature and surface energy distributions, which promotes anisotropy during the initial symmetry-breaking stage. By decoupling this anisotropy-inducing step from the subsequent elongation phase, the CTAB-decanol system enables higher yields of monodisperse AuNRs with more uniform aspect ratios. This approach also reduces the competing formation of spherical byproducts that often plague conventional one-pot syntheses.

Beyond seed-mediated methods, alternative routes include seedless photochemical growth,^[201] electrochemical deposition,^[202] and binary surfactant systems (e.g., CTAB/BDAC) to enhance monodispersity.^[193] Attempts to synthesize AuNRs without CTAB generally suffer from poor reproducibility and shape heterogeneity, underlining its critical role in directing

growth.^[203-204] The synthesis requires concentrated CTAB solutions (~0.1 M), even though surface coverage requires only micromolar amounts. Moreover, AuNRs become unstable when transferred to low surfactant concentration solutions (~0.1 mM < CTAB < 1 mM, in the order of their critical micelle concentration) and the continuous exchange between the free, bound and micellar CTAB maintains the stability.^[205-206] CTAB forms a tightly bound bilayer, confirmed by IR spectroscopy, thermogravimetric analysis, and ζ -potential.^[22, 207-209] The appearance of a Raman signal due to the Br-Au bond suggests that the hydrophobic alkane chain would be exposed to the solution while the trimethyl ammonium head would interact with the bromide adsorbed in the surface.^[210] This organization facilitates the formation of the second layer. This structure ensures colloidal stability but is also strongly cytotoxic.^[206, 211-213] CTAB known to disrupt cellular membranes and compromise viability.^[214]

As a result, ligand exchange after synthesis becomes essential, replacing CTAB with biocompatible molecules that preserve colloidal stability while enabling biomedical use.^[204, 215-220] Monodentate thiols such as mercaptoundecanoic acid (MUA) represent one of the simplest exchange strategies, replacing CTAB with a carboxyl-terminated ligand that improves water dispersibility and provides reactive -COOH groups for further conjugation.^[204, 216, 221] Similarly, cationic thiols such as (11-mercaptoundecyl)-N,N,N-trimethylammonium bromide (MUTAB) impart positive surface charge, facilitating interactions with negatively charged biomolecules like nucleic acids and proteins.^[14, 168, 219, 222] These two ligands are central to this work, offering complementary functionalities: carboxyl groups for covalent coupling and cationic surfaces for electrostatic assembly.

However, simple thiol ligands often lead to reduced colloidal stability under high ionic strength. To address this, PEG-thiols are widely employed. PEGylation confers “stealth” properties, minimizing nonspecific protein adsorption and extending circulation times in vivo.^[223-225] Zwitterionic ligands represent another class, balancing charges to achieve ultra-stable dispersions under physiological conditions.^[226-227]

Multidentate ligands, such as lipoic acid derivatives and polymers, bind more strongly and resist desorption, yielding robust AuNR dispersions.^[228-229] Phase transfer methods, including the “round-trip” strategy, temporarily move AuNRs into organic solvents for ligand replacement, followed by re-transfer into water, offering efficient functionalization routes.^[168] Quantitative NMR and spectroscopy studies have revealed that exchange efficiency depends strongly on ligand denticity and head-group chemistry, with multidentate ligands achieving more complete CTAB removal.^[216] Ultimately, ligand exchange balances colloidal stability, optical retention, and biocompatibility. Careful engineering enables AuNRs to maintain sharp plasmon resonances while becoming compatible with biological media which is a prerequisite for downstream biomedical applications.

In this thesis, AuNRs are employed alongside CdSe/CdS DiRs to generate a hybrid bionanomaterial. Following synthesis via the seed-mediated route, AuNRs were subjected to ligand exchange with MUTAB and MUA. By integrating ligand-exchanged AuNRs into protein frameworks, this work leverages their strong NIR absorption, high photothermal conversion efficiency, and stable surface chemistry to enable applications in biosensing, bioimaging, and diagnostics. In this context, AuNRs provide not only a model plasmonic system but also a practical nanoplatform with significant translational potential.

2.1.2.1 Gold Nanoclusters

Gold nanoclusters (AuNCs) represent a unique class of nanostructures that bridge the gap between small molecules and larger plasmonic nanoparticles. Unlike AuNRs or nanoparticles, which exhibit size-dependent surface plasmon resonance (SPR), nanoclusters typically consist of fewer than a few hundred atoms, with sizes below 2 nm. At this ultrasmall regime, the electronic structure of AuNCs is discretized, resembling molecular orbitals rather than continuous bands, which fundamentally alters their optical and chemical behavior. Consequently, AuNCs often exhibit intrinsic photoluminescence, high catalytic activity, and unusual stability, distinguishing them from larger gold nanostructures.^[230-231]

The synthesis of gold nanoclusters has been achieved by a variety of methods, most of which rely on strong ligand stabilization to prevent aggregation and growth into larger particles. Common approaches include reduction of Au precursors (e.g., HAuCl₄) in the presence of thiols, dendrimers, or proteins, where the ligands stabilize the cluster surface and dictate nuclearity.^[232-233] Of particular interest to the present work is the formation of AuNCs via chemical etching of larger nanostructures such as AuNRs or AuNPs. In these processes, oxidative etching agents selectively corrode the metallic framework, releasing small, ligand-stabilized clusters. Banerjee *et al.* demonstrated that blue-emitting AuNCs could be generated by etching AuNRs in the presence of CTAB and halide ions, with luminescence emerging as the plasmonic structure disintegrated into molecular-sized species.^[234] This etching pathway has been exploited both as a method of synthesizing luminescent clusters and as a sensing platform. Similarly, other studies have reported that oxidative species such as hydrogen peroxide or halogens accelerate etching processes, producing ultrasmall clusters stabilized by residual ligands or added thiols.^[181, 235] The exact mechanism depends strongly on the balance between oxidative agents and available ligands: while excess oxidants drive dissolution, the ligands cap emerging nuclei, kinetically arresting growth at the cluster stage.

The physicochemical properties of AuNCs are distinct from plasmonic nanoparticles. Due to their ultrasmall size, they lack collective electron oscillations and instead exhibit molecule-like

absorption features. Photoluminescence is a hallmark property: AuNCs display size- and ligand-dependent emission spanning the visible to near-infrared range, with quantum yields that can exceed 40% when surface passivation is optimized.^[233] The emission arises from metal-ligand charge transfer or core-shell transitions, both tunable through ligand selection and cluster nuclearity. Their ultrasmall size also confers renal clearance and reduced cytotoxicity, making them attractive for biomedical applications.^[236]

In the context of this work, the appearance of AuNCs was unplanned, emerging from attempts at ligand exchange on AuNRs. While the precise mechanism of their formation in this system remains unresolved, the literature on chemical etching of AuNRs and AuNPs suggests that oxidative pathways, combined with ligand stabilization, are likely responsible for cluster formation. Although a reducing agent was present in the system, localized oxidative conditions or imbalances in redox dynamics may still allow partial etching to occur. The resulting clusters, despite being unexpected, offer an opportunity to explore their optical and biochemical behavior. Their strong intrinsic luminescence and biocompatibility make them attractive probes for biosensing and diagnostics, complementing the broader focus of this study on fluorescent nanomaterials.

2.1.3 Gold Nanoparticles

Gold nanoparticles (AuNPs) are among the earliest known nanomaterials, with their use dating back centuries in stained glass and decorative ceramics. Their scientific exploration began with Faraday's work in the mid-19th century, which established the link between their vibrant optical properties and nanoscale size rather than bulk gold behavior.^[115] Since then, AuNPs have become one of the most extensively studied nanomaterials, owing to their remarkable plasmonic, electronic, and chemical properties. In modern research, AuNPs are considered model systems in nanoscience and indispensable tools across catalysis, sensing, imaging, and medicine.^[57, 237-240]

Several synthetic strategies have been developed for producing colloidal gold nanoparticles, but chemical reduction remains the most widely applied due to its simplicity and reproducibility.^[241-242] Among these, the classical Turkevich method, introduced in the 1950s, is still regarded as a cornerstone in colloidal gold chemistry.^[243] In this approach, HAuCl_4 is reduced by trisodium citrate in boiling aqueous solution, where citrate simultaneously acts as a reducing and stabilizing agent. The method produces spherical nanoparticles with sizes typically in the range of 10-20 nm, and particle size can be tuned by varying the citrate-to-gold ratio.^[244] Despite its limitations in controlling anisotropy or polydispersity, the Turkevich synthesis laid the groundwork for modern developments such as the Frens modification^[245]

and seed-mediated approaches, which extend size control and enable the generation of anisotropic structures like AuNRs.^[119, 246-247]

In the seed-mediated method, small gold seeds are first generated by reducing HAuCl_4 with a strong reductant such as NaBH_4 , and then added to a growth solution containing additional precursor, a mild reductant, and stabilizing surfactants.^[195, 247-248] Hexadecyltrimethylammonium chloride (CTAC) is commonly used as the surfactant in this process, forming a bilayer on the nanoparticle surface to direct growth and prevent aggregation.^[195, 249] It also strongly influences nucleation and growth kinetics by modulating the local ionic environment and binding selectively to crystal facets; thus contributing to the growth of spherical seeds without noticeable shape change.^[250-251] Control over reaction parameters such as seed concentration, reductant strength, and CTAC concentration enables fine-tuning of particle size, monodispersity, and stability.^[195, 252]

However, CTAC (just like its analogue CTAB) presents a significant challenge for biomedical applications. These surfactants form a tightly bound bilayer on the AuNP surface, which is cytotoxic and unstable under physiological conditions.^[206, 211-213] To address this, ligand exchange strategies are employed to replace surfactants with biocompatible ligands while retaining colloidal stability and functional surface chemistry. A wide range of ligands have been explored for this purpose.^[253-256] Thiol-containing small molecules such as mercaptohexanoic acid or mercaptopropionic acid bind strongly to gold surfaces via Au-S bonds, introducing carboxylate or amine groups for further functionalization.^[255-256] Poly(ethylene glycol) (PEG)-based ligands are especially important, as they provide steric stabilization, extend circulation times in vivo, and reduce nonspecific protein adsorption.^[229, 257-258] Zwitterionic ligands, bearing both positive and negative charges, confer exceptional resistance to nonspecific interactions in biological fluids, making them attractive for long-term stability.^[259-260] Polymer coatings, such as polyvinylpyrrolidone (PVP), also stabilize nanoparticles while permitting functionalization.^[261-262]

Beyond small-molecule ligands, direct functionalization with biomolecules has become a central strategy in tailoring AuNPs for biomedical use. Peptides and proteins can be attached through thiol or amine groups, enabling specific interactions with biological targets.^[263-265] DNA-functionalized AuNPs are a particularly well-developed system: the strong and programmable hybridization properties of DNA allow construction of highly ordered assemblies and ultrasensitive biosensors.^[266-268] Antibodies, aptamers, and other targeting ligands have also been conjugated to AuNPs, allowing selective recognition of cells or biomolecules of interest.^[269-270] These ligand-exchange and bioconjugation strategies not only transform AuNPs into water-soluble and biocompatible probes but also provide modular functional handles for integration into more complex architectures.

The intrinsic properties of AuNPs further justify their widespread adoption. Their most characteristic feature is localized surface plasmon resonance (LSPR), arising from the collective oscillation of conduction electrons under incident light.^[271] (Figure 2.6) LSPR leads to intense absorption and scattering, with resonance wavelength tunable by particle size, shape, and surrounding dielectric environment.^[272-273] This sensitivity makes AuNPs powerful optical probes and provides the basis for colorimetric detection, where aggregation or refractive index changes shift the plasmon band.^[274-275] Their high extinction coefficients, resistance to oxidation, and strong photothermal conversion efficiency distinguish them from other metal nanostructures.^[202, 242, 276] At smaller sizes, AuNPs also show unique catalytic behavior, acting as efficient platforms for reactions such as CO oxidation or selective hydrogenation.^[277-279] When surface-modified, their biocompatibility and stability in physiological environments further expand their range of applications.

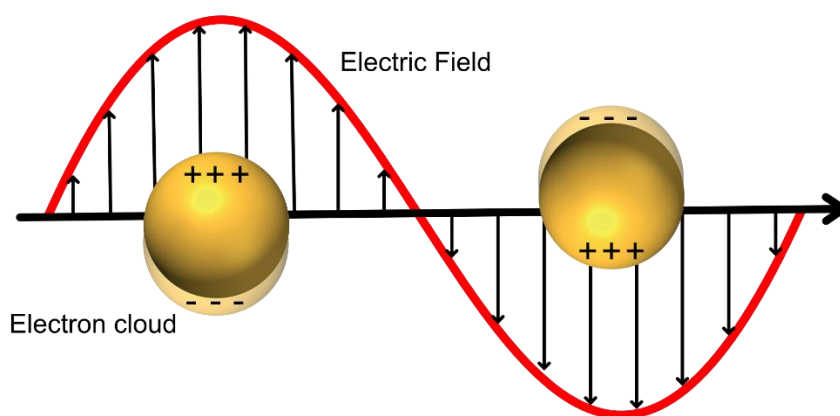


Figure 2.6: Schematic diagram of localized plasmon resonance in nanoparticles.

These properties translate directly into diverse applications. AuNPs are used as contrast agents in imaging modalities such as dark-field microscopy, computed tomography, and optical coherence tomography, where their strong scattering and high electron density enhance visibility.^[171, 280-281] Their tunable LSPR and ability to enhance electromagnetic fields underpin their role in sensing platforms, particularly in surface-enhanced Raman scattering (SERS) and localized plasmonic biosensors.^[238, 268, 276] In therapeutics, AuNPs are employed in photothermal therapy, where near-infrared irradiation of tumor-localized particles produces localized heating and selective destruction of cancer cells^[176, 265, 282-283] Their surface chemistry also enables drug and gene delivery: Conjugation with small molecules, peptides, or nucleic acids provides targeted transport and controlled release.^[284-285]

In the context of this work, AuNPs synthesized with CTAC surfactant and subsequently subjected to ligand exchange will be further integrated into protein nanocages. Encapsulation in protein cages not only stabilizes the inorganic core but also provides biocompatibility and programmability through engineered amino acid residues. This dual strategy, ligand exchange

for water solubility and bioconjugation, followed by encapsulation for structural control; positions AuNPs as versatile, bright, and stable platforms for biosensing, bioimaging, and diagnostic applications.

2.2 Protein Cages

Protein cages are a diverse class of supramolecular assemblies that form hollow, nanoscale compartments through the self-assembly of protein subunits. Typically ranging from 10 to 50 nm in diameter, (Figure 2.7) these cages adopt highly symmetrical geometries such as icosahedrons, octahedrons, or dodecahedrons.^[8, 286] They are defined by structural regularity, monodispersity, and robustness, and, unlike membrane-bound organelles, they rely exclusively on protein-protein interactions for their assembly and integrity. Protein cages occur broadly in nature, serving roles in iron storage, genome protection, enzymatic compartmentalization, and metabolic channeling. Their genetically encoded structures provide direct links between sequence and architecture, enabling rational manipulation and making them attractive platforms for bioengineering and nanotechnology.^[286-287]

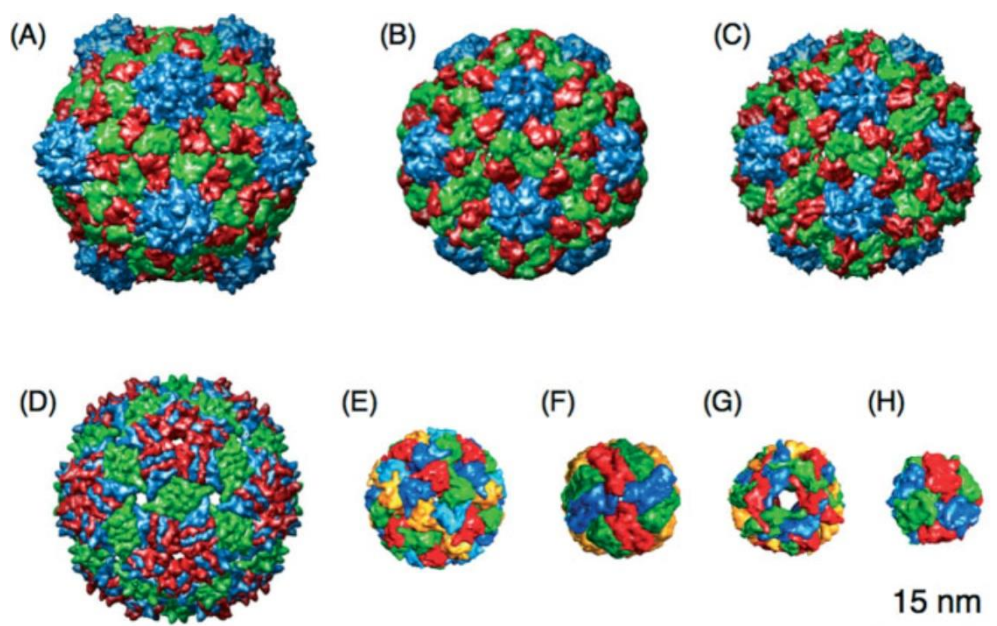


Figure 2.7: Schematic overview of major protein cage types. A) Cowpea mosaic virus 31 nm in diameter, B) Brome mosaic virus 28 nm in diameter, C) Cowpea chlorotic mottle virus 28 nm in diameter, D) MS2 bacteriophage 27 nm in diameter, E) lumazine synthase 15 nm in diameter, F) ferritin 12 nm in diameter, G) small heat shock protein 12 nm in diameter, H) DNA binding protein from starved cells 9 nm in diameter. Figure adopted from Uchida et. al^[8] with permission from Wiley & Sons, copyright 2007.

Protein cages are highly symmetrical assemblies, most commonly icosahedral, formed through non-covalent interactions between protomers. Shell complexity is described by the triangulation number (T), which defines diameter and subunit count.^[288-289] Three chemically distinct interfaces are functionally important: the interior (for encapsulated cargo or mineralization), the exterior (for surface display and targeting), and the inter-subunit contacts (governing stability and assembly).^[8, 286] The examples that follow illustrate how this basic architectural principle has been adapted to create compartments with varying levels of complexity and function, from simple symmetric shells to highly anisotropic nanomachines.

2.2.1 Anisotropic Protein Containers in Nature

While many protein cages exhibit high symmetry, some of the most functionally sophisticated systems in nature are characterized by a deliberate break in symmetry, or anisotropy. This structural and functional directionality is essential for complex tasks such as directional assembly, targeted delivery, and the establishment of biochemical polarity.

The most overt examples of anisotropy are found in non-spherical viruses (Figure 2.8). The Tobacco Mosaic Virus (TMV) is a classic example, forming a rigid helical rod that is anisotropic in all dimensions. Its coat proteins assemble around a single RNA genome into a filament of precisely defined length, a structure fundamentally different from an icosahedral cage.^[290-291] Similarly, the Alfalfa Mosaic Virus (AMV) forms bacilliform particles, a clear departure from spherical symmetry. Unlike true spherical viruses, AMV assembly is governed by a specific protein-RNA interaction that initiates the formation of its characteristic tapered rods. This results in a series of particles with varying lengths, all based on a bacilliform architecture rather than a fixed icosahedral shell.^[292-293]

A more complex form of anisotropy is exhibited by tailed bacteriophages. Viruses like the T4 phage combine an icosahedral head with a unique portal complex at a single vertex.^[294-296] This portal serves as the exclusive channel for genome packaging and is the attachment point for a complex tail structure. The entire assembly, symmetric head, asymmetric portal, and anisotropic tail, creates a molecular machine with a definitive front and back, optimized for host recognition and DNA injection.

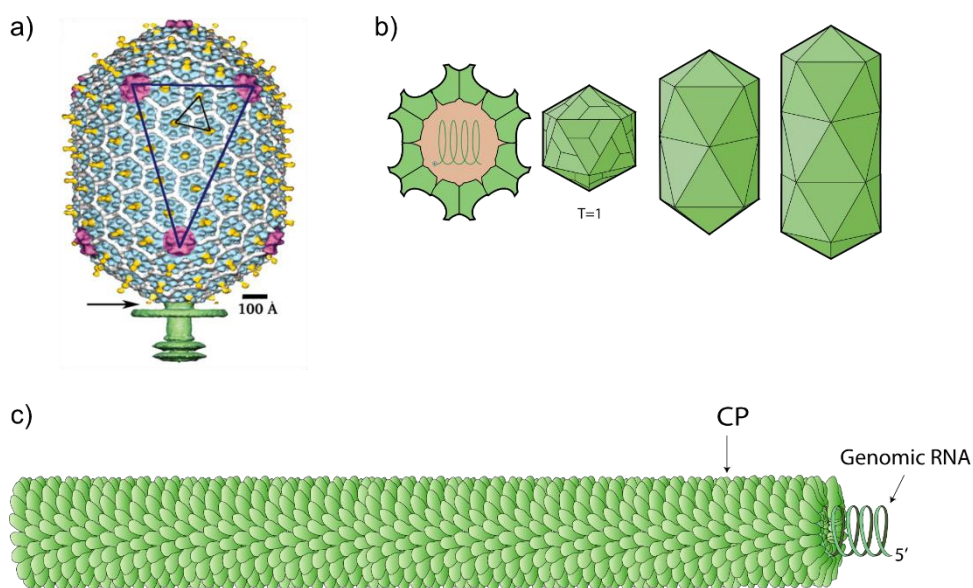


Figure 2.8: Schematic showing the anisotropic containers found in nature. a) Structure of the bacteriophage T4 head. Shaded surface representation of the cryo-EM reconstruction viewed perpendicular to the fivefold axis. Image adapted from Fokine et. al^[296] with permission from PNAS, copyright 2004. b) Bacilliform virions of Alfalfa mosaic virus, with a constant diameter of 18 nm. Three genomic and one subgenomic RNA segments are encapsidated in distinct particles, resulting in different virion types. Adapted from ViralZone, Swiss Institute of Bioinformatics (<https://viralzone.expasy.org/>), licensed under CC BY 4.0. c) Tobacco mosaic virus virions are non-enveloped, rigid helical rods with helical symmetry. Each virion is approximately 18 nm in diameter and 300–310 nm in length. CP: Coat Protein. Adapted from ViralZone, Swiss Institute of Bioinformatics (<https://viralzone.expasy.org/>), licensed under CC BY 4.0.

On a larger scale, Bacterial Microcompartments (BMCs) represent a larger class of protein cages, typically 50-200 nm, built from multiple protein families forming hexameric, pentameric, and trimeric building blocks.^[297] They encapsulate metabolic pathways such as CO₂ fixation (carboxysomes) or catabolism of ethanolamine and propanediol (metabolosomes).^[298] Their modularity allows bacteria to isolate toxic intermediates or enhance flux through metabolic bottlenecks. Their modular shell composition creates a compartment with functional anisotropy, where distinct pores and surfaces serve specialized roles in substrate selectivity.

In summary, these examples demonstrate that anisotropy is a powerful and recurring design principle in natural protein containers. It enables functionalities that are impossible for purely symmetric spheres, providing a clear inspiration for engineering directional properties into synthetic biohybrid systems.

2.2.2 Common Symmetric Protein Cages

The majority of well-studied protein cages exhibit high symmetry, which provides a robust and efficient framework for encapsulation. Ferritin is one of the most studied protein cages and functions as the primary intracellular iron reservoir. It assembles from 24 identical subunits

into an octahedral cage with an outer diameter of ~12 nm and an internal cavity of ~8 nm.^[299] Iron ions enter through gated pores and are oxidized at ferroxidase centers, leading to nucleation of ferric oxyhydroxide inside the cavity. This coupling of transport and catalysis allows ferritin to safely mineralize up to 4,500 iron atoms per cage.^[299] Beyond iron, engineered ferritins have been used to mineralize other metals such as cobalt, nickel, and palladium as the respective oxides, positioning them as versatile biological nanoreactors.^[300]

Viral capsids exemplify protein cages optimized for stability and delivery. Their structures follow rules of icosahedral symmetry, where $T = 1$ corresponds to 60 subunits and $T = 3$ to 180.^[289] This symmetry allows identical subunits to assemble into progressively larger and more complex shells. Capsids are metastable: resistant to external stress yet primed to disassemble upon infection, making them central models of self-assembly and dynamics. Virus-like particles (VLPs), which are the capsids composed only of coat proteins but not viral cargo are widely used in vaccine development and nanotechnology.^[301-302]

Lumazine synthase, an enzyme in riboflavin biosynthesis, forms a native 60-mer cage of ~16 nm diameter.^[303] Engineering of its luminal residues has produced expanded 180- and 360-subunit cages with larger diameters and pores, enabling encapsulation of additional or non-native cargo.^[304]

Pores located at symmetry axes regulate transport, typically 3-5 Å in ferritin and up to 15 Å in engineered cages.^[299, 303] Dynamic pores that undergo conformational switching have also been observed, suggesting mechanisms for regulated gating.^[305]

Beyond their architectural diversity, protein cages share a functional strategy: encapsulation of specific cargo. This feature underlies their advantages in nature and explains why they have been repeatedly adapted for different tasks. Encapsulation provides distinct advantages. Cargo proteins experience enhanced local concentrations and increased catalytic rates, while toxic intermediates are sequestered from the cytosol.^[306] Encapsulation can also stabilize proteins against proteolysis or denaturation. These features reflect evolutionary convergence: structural motifs like the Hong Kong 97 (HK97) fold, originally viral in origin, have been repurposed in prokaryotic systems to achieve metabolic regulation through compartmentalization.^[307]

Protein cages are genetically encoded, making them highly tractable for engineering (Figure 2.9). Interior modifications enable loading of peptides, enzymes, or nanoparticles; ferritin variants with metal-binding motifs have been used to nucleate silver and palladium nanoparticles.^[300] Exterior surfaces have been functionalized with epitopes, fluorophores, and polymers for targeting or imaging.^[308] Subunit mutagenesis enables control over pore size and permeability, as demonstrated in engineered lumazine synthase.^[304-305] Applications include

nanomaterial synthesis (templating of inorganic nanoparticles), biocatalysis (cage-based nanoreactors), and biomedicine (drug delivery vehicles, vaccines, and imaging agents).^[309-311] Their robustness and programmability make protein cages unique scaffolds bridging biology and materials science.

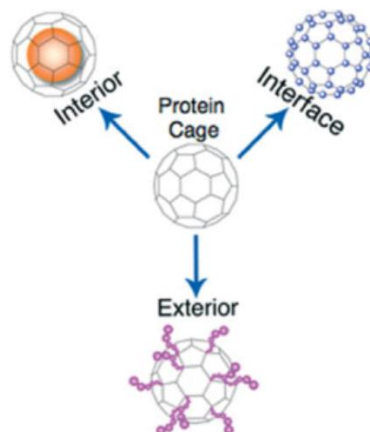


Figure 2.9: Schematic illustration of the three interfaces in a protein cage architecture available for chemical or genetic modification. Image adopted from Uchida et. al^[8] with permission from Wiley & Sons, copyright 2007.

Other related systems include vault particles in eukaryotes and bacterial magnetosomes. Vaults are ribonucleoprotein cages (~40 nm) of uncertain physiological function, while magnetosomes, though membrane-bound, illustrate nanoscale control of mineralization: Magnetotactic bacteria align chains of magnetite or greigite crystals to create cellular magnetic dipoles.^[312]

The examples above illustrate how protein cages use symmetry, confinement, and selective transport to achieve storage, protection, and compartmentalized chemistry. Encapsulins are a distinct subclass of these cages, found widely in bacteria and archaea, which encapsulate specific enzymes via short peptides, also called cargo-loading peptides (CLP). They combine viral-like architecture with defined biochemical functions, making them versatile models for programmable nanocompartments. In the next section, encapsulins will be discussed with a focus on their structural features, cargo selectivity, and representative examples from *T. maritima* and *M. xanthus*.

2.2.3 Encapsulins

Encapsulins are a class of protein nanocompartments that have been identified in a wide range of bacteria and archaea.^[287, 306, 313] First described in *Brevibacterium linens* in the mid-1990s as unusually large protein complexes, they have since been recognized as widespread elements of microbial genomes, often associated with operons that also encode dedicated

cargo proteins.^[314-315] Their defining feature is the ability to self-assemble into icosahedral protein shells that specifically encapsulate enzymatic or structural cargo. These shells typically range in size from 24 to 42 nm, depending on their triangulation number, with $T = 1$ encapsulins composed of 60 subunits, $T = 3$ of 180 subunits, and $T = 4$ of 240 subunits (Figure 2.10).^[10, 288, 316] The shell protomers adopt the HK97 phage-like fold, a motif otherwise best known from viral capsid proteins, indicating that encapsulins likely share an evolutionary origin with bacteriophages.^[307, 317]

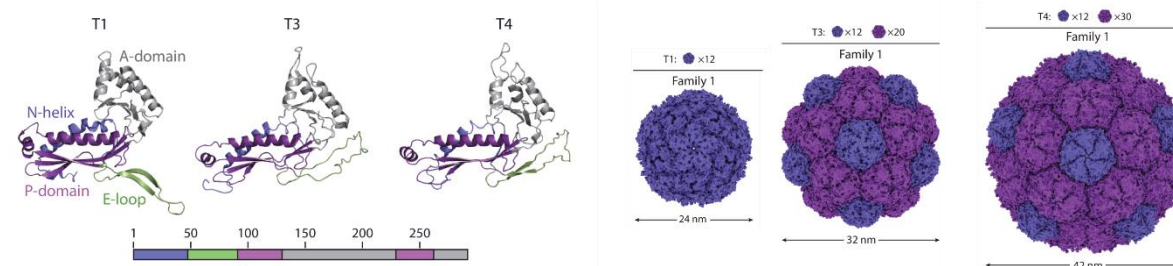


Figure 2.10: Overview of structural features of encapsulin of the first family. (A) and (B) from left to right: $T = 1$ (PDB: 3DKT), $T = 3$ (PDB: 4PT2) and $T = 4$ (PDB: 6NJ8) encapsulins. Figure adapted from Giessen et. al^[10] with permission from Annual Reviews, Inc., copyright 2022.

The structural organization of encapsulins has been elucidated through crystallography and, more recently, cryo-electron microscopy. Each protomer contributes a peripheral domain, an axial domain, and an extended E-loop that mediates subunit contacts and stabilizes the overall lattice.^[316] The arrangement of protomers around the five-, three-, and two-fold symmetry axes results in regular pores that range from 5 to 25 Å in diameter. These pores serve as molecular gates, allowing the controlled exchange of metabolites, cofactors, and ions between the lumen and the cytosol.^[294] In some systems, the pores are static, while in others conformational switching has been observed, producing dynamic pores that can adopt open or closed states. Such dynamic gating may represent a regulatory mechanism for modulating substrate flux in response to environmental or cellular conditions.^[318-319]

Cargo encapsulation is directed by short peptide signals, most often located at the N- or C-terminus of the cargo protein. These cargo-loading peptides, typically 10-20 amino acids in length, interact with conserved hydrophobic pockets on the luminal surface of the encapsulin shell.^[320-321] In certain systems, longer targeting domains that are partially disordered provide additional binding capacity, typically at the threefold symmetry axes.^[319] This simple genetic logic allows cells to ensure that only specific proteins are packaged inside encapsulins, and it also provides an avenue for engineering: Non-native proteins can be loaded into encapsulins by fusion to these short peptides.^[322] The stoichiometry of encapsulated cargo depends both on the size of the shell and the number of targeting sequences, but in all cases the cargo is sequestered away from the cytosol and confined to the protein cavity.

Comparative genomic and structural studies have revealed that encapsulins fall into at least four distinct families. The best characterized are the so-called Family 1 or “classical” encapsulins, which are broadly distributed and typically encapsulate ferritin-like protelins, peroxidases, or hemerythrins.^[10] Family 2 encapsulins are even more abundant in sequence databases and are associated with sulfur metabolism and natural product biosynthetic genes; they can be subdivided into types with or without C-terminal cyclic nucleotide-binding domains.^[323] Families 3 and 4 are less well understood: the former appears linked to secondary metabolite pathways, while the latter consists of highly truncated forms that occur mainly in hyperthermophilic archaea.^[323] Despite this diversity, all encapsulins share the same underlying principle of encapsulating dedicated enzymes via targeting motifs.

The biological functions of encapsulins depend entirely on the identity of their cargo proteins. In many bacteria, ferritin-like proteins encapsulated within the shell mineralize iron, providing both storage and protection against oxidative stress.^[288, 316] Other systems encapsulate dye-decolorizing peroxidases, which degrade hydrogen peroxide and aromatic compounds, thereby contributing to stress resistance.^[322, 324-325] In Family 2 encapsulins, desulfurases and related enzymes are confined within the shell, supporting sulfur metabolism.^[323] Still other encapsulins have been implicated in natural product biosynthesis, where they may function as nanoscale assembly lines for complex secondary metabolites.^[10] In pathogenic bacteria such as *Mycobacterium tuberculosis*, encapsulin systems are thought to contribute to survival under host-induced stresses and may play roles in virulence.^[326] Across all these examples, encapsulins act as modular, protein-based organelles that extend the range of metabolic strategies available to prokaryotes.

The combination of genetic simplicity, structural robustness, and modularity has also made encapsulins attractive platforms for engineering. Because their shells are encoded by a single gene, they can be heterologously expressed in a range of organisms, from *E. coli* to mammalian cells.^[327] Fusion of non-native proteins to targeting peptides enables encapsulation of designed cargos, effectively turning encapsulins into customizable nanoreactors.^[322] The shell exterior can be modified by chemical conjugation or genetic fusion to display epitopes, fluorophores, or targeting ligands.^[306] Meanwhile, pore engineering by site-directed mutagenesis allows modulation of substrate selectivity and flux.^[294] Applications have already been demonstrated in several areas. In nanotechnology, encapsulins have been used to mineralize iron oxide within their cavities, producing genetically encoded MRI contrast agents.^[328] In medicine, engineered encapsulins have been explored as drug delivery systems and vaccine platforms, benefiting from their biocompatibility and stability.^[327, 329] In synthetic biology, encapsulins are being investigated as chassis for artificial organelles, capable of organizing metabolic pathways in heterologous hosts.^[11]

Taken together, encapsulins represent a distinct subclass of protein cages that merge viral-like architecture with microbial metabolism. They achieve specificity through targeting peptides, versatility through diverse cargo types, and robustness through highly conserved shell structures. This combination of features has allowed encapsulins to spread widely across microbial lineages and has made them increasingly valuable as templates for nanotechnology. In the following subsections, encapsulins from *T. maritima* and *M. xanthus* will be described in detail, providing organism-specific case studies that illustrate how shell geometry, operon structure, and cargo identity define functional outcomes.

2.1.1.1 Encapsulin from *T. maritima*

T. maritima is a hyperthermophilic gram-negative bacterium isolated from marine hydrothermal vents and hot springs, growing optimally between 80-90 °C.^[330] Its proteome is remarkably stable under such extreme conditions, and this property extends to its encapsulin nanocompartment (TmEnc), which has become the reference system for structural and functional studies of encapsulins.^[331]

The TmEnc shell is a T = 1 icosahedron, ~24 nm in diameter, composed of 60 identical protomers adopting the HK97-like capsid fold.^[316] The first structure was determined by X-ray crystallography at 3.1 Å (PDB: 2E0Z), followed by cryo-EM reconstructions at higher resolution (PDBs: 7MU1, 7KQ5), which confirmed the interdigitating E-loops as key stabilizing features.^[288] These structural adaptations account for the exceptional thermostability of TmEnc, which resists disassembly even at 90 °C, in contrast to other encapsulin variants.^[332] An unusual characteristic of TmEnc is its flavoprotein nature. Isolated shells exhibit a yellow coloration, consistent with bound flavins such as riboflavin or FMN. Cryo-EM studies confirmed density corresponding to a flavin cofactor π -stacked with Trp90 (W90) on the luminal surface.^[288] Mutagenesis of W90 to glutamic acid or alanine eliminated flavin binding, confirming its structural role. While flavins may act as electron acceptors during iron oxidation, comparative assays between wild-type and W90 mutants showed no measurable differences in iron storage or release, leaving the physiological role of this ligand unresolved.^[288]

The lumen of TmEnc naturally encapsulates ferritin-like proteins (FLPs), which contain ferroxidase centers for Fe(II) oxidation and Fe(III) mineralization.^[317] Cargo encapsulation is directed by short cargo loading peptides (CLPs), typically located at the C-terminus of cargo proteins, which bind conserved pockets on the shell interior.^[306, 315, 321] Structural data (PDB: 3DKT) suggest that each subunit provides one CLP-binding site, allowing up to 60 cargo proteins per shell.^[288] The CLP-shell interaction is stabilized by hydrophobic and ionic

contacts, with sufficient flexibility to accommodate different cargo geometries.^[306] This modularity has been exploited to package heterologous cargos such as GFP,^[321] confirming that CLPs provide a generalizable mechanism for engineering encapsulation.

Crucially, CLPs have also enabled the encapsulation of inorganic nanoparticles. In pioneering work, plasmonic gold nanoparticles functionalized with CLPs were successfully encapsulated inside TmEnc with high efficiency.^[14] The process relies on disassembly of the shell under acidic or basic pH or in the presence of chaotropic agents such as guanidinium hydrochloride at 4 °C, followed by reassembly under neutral conditions with the nanoparticle cargo present. This “peptide-directed encapsulation” strategy, first demonstrated by Beck and co-workers,^[14] provides a robust method for packaging synthetic nanoparticles into TmEnc (Figure 2.11). The reassembly process occurs over several hours, with the presence of nanoparticle cargo influencing the efficiency of shell formation. Reassembly of encapsulins has been examined across different variants and generally occurs on the timescale of several hours, with kinetics dependent on the specific shell protein. Thermal stability assays demonstrated that while some encapsulins undergo disassembly at elevated temperatures, the *T. maritima* encapsulin remains intact even at 90 °C. This exceptional resistance to heat-induced disassembly is consistent with its origin from a hyperthermophilic bacterium.^[333]

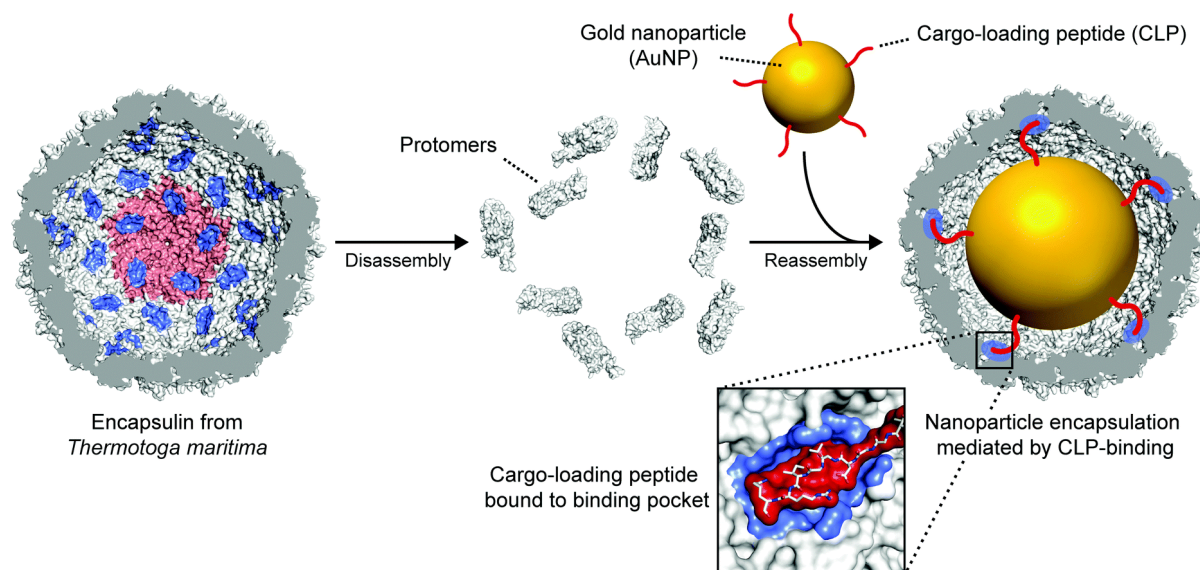


Figure 2.11: Schematic illustration visualizing the peptide-directed encapsulation of gold nanoparticles into *T. maritima* encapsulin. One out of 12 pentamers is highlighted in light red. The protein cage is disassembled into protomers. Gold nanoparticles functionalized with a cargo-loading peptide (CLP) are added to the disassembled protein cage while the reassembly is initiated. Afterwards, the gold nanoparticle is encapsulated into the protein cage. The cargo-loading peptide is bound to the binding pocket (inset). Each of the 60 monomers features one CLP-binding pocket, as highlighted in blue. Figure adopted from reference Künzle et. al^[14] with permission from Royal Society of Chemistry, copyright 2009

Beyond gold nanoparticles, encapsulins have also been used for *in situ* mineralization. A study by Giessen and Silver fused a silver-mineralization peptide to the N-terminus of the TmEnc shell protein, projecting it into the cavity where it nucleated silver nanoparticles (AgNPs).^[334] This approach builds on earlier demonstrations in ferritin,^[8, 300] highlighting the potential of encapsulins as genetically programmable templates for metal nanoparticle synthesis. These results underscore the versatility of encapsulins as size-constrained nanoreactors capable of templating diverse inorganic materials.

The pores of TmEnc provide additional control over cargo chemistry. Located at the twofold, threefold, and fivefold symmetry axes, they exhibit different electrostatic properties: the fivefold pores (~3 Å, positively charged) are the most likely entry routes for cations, while the threefold (~5 Å, neutral) and twofold (~6 Å, negatively charged) pores allow passage of small metabolites.^[288] Pore engineering has been employed to modulate this permeability: deletion of residues from the pore-forming loops expanded the fivefold channels from 3 Å to ~11 Å, significantly enhancing molecular flux.^[318] Such engineering enables encapsulins to be tailored for nanoparticle growth, catalysis, and synthetic biology applications requiring customized permeability.

In sum, the *T. maritima* encapsulin is the best-characterized member of this protein family. It combines high thermostability, modular CLP-mediated encapsulation, and tunable permeability with the ability to undergo disassembly and reassembly. These properties have made it a central platform for both fundamental studies and engineering efforts.

2.1.1.2 Encapsulin from *M. xanthus*

M. xanthus is a Gram-negative, soil-dwelling bacterium distinguished by its cooperative social behavior, and predatory lifestyle.^[335] Its encapsulin system has become a central model for understanding encapsulin structural diversity, as it demonstrates the unusual ability to assemble into two different capsid geometries from the same protomer.

The *M. xanthus* encapsulin system comprises the shell protein EncA (MxEnc) and three distinct cargo proteins: EncB, EncC, and EncD.^[336] EncA self-assembles into the icosahedral protein shell, while EncB and EncC are FLPs that catalyze Fe(II) oxidation, and EncD is less well understood but is thought to contribute reductase activity or redox balancing.^[336-337] Together, these components establish *M. xanthus* encapsulin as a multi-cargo nanocompartment specialized in iron storage and oxidative stress management.^[306, 337]

MxEnc adopts the conserved HK97-like phage capsid fold and can assemble into two alternative architectures: A T = 1 capsid composed of 60 subunits and a T = 3 capsid with 180

subunits (Figure 2.12A).^[336] Cryo-EM structures at 3.4 Å resolution revealed that both architectures are formed from the same protomer, which contains a peripheral (P) domain, an axial (A) domain, and an extended E-loop. The smaller $T = 1$ state measures ~18 nm in outer diameter, enclosing a cavity of ~14 nm, whereas the $T = 3$ state reaches ~32 nm with an inner cavity of ~26-28 nm.^[336] Structural plasticity arises from the E-loop: In the $T = 1$ state, it rotates ~90°, forming β -sheet contacts that stabilize dimeric interfaces, while in the $T = 3$ state the E-loop relaxes, permitting expansion into a larger lattice (Figure 2.12B). In vivo, $T = 3$ state dominates (~94%), while $T = 1$ state only forms in recombinant systems in the absence of cargo, showing that ferritin-like proteins bias assembly toward the larger geometry.^[336-337]

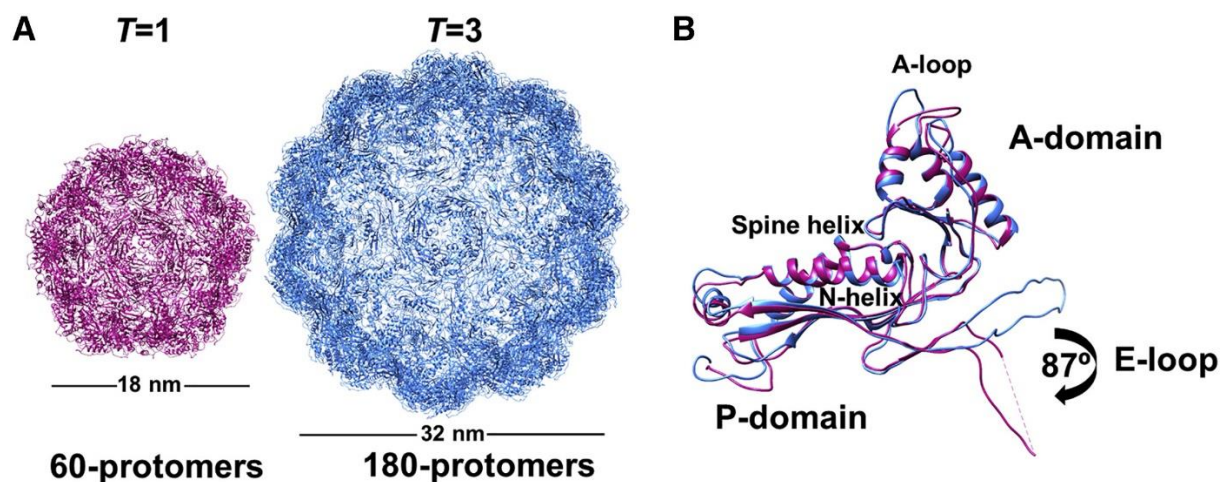


Figure 2.12: Structural comparison of assembled encapsulin shells from *M. xanthus*. a) Icosahedral EncA shell arranged in $T = 1$ formed from 60 protomers (pink) and $T = 3$ from 180 protomers (blue). b) Superimposed structures of EncA monomers from a $T = 1$ shell (pink) and $T = 3$ shell (blue) showing a conformational rotation in the E-loop. Both structures display a classic HK97-fold with spine α -helix, A- and P-domains with β -hairpin loop (E-loop). Figure adopted from Eren et. al^[337] with permission from ScienceDirect, copyright 2022.

The natural cargos of *M. xanthus* encapsulin are EncB, EncC, and EncD. EncB and EncC assemble into decameric rings with diiron ferroxidase centers that oxidize Fe(II) to Fe(III), enabling mineralization inside the shell.^[336] Crystal structures of EncB (PDB: 7S5C) and EncC (PDB: 7S8T) revealed canonical diiron sites and additional peripheral binding motifs, including a glutamate-histidine ladder in EncB that may act as an Fe(II) entry pathway.^[337] EncD lacks a canonical ferroxidase motif and its role remains unclear, though reductase activity has been proposed.^[337] Their co-encapsulation allows both oxidation and reduction of iron to be confined within the lumen, producing electron-dense mineral deposits visible by transmission electron microscopy. Quantitative studies have shown that a single $T = 3$ MxEnc cage can store up to ~30,000 iron atoms, far exceeding the capacity of ferritin and significantly greater than the $T = 1$ *T. maritima* encapsulin.^[315, 336]

Cargo encapsulation in MxEnc relies on short C-terminal CLPs, which are essential signals for shell recruitment.^[338-339] These motifs, typically 7-12 amino acids long, terminate the cargo proteins and bind to conserved grooves on the luminal surface of MxEnc. High-resolution cryo-EM reconstructions have shown that the binding pocket lies within the P-domain of each MxEnc subunit, between an N-terminal helix and a β -sheet, forming a hydrophobic and electrostatically complementary groove.^[336] Each MxEnc protomer (60 in T = 1, 180 in T = 3) provides a discrete binding site, as the pocket is self-contained rather than spanning subunit interfaces.^[340] The interaction is mediated by a combination of hydrophobic packing and salt bridges, while the arginine residues at the peptide termini contribute additional electrostatic stabilization.^[341] Although every MxEnc subunit carries a binding site, steric constraints and the oligomeric state of EncB/C limit actual occupancy to approximately one-third of available sites.^[288, 342] For the other encapsulins, the portability of CLPs has been exploited in engineering studies: fusion of these motifs to fluorescent proteins, enzymes, or nanoparticles directs efficient encapsulation into MxEnc.^[321, 338] This makes the MxEnc CLP-binding pocket the central determinant of encapsulation specificity, acting as a modular recruitment site that can be repurposed for natural and synthetic cargos alike.

The geometry of MxEnc appears to be influenced by cargo.^[341] In vitro assembly experiments demonstrated that in the presence of ferritin-like proteins, the T = 3 geometry is strongly favored, while in their absence, T = 1 state can assemble.^[336-337] This suggests that encapsulation is not a passive process but can guide the assembly pathway, coupling shell geometry to metabolic function. MxEnc shells can also undergo reversible disassembly in chaotropic agents such as urea or guanidine hydrochloride, followed by reassembly into functional cages upon buffer exchange.^[13, 333] The kinetics of reassembly occur over several hours and depend on the cargo present, underscoring the dynamic interplay between encapsulation and structural state.

Beyond its biological role in iron storage and oxidative stress protection, MxEnc has attracted significant interest as a scaffold for engineering. Surface engineering has been applied to display peptides and ligands for mammalian cell targeting, enabling encapsulins to act as delivery vehicles.^[343] Mutational studies of the pores have demonstrated control over ion flux and substrate permeability, with engineered pores allowing selective enhancement of reactivity.^[344] Furthermore, synthetic CLPs have been used to encapsulate diverse non-native cargos with high fidelity, including enzymes and fluorescent proteins.^[338] In vivo studies indicate that encapsulins can circulate systemically with organ-specific accumulation patterns influenced by surface chemistry, highlighting translational considerations (biodistribution, immunogenicity).^[329] These advances extend the utility of MxEnc beyond natural metabolism, positioning it as a versatile chassis for nanotechnology, synthetic biology, and potentially for

templating the encapsulation of inorganic nanoparticles, where the larger $T = 3$ cavity provides unique advantages.^[8, 14, 345]

In summary MxEnc exemplifies the structural plasticity of the family, with a single protomer assembling into both $T = 1$ and $T = 3$ architectures, and functional adaptability through its multi-cargo system. Its cargo-loading logic and reversible assembly make it not only an efficient iron-storage compartment but also a versatile scaffold for the encapsulation of synthetic and inorganic cargos, including anisotropic nanoparticles.

2.3 Biohybrid Nanostructures

Biohybrid nanostructures integrate biological macromolecules with synthetic or inorganic components to form functional assemblies with enhanced structural and chemical capabilities. Proteins, nucleic acids, and peptides are frequently employed as biological scaffolds, while metals, polymers, and ceramics provide mechanical stability, catalytic activity, or responsiveness to external stimuli.^[1, 346-347] These systems exploit molecular self-assembly, biorecognition, and templating strategies to control nanoscale architecture with high spatial resolution.^[348-349]

Various classes of biohybrid assemblies have been developed, each leveraging different biomolecular scaffolds to achieve structural and functional integration with inorganic components. DNA-based assemblies, particularly those using DNA origami, offer precise spatial control over nanoscale positioning.^[350] These structures are widely used to organize metallic nanoparticles, enzymes, and fluorescent probes into defined geometries for applications in biosensing, catalysis, and photonics.^[351-353] Their programmability and addressability make them highly versatile, though they are often limited by mechanical fragility and environmental sensitivity.^[354] In contrast, polymer-based biohybrids exploit the tunable properties of synthetic polymers, such as flexibility, charge, and environmental responsiveness to construct dynamic and protective nanostructures. These systems are especially valuable in drug delivery, responsive coatings, and soft electronic interfaces.^[355]

Hybrid systems that integrate proteins with DNA or polymers further expand this design space. DNA-protein conjugates combine the spatial resolution of nucleic acid frameworks with the catalytic or structural roles of proteins, enabling multifunctional platforms with both programmability and biological activity.^[356] Protein-polymer hybrids, created through grafting or covalent coupling, enhance protein solubility, thermal stability, and resilience under non-physiological conditions.^[357] These systems are increasingly used to immobilize enzymes or assemble responsive nanogels for biomedical applications.

While a range of biological scaffolds have been explored in the context of biohybrid nanostructures, protein nanocages distinguish themselves by offering robust encapsulation, genetically programmable interfaces, and monodisperse architecture suitable for precise nanoengineering.^[358-359] Their capacity to host inorganic materials under controlled conditions has led to diverse applications in catalysis, optics, and materials assembly.^[358-359] In the following sections, we examine the principles governing cargo encapsulation in protein cages, and how these nanocages can be used as structural elements to form ordered superlattices.^[360-364]

2.3.1 Protein Nanoparticle Interaction

Ferritin has long served as a model for nanoparticle encapsulation. Its negatively charged inner cavity promotes the loading of positively charged gold nanoparticles (AuNPs) when combined with disassembly and reassembly protocols performed in aqueous solutions.^[360] For high encapsulation efficiency, several factors must be considered: The ligand shell of the AuNP must be positively charged to ensure favorable electrostatic interactions with the cavity; the nanoparticles must be colloidally stable under aqueous conditions to prevent aggregation during reassembly; and the overall diameter of the core plus ligand must not exceed the ~6 nm lumen of ferritin (Figure 2.13) Earlier studies with *Archaeoglobus fulgidus* ferritin used salt-triggered disassembly to encapsulate AuNPs, but the resulting products were polydisperse, likely due to nonspecific adsorption of protein onto the nanoparticle surface rather than true cage reassembly.^[365-367] More recent work with redesigned ferritin nanocages has shown that properly stabilized and size-matched AuNPs can be encapsulated with high monodispersity, yielding well-defined protein-nanoparticle composites.^[360]

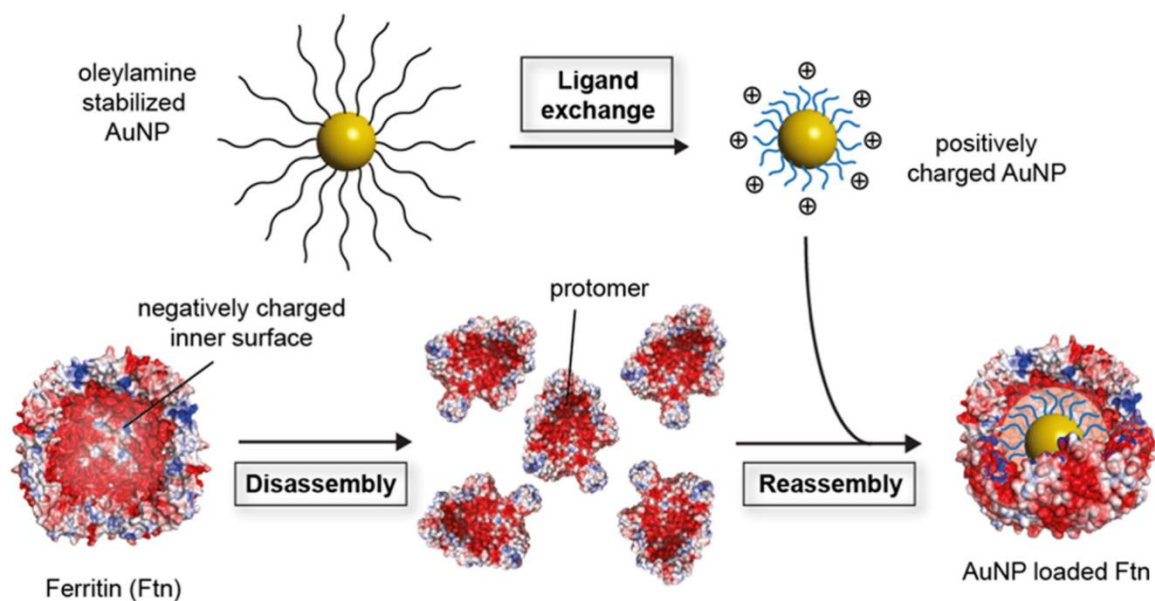


Figure 2.13: Strategy for the encapsulation of gold nanoparticles into the ferritin protein nanocage.

Oleylamine-stabilized AuNPs are synthesized and functionalized by ligand exchange reactions to obtain positively charged AuNPs. For encapsulation, the ferritin protein nanocage is disassembled under chaotropic conditions and the functionalized AuNPs are added before the reassembly of the ferritin takes place. The interaction between the positively charged AuNPs and the negatively charged inner surface enables successful encapsulation of the AuNPs. Figure adapted from Lach et. al.^[360] with permission from American Chemical Society, copyright 2022.

Encapsulins represent a second major class of protein cages used for nanoparticle encapsulation. In the case of *T. maritima* encapsulin, short CLPs provide a lock-and-key mechanism by binding to specific sites on the luminal surface. As discussed in section 2.1.1.1, this system has been adapted to direct the encapsulation of AuNPs functionalized with CLPs.^[14] The process exploits pH-dependent shell stability: At strongly acidic pH (~2), encapsulins disassemble into subunits, which can reassemble at neutral pH (~7) around CLP-modified nanoparticles, yielding encapsulation efficiencies approaching 99%. Importantly, CLP-directed encapsulation is robust to changes in ionic strength, in contrast to purely electrostatic loading, which depends strongly on salt concentration. Electrostatic encapsulation of cationic AuNPs into encapsulins produced only partial loading (~66%) and was limited to a narrow salt window, with aggregation occurring at low ionic strength and charge screening at high ionic strength.

VLPs such as cowpea chlorotic mottle virus (CCMV) use yet another strategy, relying on their natural affinity for nucleic acids. AuNPs functionalized with thiolated single-stranded DNA mimic the polyanionic viral genome and interact with the positively charged N-terminal domains of CCMV coat proteins.^[362] Upon lowering the pH to ~4.8-5.0, the capsid disassembles into coat proteins, which reassemble at near-neutral pH around the DNA-coated

nanoparticles, generating intact AuNP-loaded capsids with nearly identical morphology to native CCMV.

Together, these examples highlight three distinct encapsulation strategies: charge- and size-matched disassembly/reassembly in ferritin, CLP-directed lock-and-key loading in encapsulins, and nucleic-acid-templated reassembly in viral protein cages. Each approach yields monodisperse cage-nanoparticle composites that can subsequently be used as modular units for higher-order assembly into ordered lattices.

2.3.2 Biohybrid Assemblies

The ordered assembly of protein nanocages into crystalline lattices has emerged as a versatile strategy to create biohybrid materials with tunable optical, catalytic, and electronic properties. By exploiting the atomically precise geometry and programmable surface chemistry of protein cages, researchers have demonstrated that both unitary and binary lattices can be constructed under controlled conditions.^[361, 368]

Ferritin-based systems have been central to this development. Beck and co-workers demonstrated that oppositely charged ferritin variants can co-crystallize into binary superlattices with well-defined tetragonal symmetry.^[363] These lattices also host inorganic cargo, as two different nanoparticle types were encapsulated into distinct ferritin variants prior to crystallization, yielding quaternary protein-nanoparticle superlattices (Figure 2.14). The lattice symmetry and periodicity were determined by the protein cage architecture rather than the encapsulated cargo. This highlights the role of ferritin as a structural rather than passive component in lattice construction.^[363] Building on this foundation, subsequent studies introduced design refinements to tune assembly outcomes. Lach and colleagues showed that redesigned ferritin nanocages loaded with gold nanoparticles or fluorophores could be co-assembled into binary superlattices, with lattice symmetry controlled by the balance of electrostatic interactions and ionic strength.^[360] More recently, they demonstrated that by carefully adjusting electrolyte conditions, the same ferritin variants can form multiple crystalline phases without requiring genetic modification, underscoring the adaptability of ferritin-based crystallization strategies.^[368]

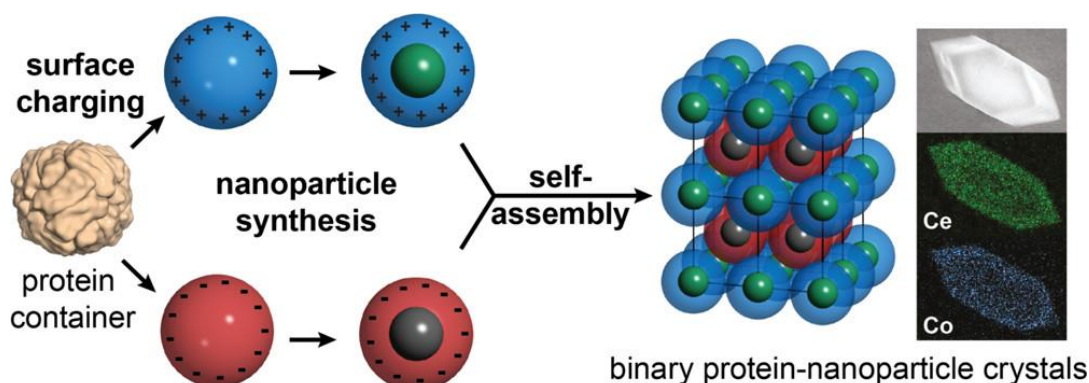


Figure 2.14. A general strategy to assemble binary protein-nanoparticle crystals. The surface charging of a protein cage leads to either positively or negatively surface charged protein cages. After nanoparticle synthesis inside the cages, self-assembled structures can be achieved. These binary protein-nanoparticle crystals can be analyzed via energy dispersive X-ray (EDX) mapping to visualize the elemental distribution of the nanoparticle. Figure adapted from reference Künzle et. al.^[363] with permission from American Chemical Society, copyright 2016.

Recently Beck and coworkers clarified the broader assembly requirements for binary ferritin lattices. They identified three critical features: (i) interface-mediating residues at specific crystal contacts to stabilize the lattice, (ii) charged surface patches outside the contacts to maintain long-range electrostatics, and (iii) sufficient chemical distinctiveness between cage variants to favor binary over unitary packing.^[369] Without these features, the system reverts to unitary assembly, underscoring how subtle adjustments in protein surface chemistry can dictate crystal symmetry and stability. Beyond electrostatics, ferritin has also been adapted to assemble into metal-organic frameworks (MOFs), where engineered coordination motifs at the threefold symmetry axes direct lattice formation via metal ion-organic linker bridging.^[370] Such approaches highlight the structural plasticity of ferritin as a crystalline building block.

Beyond ferritin, recent advances extend to encapsulin and VLP systems. Rütten and coworkers showed that differently sized, supercharged protein nanocages can co-assemble into binary crystals despite symmetry mismatch, with electrostatic interactions overcoming geometric incompatibility.^[361] This strategy demonstrates that structural variety can be achieved by combining cages of distinct dimensions and charge states, thereby expanding the accessible lattice types. VLPs also provide powerful scaffolds for lattice formation. Zhou and co-workers reported co-crystallization of CCMV and previously redesigned ferritin cages of the Beck group into large, micrometer-sized binary crystals, where the assembly was guided by surface charge complementarity and controlled electrolyte conditions (Figure 2.15).^[362] Importantly, when the cages were loaded with gold and iron oxide nanoparticles, the resulting lattices adopted AB_2 -type FCC configurations, enabling dipolar coupling between the encapsulated cargo. This demonstrates how protein cage lattices can act not only as structural matrices but also as platforms for emergent photonic and magnetic properties.

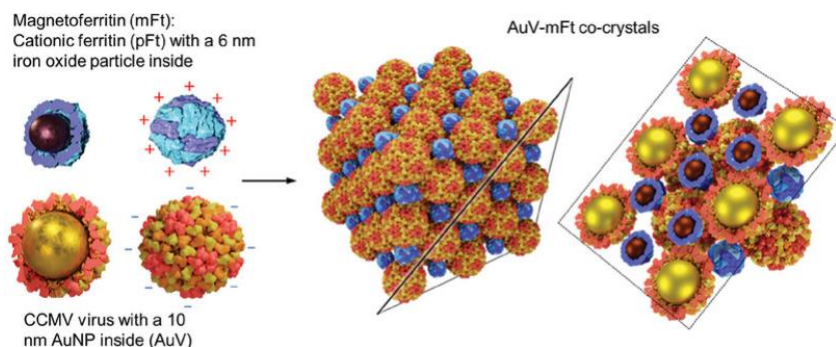


Figure 2.15: Schematic representation of the formation of heterogeneous binary crystals, composed of AuV and mFt. Figure adapted from Zhou et. al^[362] with permission from Wiley & Sons, copyright 2024.

Beyond three-dimensional crystals, protein cages have also been used to generate compartmentalized thin films. For instance, interfacial cross-linking of CCMV cages yielded free-standing films with encapsulated gold nanoparticles or enzymes, which retained catalytic activity after assembly.^[371] Such two-dimensional architectures highlight the breadth of formats in which protein cage assemblies can be realized.

Together, these examples establish protein nanocages as programmable colloidal units capable of forming highly ordered superstructures. Their combination of uniform geometry, tunable surface chemistry, and robust encapsulation capacity positions them as versatile building blocks for next-generation metamaterials and functional hybrid systems.^[360-364, 368-373]

3. Basis of the present work

The present work is built upon foundational research established within the Beck group, extending existing methodologies to address new challenges in nanobiotechnology. One of the two main protein scaffolds used for the encapsulation of nanoparticles is the *T. maritima* encapsulin. The thesis utilizes two key resources from previous work: (1) the strategic redesign of *T. maritima* encapsulin to create supercharged variants designed for controlled assembly, and (2) the established protocols for the synthesis, functionalization, and encapsulation of spherical nanoparticles into *T. maritima* encapsulin.

3.1 Supercharging of the *T. maritima* encapsulin

The rational design of protein cages with tailored surface properties is a prerequisite for their use as programmable building blocks in materials science. For the *T. maritima* encapsulin (TmEnc), this was achieved through computational surface redesign using the Rosetta molecular modelling package.^[374-375] The design protocol was based on the crystal structure of the wild-type protein (PDB: 3DKT). A fixed-backbone design strategy was employed, allowing for the mutation of solvent-exposed amino acids to alter surface charge while rigorously preserving the structural integrity and symmetry of the native protein cage. In this approach, two distinct supercharged variants were designed (Figure 3.1). For the positively supercharged encapsulin (TmEnc^(pos)), surface residues were mutated to the positively charged amino acids lysine or arginine. Conversely, for the negatively supercharged variant (TmEnc^(neg)), no additional negative residues were introduced, as the protein cage is already negatively charged. Instead, a tryptophan mutation was introduced to disrupt the flavin-binding site. The energy function weights within Rosetta were strategically adjusted to increasingly favor these charged residues during the simulation, ensuring a comprehensive redesign of the electrostatic surface landscape.

This design work, initiated by Dr. Matthias Künzle, was subsequently advanced through the doctoral research of Dr. Michael Rütten, who carried out the production, purification, and thorough biophysical characterization of these novel TmEnc^(pos) and TmEnc^(neg) variants.^[364] The successful generation of these monodisperse, structurally intact protein cages with defined surface charges provides the essential engineered building blocks that form the basis for the encapsulation and assembly strategies pursued in this thesis.

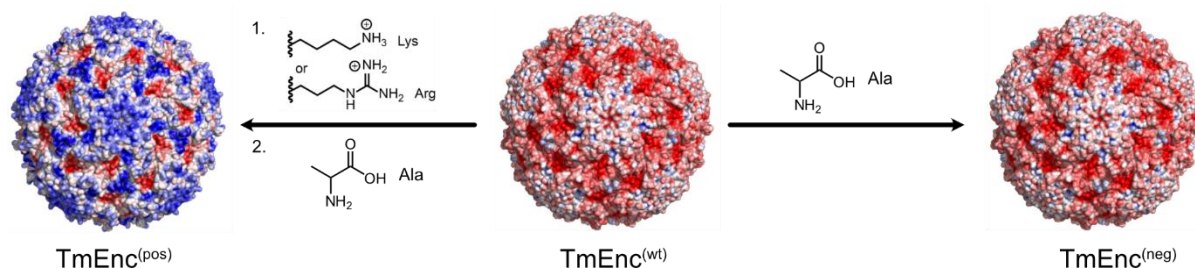


Figure 3.1: Schematic visualization of encapsulin surface. By either altering the amino acids to lysine (Lys) or arginine (Arg) positively charged residues are introduced. The tryptophan (Trp) residue at position 90 is replaced with alanine (Ala) to remove the flavin binding side. For negatively charged, only the flavin binding site is removed. TmEnc^(wt) surface model based on crystal structure (PDB: 3DKT). Blue and red indicate positively or negatively supercharged protein cages, respectively.

3.2 Encapsulation of spherical gold nanoparticles via CLP

A well-established methodology within the Beck group for creating protein-nanoparticle hybrids involves the encapsulation of spherical AuNPs into the *T. maritima* encapsulin.^[14] This process is mediated by a specific cargo loading peptide (CLP), which is genetically encoded as an extension to the cargo protein. This CLP facilitates the highly efficient and specific uptake of AuNPs into the large internal cavity of the encapsulin during protein assembly. The standard protocol encompasses the synthesis of monodisperse, citrate-stabilized AuNPs, followed by a ligand exchange step to functionalize the nanoparticle surface with thiolated molecules, making them compatible with the hydrophobic interior of the protein cage. Subsequently, the functionalized AuNPs are incubated with the disassembled encapsulin subunits. Upon reassembly of the protein cage, the CLPs guide the encapsulation process, resulting in a homogeneous population of AuNP-filled encapsulin complexes. The critical analytical step for confirming successful encapsulation is size-exclusion chromatography (SEC), where the AuNP-loaded encapsulin elutes at a distinct volume compared to the empty protein cage, indicated by a concurrent absorbance peak at 280 nm (protein) and 520 nm (AuNPs). This is complemented by visualization via transmission electron microscopy (TEM), which provides direct evidence of the AuNPs located within the protein cavity (Figure 3.2).

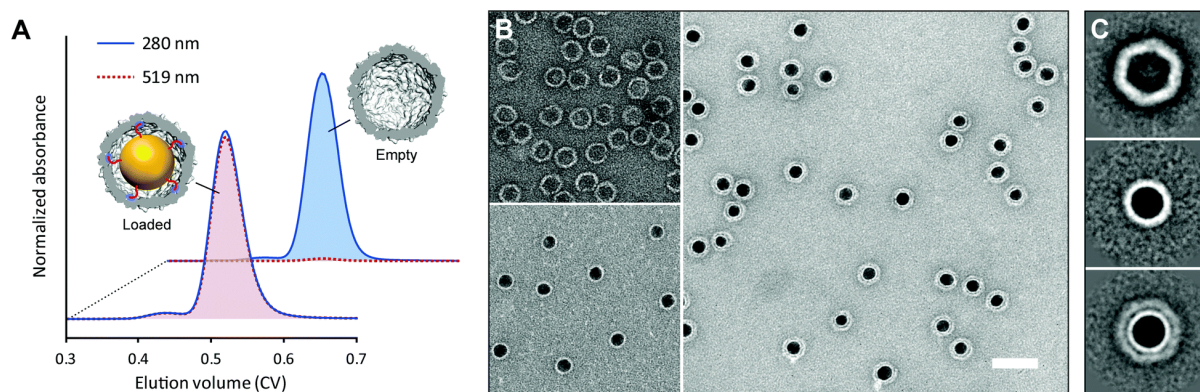


Figure 3.2: Analytical data for the CLP-mediated encapsulation of gold nanoparticles. (A) Size-exclusion chromatogram of empty and gold nanoparticle-loaded encapsulin. Absorbance at 519 nm indicates successful encapsulation. Elution volumes of both samples are nearly the same. (B) Negatively stained TEM images: (top left) empty encapsulin cages; (bottom left) CLP-functionalized gold nanoparticles with visible ligand shell; (right) Encapsulated gold nanoparticles. Scale bar is 50 nm. (C) Class-averages of empty encapsulin cages (top), gold nanoparticles (middle) and AuNP-loaded encapsulin cages (bottom). Figure adopted from reference Kunzle et. al^[14] with permission from Royal Society of Chemistry, copyright 2009.

The established success of this CLP-mediated encapsulation for spherical nanoparticles provides the fundamental technical and analytical groundwork for the efforts in this thesis to adapt this methodology for the more complex challenge of encapsulating anisotropic nanoparticles.

4. Concept and aim of this thesis

The overall aim of this thesis is to establish a comprehensive methodological framework for the encapsulation of anisotropic nanoparticles into protein cages, thereby creating defined biohybrid building blocks for future optical materials. This work planned to utilize the supercharged *T. maritima* encapsulin variants (TmEnc^(pos) and TmEnc^(neg)) developed within the group, as detailed in Chapter 3. As described in detail in chapter 2.2.2.1, the *T. maritima* encapsulin cage is 24 nm in diameter and features 18 nm large cavity with icosahedral ($T = 1$) symmetry. The protein cage has gained interest as a template for nanoparticle synthesis inside the cavity or a modular platform for tagging on the outer surface.^[287, 376] The Beck group has already established the encapsulation of spherical gold nanoparticles into the wild type encapsulating, Enc^(wt) and negatively supercharged variant, Enc^(neg).^[14] However, the introduction of anisotropic cargo into this symmetrical cage may conflict with the icosahedral geometry, potentially inducing structural strain or requiring a reorientation within the cavity.

The encapsulation of non-spherical cargo presents unique challenges not encountered with spherical particles, primarily due to complex shape, aspect ratio, and incompatible native ligand shells. This work systematically addresses these challenges for two key anisotropic nanoparticles: CdSe/CdS DiRs and AuNRs. The strategic approach involves two key aspects: (i) the encapsulation of cargo within the protein cavity and (ii), the surface deposition of the cargo loaded containers, as illustrated in Figure 4.1.

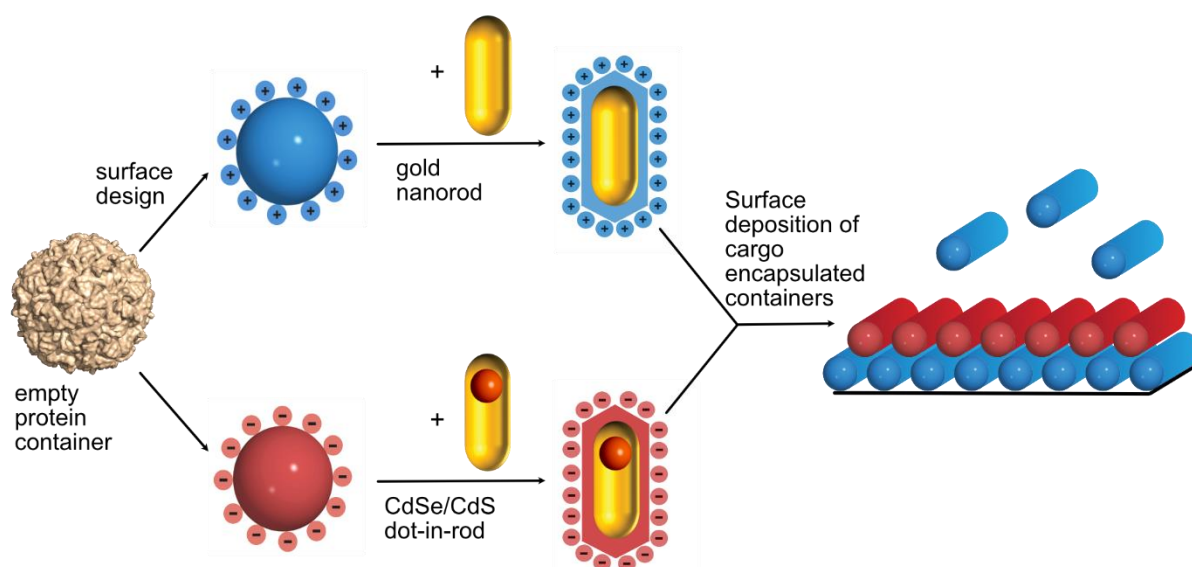


Figure 4.1: Schematic overview of the concept. (Left) Engineered encapsulin variants with redesigned surfaces. (Middle) Strategy for encapsulating anisotropic nanoparticles (DiRs and AuNRs) through ligand exchange and CLP-mediated loading. (Right) Surface deposition of cargo encapsulated cages.

CdSe/CdS DiRs were chosen as a target cargo due to their exceptional optoelectronic properties, including high quantum yield, strong and tunable light emission, and a high degree of linear polarization. AuNRs were selected for their strong, tunable plasmonic properties in the visible and near-infrared spectrum, which are highly dependent on their aspect ratio. Once reliable cargo encapsulation is established, this system will enable exploration of the optical coupling between the two types of nanorods assembled within a protein-based matrix. When arranged on a surface or within a lattice, the plasmonic field generated by the AuNRs can interact with the excitons in the nearby fluorescent DiRs. The effect of parameters such as the distance between the cargo, the structure of the assembly, and the number of layers will critically influence these optical interactions, potentially leading to effects such as fluorescence enhancement or quenching.

Furthermore, the encapsulin from *M. xanthus* is explored as an alternative scaffold given its larger size and $T = 3$ icosahedral symmetry, which features hexagonal facets and a significantly larger internal cavity. This work aims to evaluate whether this larger volume and altered geometry can accommodate anisotropic cargo and mitigate the geometric constraints imposed by the smaller *T. maritima* encapsulin.

In conclusion, this thesis aims to provide a detailed investigation into the parameters governing the encapsulation of DiRs and AuNRs into protein cages. By developing reliable functionalization and encapsulation protocols, this work seeks to create well-defined biohybrid building blocks and lay the essential groundwork for their future assembly into structured optical materials, where plasmon-exciton interactions can be studied and harnessed.

5. Results and Discussion

This chapter presents the synthesis, functionalization, and encapsulation of nanomaterials into protein cages, followed by a detailed analysis of the resulting biohybrid assemblies. The work is divided into three key parts. The first part focuses on the synthesis of various nanomaterials, including CdSe/CdS DiRs, AuNRs, and spherical AuNPs (Section 5.1). The second part examines the functionalization and ligand exchange strategies employed to modify the surface of these nanomaterials, optimizing them for encapsulation within protein cages (Section 5.2). The third part details the production, purification, and structural analysis of protein cages, as well as their subsequent cargo encapsulation (Sections 5.3 to 5.5). This chapter concludes with a discussion on the effects of particle size and protein cage type on the encapsulation efficiency and properties of the assembled biohybrids.

5.1 Synthesis of Nanomaterials

This section describes the synthesis of three types of nanomaterials: CdSe/CdS DiRs, AuNRs, and AuNPs. CdSe/CdS DiRs were synthesized via a seeded growth method that involved the deposition of CdS onto a CdSe core, resulting in enhanced photoluminescence properties. AuNRs were synthesized using a seed-mediated growth method, allowing for precise control over their aspect ratio and size. AuNPs were synthesized using a modified seed-mediated growth method, resulting in uniform nanoparticles with a narrow size distribution. These nanomaterials were then characterized using a combination of techniques, including UV-Vis spectroscopy, TEM, and DLS, to confirm their size, shape, and optical properties.

5.1.1 Synthesis of CdSe/CdS DiRs

CdSe/CdS DiRs were synthesized using a seeded growth method adapted from Carbone *et al.*^[70] This approach is widely used for producing anisotropic semiconductor nanocrystals with a well-defined core-shell architecture. The size, uniformity, and crystallinity of the CdSe seeds are known to play a critical role in determining the final geometry and properties of the dot-in-rod heterostructures. In this work, the synthesis of CdSe seeds was deliberately carried out to yield larger cores for a separate set of experiments led by Dr. Mittag, which required increased core size for subsequent overgrowth. To avoid redundant synthesis, smaller CdSe seeds, previously synthesized by Dr. Mittag under similar conditions but optimized for smaller sized rod formation, were borrowed and used in the CdSe/CdS DiRs synthesis described here. This planned coordination allowed for efficient resource use while ensuring optimal seed size for

high-quality rod growth. A representative TEM image of the larger CdSe seeds synthesized in this work is shown later. The particles appear spherical, well-separated, and monodisperse, consistent with high-quality quantum dot formation. Although these seeds were not used in the rod synthesis presented here, they were fully characterized optically and provide a useful benchmark for comparison. A schematic illustration of the rod formation process, showing the seeded growth of a CdS shell around a CdSe core, is shown in Figure 5.1.

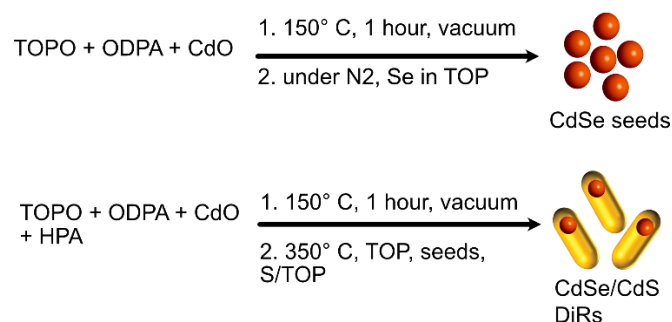


Figure 5.1. Schematic representation of the seeded growth method for synthesizing CdSe/CdS DiRs. Top: Preparation of CdSe seeds (orange) Bottom: Seeded growth of a CdS rod around the CdSe seed to yield CdSe/CdS dot-in-rods (orange core in yellow rod). Drawings are not to scale.

UV-Vis absorption and PL spectra were collected for both the CdSe seeds (synthesized in this study) and the resulting CdSe/CdS DiRs. To emphasize the optical properties of the final rod-shaped heterostructures, UV-Vis and PL spectra of the CdSe/CdS DiRs are presented together in Figure 5.2a, normalized to their respective maxima to highlight key spectral features. The absorption spectrum exhibits a broadened, red-shifted excitonic feature with a shoulder near 580 nm, attributed to the CdSe core. This red-shift and broadening reflect enhanced electronic delocalization along the anisotropic core-shell geometry. In addition, a broad shoulder between 470-500 nm is observed, commonly associated with CdS shell absorption, confirming successful shell overgrowth. The PL spectrum of the DiRs shows a red-shifted emission peak centered at 585 nm with enhanced intensity and a narrower full width at half maximum (FWHM), indicating strong core-shell coupling and improved surface passivation. These spectral features collectively support the formation of elongated dot-in-rod structures and highlight the impact of shape anisotropy on the optical properties.

TEM confirmed the successful formation of rod-like CdSe/CdS heterostructures (Figure 5.2b). Each nanocrystal exhibits a dark contrast CdSe core located asymmetrically within a lighter CdS rod, consistent with a dot-in-rod architecture. The particles appeared monodisperse and well-separated, indicating effective surface capping and minimal aggregation during purification. Statistical analysis of the rod dimensions is presented in Figures 5.2c and 5.2d. The measured average rod length was 10.90 ± 1.47 nm, with an average diameter of 4.00 ± 0.35 nm, yielding an aspect ratio of 2.72. The relatively narrow distributions observed

in both length and diameter histograms reflect controlled and reproducible growth conditions. No significant secondary populations or morphological defects were detected in the imaged regions.

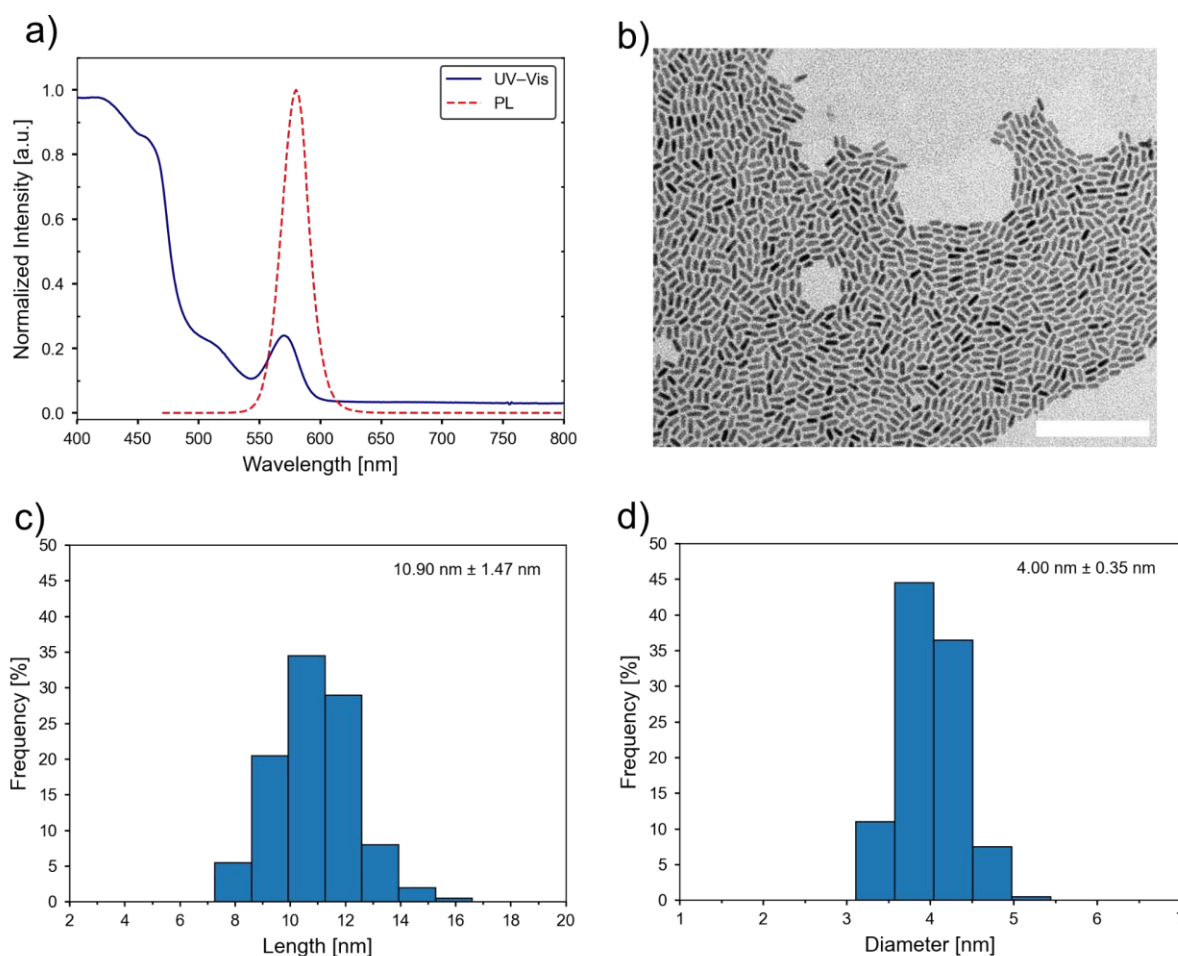


Figure 5.2: Characterization of CdSe/CdS DiRs. (a) Normalized UV-Vis (blue) and normalized emission (red) spectra of CdSe/CdS DiRs. (b) TEM image showing rod-shaped morphology and uniform distribution. (c, d) Corresponding histogram of DiR lengths and diameters with average length of 10.90 ± 1.47 nm and average diameter of 4.00 ± 0.35 nm, respectively. Scale bar is 100 nm. For comparative purposes, the UV-Vis absorption, PL spectra, and TEM data of the CdSe seed quantum dots are compiled in Figure 5.3. The normalized absorption spectrum exhibits a distinct excitonic peak centered near 625 nm, characteristic of relatively large, monodisperse CdSe quantum dots. The corresponding PL spectrum shows a narrow emission peak at 635 nm with a small Stokes shift, suggesting efficient band-edge recombination and minimal trap-assisted emission. A representative TEM image of these CdSe seeds is shown in Figure 5.3c, revealing spherical, well-dispersed nanocrystals consistent with high-quality synthesis. While these seeds were not used in the rod growth reported here, their characterization provides a useful benchmark for understanding the influence of seed properties on final heterostructure behavior.

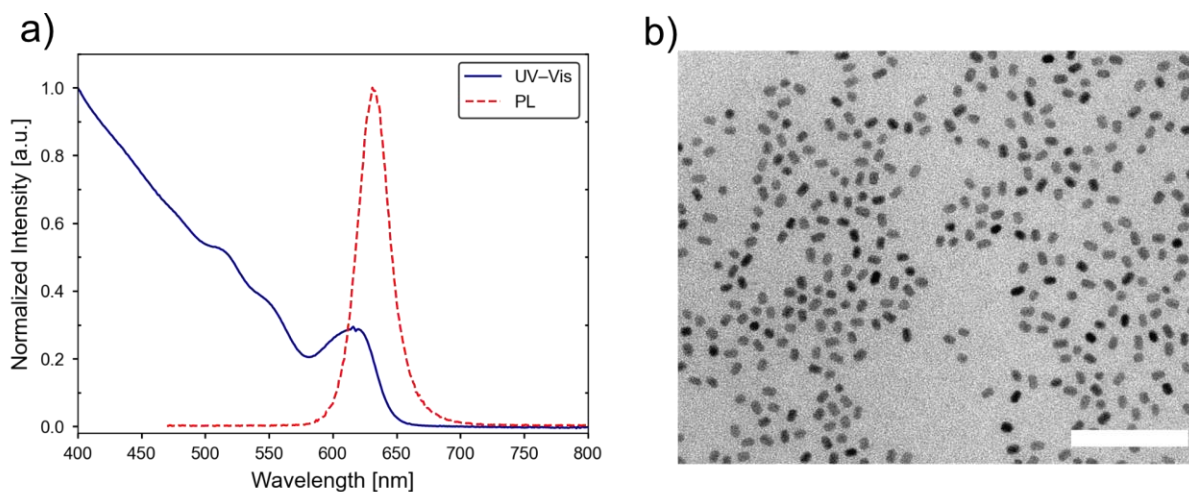


Figure 5.3: Characterization of CdSe seeds. (a) Normalized UV-Vis (blue) and PL (red) spectra of CdSe seeds. (b) TEM image showing elliptical morphology and uniform distribution. Scale bar is 100 nm.

In conclusion, the optimized seeded growth method enabled the synthesis of homogeneous CdSe/CdS DiRs at a high concentration. The as-synthesized DiRs were dispersed in an organic solvent (toluene), making them incompatible with proteins. To make them suitable for encapsulation, they were subjected to a ligand exchange process, which is discussed in detail in section 5.2.1.

5.1.2 Synthesis of Gold Nanorods

AuNRs were synthesized using two different methods to optimize size and yield for encapsulation into protein cages. Each method allows a precise control over the size and aspect ratio of the nanorods, with the first method being more reproducible and the second method designed for larger-scale production.

5.1.2.1 H₂O₂ Method

AuNRs were synthesized via a modified seed-mediated protocol adapted from Xu *et al.*^[199] using hydrogen peroxide as a mild reducing agent to promote anisotropic growth. The resulting particles were stabilized by CTAB, which formed a surface bilayer and maintained colloidal stability during and after synthesis. The synthesis was designed to produce AuNRs with moderate aspect ratios and narrow size distributions in a compact reaction volume. The schematic representation is shown in Figure 5.4.

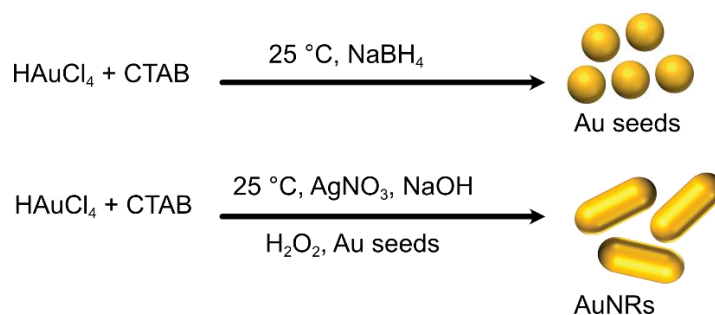


Figure 5.4: Schematic representation of the seeded growth method for synthesizing gold nanorods. Top: Preparation of Au seeds from HAuCl₄ using NaBH₄. Bottom: Seeded growth of AuNRs in presence of AgNO₃, NaOH and H₂O₂. Drawings are not to scale.

Initial syntheses were conducted using different NaOH volumes (100 μL , 50 μL , 40 μL , and 37.5 μL) to study the effect of NaOH concentration on nanorod formation. This range was chosen based on previous reports, showing that NaOH additions between 22.5 and 100 μL result in less than ~2% impurity, while more basic conditions tend to promote the formation of nanocubes and other irregular particles. In this study, 100 μL NaOH produced smaller particles with relatively fewer deformities, but the number of nanorods was low and the sample contained a significant portion of non-rod-shaped species. Reducing the NaOH volume to 37.5 μL led to the formation of larger, less defined structures including dog-bone-like shapes and aggregated chunks. The 50 μL NaOH condition provided a more balanced outcome, producing a consistent population of nanorods with lower shape irregularities, and better reproducibility. As a result, this condition was selected for further purification and detailed characterization. For reference, UV-Vis spectra and representative TEM images from syntheses using 100, 40, and 37.5 μL NaOH are provided in the Appendix (Figure 8.1-8.3) to illustrate the effect of NaOH concentration on product morphology and purity.

Following synthesis under the optimized 50 μL NaOH condition, the AuNR dispersion was purified using a two-step differential centrifugation process to fractionate particles by size and shape. The first centrifugation (12,000 \times g for 30 minutes) yielded a supernatant (Sample A) and a pellet. The pellet was redispersed and subjected to a second centrifugation step (15,000 \times g for 30 minutes), resulting in another supernatant (Sample B) and a final pellet (Sample C), which was also redispersed in water for analysis. Due to its high optical density, Sample C was diluted 5 times prior to UV-Vis measurement to avoid detector saturation.

The UV-Vis absorption spectra of all three fractions are shown in Figure 5.5. Raw absorbance spectra revealed the typical plasmonic features of AuNRs, with a transverse mode near 520 nm and a longitudinal resonance between 700-800 nm (Figure 5.5a). Sample A exhibited a strong, narrow longitudinal peak at approximately 760 nm, consistent with a monodisperse population of long, high-aspect ratio rods. Sample B displayed a much weaker and broader peak centered around 730 nm, suggesting the presence of fragmented, spherical, or otherwise

less anisotropic particles. Sample C showed a relatively broad longitudinal peak near 750 nm, despite being measured at a 5 times dilution, indicating a high particle concentration but with increased size and shape variability.

To isolate spectral differences independent of concentration, the data were normalized to the intensity of the longitudinal peak (Figure 5.5b). In this view, Sample A retained the most red-shifted and narrowest longitudinal mode, confirming high uniformity and aspect ratio. Sample B showed a slight blue shift and broadening, consistent with a lower aspect ratio and greater heterogeneity. Sample C displayed a more prominent transverse peak relative to A and B, as well as a longitudinal peak positioned between the two, pointing to a polydisperse rod population skewed toward shorter or thicker rods. These spectral features confirm the effectiveness of the purification strategy: Sample A and B contain predominantly smaller or isotropic particles; and Sample C includes a broader, rod-rich mixture with moderate polydispersity.

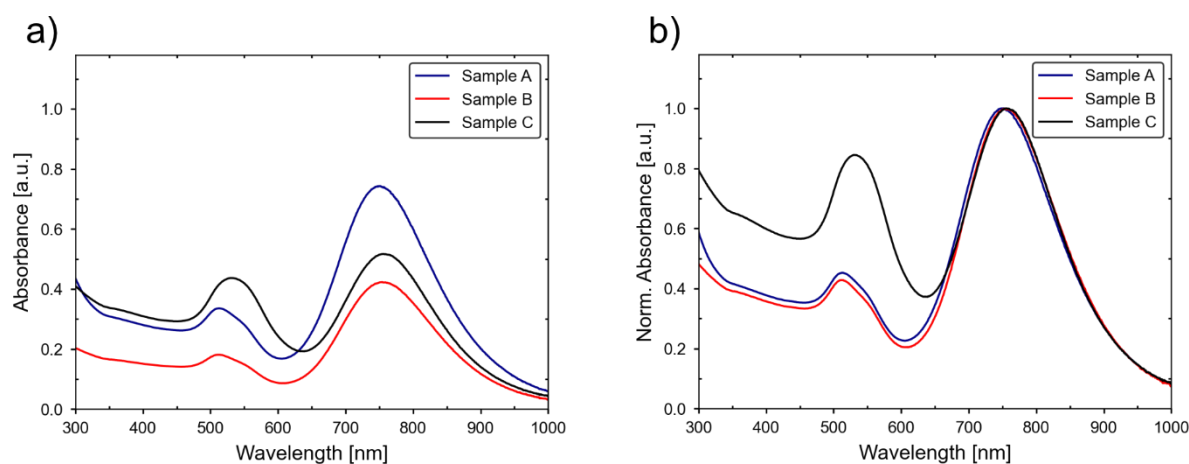


Figure 5.5: UV-Vis absorption spectra of gold nanorod fractions after two-step centrifugation. (a) Raw absorbance spectra of Samples A-C, highlighting differences in concentration and optical density. Sample C was diluted 5x prior to measurement. (b) Normalized spectra showing differences in spectral shape and peak positions, independent of concentration, reflecting differences in nanorod aspect ratio and polydispersity across the samples.

TEM further confirmed these interpretations. Sample A contained sparsely distributed nanorods with shape irregularities and spherical byproducts. Sample B was dominated by small, disordered, or isotropic particles with few noticeable nanorods. In contrast, Sample C showed a dense population of well-defined nanorods with consistent morphology and minimal impurities (Figure 5.6). These observations confirmed that Sample C was enriched in anisotropic particles suitable for further experiments. Quantitative image analysis of Sample C was performed using ImageJ on 200 individual nanorods. The average length was 22.70 ± 2.87 nm and the diameter was 6.26 ± 0.51 nm, yielding an average aspect ratio of approximately 3.63. The histograms, as shown in Figure 5.6, show a narrow diameter

distribution and a moderately broad length distribution, consistent with controlled anisotropic growth and minor polydispersity. These measured dimensions align with the observed longitudinal plasmon resonance near 750 nm in the UV-Vis spectra.^[377]

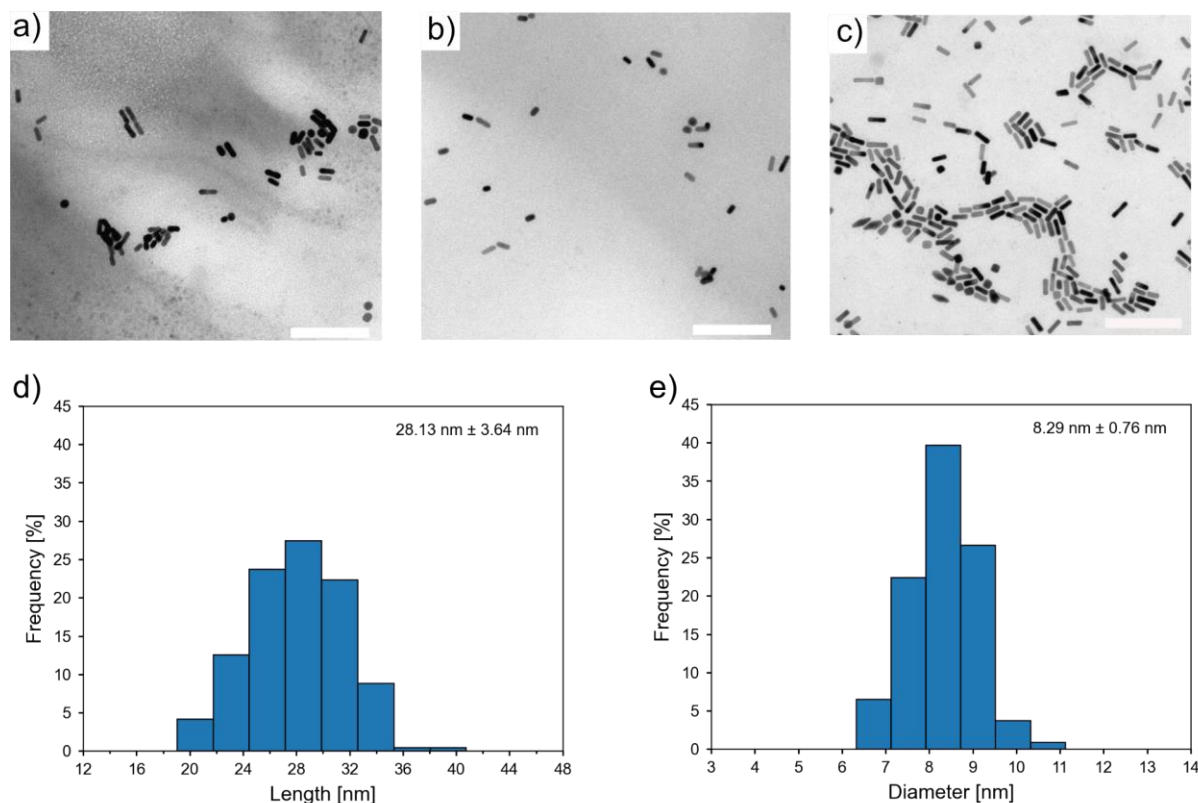


Figure 5.6: TEM images and size distribution of gold nanorods from different fractions after two-step centrifugation. (a-c) TEM images of Samples A, B, and C after two-step centrifugation. (d, e) For sample C, corresponding histogram of AuNR lengths and diameters with, average length of 22.70 ± 2.87 nm and average diameter of 6.26 ± 0.51 nm, respectively. Scale bar is 100 nm.

Notably, further analysis focused exclusively on Sample C. Samples A and B contained excessive residual CTAB, which led to crystallization during storage and interfered with surface modification procedures. Moreover, earlier synthesis protocols using lower reagent volumes produced limited nanorod yields. To address this, a modified synthesis protocol with increased reagent volumes was followed, leading to a more robust and scalable production of AuNRs suitable for further functionalization and application.

5.1.2.2 CTAB-Decanol Method

To address the yield limitations and batch variation issues associated with the H_2O_2 method, a second synthesis approach using a CTAB/*n*-decanol mixed surfactant system was employed.^[200] The schematic is shown in Figure 5.7. This method supported large-volume

synthesis and was expected to produce smaller, highly uniform nanorods suitable for encapsulation. Unlike in the original protocol from which this method was adapted, the synthesized nanorods were not subjected to secondary growth using themselves as seeds. This step was intentionally omitted to preserve the smaller rod dimensions required for subsequent encapsulation experiments.

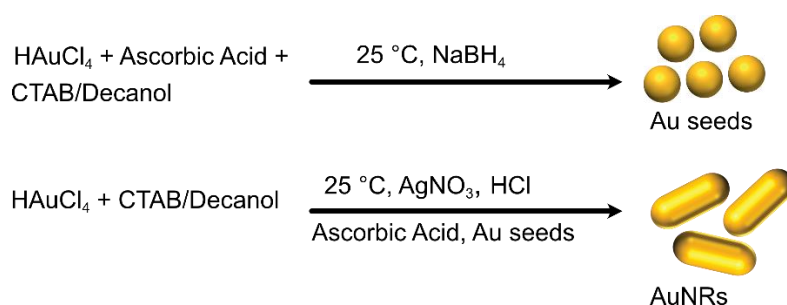


Figure 5.7: Schematic representation of the seeded growth method for synthesizing gold nanorods with CTAB/*n*-decanol as solvent. Top: Preparation of Au seeds from HAuCl₄ using NaBH₄ in presence of ascorbic acid. Bottom: Seeded growth of a AuNRs in presence of AgNO₃, HCl and ascorbic acid. Drawings are not to scale.

The UV-Vis spectrum of the resulting AuNRs featured a well-defined transverse plasmon resonance at 508 nm and a sharp, symmetric longitudinal resonance centered at 760 nm, consistent with a highly monodisperse population of anisotropic particles. The absence of shoulders or peak broadening indicated minimal by-product formation. As shown in Figure 5.8, the UV-Vis spectra of Sample A (before decanol wash) and Sample B (after wash and redispersion in 10 mM CTAB) are nearly identical, with no significant shift or change in intensity. This confirms that the purification process had no measurable impact on the optical properties or morphology of the nanorods, preserving their uniformity and structural integrity.

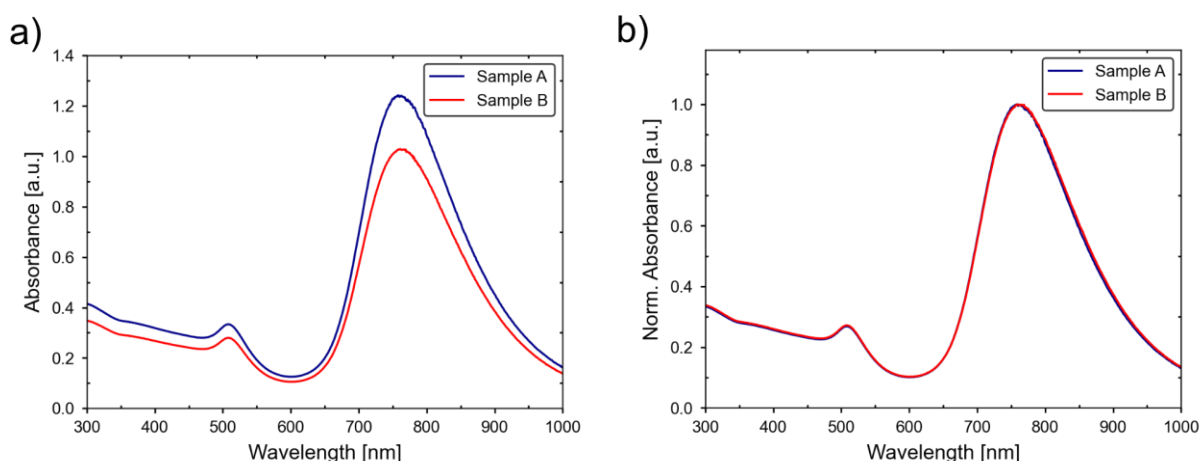


Figure 5.8: UV-Vis absorption spectra of gold nanorods after transfer from CTAB/*n*-decanol mixture to CTAB. (a) Raw absorbance spectra. (b) Normalized spectra.

TEM analysis confirmed the high structural integrity and morphological uniformity of the synthesized nanorods (Figure 5.9). The particles were well-dispersed, with smooth surfaces and rounded tips, and no evidence of aggregation or malformed structures was observed. Statistical analysis of 200 individual nanorods yielded an average length of 28.13 ± 3.64 nm and an average diameter of $8.29 \text{ nm} \pm 0.76$ nm, corresponding to an aspect ratio of approximately 3.39. While a moderate degree of size dispersion was observed, particularly in the length distribution, the overall uniformity remains commendable given the scale and complexity of the synthesis.

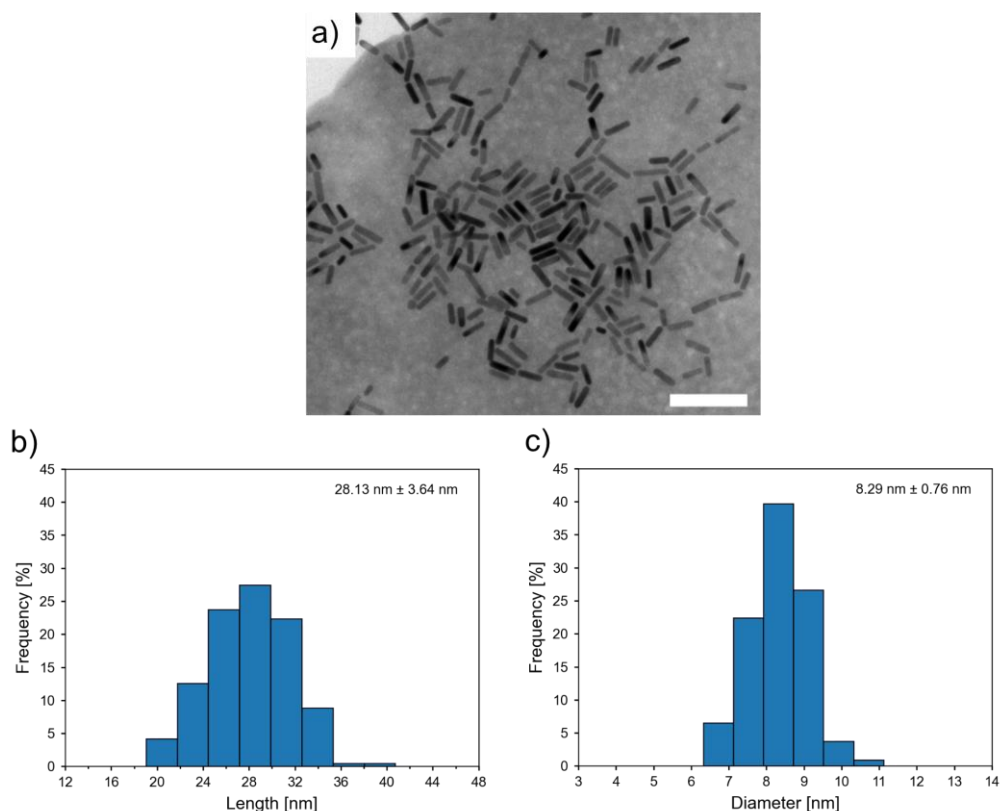


Figure 5.9: TEM images and size distribution of gold nanorods from different fractions after two-step centrifugation. (a) TEM image of rods. (b, c) Corresponding histogram of AuNR lengths and diameters with, average length of 28.13 ± 3.64 nm and average diameter of $8.29 \text{ nm} \pm 0.76$ nm, respectively. Scale bar is 100 nm.

A total of 330 mL of colloidal solution containing nanorods at a concentration of 6.3 nM was successfully produced. Achieving this level of control over anisotropic growth in an aqueous-phase system, known to be inherently less tunable than organic-phase syntheses, underscores the robustness and scalability of the employed CTAB/*n*-decanol approach. These results highlight not only the structural quality of the nanorods but also the practical feasibility of producing them in large quantities under environmentally benign conditions. To ensure biocompatibility for encapsulation, the CTAB-capped AuNRs underwent a ligand exchange procedure, as detailed in Section 5.2.2.

5.1.3 Synthesis of Spherical Gold Nanoparticles

In the later part of the work gold nanoparticles were required and hence AuNPs were synthesized as a part of this work. The synthesis was carried out via a surfactant-assisted growth method adapted from Schulz *et al.*^[248] The resulting nanoparticles were stabilized by a bilayer of CTAC, which provided electrostatic and steric stabilization throughout the process. The goal of this synthesis was to obtain uniform, colloiddally stable spherical nanoparticles with a target diameter of ~18 nm. The schematic is shown in Figure 5.10. For encapsulation of the particles, a higher concentration of AuNPs is required. To avoid the variability that can arise from preparing multiple small-scale batches, a scaled-up synthesis (Sample B) was performed by increasing all reactant quantities tenfold while maintaining the same molar ratios and conditions. This approach aimed to produce a larger quantity of particles in a single, uniform batch.

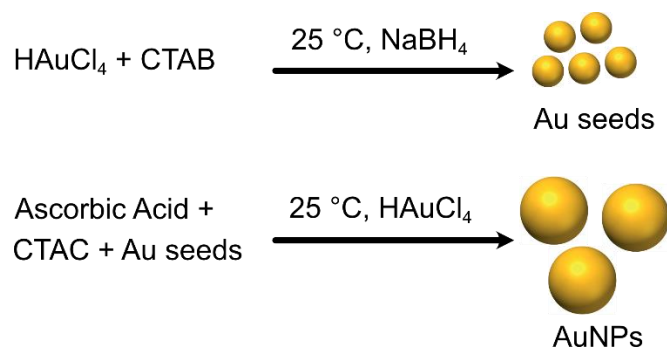


Figure 5.10: Schematic representation of the seeded growth method for synthesizing gold nanoparticles.

Top: Preparation of CTAB stabilized Au seeds from HAuCl_4 using NaBH_4 . Bottom: Seeded growth of CTAC stabilized AuNPs in presence of Ascorbic Acid. Drawings are not to scale.

The optical properties of both samples were analyzed by UV-Vis spectroscopy, with the results shown in Figures 5.11. Figure 5.11a shows the raw UV-Vis spectra of both the standard synthesis (Sample A, red curve) and the scaled-up batch (Sample B, blue curve). Sample A exhibited a strong and symmetric surface plasmon resonance (SPR) peak at 524 nm, characteristic of monodisperse spherical AuNPs in the 15-20 nm range. Sample B showed a nearly identical SPR peak, with slightly higher absorbance due to the increased particle concentration.

To isolate spectral shape from concentration effects, normalized spectra were compared (Fig. 5.11b). Both Sample A and Sample B show nearly identical peak shapes and positions, confirming that the scale-up preserved particle size distribution and optical uniformity. No spectral broadening or red-shift was observed during storage or after purification, indicating that the particles retained their colloidal stability. The well-defined SPR peak is indicative of

high optical quality and uniform particle size, consistent with previous studies of spherical gold nanoparticles. A subtle shoulder can be observed in the spectra of scaled-up batch (blue curve), suggesting presence of a minor population of non-uniform particles.

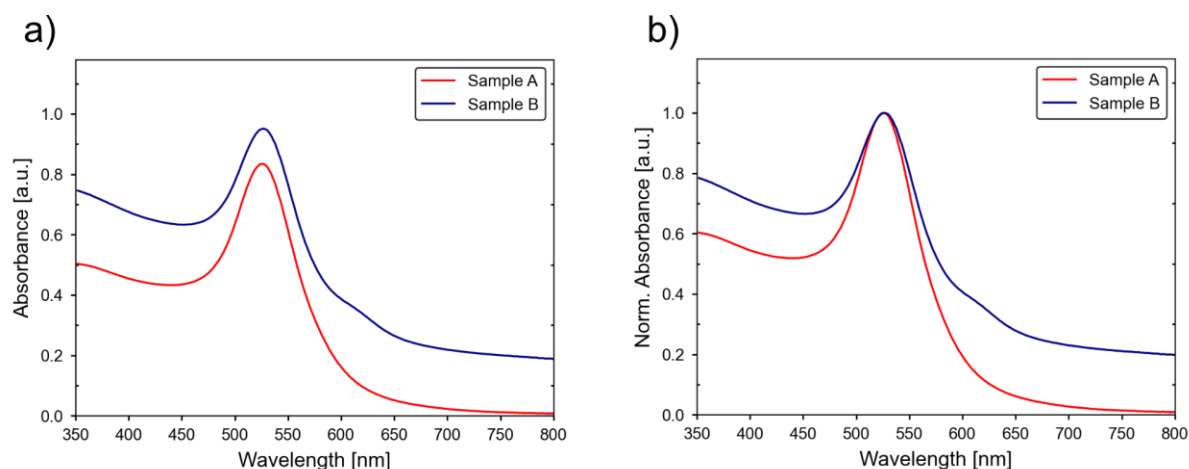


Figure 5.11: Normalized UV-Vis absorption spectra of gold particles of standard and scale up synthesis. (a) Raw absorbance spectra. (b) Normalized spectra.

TEM images from sample B, as shown in Figure 5.12, confirmed the formation of spherical, monodisperse nanoparticles. The particles appeared well separated, with no visible aggregation or deformation. High-magnification images showed smooth particle surfaces and consistent shape across the sample. Statistical size analysis was performed on 200 particles. The average diameter was measured to be 18.69 nm, with a standard deviation of 0.69 nm. The size histogram revealed a narrow, unimodal distribution, in agreement with the UV-Vis results. The particle size closely matched the expected diameter based on the synthesis conditions and SPR peak position. No significant populations of smaller or irregularly shaped particles were observed, suggesting that secondary nucleation was suppressed and that growth occurred predominantly through surface-controlled deposition.

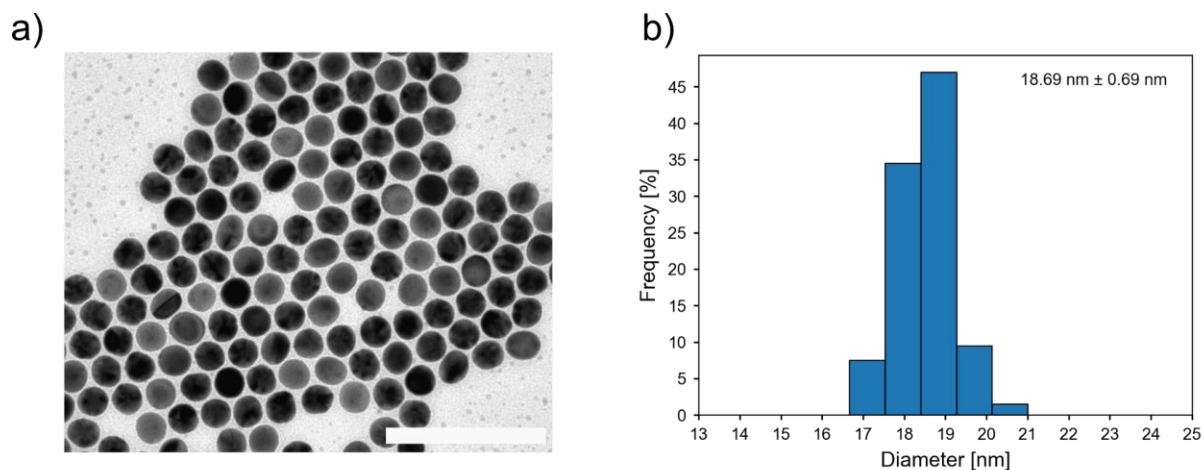


Figure 5.12: TEM images and size distribution of AuNPs. a) TEM images of particles. Scale bar is 100 nm. b) Corresponding histogram of AuNP diameter, with average of 18.69 ± 0.69 nm.

In summary, the tenfold scale-up of the AuNP synthesis was successful, producing a high-concentration batch while maintaining the monodispersity, spherical shape, and optical properties of the standard preparation. To make these CTAC-stabilized nanoparticles compatible with proteins for encapsulation, a ligand exchange was performed to replace the CTAC coating, as detailed in Section 5.2.3.

5.2 Ligand Exchange Strategies

To enable efficient encapsulation of nanoparticles into engineered protein cages, surface functionalization via ligand exchange was required. All native ligands were replaced with molecules bearing a thiol group for strong binding to the nanoparticle surface and a polar moiety to ensure solubility in aqueous environments. The choice of ligand was guided by the intended surface charge and the need for electrostatic complementarity with the encapsulating protein. For all systems, DLS, ζ -potential, and TEM were used to confirm successful ligand exchange and assess colloidal stability.

5.2.1 Functionalization of CdSe/CdS DiRs

Achieving aqueous dispersibility and functional surface chemistry on anisotropic nanoparticles such as CdSe/CdS DiRs is a nontrivial challenge. The goal was to develop a ligand exchange strategy that would enable water solubility and successful conjugation of CLP while maintaining colloidal stability and particle integrity. As-synthesized DiRs are stabilized with octadecylphosphonic acid (ODPA), a long-chain hydrophobic ligand that stabilizes them in organic solvents such as toluene or chloroform but makes them completely insoluble in water. [378] ODPA binds strongly to Cd-rich facets through its phosphate group, and due to this strong binding, incomplete displacement can lead to patchy or unstable surface coverage. Compared to spherical quantum dots, the rod-like geometry of DiRs adds complexity for two reasons: first, different crystal facets present distinct surface chemistries and ligand binding affinities, making uniform ligand exchange more difficult; second, the anisotropic shape promotes directional interactions that increase the tendency for aggregation, especially in polar solvents.

To ensure aqueous stability and compatibility with the protein cage, whose inner surface is negatively charged, the native ODPA ligand was replaced with positively charged thiol-containing molecules, such as (11-Mercaptoundecyl)-*N,N,N*-trimethylammoniumbromide (MUTAB) or 11-Amino-1-undecanethiol hydrochloride (AUT). [160] These molecules possess a thiol group that forms a strong Cd-S bond with the nanoparticle surface, replacing the weakly bound ODPA. In addition, their polar terminal groups improve solubility in water and promote electrostatic compatibility with the protein interior. Structures of the ligands are shown in Figure 5.13. The exchange was carried out via an organic-to-aqueous phase transfer method, during which the DiRs transitioned into the aqueous phase upon successful binding of the new ligands.

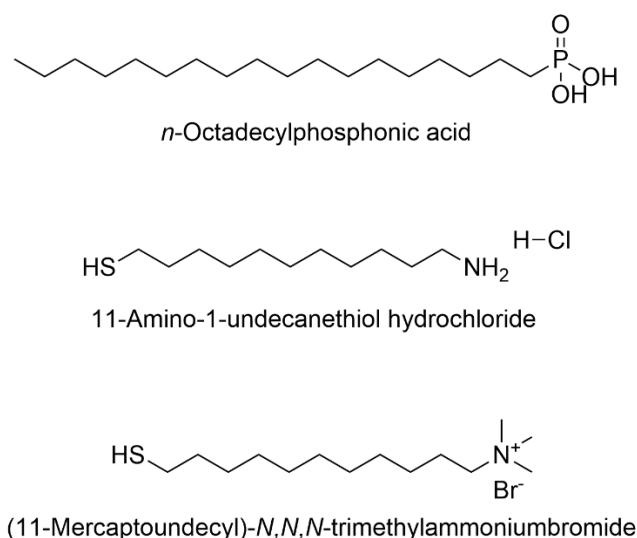


Figure 5.13: Chemical structures of ligands used for surface modification of CdSe/CdS DiRs. Top: Octadecylphosphonic acid (ODPA), the native hydrophobic ligand. Middle: 11-Amino-1-undecanethiol hydrochloride (AUT). Bottom: (11-Mercaptoundecyl)-*N,N,N*-trimethylammonium bromide (MUTAB)

A two-phase ligand exchange protocol was employed. Rather than attempting a direct transfer from toluene to water, which often results in precipitation or incomplete ligand coverage due to the abrupt change in solvent polarity, the DiRs were first transferred from toluene to methanol, and then from methanol to water. This gradual transition helps preserve colloidal stability by reducing interfacial stress and allowing more controlled ligand binding. A schematic representation of ligand exchange process is shown in Figure 5.14, left. Following ligand exchange, the DiRs were further functionalized with a CLP. The CLP binds to the nanoparticle surface via a terminal cysteine thiol and is designed to interact specifically with the interior of the encapsulin protein cage.^[14] This secondary functionalization enables high-affinity encapsulation, independent of solution ionic strength.^[14] The final CLP-functionalized DiRs, stabilized in aqueous solution and ready for encapsulation, are illustrated in Figure 5.14, right.

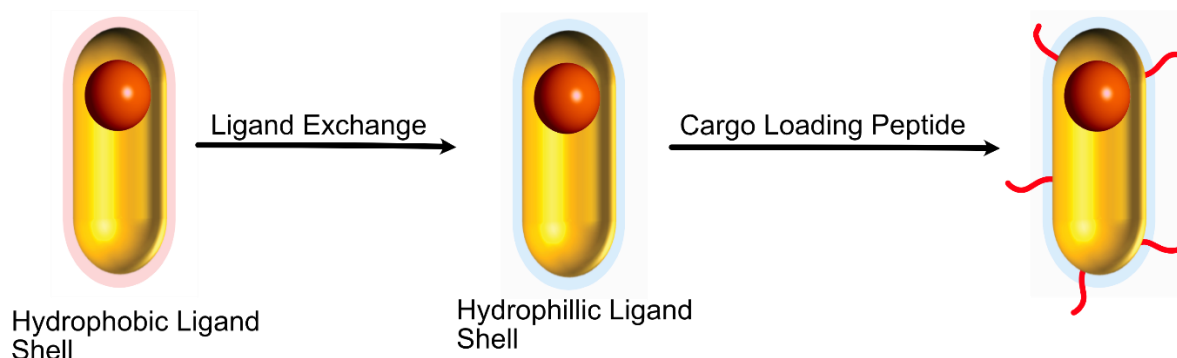


Figure 5.14: Schematic showing ligand exchange strategy for CdSe/CdS DiRs. The hydrophobic ligand shell from the as-synthesized rods is exchanged with aminothiols, and further functionalized with cargo-loading peptide.

Each step of the modification process was monitored using a combination of water dispersibility, UV-Vis spectroscopy, DLS, ζ -potential, and TEM to evaluate surface chemistry, colloidal stability, and structural integrity.

AUT-Only Ligand Exchange

The initial ligand exchange was performed using AUT, a cationic thiol-bearing ligand featuring a secondary amine. This strategy was inspired by prior success using short-chain AET for aqueous solubilization of semiconductor nanocrystals.^[160] AUT was selected over AET due to its longer alkyl chain, which was expected to enhance ligand packing and surface coverage, thereby improving colloidal stability.

To estimate the required ligand concentration for complete surface coverage, the molar concentration of DiRs was first calculated from UV-Vis absorbance measurements using extinction coefficients reported by Yu *et al.* for CdSe nanocrystals.^[379] From the molar concentration and known sample volume, the total number of particles was obtained. The surface area of a single rod was approximated by modeling the DiRs as a cylinder with two hemispherical caps. Multiplying this by the total number of particles yielded the total nanoparticle surface area in solution. Based on literature-reported ligand footprints of 4.5-5.0 molecules per nm² for similar alkylthiols, the number of ligand molecules required for full monolayer coverage was estimated.^[380-381] To drive the exchange to completion, a 100-fold molar excess of AUT relative to the estimated surface coverage was added.

For example, the extinction coefficient of the CdSe core was estimated using its diameter d_{core} which was calculated from the first excitonic absorption peak (λ) using the empirical sizing curve reported by Yu *et al.*^[379]

$$d_{core} = (1.6122 \times 10^{-9})\lambda^4 - (2.6575 \times 10^{-6})\lambda^3 + (1.6242 \times 10^{-3})\lambda^2 - (0.4277)\lambda + 41.57$$

The extinction coefficient was then calculated as:

$$\epsilon = 5857 \cdot d_{core}^{2.65}$$

The particle concentration c was obtained from the measured absorbance A and path length l using the Beer-Lambert law:

$$A = \epsilon \cdot c \cdot l$$

From this, the total number of particles was determined by multiplying c with the solution volume and Avogadro's number. To estimate the total ligand requirement, the surface area of a single DiR was calculated by modeling it as a cylinder with two hemispherical caps, using the total rod diameter d_{rod} and length l_{rod} :

$$A_{\text{rod}} = 2\pi \left(\frac{d_{\text{rod}}}{2} \right) (l_{\text{rod}} - d_{\text{rod}}) + 4\pi \left(\frac{d_{\text{rod}}}{2} \right)^2$$

This surface-area-based approach proved particularly useful when working with different DiR batches, as it allowed the ligand amount to be scaled appropriately based on particle size and concentration, improving reproducibility across samples.

Post ligand exchange, the particles could be dispersed well in water. Photoluminescence (PL) measurements showed that both ODPa- and AUT-capped DiRs exhibit emission peaks centered around 578 nm, indicating no significant spectral shift upon ligand exchange (Figure 5.15 a) However, the AUT-capped sample displayed a broader peak and noticeably reduced emission intensity compared to the ODPa-capped counterpart. This broadening likely reflects increased inhomogeneous surface disorder or variations in the local dielectric environment introduced by the new ligands. The reduction in PL intensity corresponds to an approximate 11% drop in integrated emission, suggesting the formation of surface trap states during exchange. This trend is consistent with previously reported decreases in quantum yield upon aqueous phase transfer using thiol ligands, where QY dropped from 48% to 38%.^[160] Despite these changes, the preserved emission peak position indicates that the core electronic structure of the nanocrystals remains largely intact. For comparison, both spectra were normalized to their respective maxima. TEM imaging of the DiRs in water shows limited contrast, making it difficult to clearly resolve individual particles (Figure 5.15b)

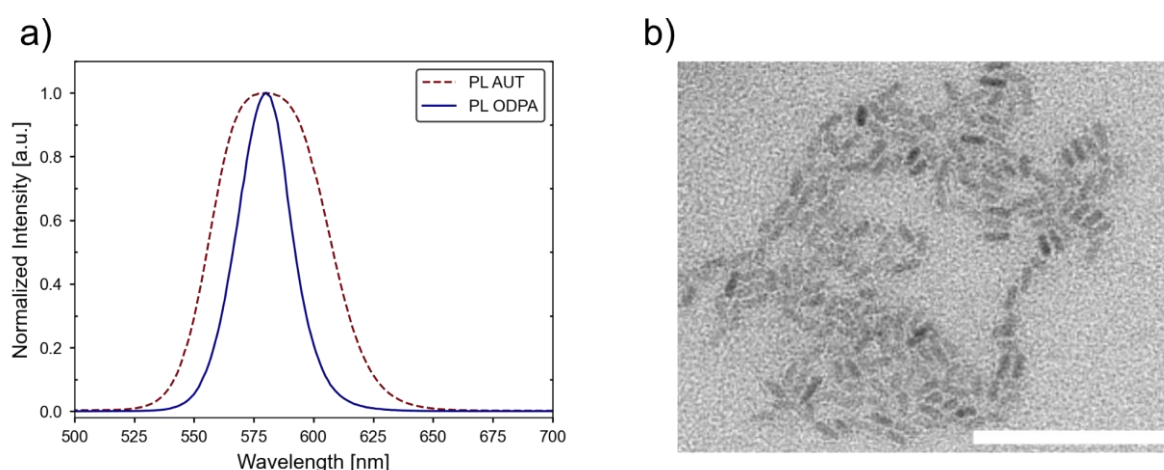


Figure 5.15: Normalized emission spectra and TEM images of CdSe/CdS DiRs. a) DiRs with native ligand shell in toluene (blue) and stabilized with AUT in water (dashed red). Excitation wavelength is 405 nm. b) TEM images of AUT stabilized DiRs. Scale bar is 100 nm.

To assess colloidal stability and dispersion, DLS and ζ -potential measurements were performed. It is critical to note that DLS analysis of anisotropic nanoparticles such as nanorods is non-trivial, as the standard Stokes-Einstein equation assumes spherical morphology. The reported hydrodynamic size is therefore an effective spherical equivalent and includes the

hydrated ligand shell, explaining why it is larger than the core dimensions observed by TEM. Both intensity-weighted and volume-weighted size distributions were analyzed to get a more complete picture of the sample. The intensity distribution, as shown in Figure 5.16a, revealed two peaks, one around 28 nm and another at ~122 nm. However, since DLS intensity is proportional to the d^6 , the larger peak is likely overrepresented and could stem from minor aggregation, elongated particle orientation, or simply a few larger scatterers like dirt in the sample. Intensity data are useful for detecting such outliers, but not reliable for accurate size quantification, especially in anisotropic systems like rods.

The volume distribution, which compensates for this size-bias, showed a single dominant peak around 21 nm, which is more consistent with expectations. This size should not be taken as the physical rod dimension, but rather as the effective hydrodynamic diameter: The diameter of a sphere that would diffuse at the same rate. Importantly, no significant secondary peaks were observed in the volume data, suggesting that the sample is mostly monodisperse and free from aggregation. Both intensity and volume data are shown here to highlight the distinction: intensity plots help flag larger features, while volume plots offer a better approximation of the actual particle population, especially when smaller species dominate the sample.

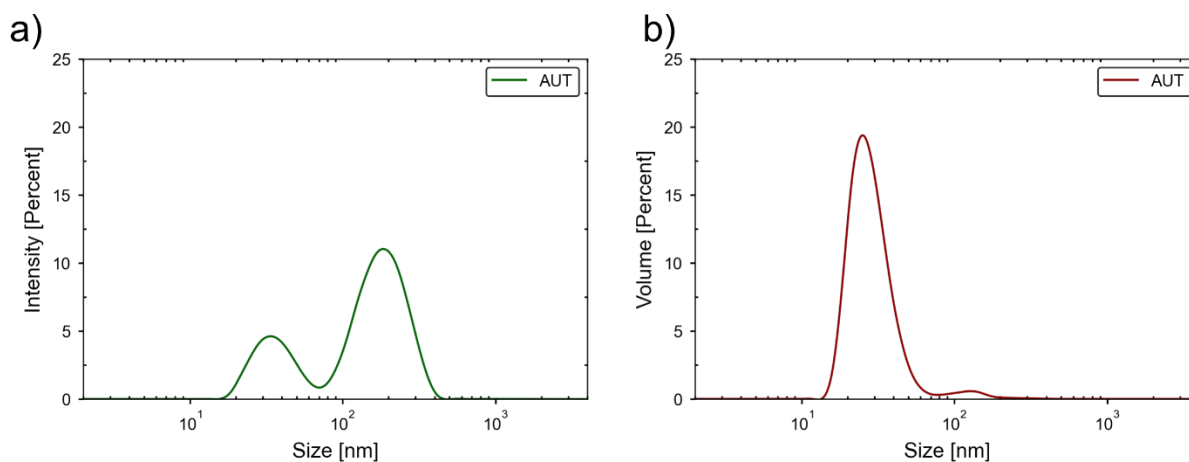


Figure 5.16: Hydrodynamic size distribution of CdSe/CdS DiRs. a) Intensity weighted. b) Volume-weighted. The intensity distribution shows multiple size modes, while the volume distribution indicates a predominantly monomodal population.

ζ -potential measurements revealed a surface charge of +49.8 mV, consistent with successful exchange to amine-terminated ligands. This high positive value indicates strong electrostatic stabilization in water, which aligns with the observed colloidal stability from DLS. The positive charge likely arises from protonated amine groups on the AUT ligands at neutral pH, which also supports the water solubility of the nanorods post-exchange. ζ -potential for the ODPACapped rods could not be measured as standard cuvettes are incompatible with organic

solvents, and alternative methods were not available. Nonetheless, the lack of aggregation after transfer and the high ζ -value post-exchange suggests effective ligand replacement and stabilization in aqueous conditions.

However, the long-term stability of these AUT-functionalized particles was a concern, particularly under buffered conditions relevant for subsequent encapsulation steps. This is due to the nature of AUT as a secondary amine, which can undergo protonation-deprotonation equilibria depending on pH and ionic strength. In contrast, quaternary amines, such as those present in MUTAB, carry a permanent positive charge that is unaffected by buffer conditions. Given this limitation, a mixed-ligand strategy combining AUT and MUTAB was explored to enhance colloidal robustness while maintaining aqueous dispersibility.

AUT:MUTAB Mixed Ligand Exchange

MUTAB carries a quaternary ammonium headgroup, offering a permanent positive charge, independent of the pH value. By blending it with AUT, the goal was to introduce a permanent positive surface charge that remains stable across different pH and ionic conditions, while leveraging AUT to support consistent surface coverage. The total ligand excess was maintained at 100 times the estimated coverage requirement, while varying the AUT:MUTAB molar ratio. Initial attempts using AUT and MUTAB in equal amounts failed to yield a clearly stable dispersion. No obvious phase separation was seen by eye, but centrifugation produced a pellet. This pellet could be redispersed in a propanol-water mixture after sonication, and the resulting suspension had a low ζ -potential of +5.94 mV. Based on this, additional ligand ratios were tested to better understand and optimize stability.

A fixed total ligand excess of 100-fold the estimated surface coverage requirement was used while varying the AUT:MUTAB molar ratios as shown in Table 5.1.

Table 5.1: Molar ratios of AUT:MUTAB

Sample	AUT:MUTAB
A	1:2
B	2:1
C	1:4
D	4:1

All formulations resulted in water-dispersible suspensions. ζ -potential measurements showed that all samples exhibited positive surface charges above +30 mV, consistent with colloidal stability under electrostatic repulsion (Figure 5.17) Sample A had the highest ζ -potential value, followed by Sample C, Sample B, and lastly Sample D.

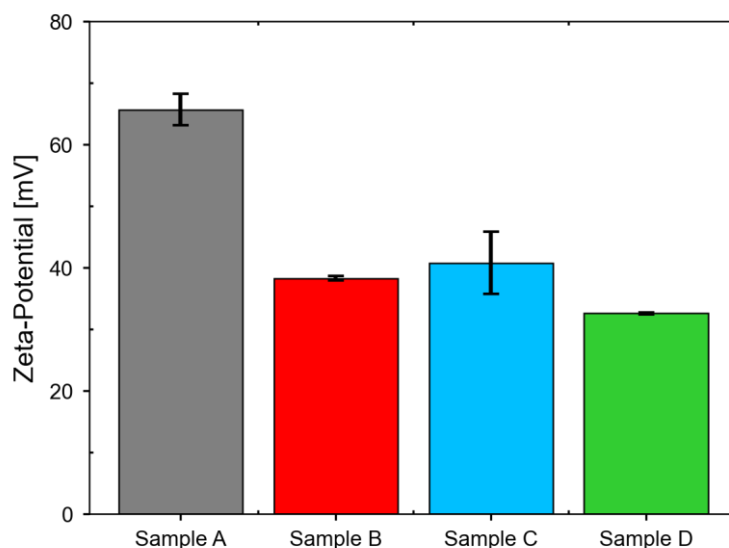


Figure 5.17: ζ -potential measurements of CdSe/CdS DiRs capped with AUT:MUTAB mixture. Sample A=1:2, Sample B=2:1, Sample C=1:4, Sample D=4:1

Photographs of the samples after a few days revealed differences in long-term stability (Figure 5.18). Samples A and C, which had higher MUTAB amount, showed visible aggregation and sedimentation. In contrast, Samples B and D, which contained higher proportions of AUT, remained visually stable. This divergence in stability is notable given that both ligands possess identical C11 alkyl chain lengths, ruling out steric effects as the distinguishing factor. The results indicate that while initial ζ -potential values were sufficient for short-term stabilization, they were not predictive of long-term behavior. The aggregation in MUTAB-rich samples suggests a mechanism rooted in headgroup chemistry rather than chain length. The trimethylammonium headgroup of MUTAB may promote instability through specific ion effects or charge correlation, potentially leading to attractive interactions between particles over time. Conversely, the ammonium headgroup of AUT appears to foster a more stable nanoparticle-solvent interface, possibly due to differences in hydration, hydrogen bonding capacity, or a reduced tendency for interfacial charge imbalance. These findings underscore that the molecular architecture of the ligand headgroup is a critical, and often overlooked, determinant of colloidal stability.

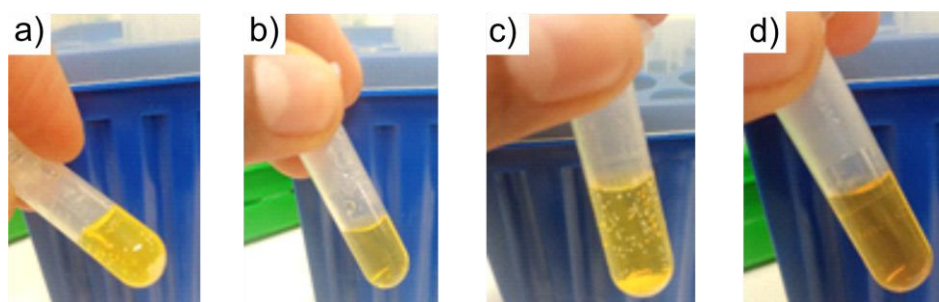


Figure 5.18: Photographs of CdSe/CdS DiRs capped with AUT: MUTAB Mixture. a) Sample A , b) Sample B, c) Sample C, and d) Sample D. Differences in turbidity and visible precipitation reflect variations in colloidal stability among the samples.

CLP functionalization

To better understand the interactions at play during CLP functionalization, a schematic representation of the system is shown in Figure 5.19. The CLP, illustrated in the schematic, is a 16-amino acid sequence with three functional segments. The N-terminal region is embedded within the ligand shell and contains a cysteine residue for covalent binding to the DiRs surface, along with a glutamic acid that electrostatically interacts with the positively charged MUTAB and AUT, enhancing surface association. This is followed by a flexible hinge motif, and finally, a C-terminal anchor sequence that mediates binding to the inner surface of the encapsulin shell.^[14]

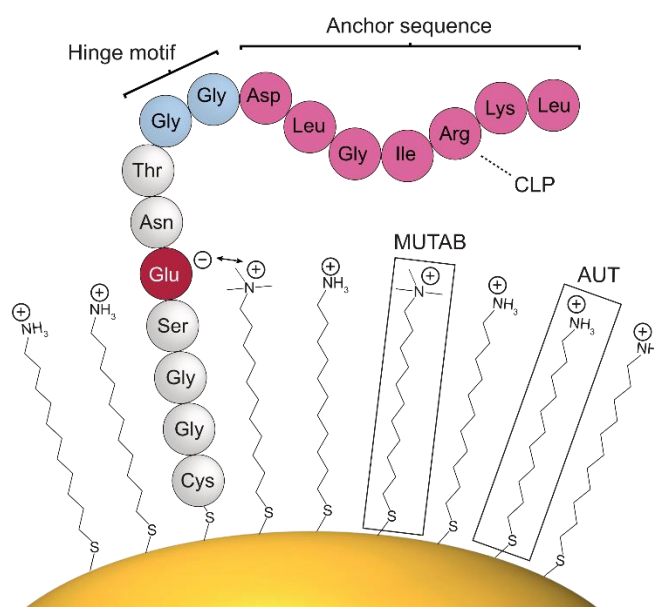


Figure 5.19: Schematic a of AUT/MUTAB-stabilized CdSe/CdS DiR functionalized with a 16-amino acid long CLP. The CLP can be divided into three parts: First, an N-terminal part buried in the ligand shell containing a cysteine for covalent binding to the DiR surface and a glutamic acid residue, which electrostatically interacts with

the positive charge of the AUT or MUTAB shell providing increased stability. Second, a flexible hinge motif, and lastly, a C-terminal anchor sequence, which binds to CLP-binding pocket of the inner encapsulin surface.

As discussed in the previous paragraph, most stable particles are co-functionalized with two ligands: AUT and MUTAB in the ratio 4:1 or 2:1. AUT carries a terminal primary amine group (pKa ~9-10). At acidic and near neutral pH, it is predominantly protonated ($-\text{NH}_3^+$), imparting positive surface charge. At alkaline pH (≥ 10), the amine is increasingly deprotonated to the neutral $-\text{NH}_2$ form, reducing its electrostatic contribution. By contrast, MUTAB presents a pH-independent positive charge.

Upon incubation with CLP, DLS measurements based on volume-weighted distributions revealed a clear contrast in particle size profiles (Figure 5.20) Volume-weighted data were chosen for analysis as they offer a more accurate representation of the particle population, particularly in rod-like systems where scattering intensity can distort apparent size. The 4:1 sample exhibited a single, sharp peak centered at ~13 nm, consistent with a stable, monodisperse suspension. In contrast, the 2:1 formulation showed a bimodal distribution, with one peak at ~58.8 nm and a second peak at ~955 nm. This indicates the presence of both smaller particles and large aggregates in the system. These findings suggest that surface architecture at the 2:1 ratio may promote interparticle association or destabilization upon peptide binding, while the 4:1 formulation offers a more stable surface environment that better tolerates CLP functionalization.

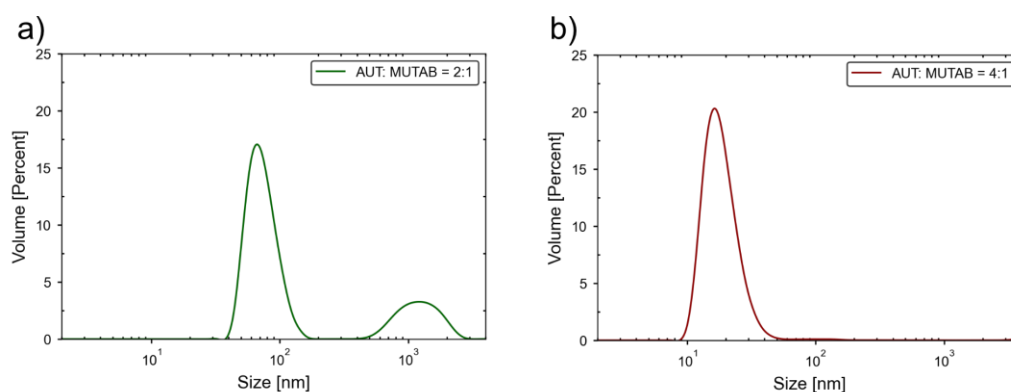


Figure 5.20: Hydrodynamic size distribution of CdSe/CdS DiRs capped with different AUT: MUTAB ratios and CLP. Volume-weighted DLS measurements with AUT:MUTAB ratio of a) 2:1 and b) 4:1 in presence of CLP.

To further confirm the differences in colloidal behaviour, TEM imaging was performed on both 2:1 and 4:1 formulation after CLP functionalization (Figure 5.21) The 4:1 sample appeared well-dispersed, with clearly visible, non-aggregated nanorods. In contrast, the 2:1 formulation showed irregular clustering and poor particle separation, consistent with DLS measurements and visible aggregation during storage. These images support the conclusion that while both formulations maintained high surface charge after CLP addition, only the 4:1 sample remained structurally stable.

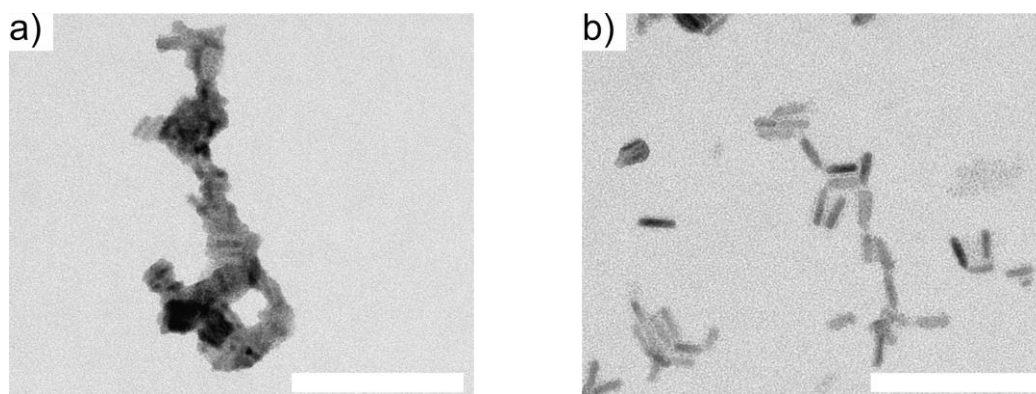


Figure 5.21: TEM images of CdSe/CdS DiRs capped with different AUT: MUTAB ratios and CLP. a) 2:1 b) 4:1. Scale bar is 100 nm.

Although the 4:1 AUT:MUTAB formulation successfully stabilized smaller nanorods ($\sim 10.9 \times 4.0$ nm), initial encapsulation experiments yielded inconclusive results. To achieve a more robust interaction, the strategy was tested on larger rods (18.6×5.4 nm and 18.5×5.0 nm); however, the mixed-ligand system did not yield positive encapsulation outcomes at this size. This suggested that the two-ligand architecture might not provide a sufficiently consistent or accessible interface for the CLP on larger surfaces. To simplify the system and ensure direct CLP access, a one-step MUTAB/CLP functionalization was pursued.

One-Step MUTAB/CLP Functionalization

A schematic representation of this setup is shown in Figure 5.22. The functionalization was achieved by first dissolving MUTAB in methanol, adding the DiRs, and then introducing this mixture to an aqueous solution containing MUTAB and CLP. Initial attempts using sequential functionalization (MUTAB followed by CLP) proved unreliable and led to poor dispersion. Instead, the simultaneous addition of both components was found to improve binding uniformity and dispersion quality. The resulting samples were concentrated using centrifugal concentrators. Dialysis was also attempted but did not perform well in retaining stability or removing unbound material.

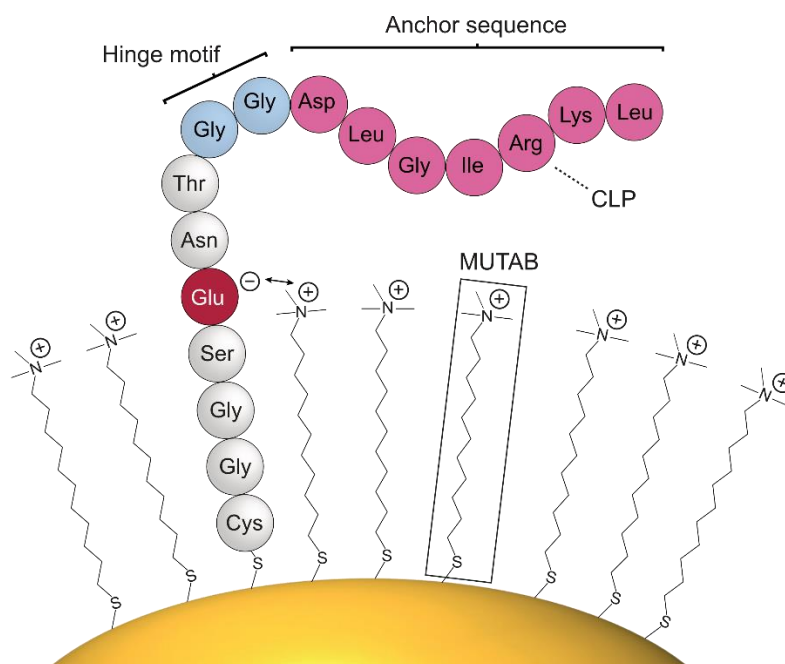


Figure 5.22: Schematic a of MUTAB-stabilized CdSe/CdS DiR functionalized with a 16-amino acid long CLP.

The CLP can be divided into three parts: First, an N-terminal part buried in the ligand shell containing a cysteine for covalent binding to the DiR surface and a glutamic acid residue, which electrostatically interacts with the positive charge of the MUTAB shell providing increased stability. Second, a flexible hinge motif, and lastly, a C-terminal anchor sequence, which binds to CLP-binding pocket of the inner encapsulin surface.

The MUTAB/CLP-coated rods were characterized using ζ -potential, DLS, TEM, and PL measurements. ζ -potential measurements showed a positive surface charge of $+37.7 \pm 1.8$ mV, confirming effective surface functionalization with cationic MUTAB. Volume-weighted DLS analysis showed a narrow, monomodal distribution with a hydrodynamic diameter of 15.2 nm, as shown in Figure 5.23a, indicating good colloidal stability and uniform dispersion. TEM images revealed well-separated nanorods with no significant aggregation (Figure 5.23b)

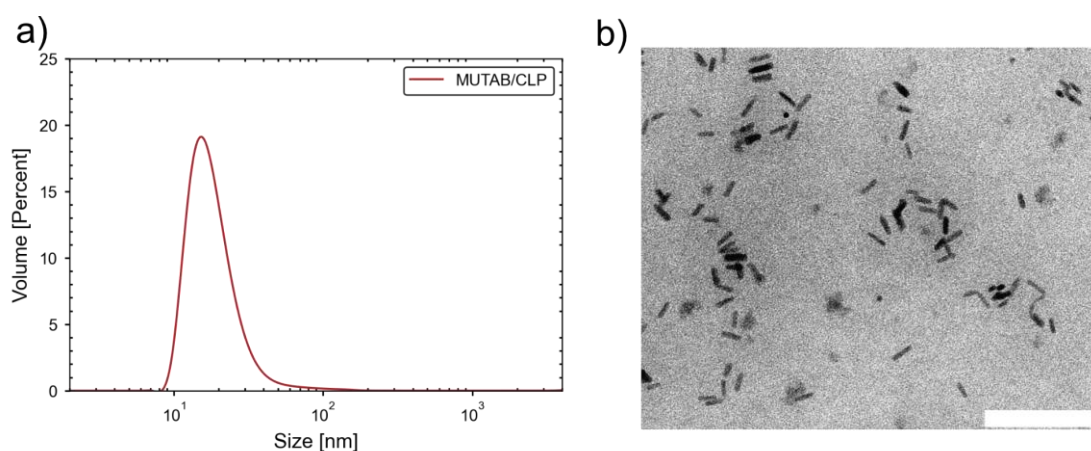


Figure 5.23: Volume weighted hydrodynamic size distribution and TEM images of MUTAB/CLP capped CdSe/CdS DiRs. a) DLS shows a monomodal distribution. b) TEM shows stable DiRs. Scale bar is 100 nm.

PL spectra showed a modest redshift in the emission maximum after ligand exchange from ODPa to MUTAB/CLP (Figure 5.24) This shift is attributed to changes in the local surface environment, particularly the introduction of a permanent positive charge from MUTAB and multiple polar and charged residues (e.g., Glu, Asp, Arg, Lys) from CLP. These groups create a strong surface dipole and enhance dielectric screening, which perturbs the nanocrystal's band edge positions and stabilizes the excitonic state, leading to a lower emission energy. Similar redshifts have been reported in the literature for nanocrystals capped with charged or highly polar ligands, where the resulting electrostatic field perturbs the exciton energy levels.^[31, 54, 382] In contrast, no significant PL shift was observed when ODPa was exchanged with AUT, despite its ability to render the particles water-soluble (Figure 5.12) The terminal amine of AUT imparts only mild polarity compared to the strong, permanent charge carried by MUTAB, leaving exciton confinement and surface potential largely unaffected. This comparison highlights that the PL shift observed with MUTAB/CLP is not a general consequence of ligand exchange or aqueous transfer, but rather a specific outcome of the combined electrostatic and dielectric effects introduced by the functional ligand system.

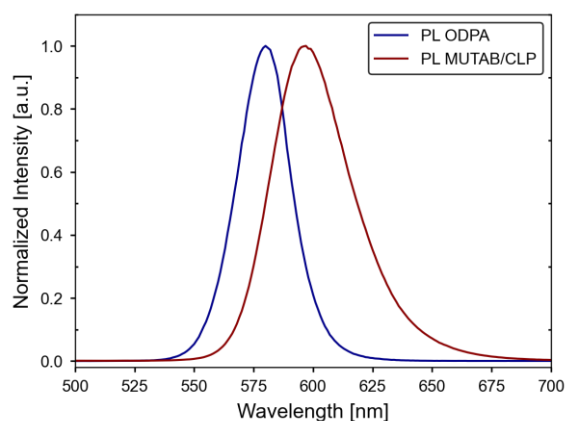


Figure 5.24: Normalized emission spectra of CdSe/CdS DiRs. DiRs with native ligand shell in toluene (blue) and stabilized with MUTAB/CLP in water (darkred)

In summary, the one-step MUTAB/CLP functionalization provided a more reliable route to stable, water-dispersible CdSe/CdS nanorods compared to earlier ligand exchange strategies. The combined cationic and peptide-based interface produced highly uniform, positively charged particles that remained well-dispersed. Together, these results validated the MUTAB/CLP approach as a robust and versatile strategy for preparing nanorods compatible with subsequent encapsulation studies.

CLP Binding Confirmation via Fluorescence Quenching Assay

To confirm that the CLP was covalently attached to the DiR surface via its cysteine residue, a disulfide cleavage assay was used.^[383] In this assay, CLP with a terminal fluorophore label, fluorescein amidites (FAM), was chosen to serve as an optical reporter of attachment. When bound to the DiR surface, the fluorophore is held in close proximity to the DiR, where interactions with the semiconductor surface can alter its emission properties.

Fluorescence spectra were first collected under two excitation conditions, 450 nm excitation and 495 nm, to separately study the fluorophore and DiRs (Figure 5.25) Excitation at 450 nm excites both the CdS component of the rods and FAM, whereas excitation at 495 nm corresponds closely to the FAM absorption maximum and is absorbed only weakly by the rods. Under 450 nm excitation, the free CLP-FAM displayed a strong emission maximum at ~522 nm (4.2×10^6 a.u.). When CLP-FAM was incubated with CdSe/CdS DiRs, the spectrum was dominated by DiR emission at ~600 nm. A weak shoulder at 524 nm (5.3×10^5 a.u.) was observed, indicating quenching of the dye in the bound state. This quenching of FAM fluorescence indicates that when the peptide is attached to the nanorod surface, non-radiative decay pathways compete with dye emission. Importantly, DiRs incubated without FAM (DiRs-CLP) showed only the rod emission peak, confirming that the 520-525 nm shoulder in the conjugate spectrum arose from FAM.

To test whether the peptide was truly attached through the cysteine–Cd coordination bond, approximately 1.5 mL of the DiR-CLP-FAM sample was treated with dithiothreitol (DTT). DTT was added to achieve a final concentration of 50 mM, providing a large excess of competing thiol groups relative to the surface-bound cysteine residues. DTT is expected to displace the cysteine-Cd interaction, thereby releasing CLP-FAM into solution. After incubation and centrifugation, the supernatant containing displayed a clear FAM emission peak at 521 nm with an intensity of 1.3×10^6 a.u., confirming that CLP-FAM had been released from the rods through thiol exchange.

Spectra were also collected under 495 nm excitation to selectively probe the dye. In this case, free CLP-FAM showed the brightest emission (4.2×10^6 a.u. at 522 nm). The DiR-CLP-FAM mixture displayed only a weak FAM signal, while the DTT-treated supernatant recovered an intermediate intensity (1.3×10^6 a.u.). The CLP-FAM emission profile showed a broad tail extending to ~650 nm, overlapping with the absorption range of the rods. This spectral overlap could in principle allow Förster-type transfer from the dye to the rods, and indeed a modest (~10%) increase in rod photoluminescence was observed for DiRs in the presence of FAM compared to DiRs without FAM. However, given the relatively small magnitude of the effect and the absence of lifetime or excitation scan-data, the results are most conservatively

interpreted as a minor enhancement of rod emission in the presence of FAM, rather than unambiguous proof of FRET.

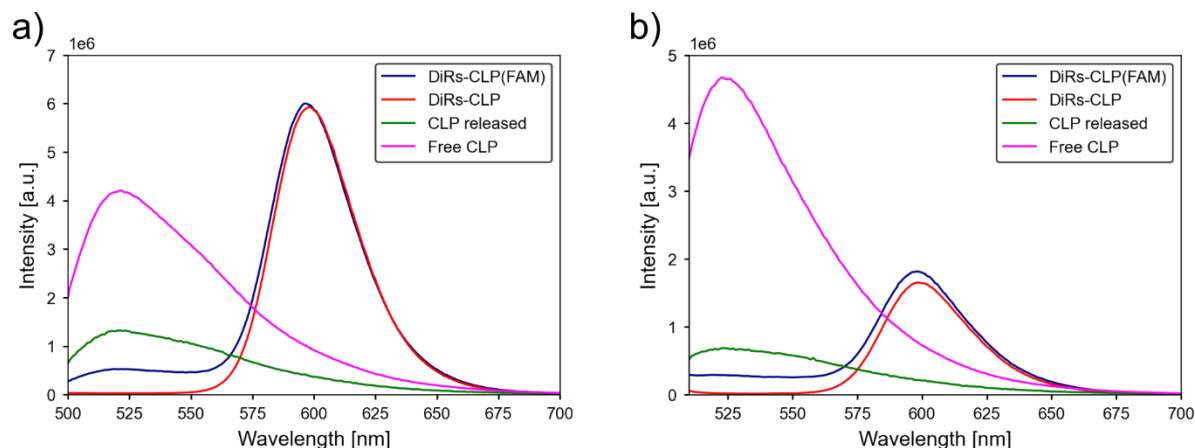


Figure 5.25: Emission spectra of CdSe/CdS DiRs and CLP-FAM conjugates under 450 nm and 495 excitation. Emission profiles are shown for free CLP-FAM in solution (magenta), DiR-CLP-FAM conjugates (blue), CLP-FAM released into the supernatant after DTT treatment (green), and DiRs-CLP, without-Fam (red). a) Excitation wavelength is 450 nm. b) Excitation wavelength is 495 nm.

Taken together, these results establish a qualitative sequence: free CLP-FAM displays bright emission, CLP-FAM bound to DiRs is strongly quenched, and DTT treatment recovers dye fluorescence in the supernatant. The data demonstrate that CLP-FAM is indeed associated with the DiRs via its cysteine residue and can be displaced through thiol exchange chemistry. It has to be noted that the unbound peptide was not removed prior to DTT treatment because centrifugal washing caused sample loss and high-speed centrifugation led to aggregation of CLP-functionalized rods. However, the observed quenching and subsequent recovery of FAM signal provides qualitative confirmation of CLP conjugation to CdSe/CdS DiRs.

Together, all the ligand strategies confirm that the DiRs are functionalized with compatible ligands and CLP and are suitable to be used for encapsulation in the protein containers. The encapsulation trials using these water soluble CdSe/CdS DiRs in the *T. maritima* encapsulin container are discussed in section 5.4.1

5.2.2 Gold Nanorods

AuNRs are widely used in biological and sensing applications due to their anisotropic shape and tunable plasmonic properties. However, their surface chemistry must be carefully controlled to ensure both biocompatibility and functional accessibility. As synthesized, AuNRs are typically stabilized with CTAB, a cationic surfactant essential for shape control during synthesis. While CTAB effectively maintains colloidal stability, it presents several major drawbacks. First, CTAB forms a bilayer that is several nanometers thick, physically separating

the particle surface from nearby biomolecules and thus obstructing the plasmonic near-field, which is most sensitive within 10 nm of the rod tip.^[384-385] Second, CTAB is cytotoxic, can denature proteins and requires a relatively high excess concentration in solution to prevent aggregation, making it unsuitable for biofunctionalization or in vivo use.^[212] These limitations make CTAB unsuitable for further functionalization or use in physiological conditions.

To address this, CTAB was replaced with two different thiolated ligands, 11-mercaptoundecanoic acid (MUA) and MUTAB. Both ligands contain thiol groups that bind strongly to the gold surface, forming compact, covalently attached monolayers. MUA introduces a negatively charged carboxyl group, while MUTAB provides a positively charged quaternary ammonium group. Unlike CTAB, these ligands form thinner coatings, improve biocompatibility, and allow stable dispersion under low-salt and physiological buffer conditions. The structures of the ligands are shown in Figure 5.26.

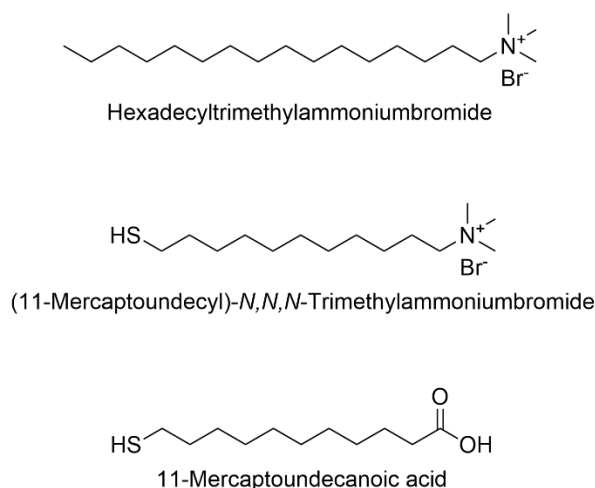


Figure 5.26: Chemical structures of ligands used for surface modification of AuNRs. Top: Hexadecyltrimethylammoniumbromide (CTAB), a native hydrophobic ligand. Middle: (11-Mercaptoundecyl)-N,N,N-trimethylammonium bromide (MUTAB). Bottom: 11-Mercaptoundecanoic acid (MUA), which is usually deprotonated in aqueous solutions and thus negatively charged.

5.2.2.1 MUA-functionalized AuNRs

To investigate the impact of surface charge on nanoparticle encapsulation, AuNRs were functionalized with MUA, a negatively charged thiol ligand. The process involved removing the native capping agent CTAB using NaBH₄, followed by ligand replacement with MUA. A schematic overview of the procedure is shown in Figure 5.27.

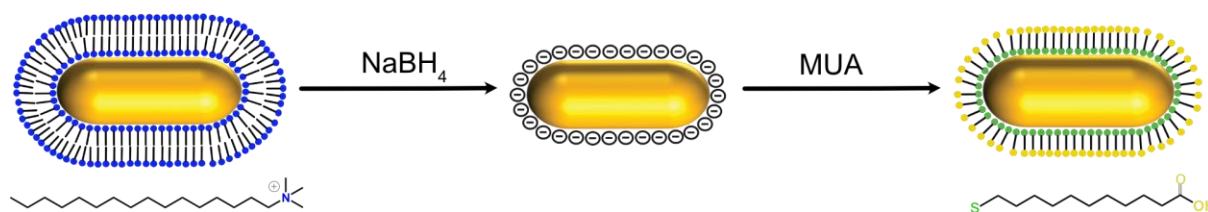


Figure 5.27: Schematic showing removal of CTAB from the nanorod surface and replacement with MUA. Sodium borohydride acts as a transient reducing agent and displaces CTAB by forming surface-bound hydride species. MUA is added immediately after the treatment to prevent aggregation.

Prior to ligand exchange, excess CTAB was removed from the AuNR dispersion through centrifugation at 10,000 g for 15 minutes. This step was essential, as free CTAB in solution can rebind to the nanorod surface and interfere with ligand exchange. The washed nanorods (OD = 1) were then treated with 100 μ L 50 mM aqueous solution NaBH_4 , which acts as a transient reducing agent capable of displacing CTAB from the gold surface through the formation of surface-bound hydride species. According to prior studies, this hydride layer temporarily stabilizes the AuNRs by preventing immediate aggregation, while leaving the surface accessible for incoming thiolated ligands.^[221] CTAB removal is driven by the hydride's high affinity for gold, but the process is inherently dynamic; over time, hydride ions react with water to form hydrogen gas and are lost from the surface, potentially leaving the AuNRs prone to aggregation. This creates a narrow time window, during which ligand exchange must be performed. To stabilize the particles, 100 μ L of 50 mM ethanolic solution of MUA was added immediately after NaBH_4 treatment. The thiol group of MUA binds strongly to the gold surface, while the carboxylic acid group imparts a net negative surface charge, restoring colloidal stability through electrostatic repulsion.

The success of the ligand exchange was confirmed using multiple characterization techniques. UV-Vis spectroscopy was used to monitor changes in the optical properties of the AuNRs during the ligand exchange process. As shown in Figure 5.28, the longitudinal plasmon peak of the CTAB-stabilized AuNRs (red) was sharp and well-defined. Following NaBH_4 treatment (blue), a slight blueshift of the peak was observed, likely due to partial surface destabilization. Upon MUA addition, the peak red-shifted back, with spectra recorded after 60 minutes and following overnight incubation and washing (green and dark green), indicating successful ligand binding and a change in the local dielectric environment. No evidence of major aggregation was observed, confirming that MUA re-stabilized the nanorods in aqueous media.

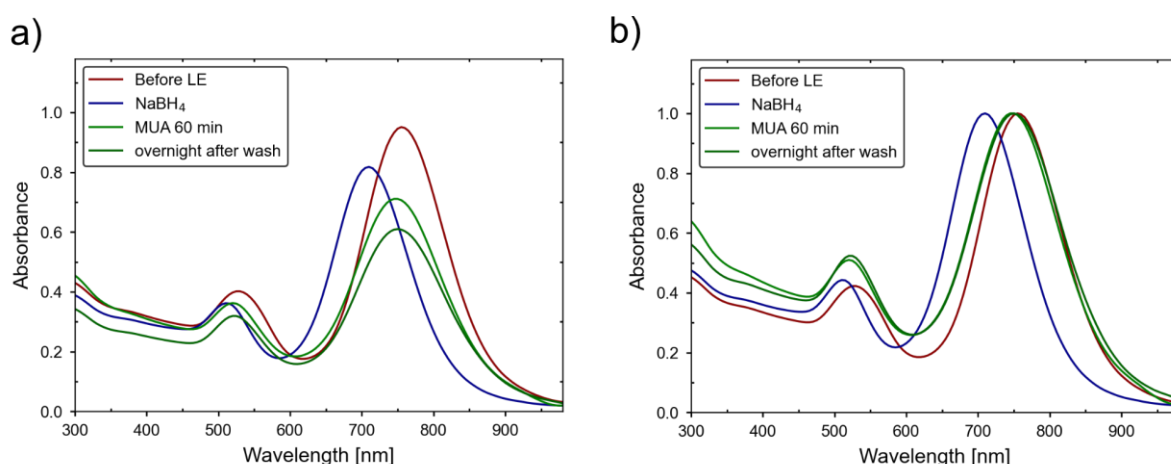


Figure 5.28: UV-Vis characterization of CTAB removal and MUA replacement. a) Addition of NaBH_4 caused continuous blue shifts and reduce in the intensity of the nanorod LSPR over time. After 1 h NaBH_4 treatment, addition of MUA created a red shift. b) Normalized spectra for a clear shift view.

ζ -potential measurements supported the shift in surface chemistry (Figure 5.29a). The initial CTAB-coated AuNRs exhibited a strongly positive surface charge ($+67.1 \pm 1.24$ mV), characteristic of the cationic surfactant. After MUA exchange, the ζ -potential reversed, becoming strongly negative (-32.5 ± 2.53 mV), consistent with successful functionalization by the carboxylate-terminated thiol. DLS further supported this, showing a shift in the hydrodynamic diameter distribution. Both CTAB- and MUA-coated rods displayed a bimodal size distribution, consistent with a mixed population of fully formed rods and unconverted spherical seeds. Such profiles are common for CTAB-synthesized AuNRs and have been reported in previous studies.^[177] However, a slight shift to a shorter size was observed for MUA-coated rods.

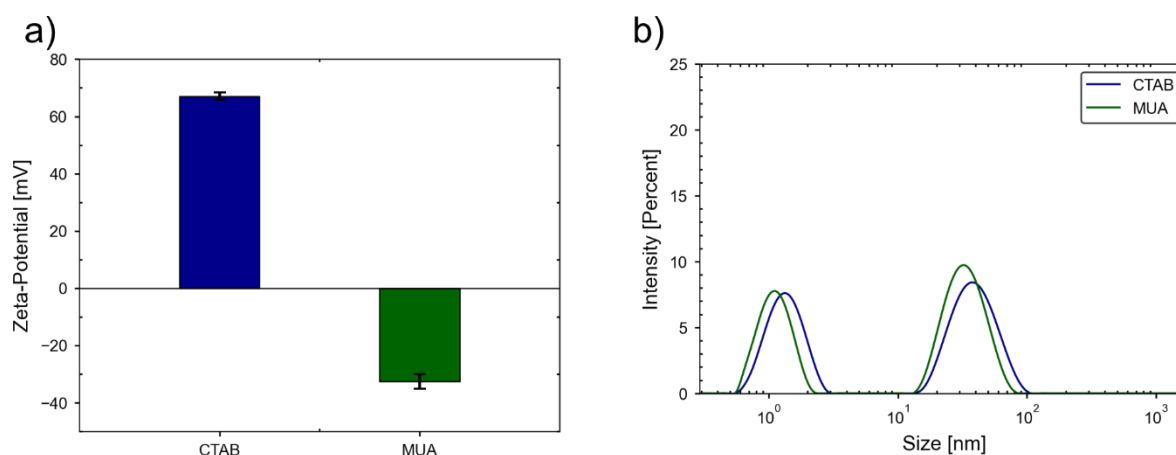


Figure 5.29: ζ -potential and hydrodynamic size distribution of CTAB and MUA-coated AuNRs. a) ζ -potential distribution for CTAB-coated AuNRs (blue) and MUA-coated AuNRs (green). b) Intensity-weighted DLS of CTAB and MUA coated AuNRs. Together, these data confirm the successful replacement of CTAB with

MUA, yielding negatively charged, colloiddally stable AuNRs suitable for encapsulation studies or charge-dependent interactions.

5.2.2.2 MUTAB-functionalized AuNRs

MUTAB ligand exchange was performed using a surface-area-based dosing strategy adapted from the literature, with modifications to suit the specific needs of this study.^[219] Prior to exchange, CTAB-stabilized AuNRs were washed twice by centrifugal precipitation to remove excess surfactant. This purification step was critical for reducing CTAB interference and minimizing aggregation during the ligand replacement process. A schematic overview of the CTAB-to-MUTAB exchange workflow is shown in Figure 5.30.

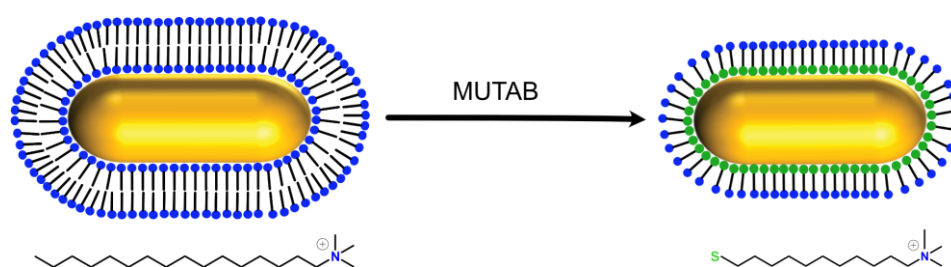


Figure 5.30: Schematic illustration showing the replacement of CTAB with MUTAB. AuNR coated with an adsorbed CTAB bilayer is functionalized with MUTAB to create a monolayer of cationic ligands covalently bound to the nanorod surface via gold-thiol bonds

The amount of MUTAB required was calculated based on the total surface area of AuNRs in each batch. Particle concentration was determined from optical density using known extinction coefficients, and surface area was estimated from TEM-derived dimensions.^[386] Based on literature-reported ligand densities of 4-5 molecules per nm² for similar alkylthiols, the number of surface binding sites was estimated.^[380-381] A 100-fold molar excess of MUTAB was added relative to the number of sites. MUTAB was dissolved in aqueous ethanol and mixed with the AuNR suspension under continuous stirring. Excess MUTAB and any residual CTAB were removed by centrifugation and the AuNRs were redispersed in Milli-Q water.

UV-Vis spectra, as shown in Figure 5.31, confirmed that AuNRs remained optically stable throughout the exchange process. A slight blue shift was observed in the longitudinal plasmon peak from 753 nm (CTAB) to 747 nm (MUTAB) while the overall spectral shape remained unchanged, indicating preserved rod morphology and dispersion.

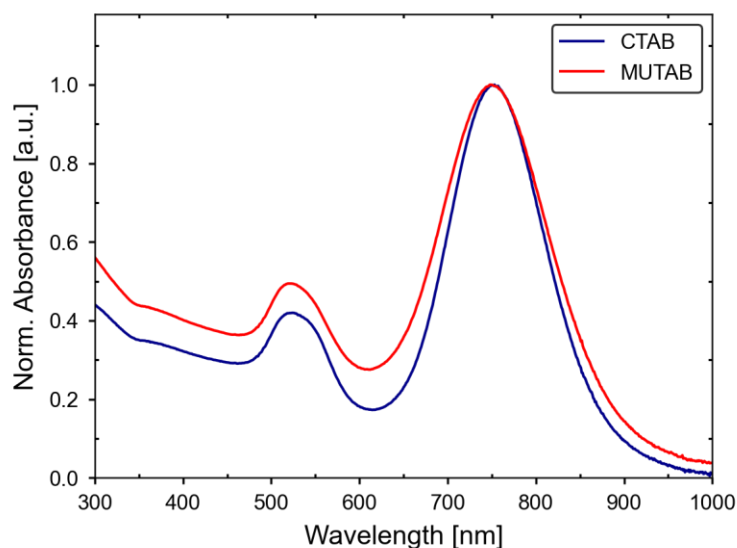


Figure 5.31: Normalized UV-Vis absorption spectra of AuNRs. AuNRs with CTAB layer (darkblue) and MUTAB layer (red).

ζ -potential measurements showed a decrease from $+62.6 \pm 1.06$ mV (CTAB) to $+43.2 \pm 1.62$ mV (MUTAB), consistent with the replacement of the bilayer CTAB with the monolayer MUTAB (Figure 5.32a) While both ligands carry permanent positive charges, the lower ζ -potential after exchange reflects reduced surface coverage and/or packing density. DLS further supported this, showing a shift in the hydrodynamic diameter distribution. Both CTAB- and MUTAB-coated rods displayed a bimodal size distribution, consistent with a mixed population of fully formed rods and unconverted spherical seeds. However, a slight shift to a shorter size was observed for MUTAB-coated rods. Finally, stained TEM images of the samples revealed that CTAB-coated AuNRs exhibited a visibly thicker corona compared to MUTAB-coated ones (Figure 5.32c,d).

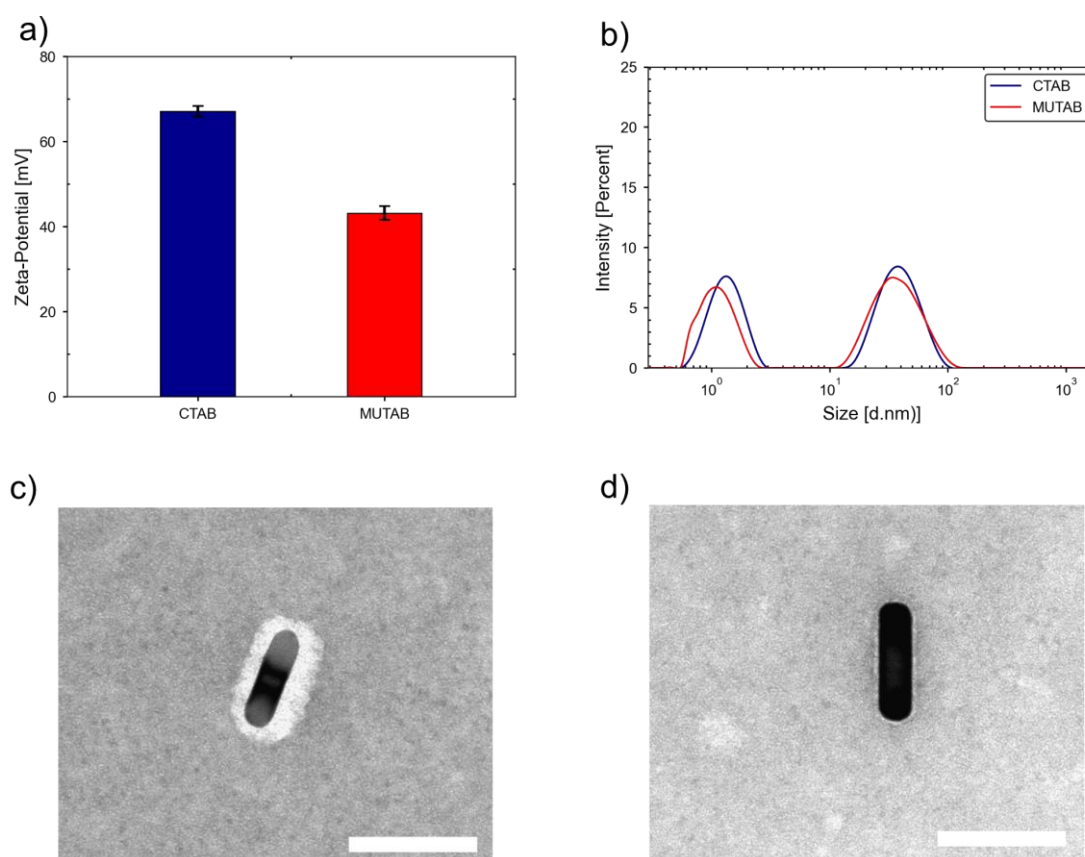


Figure 5.32: ζ -potential, hydrodynamic size distribution and stained TEM images of CTAB and MUTAB coated AuNRs. a) ζ -potential b) DLS c),d) Stained TEM images of CTAB- and MUTAB-coated AuNRs respectively. Scale bar is 100 nm.

Together, the data confirm that MUTAB forms a stable, covalently bound, polycationic monolayer that effectively replaces CTAB without compromising colloidal or structural integrity. Unlike CTAB, MUTAB does not require high-concentration micellar support and is compatible with physiological buffer systems. The resulting particles present a thin, accessible surface, suitable for electrostatic interactions and downstream functionalization. The MUTAB-coated AuNRs were then functionalized with CLP.

CLP functionalization

UV-Vis spectra confirmed that AuNRs preserved their optical stability following exchange with CLP (Figure 5.33a). The longitudinal plasmon peak was nearly identical to that of MUTAB-coated rods, with only a negligible spectral shift and no broadening, indicating that rod morphology and dispersion were maintained during the ligand exchange. DLS analysis (Figure 5.33b) supported these findings. Both MUTAB- and CLP-coated rods displayed bimodal distributions, reflecting a mixed population of rods and residual spherical byproducts. Following CLP functionalization, the main population shifted slightly toward larger

hydrodynamic sizes, consistent with the presence of the peptide layer. Importantly, no evidence of extensive aggregation was observed, indicating that CLP loading did not compromise colloidal stability. ζ -potential measurements (Figure 5.33c) showed minor shifts are expected upon CLP loading due to the amphoteric nature of the peptide (containing both acidic and basic residues).

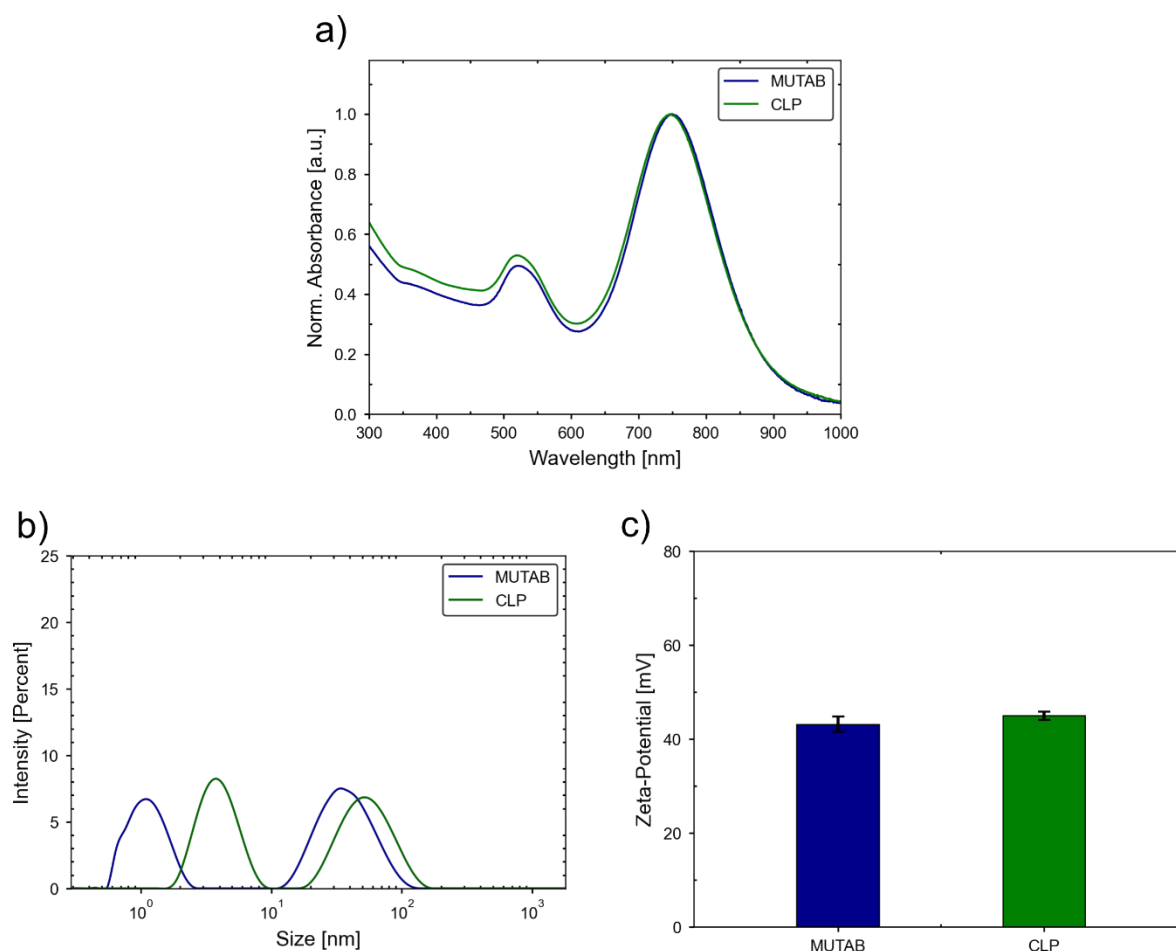


Figure 5.33: Normalized absorption spectra, hydrodynamic size distributions and ζ -potential for CLP functionalization of MUTAB coated AuNRs. a) UV-Vis spectra of MUTAB (red)- and CLP-coated AuNRs (green). b) Intensity-weighted DLS measurements of MUTAB and CLP coated AuNRs.

Together, these results confirm successful functionalization of AuNRs with CLP while maintaining the optical integrity and dispersion quality of the rods. In summary, this subsection established a progression of ligand exchange strategies to adapt AuNRs for subsequent encapsulation experiments. To introduce specific peptide functionality, MUTAB-coated rods were further modified with CLP, yielding a hybrid surface chemistry that combined electrostatic stabilization with directional peptide motifs. These MUTAB/CLP-functionalized AuNRs were selected as the most suitable candidates for encapsulation trials, which are presented in Section 5.4.2.

Formation of Nanoclusters

Initial ligand exchange for MUTAB were not successful and to test whether the NaBH_4 -assisted ligand exchange protocol used for MUA could be extended to MUTAB, a set of six samples was prepared from the same AuNR stock solution. Three samples were treated with MUTAB dissolved in ethanol (Samples A-C) and three with MUTAB dissolved in water (Samples D-F). The samples were differentiated by the number of washing steps (1x, 2x, or 3x) prior to ligand exchange, as summarized in table 5.2.

Table 5.2: AuNRs samples with washing steps and MUTAB solvent.

Sample	Washing steps	MUTAB solvent
A	1	Ethanol
B	2	Ethanol
C	3	Ethanol
D	1	Water
E	2	Water
F	3	Water

For each sample, freshly prepared NaBH_4 was added to AuNR solution ($\text{OD}=1$). The mixture was gently stirred at room temperature for 1 hour to allow the hydride ions to displace CTAB from the gold surface. Immediately after NaBH_4 treatment, MUTAB (in either ethanol and water for respective samples) was added. The reaction mixture was then left under stirring in the dark overnight to allow ligand exchange.

UV-Vis spectroscopy revealed a stark difference between the two MUTAB solvent conditions. For the ethanol-based MUTAB samples (Samples A-C), both the longitudinal and transverse surface plasmon resonance peaks (LLSPR and TLSPR) were no longer visible, indicating the disappearance or complete degradation of the AuNRs. This observation was consistent across all three washing conditions (Figure 5.34, left). In contrast, the water-based MUTAB samples (Samples D-F) retained a weak LLSPR signal, with the degree of preservation improving slightly with additional washing (Figure 5.34, right).

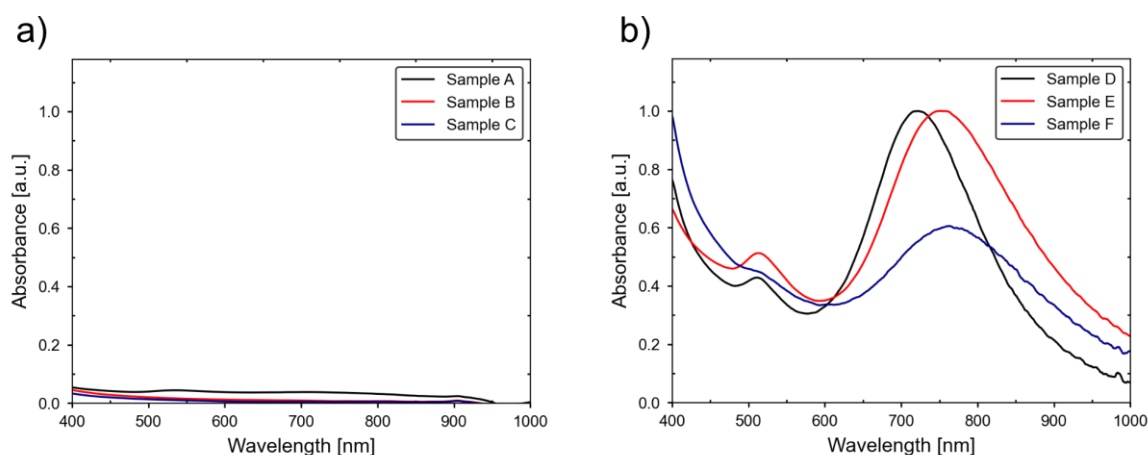


Figure 5.34: Normalized UV-Vis absorption spectra of NaBH₄ and MUTAB treated AuNRs. a) MUTAB dissolved in ethanol. b) MUTAB dissolved in water

To test whether the loss of the AuNR plasmon came from aggregation or rod breakdown, we ran DLS and TEM. DLS revealed a population of very small species (~2 nm), and TEM was inconclusive. On suggestion by Dr. Michael Rütten, we ran fluorescence to test for gold nanoclusters. Upon excitation at 346 nm, all three ethanol-based MUTAB samples (Samples A-C) showed a broad emission peak around 431 nm (Figure 5.35).

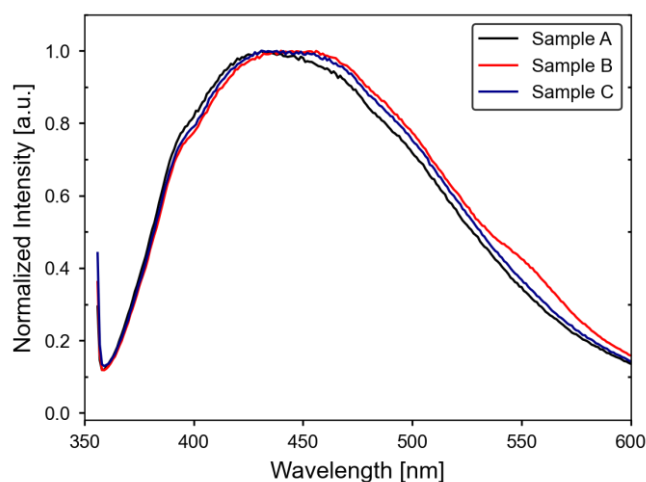


Figure 5.35: Emission spectra of NaBH₄ and MUTAB (ethanol) treated AuNRs. Excitation wavelength 346 nm.

The observed transformation of AuNRs into fluorescent AuNCs under MUTAB/NaBH₄/ethanol conditions represents a significant and specific reaction pathway. While the reductive degradation of gold nanoparticles by strong reducing agents such as NaBH₄ is known to cause instability, the specific formation of fluorescent AuNCs, and its strict dependence on MUTAB and ethanol, points to a more complex, ligand-directed mechanism.

The reason for this specificity likely lies in the unique properties of the MUTAB ligand. Unlike MUA, which provides a stabilizing anionic carboxylate group, MUTAB's quaternary ammonium headgroup is cationic and bulkier. In the ethanol solvent, which reduces the dielectric constant

of the environment and potentially affects the stability of the ligand shell on the gold surface, NaBH₄ may gain access to the gold core more readily. The combination of the strong reducing power of NaBH₄ and cationic MUTAB coating could lead to the rapid etching of the AuNRs. Instead of forming large, aggregated precipitates, the MUTAB molecules may act as stabilizing templates during this reductive decomposition, confining the eroded gold atoms into ultra-small, fluorescent nanoclusters. This is analogous to the known role of other amines and surfactants in the synthesis of AuNCs.

Further, this raises a pertinent question regarding the other cationic ligands used in this work, such as AUT for the functionalization of CdSe/CdS DiRs. While AUT shares a similar amine-based functionality, its different molecular structure (e.g., a primary amine versus a quaternary ammonium) may not induce the same reductive etching effect. In conclusion, this specific reaction is not just an experimental artifact but a finding that underscores the profound influence of ligand chemistry and solvent environment on nanoparticle stability. It provides critical guidance for developing robust functionalization protocols and suggests that MUTAB's role may extend beyond providing a positive charge to actively participating in the nanoscale transformations of gold.

5.2.3 Functionalization of Gold Nanoparticles

As mentioned in section 5.1.3, AuNPs were required for the later part of the work. The as synthesized AuNPs were stabilized by CTAC, which like its analogue CTAB presents a significant challenge for biomedical applications. The surfactant is cytotoxic and unstable under physiological conditions leading to protein aggregation.^[206, 211-213] To address this, ligand exchange strategies were employed to replace surfactants with positively charged biocompatible ligands, such as MUTAB. Positively charged ligand was chosen to compliment the negatively charged cavity of the encapsulin.

This ligand exchange protocol was inspired by a previously reported method developed for AuNRs, where particles synthesized with CTAB are first transitioned to CTAC and then exchanged with MUTAB.^[134] In contrast, the protocol described here begins with CTAC-stabilized AuNPs and proceeds directly to MUTAB exchange. This eliminates the need for intermediate ligand modification and simplifies the procedure for spherical colloids. AuNPs were first purified by two rounds of centrifugal precipitation to remove excess CTAC. The amount of MUTAB required for ligand exchange was calculated based on the particle concentration and surface area, using UV-Vis absorbance at 450 nm and the extinction coefficient reported by Haiss *et al.*^[387] A 100-fold molar excess of MUTAB relative to the estimated number of surface binding sites was used. To the ethanolic solution of MUTAB, the

AuNP suspension was added under continuous stirring. The reaction was stirred overnight at room temperature. The process of overnight incubation followed by washing free ligand using centrifugation and then redispersion in water was repeated three times to ensure thorough replacement of CTAC with MUTAB.

After each ligand exchange step, UV-Vis spectroscopy, ζ -potential, and DLS were measured. The absorption spectra, as shown in Figure 5.36a, display a plasmon peak around 522 nm. Only a minor shift was observed compared to the CTAC-coated particles, which had a peak at 525 nm. This slight blue shift is consistent with changes in the local dielectric environment following surface functionalization. DLS measurements showed stable hydrodynamic diameters and narrow size distributions across all steps, with no evidence of aggregation (Figure 5.36b). Notably, a systematic shift in the volume-weighted peak was observed from 33.0 nm for the CTAC-capped particles to 28 nm after the third MUTAB incubation. This gradual decrease suggests that the bulky CTAC bilayer was successfully replaced by a thinner, more compact MUTAB monolayer. ζ -potential decreased progressively with each round, reaching +50.5 mV after the third exchange, consistent with successful formation of a positively charged MUTAB monolayer on the AuNP surface (Figure 5.36c). This value is in good agreement with previously reported ζ -potential values for MUTAB-stabilized AuNPs, such as +48.7 mV reported for 11 nm cores and +59.7 mV reported for 13 nm cores.^[14]

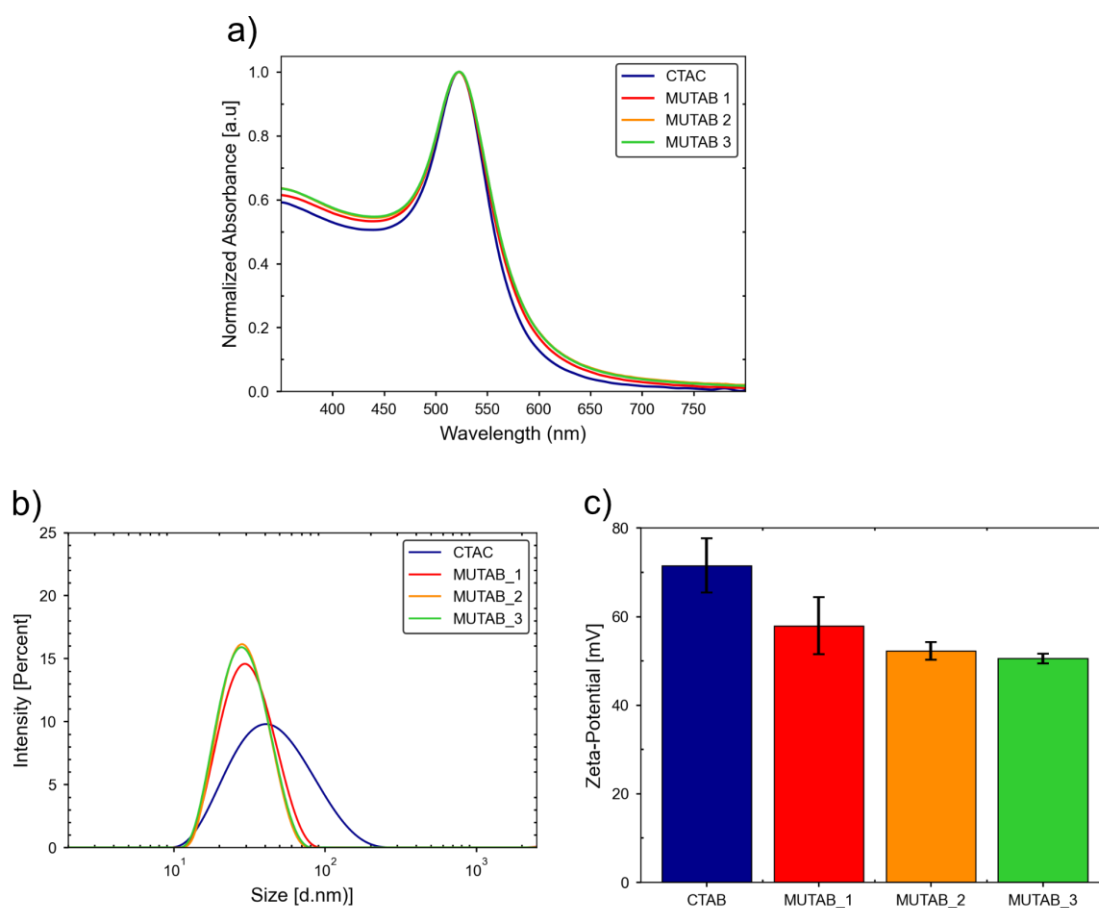


Figure 5.36: Ligand Exchange of AuNPs from CTAC to MUTAB. a) Normalized UV-Vis absorption spectra of AuNPs with CTAC and three round of MUTAB. b) Intensity-weighted DLS measurements showing a shift towards smaller diameter as CTAC is replaced by MUTAB. c) ζ -Potential values of CTAC and MUTAB coated AuNPs showing a progressive decrease.

To evaluate the nature of the surface coating, stained TEM was performed after the final exchange. CTAC-coated AuNPs showed an irregular, thicker coating layer consistent with a bilayer structure. In contrast, MUTAB-functionalized particles exhibited a thinner, more uniform shell consistent with a tightly packed monolayer, further supporting successful ligand replacement (Figure 5.37).

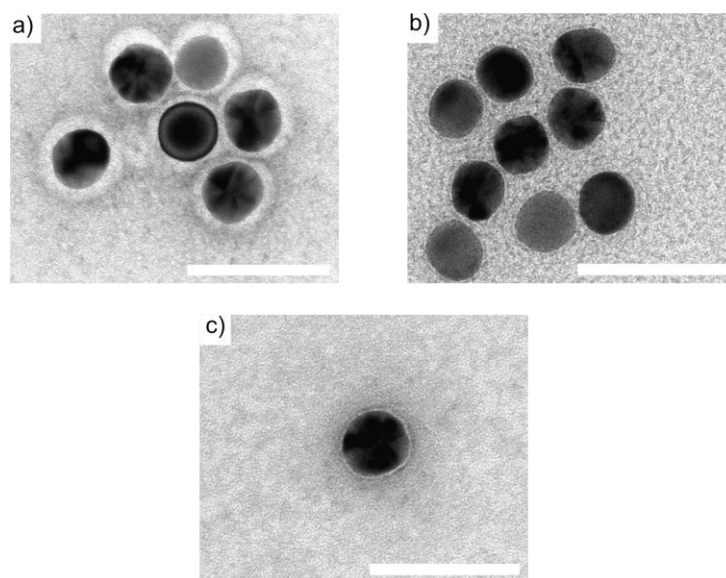


Figure 5.37: Stained TEM images of AuNPs. a) CTAC coated AuNPs showing a thicker layer. b) MUTAB coated AuNPs showing a thinner, uniform layer. c) Zoomed in image of one particle to focus on ligand shell. Scale bar is 50 nm.

Together, these results confirm successful ligand replacement of CTAC with MUTAB. Following the final MUTAB exchange, the surface-modified AuNPs were subjected to CLP loading.

CLP Functionalization

In the later part of the work, to overcome the constraints of TmEnc with anisotropic particles, a new encapsulating platform based on *M. xanthus* was established. A 16-amino acid peptide derived from MxEnc was incubated with the particles under aqueous conditions. A schematic of the CLP sequence and its interaction with the MUTAB-functionalized surface is shown in Figure 5.38. The C-terminal cysteine enables covalent binding via thiol-gold bonding, while a nearby glutamic acid residue may contribute electrostatic stabilization through interaction with the cationic MUTAB layer. The remaining residues, including a flexible hinge motif and an anchor sequence, are oriented outward, enabling potential recognition by the encapsulin interior.

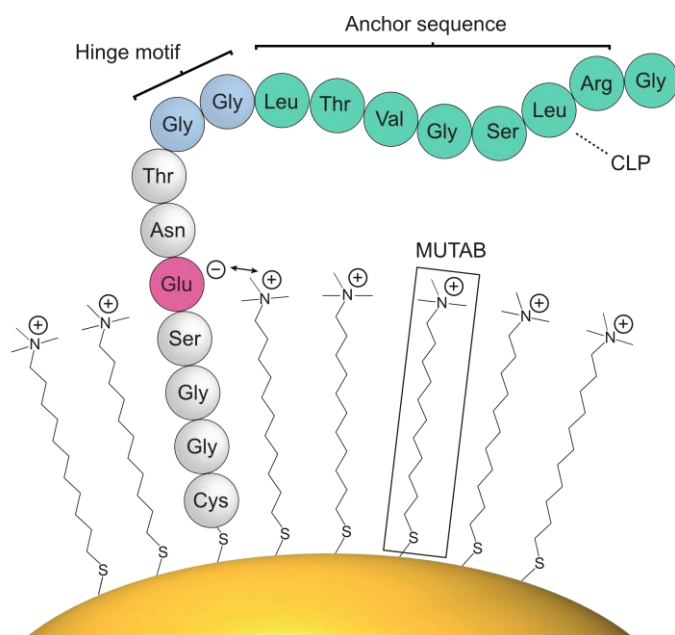


Figure 5.38: Schematic a of MUTAB-stabilized AuNP functionalized with a 16-amino acid long CLP.

UV-Vis spectra showed a slight redshift in the plasmon peak from 522 nm to 524 nm, consistent with changes in the local dielectric environment. DLS measurements revealed a modest increase in hydrodynamic diameter, from 28 nm to 32 nm, indicating additional surface contribution from the peptide layer. ζ -potential also increased from +50.5 mV to +61.0 mV, supporting enhanced surface charge density following CLP adsorption. All three results point to stable, successful surface functionalization.

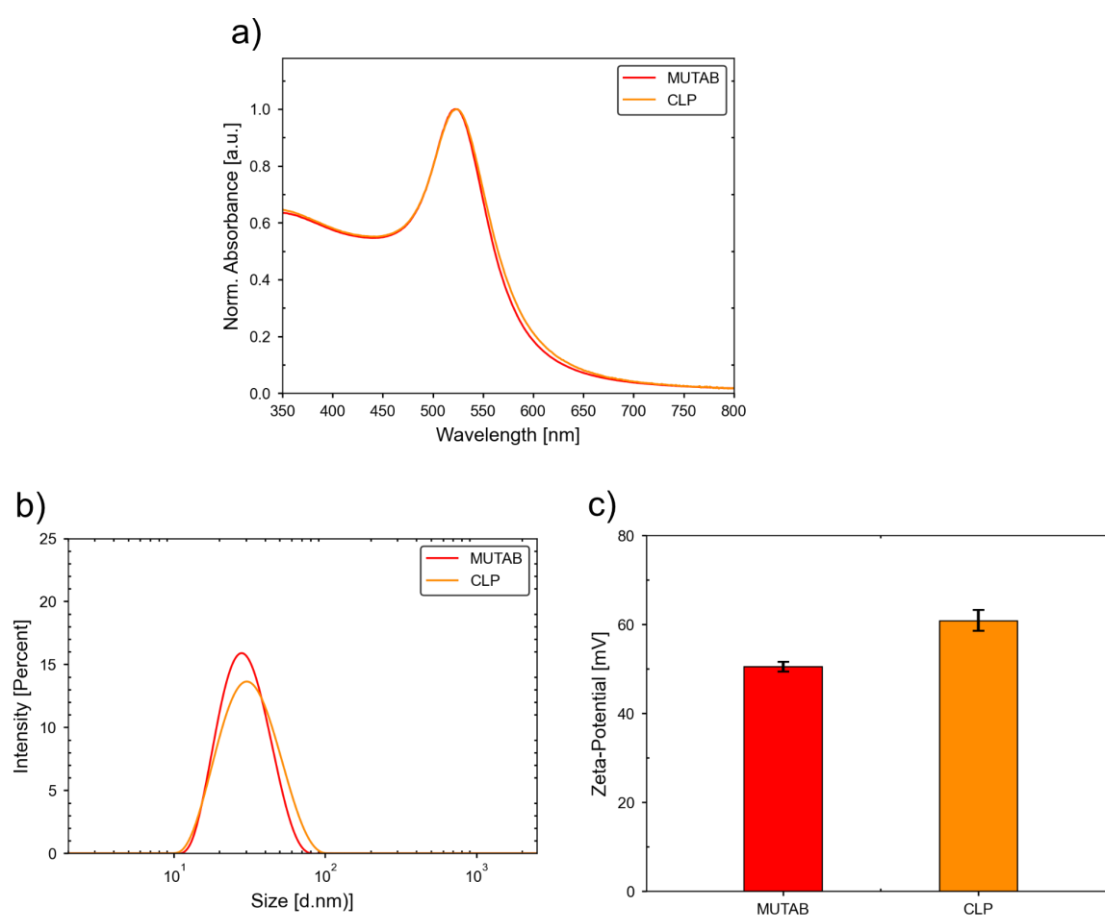


Figure 5.39: CLP-loading of MUTAB coated AuNPs. a) Normalized UV-Vis absorption spectra showing a slight red shift. b) Intensity weighted DLS measurements showing a shift towards larger hydrodynamic diameter. c) ζ -Potential measurements

CLP Binding Confirmation via Biotin-Streptavidin Assay

To qualitatively confirm the presence of CLP, a detection strategy was employed using biotinylated CLP (Bio-CLP) and its high-affinity interaction with streptavidin. Biotin-streptavidin binding is among the strongest known non-covalent interactions ($K_d \sim 10^{-15}$ M), making it a widely used tool for molecular recognition and detection. Streptavidin-conjugated 5 nm gold nanoparticles (Stp-AuNPs) served as a cross-linking probe. As a protein rich in aromatic amino acids such as tyrosine and tryptophan, streptavidin exhibits intrinsic absorbance at 280 nm and fluorescence emission around 340 nm. Upon binding to biotin, fluorescence is quenched due to altered environment and local conformational changes.^[388-389] Given that each streptavidin molecule possesses four biotin-binding sites, a low concentration of Stp-AuNPs was sufficient to induce detectable cross-linking. Non-biotinylated CLP (Normal-CLP) functionalized AuNPs were used as a negative control to account for any non-specific interactions. The interaction was probed by UV-Vis spectroscopy and fluorescence

spectroscopy. A schematic of the interaction between Stp-AuNPs and biotinylated CLP-AuNPs is shown in Figure 5.40a. Additionally, Figure 5.40b displays a structural view of the streptavidin-biotin interaction, highlighting the key hydrogen bonds that stabilize the complex.

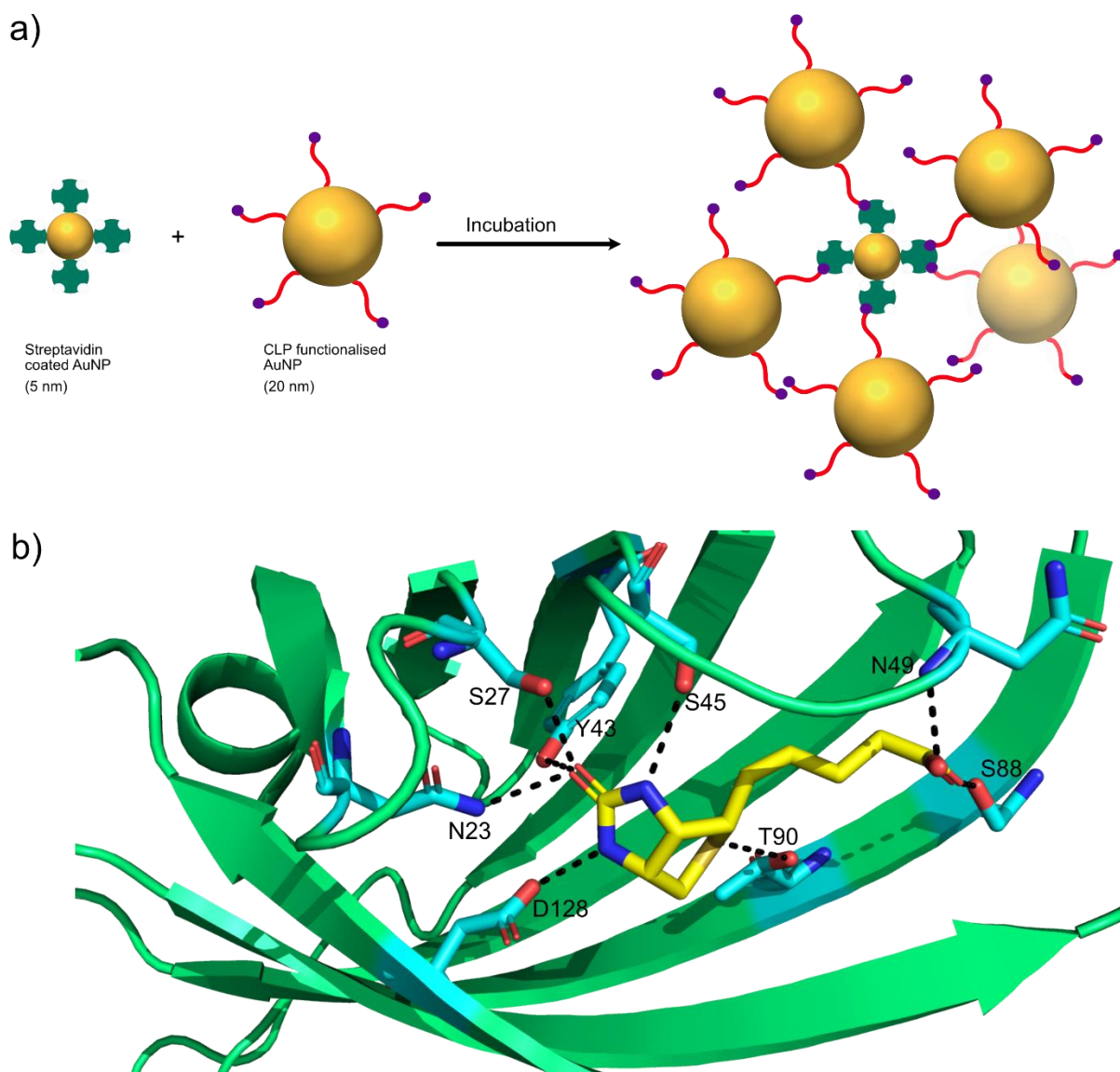


Figure 5.40: Schematic illustration of the detection strategy used to confirm CLP and Streptavidin-Biotin binding highlighting amino acids and hydrogen bonds. a) Interaction of biotinylated-CLP functionalized AuNPs and Streptavidin-coated AuNPs forming the aggregates. Drawings are not to scale. b) The complex formed by biotin-streptavidin interaction. (PDB: 1STP) Hydrogen bonds are shown as black dashes.

UV-Vis Spectroscopic Analysis of Streptavidin-Mediated Aggregation:

The interaction was probed by UV-Vis spectroscopy through two complementary assays (Figure 5.41). First, the binding was investigated kinetically by monitoring the changes in absorption spectra over time. A baseline spectrum of Bio-CLP-AuNPs was measured and then Stp-AuNPs were added. The spectra were recorded every 5 minutes for 40 minutes. The same

procedure was performed for normal CLP-AuNPs as a control. The results, as shown in Figure 5.41a, showed a clear difference. For the Bio-CLP-AuNPs, the plasmon peak broadened and shifted from 525 nm to 530 nm and a peak around 280 nm appeared. For Normal-CLP-AuNPs, even though the plasmon peak shift was not observed, the peak around 280 nm was more intense as compared to that of Bio-CLP-AuNPs.

To confirm the presence of aggregate and release of free Stp-AuNPs, the mixtures were centrifuged after incubation. Analysis of the supernatant revealed a clear distinction between the samples (Figure 5.41b). The supernatant from the Normal-CLP-AuNP control showed high absorbance at both 280 nm and 520 nm, corresponding to the presence of more amount of unbound Stp-AuNPs in the supernatant. In contrast, the supernatant from the Bio-CLP-AuNP sample exhibited a significant depletion of absorbance at both wavelengths. The reduced A_{280} and A_{520} signal indicate the specific binding and subsequent pull-down of Stp-AuNPs and co-precipitation. This coordinated depletion is characteristic of the formation of a cross-linked network mediated by the specific biotin-streptavidin interaction.

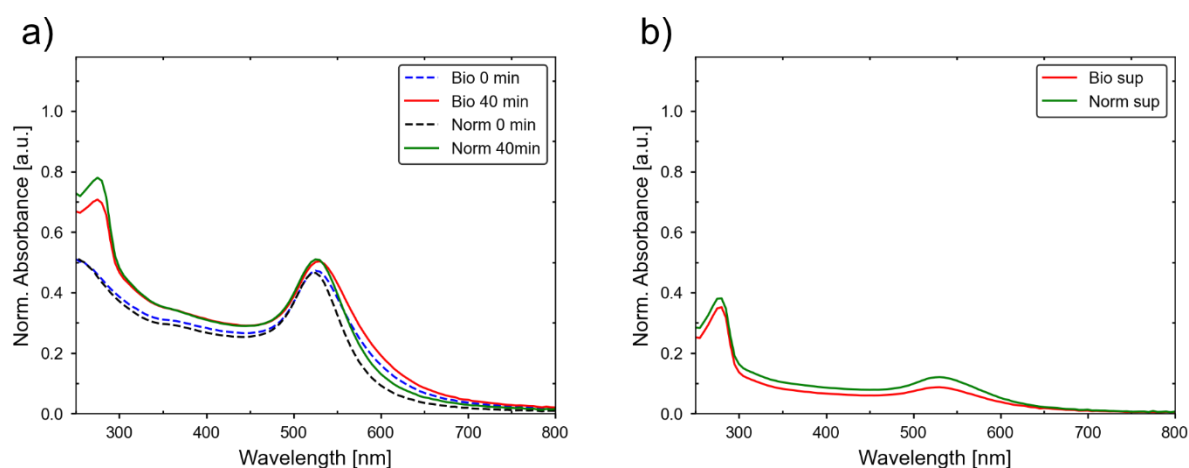


Figure 5.41: UV-Vis absorption spectra of AuNPs to confirm presence of CLP using Biotin-Streptavidin binding. a) Time dependent spectral evolution of Bio-CLP-AuNPs and Normal-CLP-AuNPs after addition of Stp-AuNPs, showing scans at 0 min and 40 minutes. Bio 0 min in Bio-CLP-AuNPs is initial sample (dashed blue), and Bio 40 min is the sample after 40 minutes (red). Norm 0 min is Normal-CLP-AuNPs is initial sample (dashed black) and Norm 40 min is the sample after 40 minutes (green). b) Absorption spectra of the supernatant obtained after centrifugating the incubated Bio-CLP-AuNPs and Normal-CLP-AuNPs with Stp-AuNPs, shown in red and green respectively.

Photoluminescence Quenching:

The specific binding and nanoscale proximity between the Bio-CLP-AuNPs and Stp-AuNPs were further verified by PL after overnight incubation (Figure 5.42). The 5 nm Stp-AuNPs exhibit intrinsic photoluminescence. When in close proximity to a larger gold surface, this

emission can be quenched via nanometal surface energy transfer (NSET).^[390-392] This quenching is analogous to FRET but does not require spectral overlap; instead, it depends on the conductive nature of the metal and the distance to its surface. The PL intensity of the Stp-AuNPs alone was defined as the baseline. As a critical control, the PL of Bio-CLP-AuNPs was also measured and showed no significant signal. This confirms that the conjugate itself does not contribute to the PL emission in the measured range. The mixture of Stp-AuNPs with Normal CLP-AuNPs showed only a minor decrease in PL intensity, attributable to non-specific interactions. Strikingly, the mixture with Bio-CLP-AuNPs exhibited pronounced quenching of the Stp-AuNP signal. This strong quenching provides direct evidence of specific binding, which brings the 5 nm Stp-AuNPs into close and consistent proximity with the 20 nm AuNP surface.

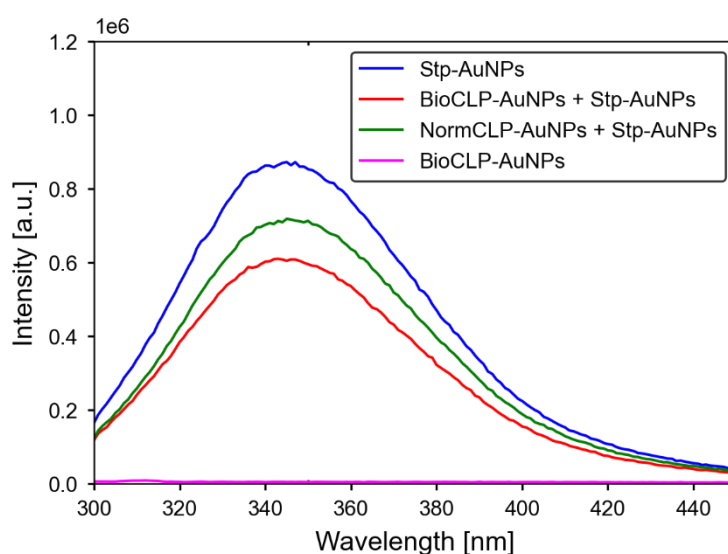


Figure 5.42: Emission spectra of AuNPs to confirm presence of CLP using Biotin-Streptavidin binding. Emission spectra of Stp-AuNPs (blue), Bio-CLP-AuNPs after incubation with Stp-AuNPs overnight (red), Norm-CLP-AuNPs after incubation with Stp-AuNPs overnight (green) and Bio-CLP-AuNPs (magenta).

Collectively, the UV-Vis aggregation assay and the PL quenching results provide complementary evidence that confirms the successful conjugation and surface presentation of biotin on the Bio-CLP-AuNPs, thereby validating the functionalization strategy. While absolute quantification is possible via 4'-hydroxyazobenzene-2-carboxylic acid (HABA) assay or thermogravimetric analysis, the primary objective was to confirm the presence of CLP and utilize the AuNPs for encapsulation experiments.

5.3 Production and Purification of Encapsulins

This section outlines the production and purification of encapsulin protein cages derived from *T. maritima* (TmEnc^(neg)) and *M. xanthus* (MxEnc). Expression systems were optimized to yield intact, self-assembling protein cages in high purity. The structural integrity and homogeneity of the encapsulins were confirmed using analytical (SEC) and complementary imaging techniques. These cages serve as the biological scaffolds for nanomaterial encapsulation and are evaluated for their suitability based on assembly behavior, cargo capacity, and monodispersity.

5.3.1 Production and Purification of *T. maritima* Encapsulin

Recombinant production of TmEnc^(neg) was performed in *E. coli* cells harboring the corresponding plasmid, following an established protocol developed in the group by Dr. Rütten^[364] (see Section 7.7.2.1). The purification of the negatively charged encapsulin variant was conducted using a standard workflow consisting of ion-exchange chromatography (IEC) followed by SEC. Initial purification via IEC effectively removed residual host proteins and nucleic acid contaminants. TmEnc^(neg), characterized by its negatively charged surface, consistently eluted at a conductivity of 46 mS/cm (Figure 5.43a). Subsequent SEC enabled separation of protein aggregates from monodisperse cages. Aggregated species eluted at 10.2 mL, while properly assembled encapsulin cages eluted at 12.8 mL (Figure 5.43b).

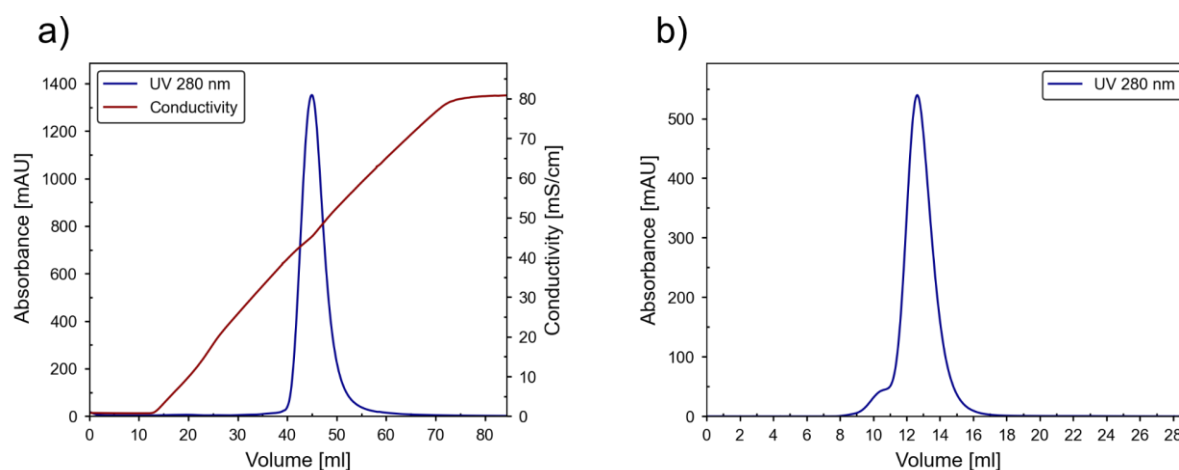


Figure 5.43: Ion-exchange and size-exclusion chromatograms of negatively surface charged TmEnc^(neg) encapsulin. a) IEC chromatogram for TmEnc^(neg). Protein elution at 46 mS/cm. b) SEC chromatogram for TmEnc^(neg). Absorbance was monitored at 280 nm (blue). Conductivity is shown in red.

The structural integrity and morphology of the purified TmEnc^(neg) particles were confirmed by stained TEM. The micrographs showed uniform, spherical particles with well-defined boundaries, characteristic of intact encapsulin shells (Figure 5.44a). Some cages contain

protein cargo (white spots in TEM). Particle size distribution was quantified based on TEM micrographs, and the resulting histogram showed a narrow size range centered around 23.85 nm (Figure 5.44b), in agreement with previously reported values for similar systems.^[288]

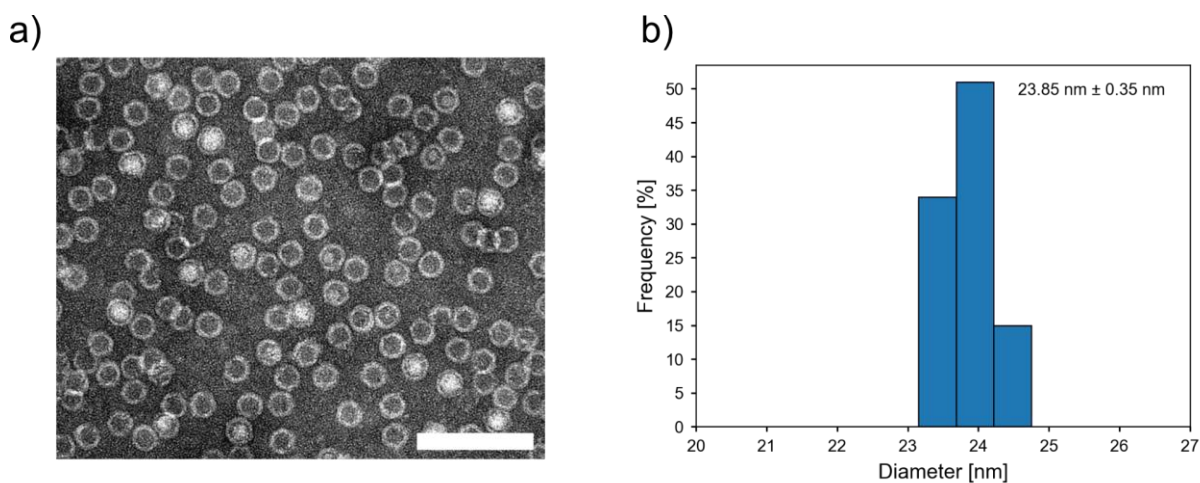


Figure 5.44: : TEM images of TmEnc^(neg) and corresponding histogram with size distribution. a) Negative stained TEM image of TmEnc^(neg). Scale bar is 100 nm. b) Histogram and size distribution with standard deviation for TmEnc^(neg). 100 protein cages were measured to determine the size distribution.

5.3.2 Production and Purification of *M. xanthus* Encapsulin

Initial production trials of the MxEnc were carried out in *E. coli* C43 cells. While transformation was successful, expression proved inconsistent. Pre-cultures grew only occasionally: Out of four test tubes inoculated from separate colonies, only one showed sufficient growth. Expression was induced with IPTG at various optical densities ($OD_{600} = 0.2, 0.4, 0.6, 0.75$), followed by a 3-hour expression period. Lysis was performed in tris buffer (50 mM tris pH 9.0, 0.15 M NaCl) supplemented with DNase and RNase, followed by sonication. Heat treatment at 45 °C and 60 °C was tested for selective denaturation of host proteins. Post-centrifugation, no visible pellet remained after either heat step, indicating successful clearance of non-target proteins. SDS-PAGE, IEC, and SEC were performed for each condition. Among these, induction at $OD_{600} = 0.6$ resulted in the highest protein yield, as evidenced by a strong IEC elution profile and a dominant SEC peak consistent with assembled encapsulin particles. Detailed data for all four conditions, including IEC and SEC chromatograms, are provided in the appendix (Figure 8.4-8.5)

Based on the small-scale expression optimization, a larger 800 mL culture was produced using induction at $OD_{600} = 0.7$. IEC of the soluble fraction yielded two peaks: a minor peak eluting at ~32 mS/cm and a dominant one at ~40 mS/cm (Figure 5.45a). The IEC-purified fractions were further processed by SEC using a HiPrep Sephacryl S-500 HR column. The SEC profile revealed three major peaks: peak 1 eluting at 55.5 mL, suggesting multimers or aggregates,

peak 2 at 66.3 mL and peak 3 around 89.8 (Figure 5.45b). Based on the known size-exclusion behavior and prior literature for MxEnc, the peak at 66.3 mL was tentatively assigned to the $T = 3$ assembly state, and the peak at 89.8 mL was tentatively assigned to the $T = 1$ state. This assignment was consistent with the expected elution volumes for protein complexes of their respective sizes and was subsequently confirmed by negative-stained TEM and DLS.

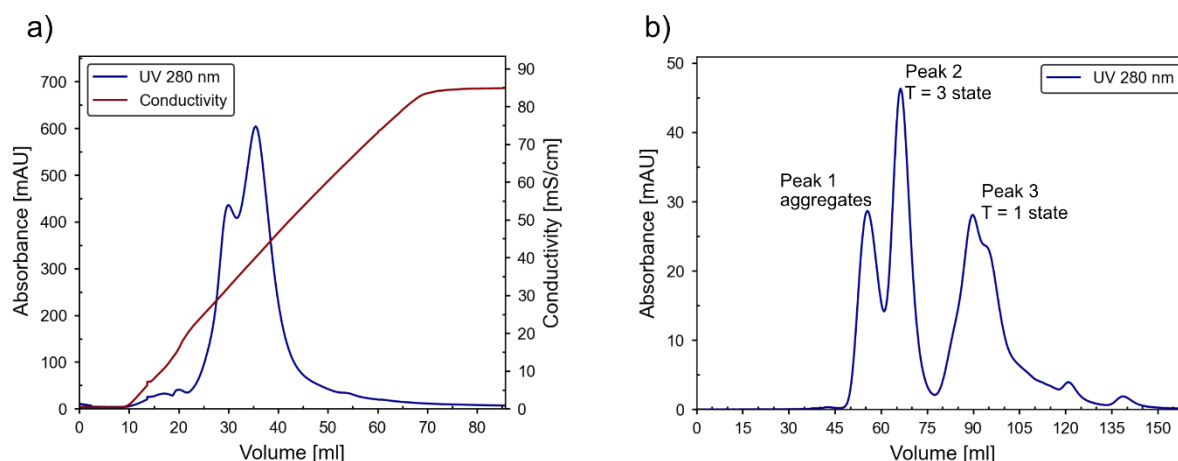


Figure 5.45: Ion-exchange and size-exclusion chromatograms of MxEnc. a) IEC chromatogram for MxEnc. Protein elution at 40 mS/cm. b) SEC chromatogram for MxEnc. $T = 3$ state elutes around ~66 ml and $T = 1$ state elutes around ~90 ml. Absorbance was monitored at 280 nm (blue). Conductivity is shown in red.

This tentative assignment was confirmed by DLS measurements of the peak fractions (Figure 5.46). The intensity-weighted size distributions revealed a major population with a hydrodynamic diameter of approximately 36.8 nm for the earlier eluting peak (peak 2), consistent with the expected size of a $T = 3$ cage. The later eluting peak (89.8 ml) showed a major population with a hydrodynamic diameter of approximately 20.1 nm, corresponding to $T = 1$ state.

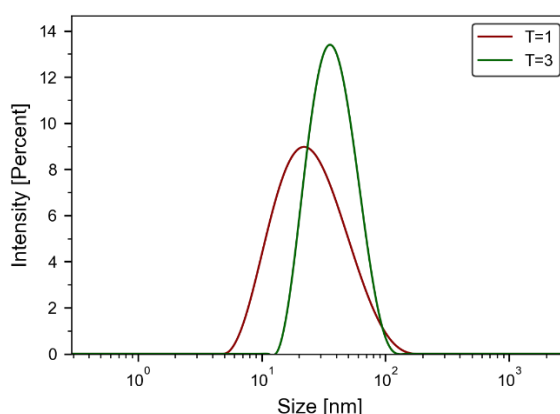


Figure 5.46: Hydrodynamic size distribution of $T = 1$ and $T = 3$ state of MxEnc. Intensity-weighted size distribution of $T = 1$ state (red) and $T = 3$ state (green).

TEM of peak fractions showed that peak 2 contained primarily T = 3 state, with a measured average diameter of $\sim 32 \text{ nm} \pm 0.58 \text{ nm}$, along with a minor presence of smaller forms (Figure 5.47a). Peak 3 consisted mostly of T = 1 state ($\sim 19.41 \text{ nm}$), though occasional T = 3 cages were also observed (Figure 5.47c). These results show that while SEC provides partial separation of MxEnc assembly states, complete resolution is limited.

The structure of the T = 1 state needs further discussion. While the T = 3 cages display the expected hexagonal profile consistent with their well-defined icosahedral symmetry, the smaller T = 1 cages exhibit a more star-like morphology (Figure 5.47). This apparent discrepancy is a well-known phenomenon in negative-stain TEM and does not indicate malformed particles. The star-like appearance, often described as a 'star-of-David' pattern, is a classic projection pattern for small, densely stained icosahedral viruses and protein cages viewed along a 2-fold symmetry axis.^[393-395] This artifact arises from the accumulation of heavy metal stain in the crevices between the capsid proteins. Surprisingly, this is not observed in the *T. maritima* capsulin. The $\sim 19.4 \text{ nm}$ diameter measured for these particles is consistent with the expected size for a T = 1 icosahedral assembly, strongly supporting that these are intact, correctly formed cages whose apparent shape is a result of the staining and imaging process.

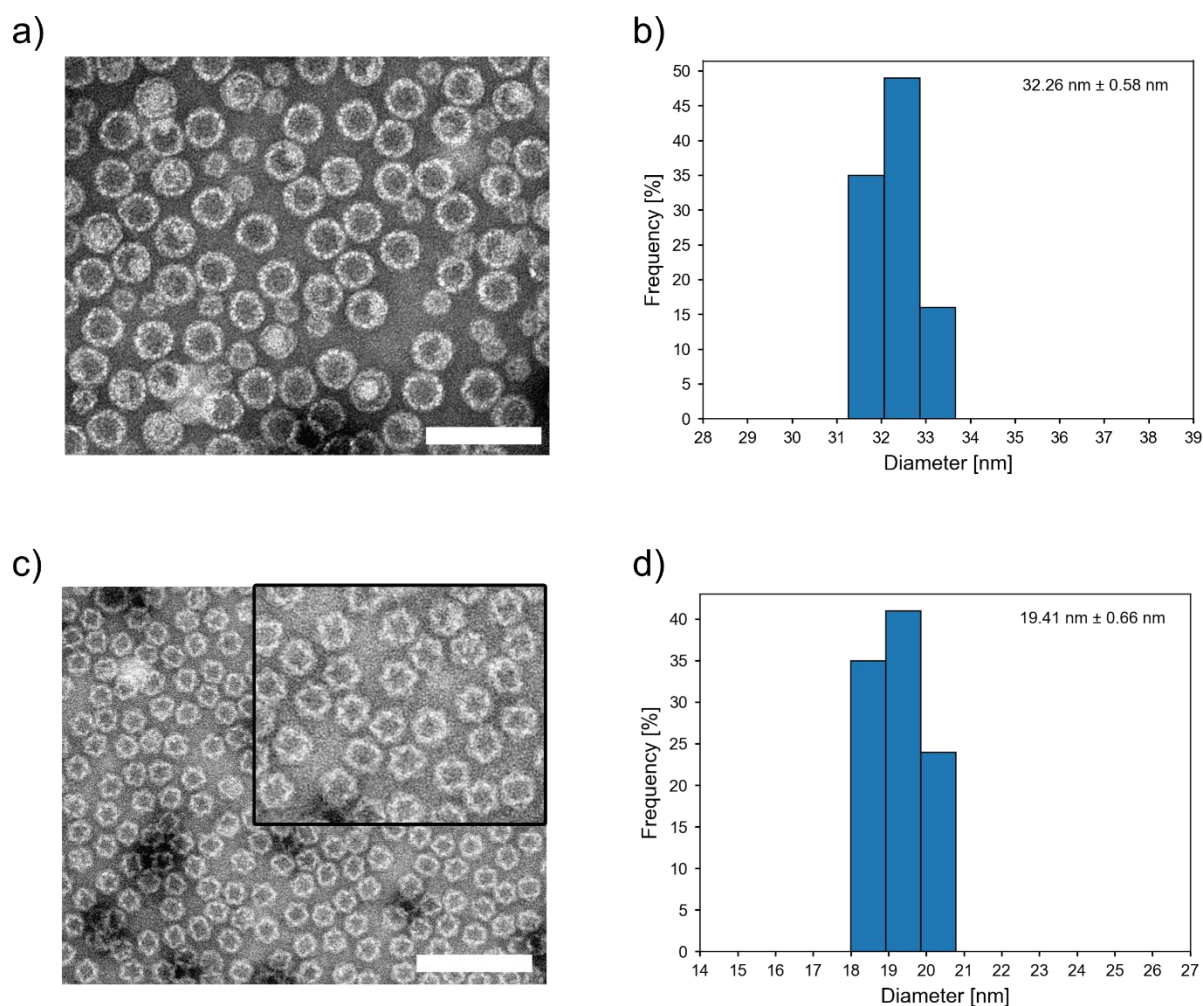


Figure 5.47: Stained TEM images of T = 3 and T = 1 state of MxEnc and corresponding histogram with size distribution. a) Negative stained TEM image of T = 3 state. Scale bar is 100 nm. b) Histogram and size distribution with standard deviation for T = 3 state. c) Negative stained TEM image of T = 1 state. Inset shows a magnified view highlighting the star-shaped morphology. Scale bar is 100 nm. d) Histogram and size distribution with standard deviation for T = 1 state. 100 protein cages were measured to determine size distribution.

A scale-up of MxEnc production (4×800 mL) cultures resulted in complete failure of IEC binding, suggesting possible misfolding, low expression levels, or improper assembly. In a subsequent batch under similar conditions, the culture was divided for parallel processing: one half underwent ammonium sulfate precipitation prior to IEC, while the other was applied directly. For the non-precipitated sample, IEC produced a broad peak eluting at 33.8 mS/cm (Figure 5.48a). SEC analysis revealed a broad, low-intensity peak spanning 40-65 mL and a second, broader peak from 75-110 mL (Figure 5.48b). The first peak suggested the presence of aggregates and T = 3 particles, though no clear separation was observed. The second peak suggested the presence of T = 1 state along with partially formed cages and/or free subunits. TEM images confirmed this distribution (Figure 5.48c,d).

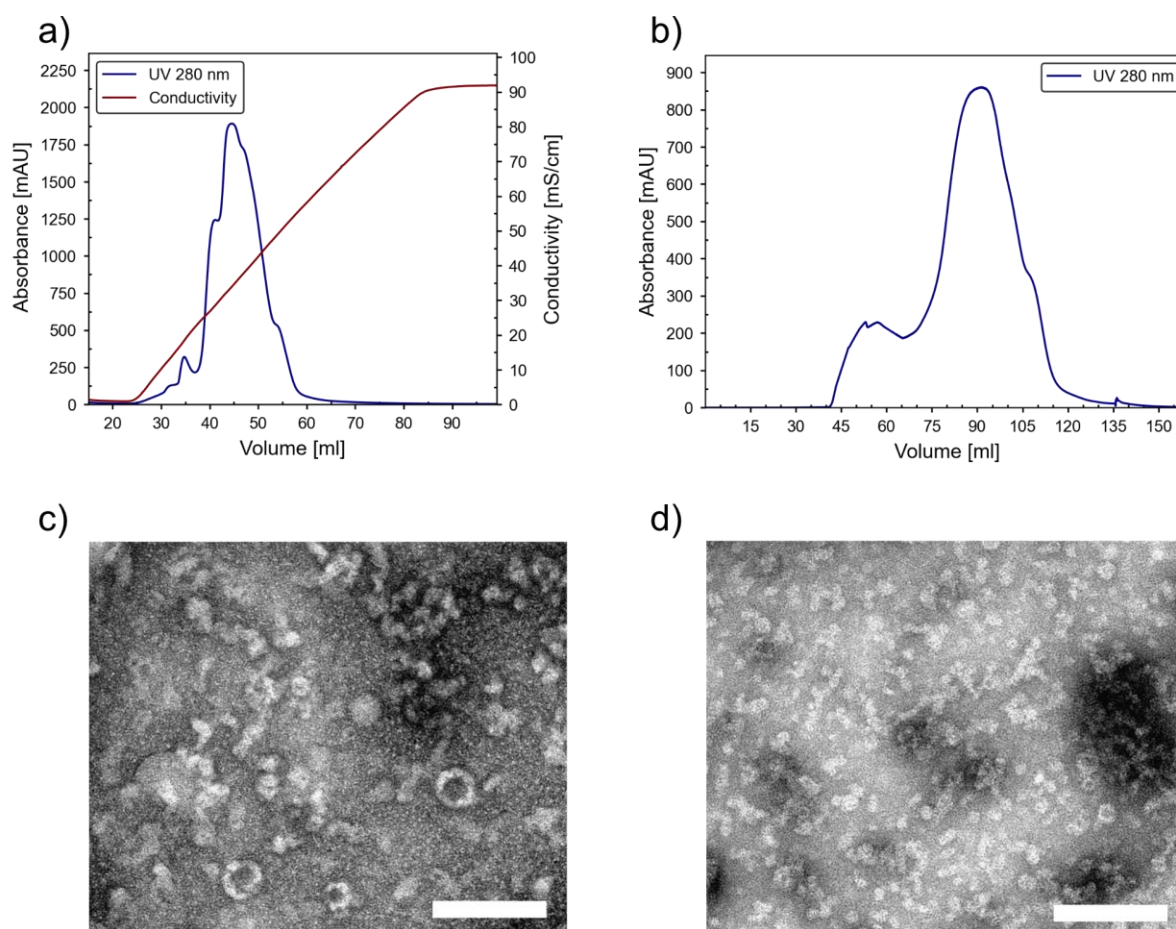


Figure 5.48: Ion-exchange and size-exclusion chromatograms of MxEnc. Samples were purified without ammonium sulfate. a) IEC chromatogram for MxEnc. Protein elution from 25 mS/cm to 55 mS/cm. b) SEC chromatogram for MxEnc. Absorbance was monitored at 280 nm (blue). Conductivity is shown in red. c) Negative stained TEM image of peak eluting around 40-65 ml. Scale bar is 100 nm. d) Negative stained TEM image of peak eluting at 75-120 ml. Scale bar is 100 nm.

The ammonium sulfate-treated sample yielded a sharp IEC peak eluting at 40.56 mS/cm. SEC showed a dominant peak at ~81 mL ($T = 1$), a minor shoulder near 64 mL ($T = 3$), and an early peak at ~45 mL consistent with aggregates. However, separation between $T = 3$ and aggregates remained indistinct. TEM images were inconclusive due to poor contrast (Figure 5.49).

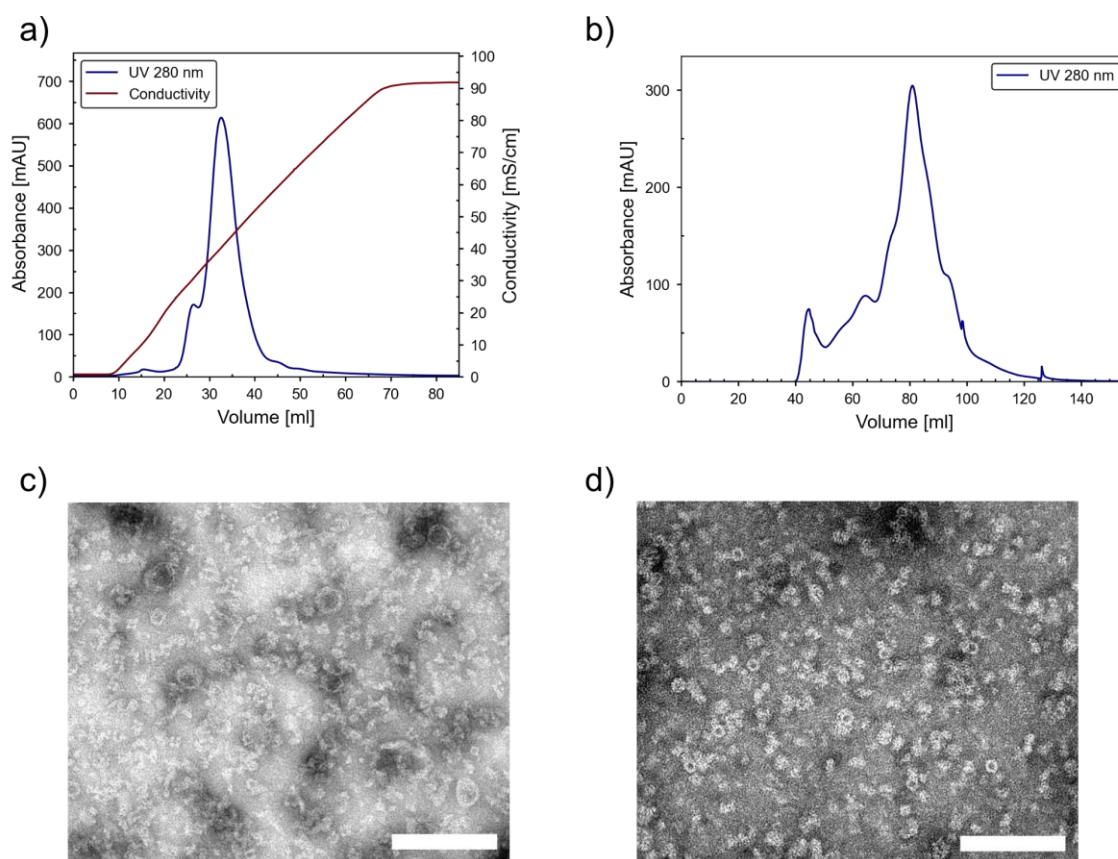


Figure 5.49: Ion-exchange and size-exclusion chromatograms of MxEnc. Samples were purified with ammonium sulfate. a) IEC chromatogram for MxEnc. Protein elution at 33.8 mS/cm. b) SEC chromatogram for MxEnc. Absorbance was monitored at 280 nm (blue). Conductivity is shown in red. c) Negative stained TEM image of T = 3 state. Scale bar is 100 nm. d) Negative stained TEM image of T = 1 state. Scale bar is 100 nm.

This pattern was reproduced in a subsequent production run, where only T = 1 particles and aggregates were detected. No evidence of T = 3 assembly was observed. Despite consistent growth and purification protocols, the shift toward T = 1 dominance highlights the sensitivity of MxEnc assembly to subtle variations in expression or lysis conditions.

To resolve these inconsistencies, the production system was transitioned to *E. coli* BL21(DE3) cells, following guidance from a recently published study.^[396] The published method used LB media, expression at 18 °C for 18 hours, and lower IPTG concentration. Lysis was performed in 50 mM tris, 200 mM NaCl, pH 8 with DNase and lysozyme, followed by sonication. No RNase, no divalent cations (MgCl₂ or CaCl₂), and no heat precipitation were used. IEC chromatograms showed a broad peak that eluted at a higher conductivity (~60 mS/cm) than usual. SEC showed only one peak corresponding to T = 1 state (Figure 5.50)

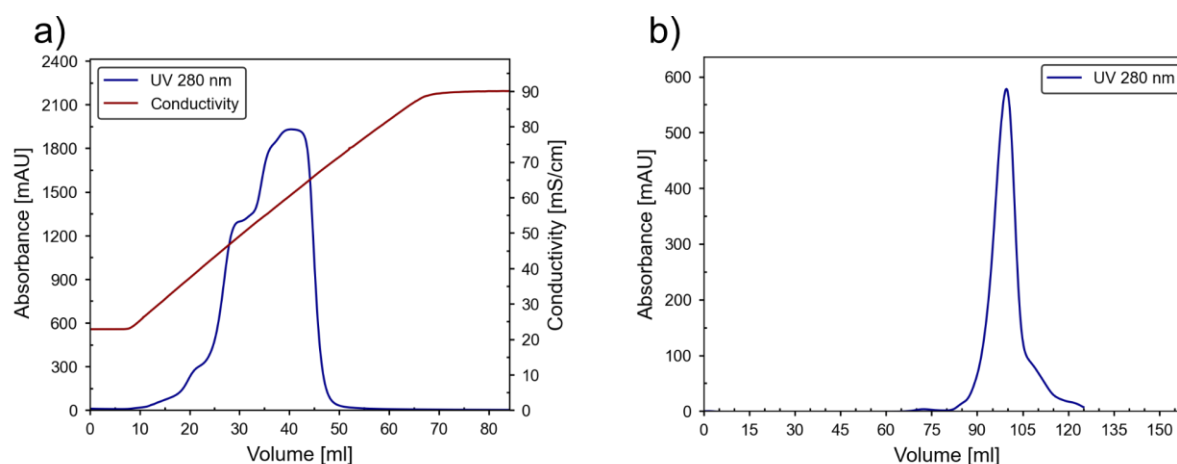


Figure 5.50: Ion-exchange and size-exclusion chromatograms of MxEnc. Samples were lysed using DNase and lysozyme. a) IEC chromatogram for MxEnc. Protein elution from 45 mS/cm to 60 mS/cm. b) SEC chromatogram for MxEnc. Absorbance was monitored at 280 nm (blue). Conductivity is shown in red.

A variant lysis condition using DNase alone, with all other parameters held constant, also failed to recover T = 3 assemblies. Similar results were obtained: protein eluted at higher conductivity during IEC, and SEC profiles showed no detectable T = 3 peak (see Appendix, Figure 8.6).

In contrast, other studies reported successful assembly of the protein cage using Terrific Broth (TB) media, with expression carried out either overnight at 30 °C or for 24 hours at 18 °C.^[344, 397] Variations in media, induction time, and temperature across these protocols pointed to expression-phase conditions as a potential factor influencing assembly state. Lysis protocols in these cases were more complex: one included lysozyme, Benzonase, MgCl₂, and SIGMAFAST EDTA-free protease inhibitor, with cells incubated on ice for 20 minutes. Another variation used a tris Buffered Saline (20 mM tris, 300 mM NaCl, pH 8.0) resuspension, supplemented with lysozyme, DNase, Benzonase, and the same protease inhibitor cocktail. Variations in media, induction time, and lysis composition across these protocols pointed to expression-phase and post-harvest conditions as potential factors influencing assembly state.

A systematic screen was performed comparing expression media (LB vs. TB), expression temperature and duration (18 h at 30 °C vs. 72 h at 18 °C) and application of heat post-lysis (60 °C). All three lysis enzymes - DNase, RNase and lysozyme were added. A summary of the tested conditions is provided in Table 5.3.

Table 5.3: Screening conditions for optimizing the production of MxEnc.

Media	Growth Time	Growth Temperature	Heat
LB	18h	30 °C	-
LB	18h	30 °C	60 °C
LB	72h	18 °C	-
LB	72h	18 °C	60 °C
TB	18h	30 °C	-
TB	18h	30 °C	60 °C
TB	72h	18 °C	-
TB	72	18 °C	60 °C

IEC and SEC chromatograms of all these conditions were analyzed to assess purity and assembly outcomes for each condition (see Appendix, Figures 8.7-8.12). Among the tested conditions, expression in TB medium at 18 °C for 72h with heat precipitation yielded the best results. All subsequent productions were therefore carried out under these conditions. Exemplary IEC chromatogram (Figure 5.51a) showed a single sharp elution peak corresponding to a conductivity of ~37.6 mS/cm, indicating a well-defined charge state and minimal contamination. SEC revealed a displayed a smaller early-eluting peak at ~70.6 mL, likely representing T = 3 assemblies and a dominant peak at ~89.2 mL, corresponding to T = 1 assemblies (Figure 5.51b). TEM images confirmed this distribution.

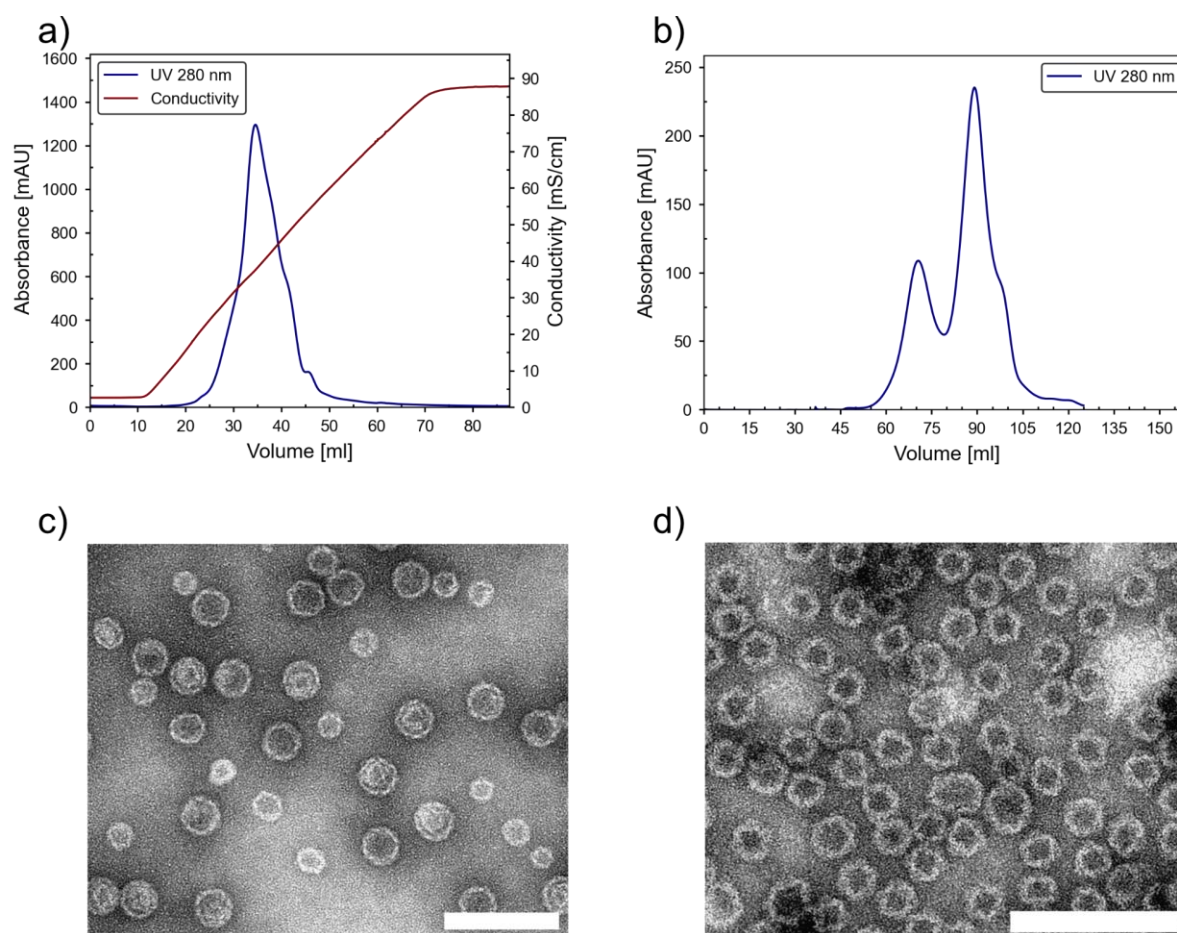


Figure 5.51: Ion-exchange and size-exclusion chromatograms of MxEnc. a) IEC chromatogram for MxEnc. Protein elution at 40 mS/cm. b) SEC chromatogram for MxEnc. Absorbance was monitored at 280 nm (blue). Conductivity is shown in red. c) Negative stained TEM image of peak eluting around 70 ml, corresponding to T = 3 state. Scale bar is 100 nm. d) Negative stained TEM image of peak eluting around 89 ml, corresponding to T = 1 state. Scale bar is 100 nm.

The SEC workflow was shifted from the Sephacryl S-500 HR column to a HiLoad 16/600 Superose 6 pg column, which features a larger pore size and is better suited for high-molecular-weight complexes. This change addressed persistent issues with elevated delta pressure on the S-500 column. While the separation profile remained comparable, elution volumes differed on the HiPrep column. An aggregate peak eluted around ~42 mL. T = 3 cages eluted at ~50 mL, T = 1 cages at ~62.5 mL and smaller proteins/monomers eluted around 79.2 ml (Figure 5.52)

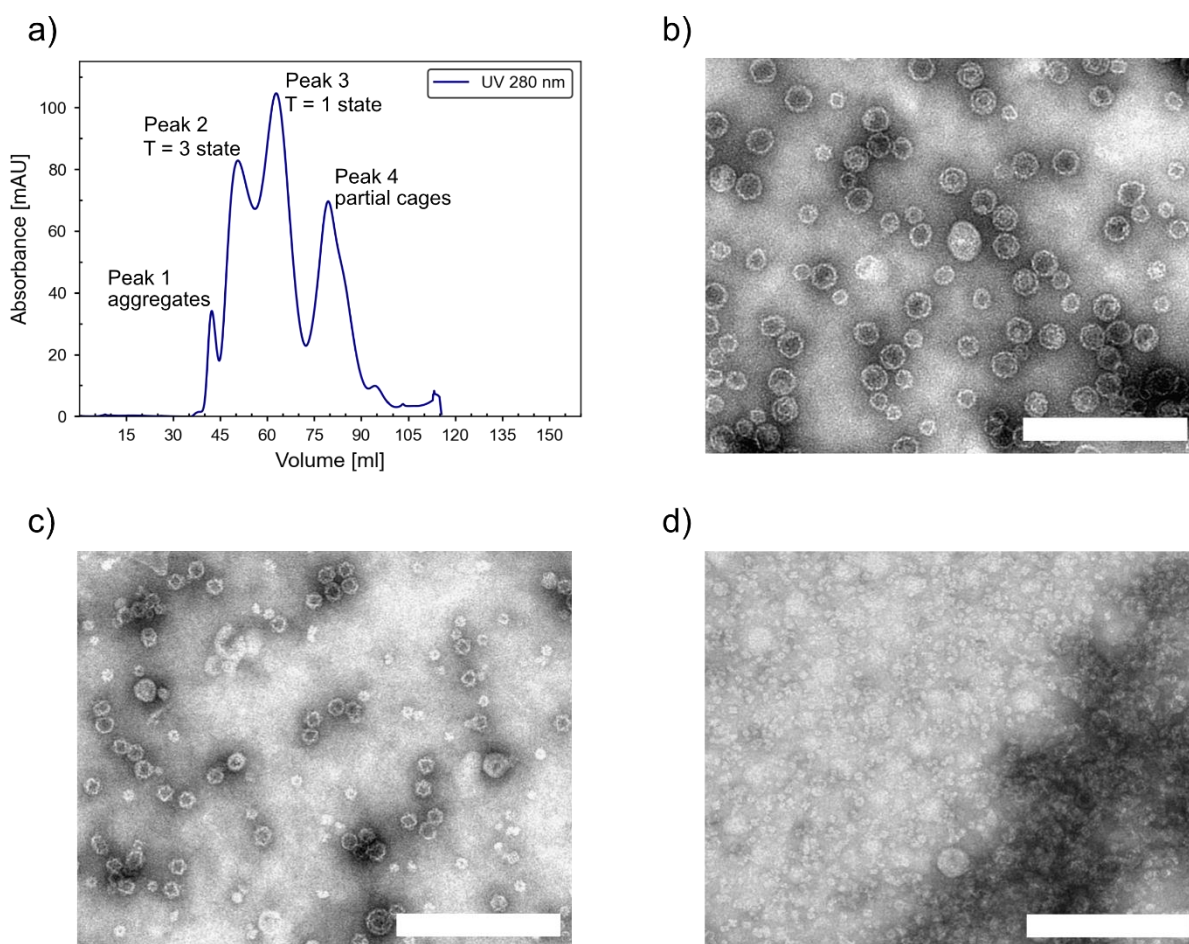


Figure 5.52: Size-exclusion chromatogram and stained TEM of MxEnc. a) SEC chromatogram for MxEnc. Chromatography done using HiLoad 16/600 Superose 6 pg column. Absorbance was monitored at 280 nm (blue). b) Negative stained TEM image of peak eluting around 50 ml. c) Negative stained TEM image of of peak eluting around 62.5 ml. d) Negative stained TEM image of of peak eluting around 80 ml. Scale bar is 200 nm.

To confirm the identity and integrity of the purified protein cage with the correct mass, it was analyzed by Electrospray ionization mass spectrometry (ESI-MS). The spectrum is shown in Figure 5.53.

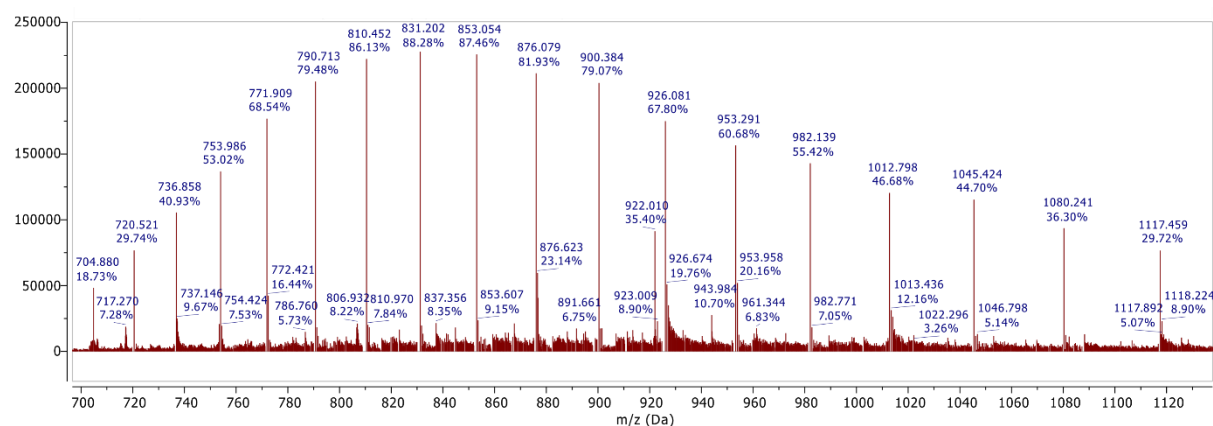


Figure 5.53. ESI-MS spectrum of MxEnc.

The measured mass was found to be 32377.8 Da, which is slightly lower than theoretical mass calculated for the protein sequence. The deviation is most likely caused by N-terminal cleaved MxEnc.^[398] Typically, a protein sequence starts with methionine since this amino acid acts as a starting point for the protein. Assuming that this first methionine is cleaved, a change of mass can be expected. The data is summarized in Table 5.4.

Table 5.4: Molecular mass determined via ESI MS for MxEnc.

Protein Species	Theoretical Molecular Mass	Observed Molecular Mass
Full sequence (with initiator Methionine)	32508.05	-
Full sequence (without initiator Methionine)	32376.86	32377.87

This batch provided sufficient material for extensive characterization, including multiple dis- and reassembly trials and initial encapsulation reactions, the results of which are described in the previous sections.

Upon requiring more material for continued experimentation, a new production run was performed using the identical protocol. This new production also resulted in a high yield. However, an unexpected shift in the IEC elution behavior was observed. The protein eluted at a conductivity of 27 mS/cm, significantly lower than the ~37.6 mS/cm recorded for previous batches (Figure 5.54a). The corresponding fraction was analyzed on both HiLoad Superose 6 pg and Superose S6 Increase 10/300 columns. Surprisingly, both chromatograms showed a stronger T = 3 peak relative to T = 1, suggesting a shift in the assembly state population. This difference in IEC elution conductivity likely reflects changes in the surface charge and assembly dynamics that favor T = 3 formation under these conditions. On the HiLoad Superose 6 pg column (Figure 5.54b), a broad peak with a maximum around 50 mL was observed for T = 3 but extended up to 72 mL, indicating that the separation between T = 3 and

T = 1 was not well defined. On the Superose 6 Increase, an intense peak eluted at 10 mL corresponding to the T = 3 state (Figure 5.54c). A small shoulder was seen at 12.6 mL, followed by a peak at 17.3 mL representing the T = 1 state and another at 20 mL corresponding to free subunits.

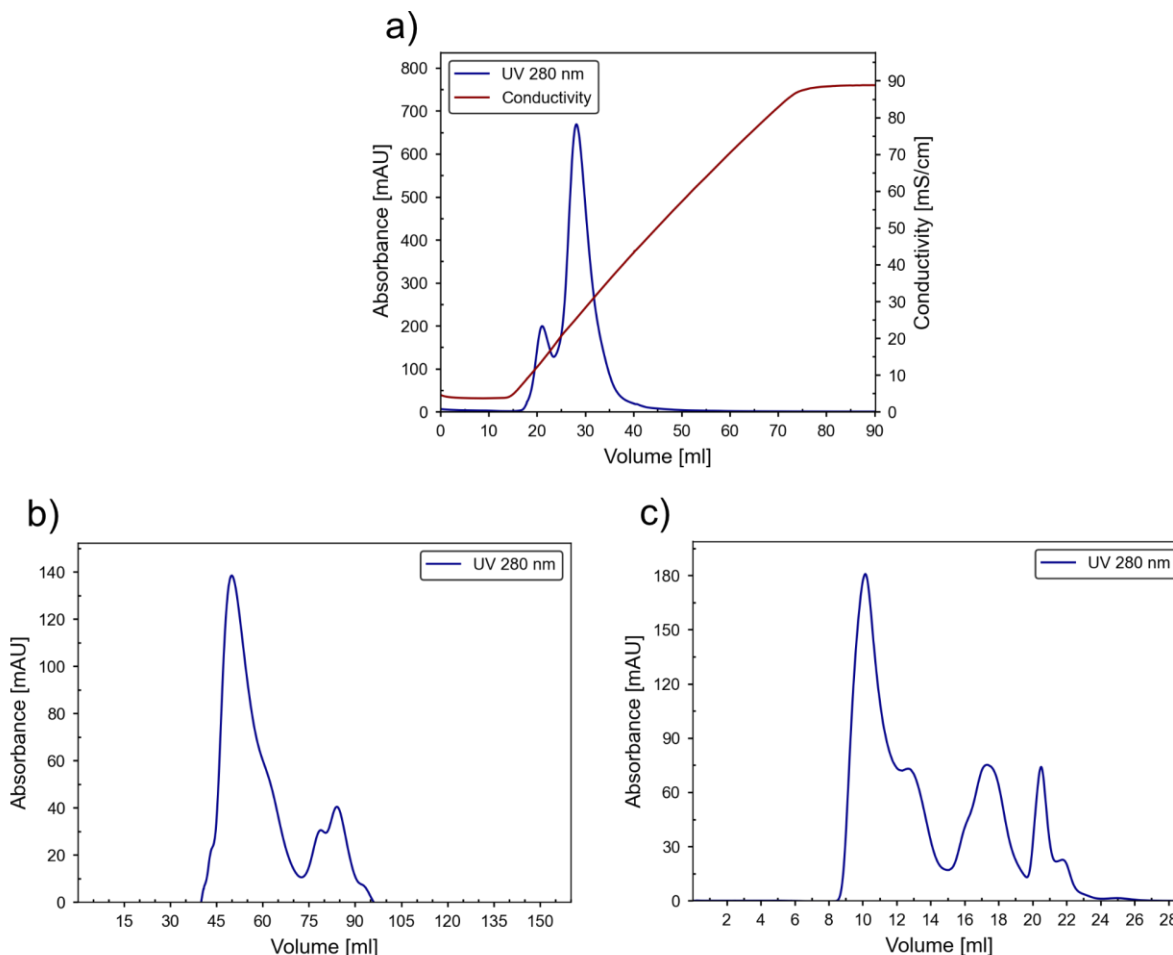


Figure 5.54: Ion-exchange and size-exclusion chromatograms of MxEnc. a) IEC chromatogram for MxEnc. Protein elution at 27 mS/cm. Conductivity is shown in red. b) SEC chromatogram for MxEnc. Chromatography done using HiLoad 16/600 Superose 6 pg 10/300 column. c) SEC chromatogram for MxEnc. Chromatography done using Superose 6 Increase column. Absorbance was monitored at 280 nm (blue).

Stained TEM confirmed these observations (Figure 5.55). Fractions from the HiLoad Superose 6 pg column contained a mixture of T = 3 and T = 1 particles, with T = 3 predominating. This was also reflected in the particle size distribution, where two populations were detected at ~18 nm (T = 1) and ~33 nm (T = 3), giving an overall mean diameter of 27.6 ± 6.7 nm (Figure 5.55b). In the case of the Superose 6 Increase, the first peak showed mostly T = 3 particles with a minor T = 1 population, whereas the second peak contained mainly T = 1 particles with low-level T = 3 contamination (Figure 5.55c). The corresponding histogram revealed a strong enrichment of T = 3, with the majority of cages in the 32-35 nm range, and

a few cages of smaller size, giving an overall mean diameter of 29.49 ± 5.1 nm, confirming that this column provided a cleaner separation between the two assembly states.

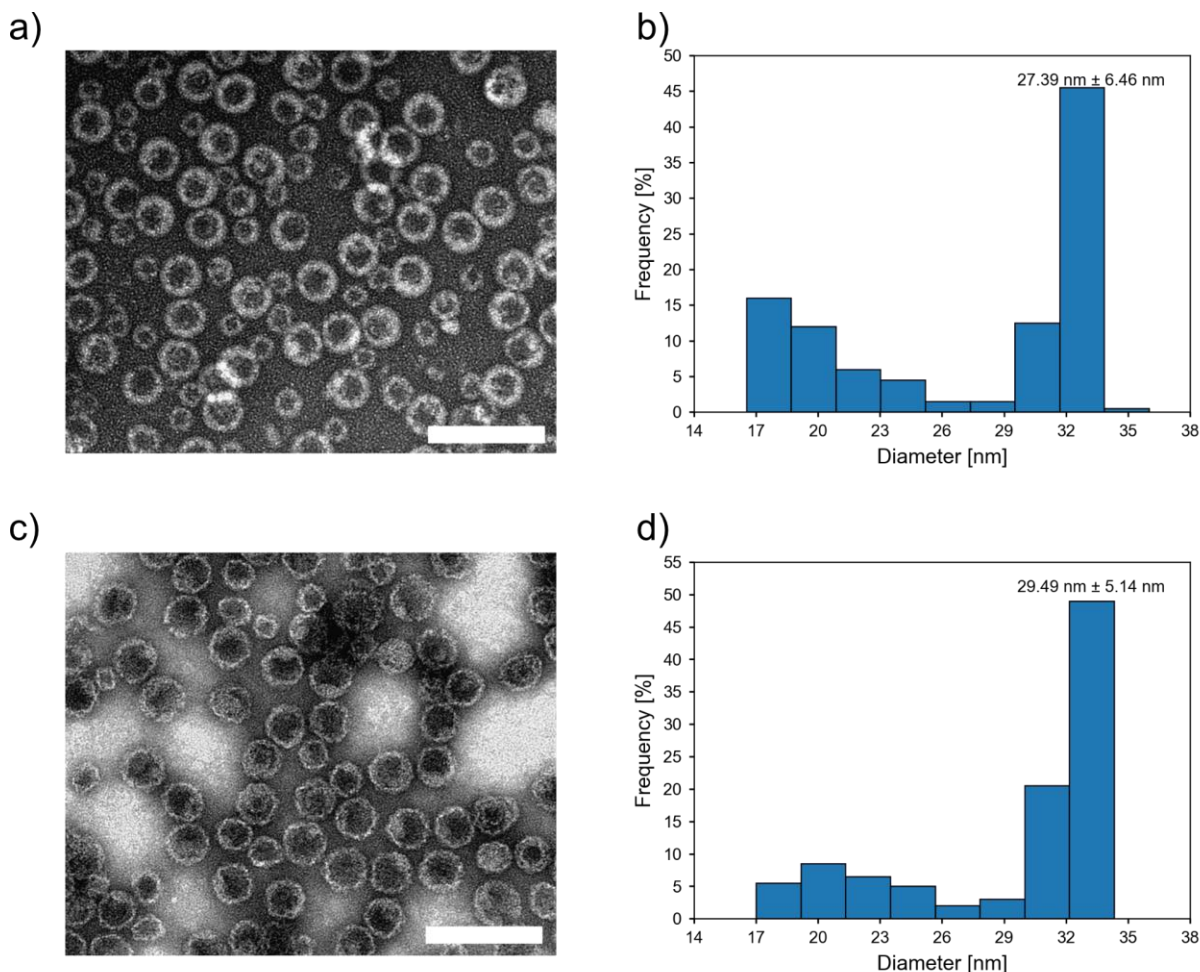


Figure 5.55: TEM images of MxEnc and corresponding histogram with size distribution. a) Negative stained TEM image of first peak from HiLoad Superose 6 pg column. b) Histogram and size distribution with standard deviation. c) Negative stained TEM image of first peak from Superose 6 Increase column. d) Histogram and size distribution with standard deviation. 100 protein cages were measured to determine size distribution. Scale bar is 100 nm.

These results confirm that while SEC does not completely resolve the two forms, it provides enrichment and establishes that $T = 3$ is the dominant assembly state under these conditions. This shift in the oligomeric equilibrium towards the $T = 3$ state is likely attributable to an elevated expression temperature. Although the protocol specified incubation at $18\text{ }^{\circ}\text{C}$, the external ambient temperature during this production run was unusually high ($\sim 22\text{ }^{\circ}\text{C}$), preventing the incubator from consistently maintaining the set point. It is well-established that expression temperature can significantly influence the folding and assembly pathways of complex protein complexes, and the higher temperature appears to have favored the kinetics and stability of the larger $T = 3$ assembly. Therefore, the combined IEC and SEC data conclusively show that the elevated expression temperature shifted the assembly equilibrium,

resulting in a batch enriched in T = 3 cages. Despite this shift, the material remained compositionally pure and was deemed suitable for downstream disassembly and encapsulation experiments, as the assembly pathway can be controlled in vitro to favor the desired oligomeric state.

5.4 Encapsulation of Cargo into *T. maritima* encapsulin

This section describes the encapsulation of nanomaterials into *T. maritima* encapsulin. The process involved controlled disassembly and reassembly of the protein cages in the presence of specific cargo, allowing for the incorporation of CdSe/CdS DiRs and AuNRs. The encapsulation efficiency and structural outcomes were assessed using a range of characterization methods, providing insight into how particle morphology influences incorporation within the *T. maritima* system.

5.4.1 Encapsulation of CdSe/CdS DiRs in *T. maritima* encapsulin

Initial trials focused on encapsulating CdSe/CdS DiRs coated with an AUT:MUTAB ligand mixture in 4:1 ratio, without the use of CLP. The rods carried a net positive charge from the quaternary ammonium group on MUTAB and protonated primary amine group on AUT, while the interior surface of the *T. maritima* encapsulin is negatively charged. This electrostatic complementarity was expected to support encapsulation without a targeting sequence.^[14] The schematic is shown in Figure 5.56.

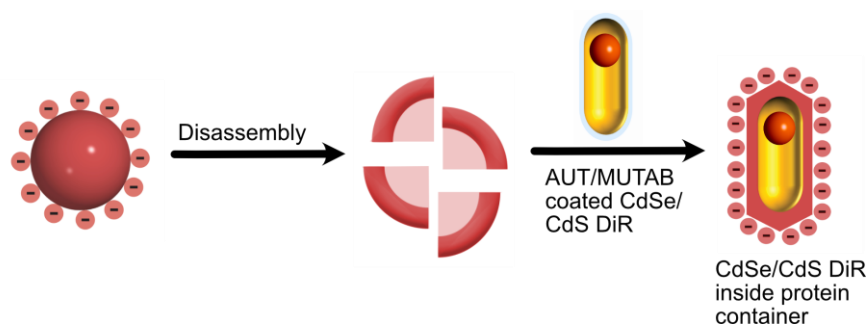


Figure 5.56: Encapsulation of DiRs into the negatively charged encapsulin cage. The spherical cage is disassembled using pH. After addition of the CdSe/CdS DiRs equipped with positively charged ligands, cage reassembly is induced and a well-defined shell will form around the template.

Encapsulin cages were disassembled by diluting the protein 10-fold into 10 mM phosphate buffer at pH 1.0, followed by incubation for one hour at 4 °C. Reassembly was then carried out by 100-fold dilution into 20 mM phosphate buffer at pH 7.0 both without and with salt (350 mM NaCl). DiRs were added slowly, and the samples were incubated overnight at 4 °C. In both conditions, the nanorods precipitated, pointing either to unsuccessful encapsulation or to instability of the rods in the buffer.

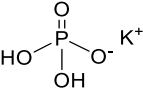
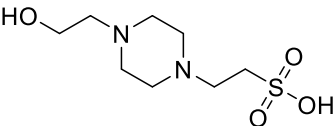
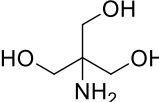
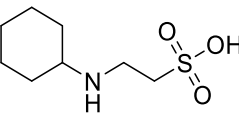
To distinguish between these possibilities, the DiRs were exposed to five different buffer systems. Each DiR sample (150 μ L) was added to 1 mL of buffer and centrifuged at 10,000 g for 15 minutes. The results are summarized in Table 5.5.

Table 5.5: Stability of DiRs in different buffer solutions.

Buffer condition	Outcome	Interpretation
10 mM phosphate, pH 7.0	Aggregation, large pellet	Unstable
20 mM tris, 300 mM NaCl, pH 7.5	Clear solution, tiny pellet	Partially stable
20 mM HEPES, 200 mM NaCl, pH 8.2	Clear solution, no pellet	Stable
20 mM tris, pH 9.0	Clear solution, tiny pellet	Partially stable
20 mM CHES, pH 10.0	Clear solution, no pellet	Stable

The initial screening revealed that DiRs were unstable in phosphate buffer, resulting in significant aggregation. In contrast, they exhibited improved stability in tris, HEPES and CHES buffers. The solutions in CHES and HEPES (with salt) were completely clear with no pellet, indicating full stability, while tris showed a clear solution with a tiny pellet, indicating stability for the vast majority of nanorods. This stark difference can be attributed to the chemical nature of the buffer ions. The multivalent phosphate anions (PO_4^{3-}) readily promote aggregation through charge neutralization and bridging. The tiny pellet observed in basic tris buffer suggests the shielding provided by hydroxide anions (OH^-) is sufficient for most nanorods but may be marginally insufficient for a small sub-population, potentially those with a lower ligand density or larger size. In contrast, the stability in CHES and HEPES buffers suggests an additional, specific stabilizing effect from their sulfonate groups ($-\text{SO}_3^-$), likely due to their strong ionic character and potential to form a more protective hydration layer. The structures of buffers along with their pH range are shown in Table 5.6.

Table 5.6: Structure of different buffers and their pH range.

Buffer	Structure	Buffer Range
phosphate Monopotassium phosphate		5.8-8.0
HEPES (4-(2-hydroxyethyl)-1-piperazineethanesulfonic acid)		2.5-3.5 and 6.8-8.2
tris tris(hydroxymethyl)aminomethane		7.1-9.1
CHES (N-cyclohexyl-2-aminoethanesulfonic acid)		8.6-10

Based on these results, a second set of encapsulation conditions was designed to systematically identify optimal reassembly buffers. Using the same disassembly protocol, reassembly was carried out in five different buffer systems. The outcomes of these experiments, which further explore the relationship between buffer chemistry and nanorod stability, are summarized in Table 5.7.

Table 5.7: Encapsulation trials in different reassembly buffers.

Reassembly Buffer	Outcome	Interpretation
20 mM HEPES, pH 7.0	Precipitation	Failure
20 mM HEPES, 200mM NaCl, pH 8.2	Precipitation	Failure
20 mM tris, 300mM NaCl, pH 7.5	Precipitation	Failure
20 mM CHES, pH 8.6	No precipitation	Success
20 mM CHES, pH 10.0	No precipitation	Success

Only the CHES buffer maintained rod stability during the reassembly process. These samples were analyzed by SEC (Figure 5.57a,b). A small peak was detected at the elution volume consistent with TmEnc^(neg), and the signal showed the presence of DiRs. While the amount was low, the data indicated that some DiRs may be encapsulated. Additional characterization was performed to support the SEC findings. PL measurements showed a broad emission band between ~550 nm, consistent with CdSe/CdS DiR fluorescence, along with a narrow feature at ~520 nm arising from the water Raman band. Because the overall PL intensity was weak, the data are shown as normalized spectra for clarity (Figure 5.57c,d). This confirmed that DiRs remained in solution after reassembly. However, PL alone could not confirm whether the rods were encapsulated or simply free in solution.

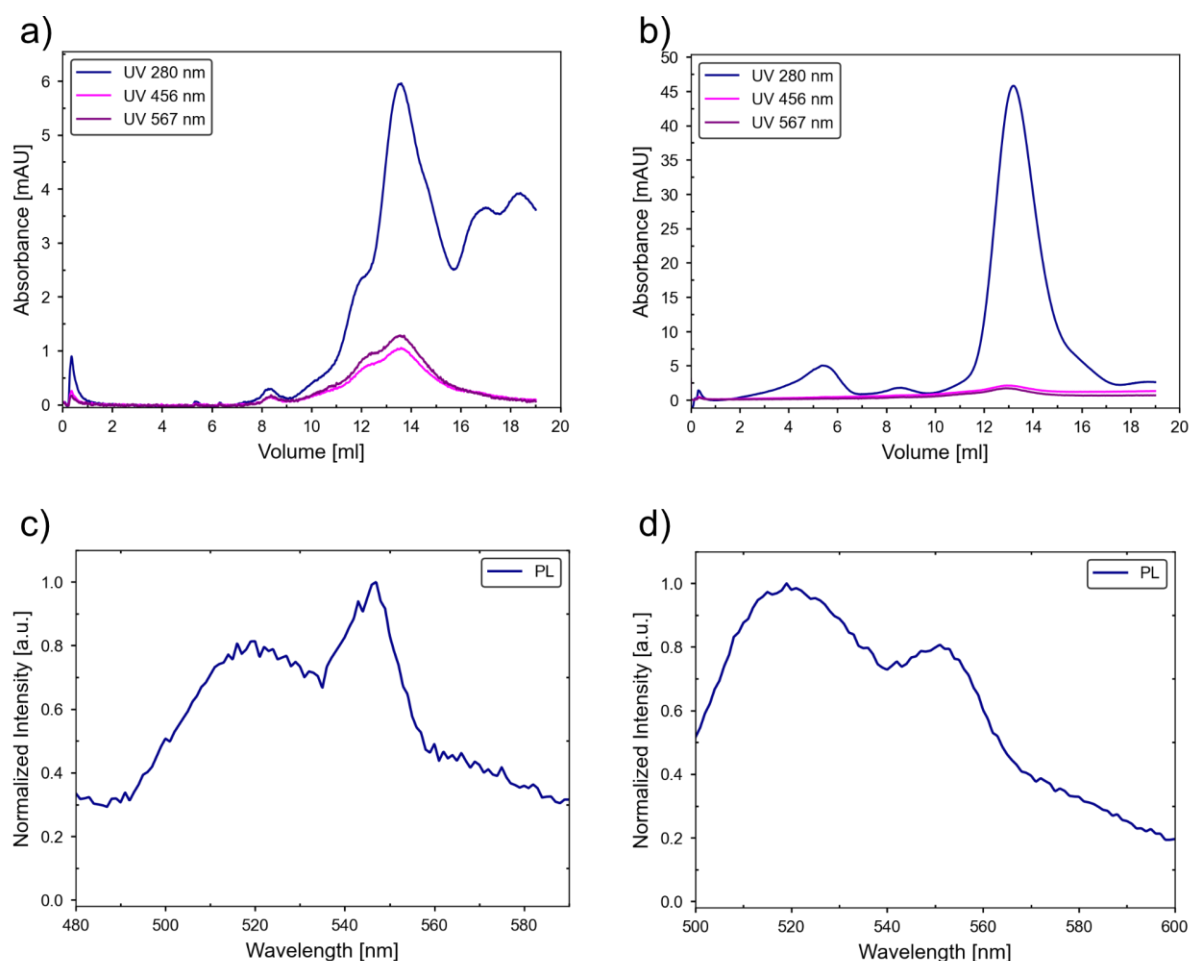


Figure 5.57: Size-exclusion chromatograms and corresponding PL spectra of the DiRs and TmEnc^(neg) in CHES buffer. a) SEC chromatogram of DiRs and TmEnc^(neg) in CHES pH 8.6. Absorbance monitored at 280 nm (blue), 456 nm (pink), and 567 nm (purple). b) SEC chromatogram of DiRs and TmEnc^(neg) in CHES pH 10.0 with the same absorbance wavelengths. (C) PL spectrum of TmEnc^(neg), excitation at 450 nm. (D) PL spectrum of DiRs, excitation at 450 nm.

TEM was also used, but no conclusive evidence of encapsulation was obtained. The rods have poorer contrast when transferred to aqueous solution, and the addition of uranyl acetate further reduced visibility, making it difficult to detect rod-like structures. As a result, although SEC and PL confirmed the presence of DiRs, it could not be confirmed that they were encapsulated in the protein cages.

The *T. maritima* encapsulin has an inner cavity diameter of approximately 18 nm. The smaller rods (11 nm length + ~2 nm ligand shell) were well below this threshold, meaning their encapsulation would not be expected to influence the shell geometry. In contrast, rods approaching the size limit of the cavity or larger were expected to induce anisotropic deformation upon successful encapsulation, providing a clearer structural readout via TEM.

Encapsulation experiments using the larger DiRs (18.6 × 5.4 nm) were carried out using same AUT:MUTAB ligand mixture as in earlier experiments. Reassembly was performed in 20 mM

CHES buffer at pH 8.6 and pH 10.0, without added salt. At pH 8.6 the sample was stable, while at pH 10.0, the rods precipitated. This outcome is in contrast with behaviour of smaller DiRs which had remained stable at both pH values. PL was not a clear indicator of encapsulation, as stable samples still produced PL even when free rods were present in solution. Because of this, stained TEM was prioritized as the primary method to directly evaluate encapsulation. Stained TEM imaging produced mixed results. The sample at pH 8.6 showed that both protein cages and DiRs were present. However, no rods were observed enclosed within protein shells (Figure 5.58). Two TEM images are shown to confirm the presence of both DiRs and protein since there is only one protein cage visible in the first image.

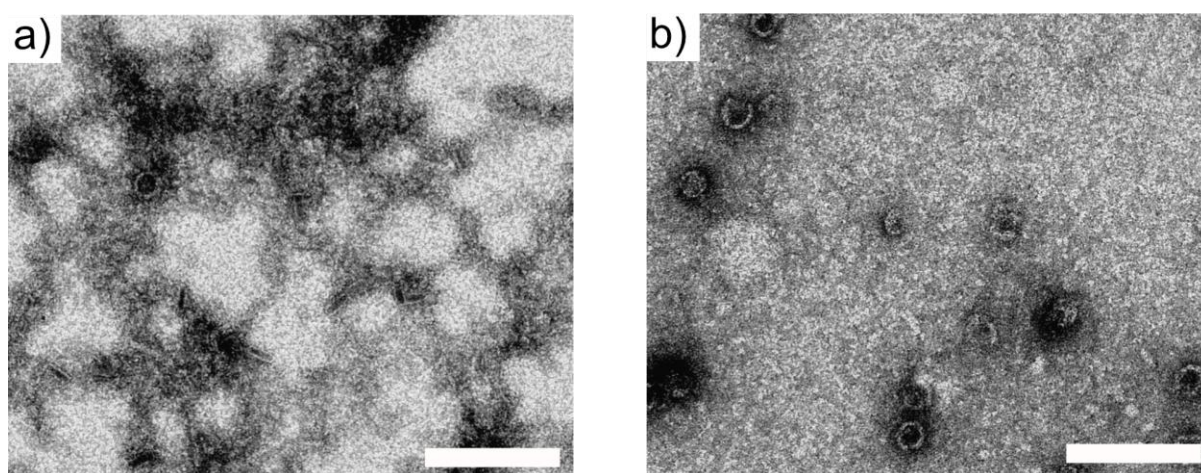


Figure 5.58: TEM images of DiRs and TmEnc^(neg) in CHES buffer without salt. a) TEM image showing the presence of DiRs in sample. There is only one protein cage visible. b) TEM image showing presence of TmEnc^(neg) in sample. Scale bar is 100 nm.

This suggests that while the larger DiRs were more detectable in TEM compared to smaller DiRs and possibly better suited for visual tracking of anisotropic structure, encapsulation efficiency remained low.

To test whether ionic strength influences encapsulation, the experiment was repeated in 20 mM CHES buffer at pH 8.6 supplemented with 300 mM NaCl. Under these conditions, the sample remained stable and no precipitation was observed. TEM imaging confirmed the presence of DiRs in solution, but again no clear evidence of encapsulation inside protein cages was obtained (Figure 5.59). The stability of the rods in the presence of salt indicates that ionic strength can influence colloidal behavior during reassembly, but no encapsulation was observed under these conditions. This idea is supported by earlier work showing that salt concentration can play a decisive role in balancing nanoparticle stability and protein-cargo interactions.^[14]

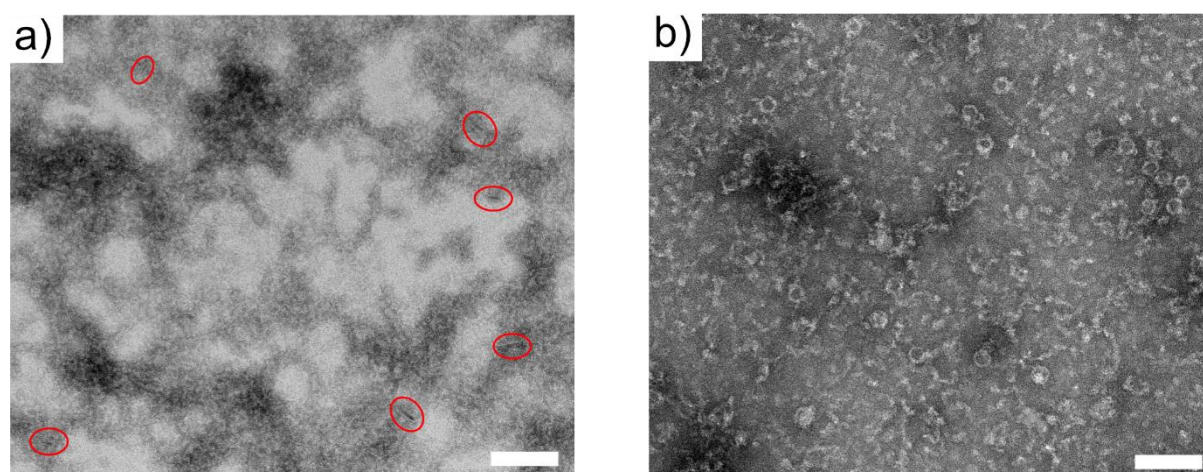


Figure 5.59: TEM images of DiRs and TmEnc^(neg) in CHES buffer with salt. a) TEM image showing the presence of DiRs in sample. DiRs are circled in red. b) TEM image showing presence of TmEnc^(neg) in sample. Scale bar is 100 nm.

These results showed that although rod stability could be maintained under optimized buffer conditions, including moderate salt concentration, encapsulation of long DiRs using AUT:MUTAB remained inefficient. The rods were stable in presence of protein but were not encapsulated.

Given the lack of encapsulation observed with AUT:MUTAB-coated DiRs, even under stable buffer conditions, the focus shifted to using MUTAB/CLP-functionalized DiRs. The CLP is known to interact with the negatively charged interior surface of the *T. maritima* encapsulin, and its inclusion was expected to improve targeting and loading efficiency.^[14] The schematic is shown in Figure 5.60.

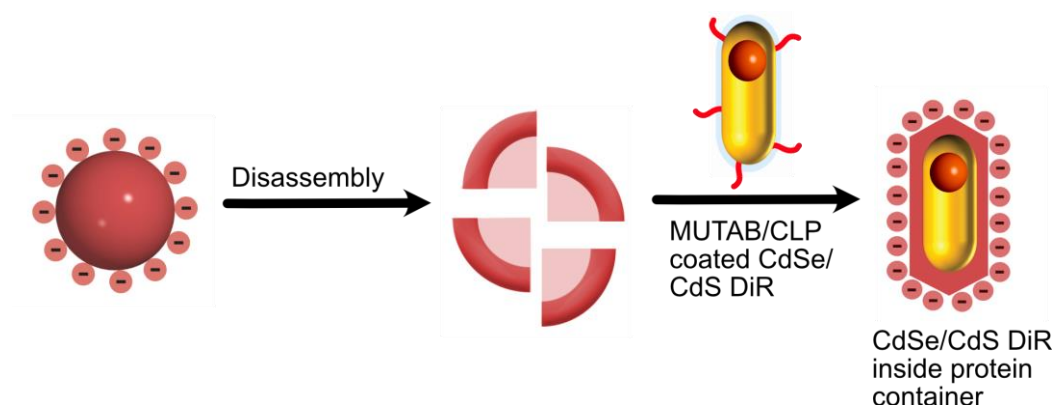


Figure 5.60: Encapsulation of DiRs into the negatively charged encapsulin cage. The spherical cage is disassembled using pH. After addition of the CdSe/CdS DiRs equipped with positively charged ligands and CLP, cage reassembly is induced and a well-defined shell should form around the template.

Before initiating encapsulation, the larger DiRs (18.5 nm × 5.0 nm) MUTAB/CLP-coated DiRs were screened for colloidal stability across a range of buffer systems. Buffers varied in pH and ionic strength, and stability was assessed by pellet formation following centrifugation. A visible

pellet indicated aggregation and poor stability, while the absence of a pellet indicated a stable suspension. The results are summarized in Table 5.8.

Table 5.8: Stability of MUTAB/CLP functionalized DiRs in different buffer solutions.

Buffer	pH	Salt	Aggregation
20 mM CHES	8.6	0 M	Yes
20 mM CHES	8.6	100 mM	Yes
20 mM CHES	9.5	300 mM	Yes
20 mM CHES	10.0	0 M	Yes
20 mM HEPES	7.0	0 M	No
20 mM HEPES	7.5	0 M	Yes
20 mM HEPES	8.2	200 mM	Yes
20 mM MES	5.5	0 M	Yes
20 mM MES	6.5	0 M	Yes
20 mM tris	7.5	0 M	No
20 mM tris	8.5	0 M	Yes
20 mM tris	9.0	0 M	Yes

Based on the stability screening, encapsulation experiments with MUTAB/CLP-functionalized DiRs were first carried out using 20 mM HEPES, pH 7.0 buffer and 20 mM tris, pH 7.5 buffer. No precipitation was observed in either condition, indicating that the particles remained colloidally stable during the reassembly process. However, TEM images obtained from the tris sample were not conclusive due to poor contrast. For the HEPES condition, stained TEM images did not show the DiRs, so additional unstained TEM was performed to confirm their presence. In case of tris, unstained TEM couldn't be performed because the sample caused green residue deposition on the grid. While DiRs and protein cages were present, the rods were not encapsulated within the cages (see Appendix, Figure 8.14)

To improve loading efficiency, the ratio of DiRs to encapsulin was adjusted in the next set of experiments. Since successful encapsulation of a single rod likely requires cage subunits from more than one protein cage, different loading ratios were tested. Experiments were performed in 20 mM HEPES buffer, pH 7.0 with the following DiR-to-protein ratios: 1:10, 1:20, 1:30, and 1:40. The samples remained stable and were concentrated for stained TEM imaging. The first indications of encapsulation were observed at the 1:10 and 1:20 ratios, where individual rods surrounded by protein shells were visible in stained TEM (Figure 5.61). By contrast, at the 1:30 and 1:40 ratios the samples primarily contained either empty protein cages or

aggregates, likely reflecting that the number of rods present was too low to drive encapsulation (see Appendix, Figure 8.15)

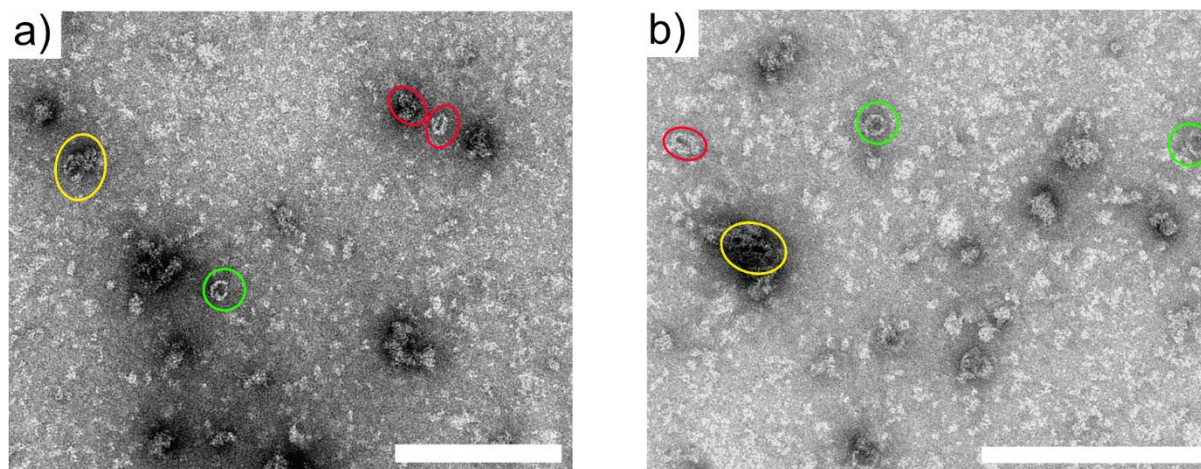


Figure 5.61: Stained TEM images of encapsulation of CdSe/CdS DiRs into *T. maritima* encapsulin at different DiR-to-protein ratios. a) 1:10 ratio, showing individual DiRs surrounded by protein shells (circled in red), aggregates of DiRs-protein (yellow) and empty protein cages (green). b) 1:20 ratio, showing individual DiRs surrounded by protein shells (circled in red), aggregates of DiRs-protein (yellow) and empty protein cages (green).

A follow-up attempt with a 1:15 DiR-to-encapsulin ratio was carried out. Stained TEM images of the dilute sample showed only scattered DiRs and protein shells, with no clear co-localization. After concentrating the sample using a 100 kDa molecular weight cutoff filter, TEM images revealed protein cages assembled around individual DiRs (Figure 5.62), indicating successful encapsulation under these conditions.

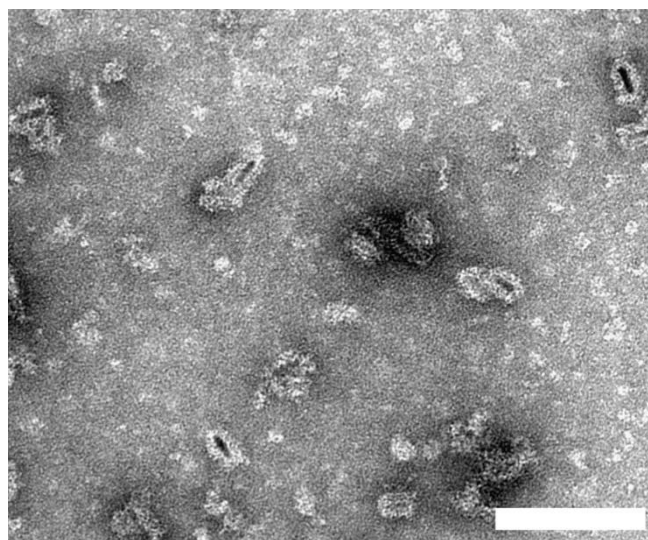


Figure 5.62: Stained TEM images of encapsulation of CdSe/CdS DiRs into *T. maritima* encapsulin at 1:15 DiR-to-protein ratio.

To further confirm and isolate the encapsulated fraction, the sample was subjected to IEC followed by SEC. IEC was carried out using 50 mM tris pH 9.0 with a salt gradient from

0-1 M. The IEC chromatogram showed strong absorbance at 280 nm (blue), indicating the presence of protein (Figure 5.63a). Distinct peaks at 460 nm (magenta) and 569 nm (purple), characteristic of the CdSe/CdS DiRs, co-eluted with the protein fraction at conductivity ~ 46.1 mS/cm. This overlap with the protein elution zone suggested that a fraction of the rods may have been associated with the encapsulin particles, potentially indicating encapsulation or strong non-specific interaction. After IEC, the fraction was concentrated and subjected to SEC. There was some sample that got stuck in the filter, indicating sample loss. The SEC analysis provided separation by size. SEC was done using 20 mM tris, 300 mM NaCl, pH 7.5 buffer (Figure 5.63b). The chromatogram revealed that the DiR-associated absorbance (460 nm and 569 nm) eluted primarily in the 8-9 mL range, along with the protein signal at 280 nm. This elution volume was smaller than that of empty encapsulin, which typically elutes at ~ 12 -13 mL, suggesting a larger hydrodynamic size consistent with DiRs incorporated into or tightly bound to the protein cages.

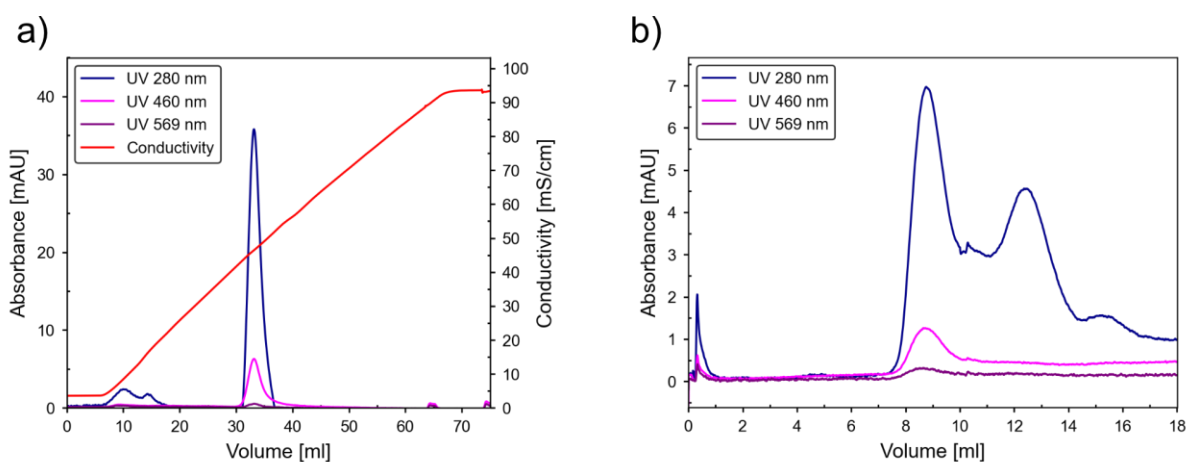


Figure 5.63: Ion-exchange and size-exclusion chromatograms of DiR-loaded TmEnc^(neg) encapsulin. a) IEC chromatogram for DiR-loaded TmEnc^(neg). Protein eluting with DiRs at 46 mS/cm. Conductivity is shown in red. b) SEC chromatogram for DiR-loaded TmEnc^(neg). Co-elution of protein and DiR peaks around 9 mL. Absorbance was monitored at 280 nm (blue), 350 nm (purple), and 569 nm (magenta).

Fluorescence spectra collected at each purification step supported the chromatographic findings. Because fluorescence intensity dropped after each purification step, spectra were normalized to allow comparison of spectral shapes. The pre-column sample showed strong emission from the DiRs, with an apparent shoulder that is most reasonably attributed to instrumental broadening from the wider slit setting rather than a true second emissive state. Following IEC, fluorescence intensity decreased slightly, likely due to partial loss of rods during the column run but the spectral shape was preserved with maxima at 580 nm (Figure 5.64). In the SEC fractions, the 6-8 mL fraction displayed clear DiR emission at 577 nm, though reduced in intensity, indicating partial loss or destabilization of encapsulated complexes. In this range a weaker additional feature at 543 nm was also present, which can be assigned to

the Raman scattering peak of water under 460 nm excitation. The 12 mL fraction, containing only empty protein cages, showed the 543 nm Raman band but no DiR emission. It can be concluded that the characteristic DiR emission profile was largely retained through IEC and partially preserved after SEC, while the Raman contribution from solvent and protein background became more apparent in later fractions.

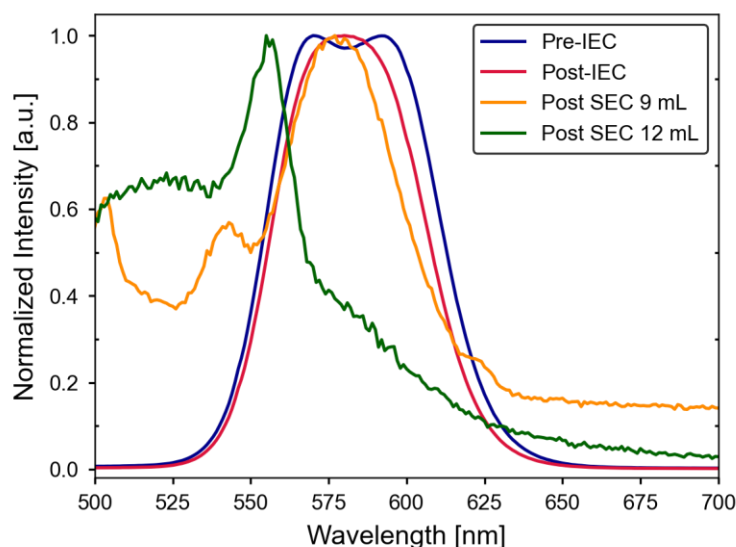


Figure 5.64: Normalized emission spectra of TmEnc^(neg) and CdSe/CdS DiRs sample. Pre-IEC (blue) shows two apparent peaks that are reasonably attributed to instrumental broadening from a wider emission-slit setting. Post-IEC (red) corresponds to encapsulated DiR with protein and displays a single emission band. Post-SEC 9 ml (orange) includes the DiR peak along with an additional narrow feature at 543 nm, assigned to the Raman scattering peak of water. Post SEC 12 ml (green) shows just the water peak confirming absence of DiRs. Excitation was done at 460 nm.

Finally, stained TEM images were collected from IEC- and SEC-purified samples (Figure 5.65). Post-IEC TEM showed mostly empty encapsulin cages with no visible DiRs. Similarly, TEM images of the SEC-purified first peak (6-8 mL) showed well-formed protein shells, but no rods could be identified. The absence of visible DiRs in these images, despite a clear fluorescence signal and co-elution in chromatograms, may be attributed to one or more of the following factors: (i) low encapsulation yield relative to protein concentration, (ii) loss of rods during column purification, or (iii) disruption of assemblies under chromatographic conditions. Additionally, unstained TEM could not be performed due to a greenish deposit on the grids that interfered with imaging.

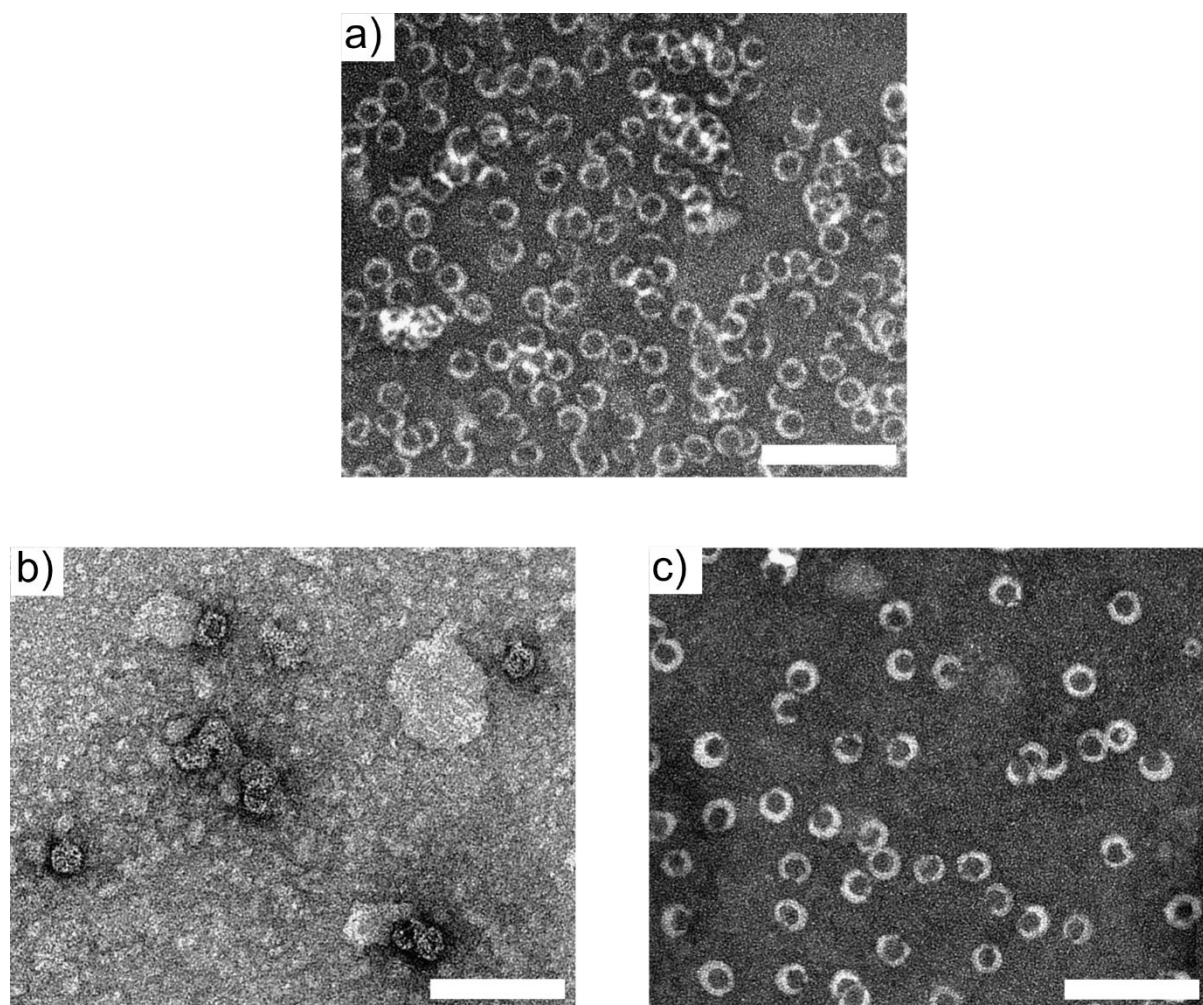


Figure 5.65: Stained TEM images of the sample post ion exchange and size exclusion chromatography. a) Stained TEM of the sample collected after IEC. b,c) Stained TEM of sample eluted around 9 ml and 12 ml post SEC. Scale bar is 100 nm.

Taken together, the combined evidence from TEM, IEC, SEC, and fluorescence suggests that while partial encapsulation of DiRs may occur under optimized loading conditions, the efficiency is low, and the resulting assemblies are not stable under purification.

To test whether ionic strength could influence encapsulation efficiency, a salt screen was performed. Reassembly reactions were carried out in 20 mM HEPES pH 7.0 buffer supplemented with NaCl at 0.2 M, 0.4 M, and 1.0 M. IEC analysis showed that while DiR-associated UV peaks were detectable, their intensity was very low compared to the protein signal. Stained TEM images from each condition revealed only intact protein cages, with no evidence of encapsulated rods.

The encapsulation experiment was repeated using the same DiR-to-protein ratios, but this time purification was carried out in HEPES rather than tris buffer. IEC was carried out in 50 mM HEPES pH 7.0 with a salt gradient from 0 to 1 M, and SEC in 20 mM HEPES pH 7.0 containing 300 mM NaCl. The aim was to determine whether buffer conditions during purification

contributed to the apparent instability of the assemblies. The resulting chromatograms (Figure 5.66) again showed co-elution of DiR absorbance with protein, suggesting that rods were still present after column runs. However, TEM images of the purified fractions showed no visible DiRs. Since the DiR absorbance consistently eluted at lower intensity compared to protein, it is likely that only a very small number of rods were present in the final samples. The fractions appeared yellow and retained fluorescence even after SEC, and in contrast to previous experiments the PL signal was higher. Still, without anisotropic structures visible by TEM, it is not possible to conclude that *T. maritima* encapsulin is capable of supporting T = 3 state.

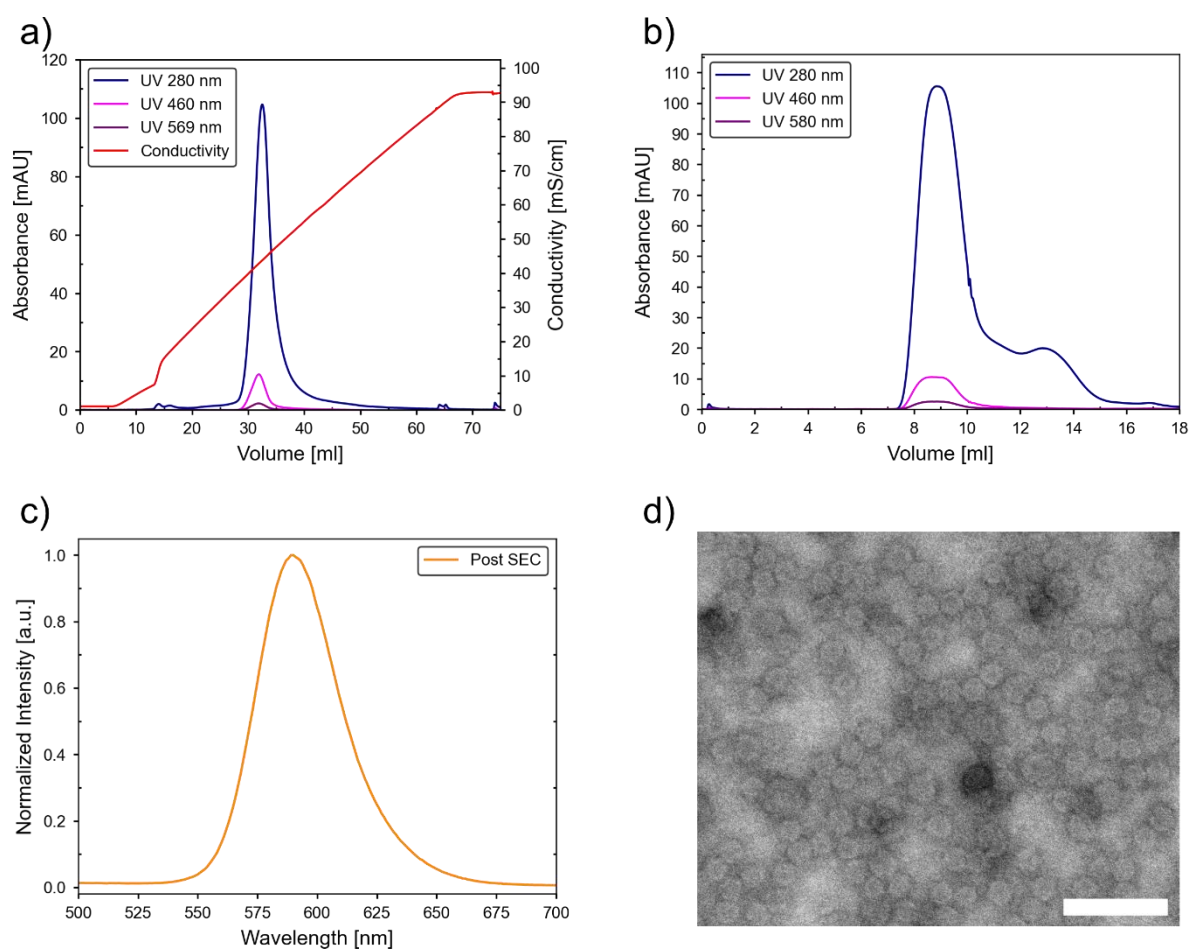


Figure 5.66: Ion-exchange and size-exclusion chromatograms of DiR-loaded TmEnc^(neg) encapsulin. a) IEC chromatogram for DiR-loaded TmEnc^(neg). Protein eluting with DiRs at 46 mS/cm. Conductivity is shown in red. b) SEC chromatogram for DiR-loaded TmEnc^(neg). Co-elution of protein and DiR peaks around 9 ml. Absorbance was monitored at 280 nm (blue), 350 nm (purple), and 569 nm (magenta). c) Normalised emission spectra of sample collected after SEC. d) Stained TEM image of the sample after SEC. Scale bar is 100 nm.

At this point, further encapsulation attempts with MUTAB/CLP-functionalized DiRs were discontinued. Multiple strategies were tested - varying buffer conditions, salt concentrations,

and loading ratios - but none yielded reproducible encapsulation. Nevertheless, these experiments provided important insights:

- Buffer and pH choice has a strong influence on nanorod stability.
- Larger protein-to-rod ratios are required to accommodate long, rigid anisotropic particles.
- Encapsulation efficiency for long DiRs appears to be inherently low, possibly due to their size, shape, or rigidity preventing cage closure.

This contrasts with prior work on spherical gold nanoparticles (~13 nm), where using an excess of particles ensured that each cage captured a particle. In the case of DiRs, the opposite strategy was needed: an excess of protein cages to surround a single rod, as encapsulation likely requires subunits from multiple cages to cooperatively assemble around a rod-shaped structure.

These findings directly informed the next stage of the project: Encapsulation trials with AuNRs. By carrying forward what was learned here, buffer stability requirements and optimized protein-to-particle ratios, it became possible to test whether material composition or particle shape is the dominant factor limiting encapsulation.

5.4.2 Encapsulation of Gold Nanorods in *T. maritima* Encapsulin

Encapsulation trials were extended to AuNRs functionalized with MUTAB/CLP. The AuNRs were found to be stable in 20 mM tris buffer at pH 9.0, and encapsulation reactions were performed using AuNR-to-encapsulin ratios of 1:30 and 1:40, based on previous insights that higher protein excess may be necessary to accommodate elongated nanostructures. Stained and unstained TEM was performed on both samples (Figure 5.67). While the rods remained well dispersed in solution and stable under the reaction conditions, no encapsulation was observed in any images.

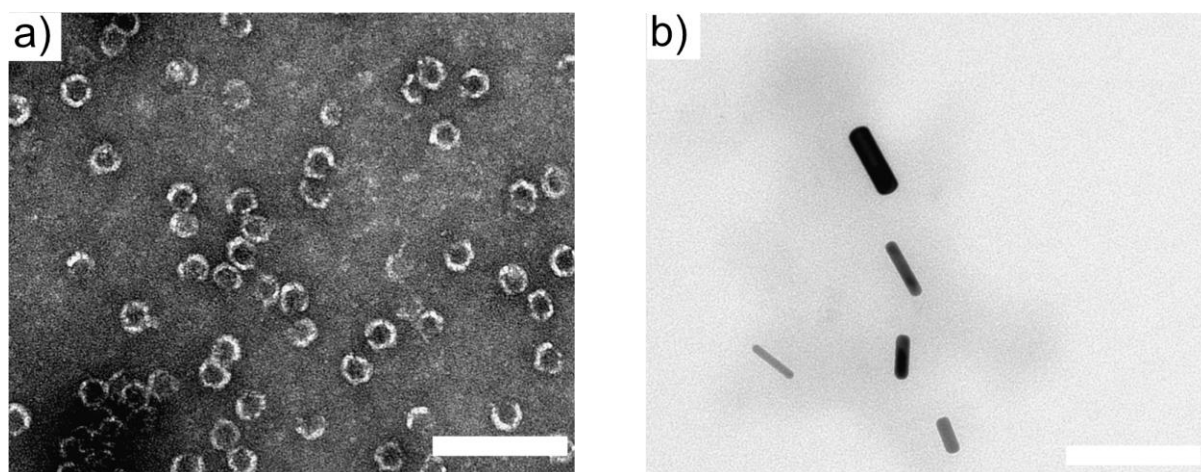


Figure 5.67: Stained and unstained TEM images of the AuNR-TmEnc^(neg) sample post encapsulation reaction. a) Stained images showing only protein cages. b) Unstained images of AuNRs. Scale bar is 100nm.

Further attempts were made to influence encapsulation by introducing salt during reassembly (0.2 M, 0.5 M, and 1 M NaCl), but this had no impact on the outcome. In all cases, protein cages were observed, but the AuNRs remained external to the cages. One of the key reasons for this can be the larger size of AuNRs.

These findings reinforce the limitations encountered with anisotropic cargo. In the case of CdSe/CdS DiRs, SEC, IEC, and PL traces suggested some degree of co-elution and fluorescence retention, hinting at possible encapsulation. However, TEM revealed no anisotropic structures, indicating that if rods were present, they were too few or too disordered to be reliably considered encapsulated. Attempts with AuNRs provided an even clearer outcome: no evidence of encapsulation was observed across methods.

Together, these results point to structural constraints imposed by the geometry of the *T. maritima* encapsulin. The *T. maritima* encapsulin assembles in a $T = 1$ icosahedral symmetry, forming a cage with an internal diameter of ~ 18 nm. While this geometry is sufficient for spherical nanoparticles or small guest proteins, it may not accommodate anisotropic cargo such as nanorods, which impose directional strain on the symmetric shell. Literature suggests that larger encapsulin variants, particularly those forming $T = 3$ icosahedral architectures, offer expanded internal volumes (~ 30 - 32 nm) and have demonstrated greater flexibility in encapsulating non-spherical cargo. This is due to the presence of hexameric facets in the $T = 3$ lattice, which allows greater geometric flexibility compared to $T = 1$ systems. This can support rod-like elongation of the cage, enabling the shell to adapt to anisotropic cargo. For example, $T = 3$ encapsulins from *Myxococcus Xanthus* and *Quasibacillus thermotolerans* have been reported to tolerate larger or more structurally complex guests due to their expanded triangulation number and shell elasticity.^[313, 328, 399]

Based on these results, it was concluded that the *T. maritima* capsid, despite its stability and icosahedral symmetry, lacks the spatial and mechanical adaptability required to accommodate nanorods, particularly when encapsulation requires cage deformation. Therefore, the focus shifted to a new system: the *Myxococcus Xanthus* capsid, which assembles in a T = 3 state and has hexameric facets, may offer the necessary environment for anisotropic cargo encapsulation. The disassembly, reassembly, and encapsulation strategy using this new protein cage will be discussed in the next section.

5.5 Encapsulation of Cargo into *M. xanthus* Encapsulin

This section presents the encapsulation of nanomaterials into MxEnc and compares their behavior to the *T. maritima* encapsulin. The disassembly and reassembly behavior of the MxEnc cages was characterized, and the impact of encapsulin architecture on cargo loading was examined. Encapsulation of spherical gold nanoparticles was performed as an initial model system and analyzed in terms of particle distribution, efficiency, and structural effects. Spherical geometry was chosen to establish a baseline for encapsulation behavior before progressing to more challenging anisotropic cargo, such as gold nanorods, which place greater geometric demands on the cage. The section concludes with a comparative discussion of how cage type and cargo size influence the final biohybrid structure.

5.5.1 *M. xanthus* Encapsulin Dis- and Reassembly

Disassembly and reassembly of encapsulins are essential prerequisites for encapsulation of cargo, and the behavior of MxEnc T = 1 and T = 3 state was systematically evaluated. Encapsulins are composed of self-assembling protein subunits stabilized through non-covalent interactions, including hydrophobic contacts, electrostatic interactions, and, in some cases, disulfide bridges. Disassembly requires disruption of these stabilizing forces to break the nanocage into its constituent subunits or oligomers. This is typically achieved with chaotropic agents such as urea or guanidinium hydrochloride, or by shifting to extreme pH. The balance is delicate: overly harsh conditions cause irreversible aggregation, while conditions that are too mild may leave intact cages in solution.

Several classical disassembly strategies were first tested. Dilution into 10 mM phosphate buffer at pH 1.0 and incubation for 1 hour at 4 °C caused no detectable change in hydrodynamic size for either T = 1 or T = 3 state. Repeating the same treatment at room temperature produced identical results. Addition of 100 mM HCl caused visible aggregation, while treatment with 100 mM NaOH led to cage disruption but no subsequent reassembly, suggesting irreversible denaturation. Incubation in 4 M guanidinium hydrochloride at 4 °C caused aggregation. Finally, direct incubation in 8 M urea at 4 °C for 1 hour produced only partial disassembly, with residual large particles remaining in solution. These results demonstrated that the classical approaches used successfully for other encapsulins were not sufficient for MxEnc, either because the cages remained intact or because the treatment led to irreversible aggregation.

To overcome these limitations, a PEG precipitation-based strategy adapted from literature was adopted.^[13] In this method, the protein was first precipitated using 10% PEG 8000 and 500 mM NaCl on ice for 1 hour. After centrifugation, the protein pellet was resuspended in either 6 M

GuHCl or 8 M urea and incubated on ice for 1 hour. The published protocol reported only the use of 8 M urea, but both conditions were evaluated here. Reassembly was then induced by diluting the solution into reassembly buffer (300 mM tris, 150 mM NaCl, 1 mM DTT, pH 7.4) and incubating overnight at 4 °C.

Disassembly and reassembly were monitored by both DLS and intrinsic tryptophan fluorescence (ITF). The data for T = 1 state is shown in Figure 5.68 and for T = 3 state in Figure 5.69. Upon chaotrope treatment, a red shift in the emission maximum was observed, reflecting increased solvent exposure of aromatic residues and disruption of the cage.^[333] Following overnight reassembly, the emission spectrum shifted back toward shorter wavelengths, indicating refolding into a more hydrophobic environment.

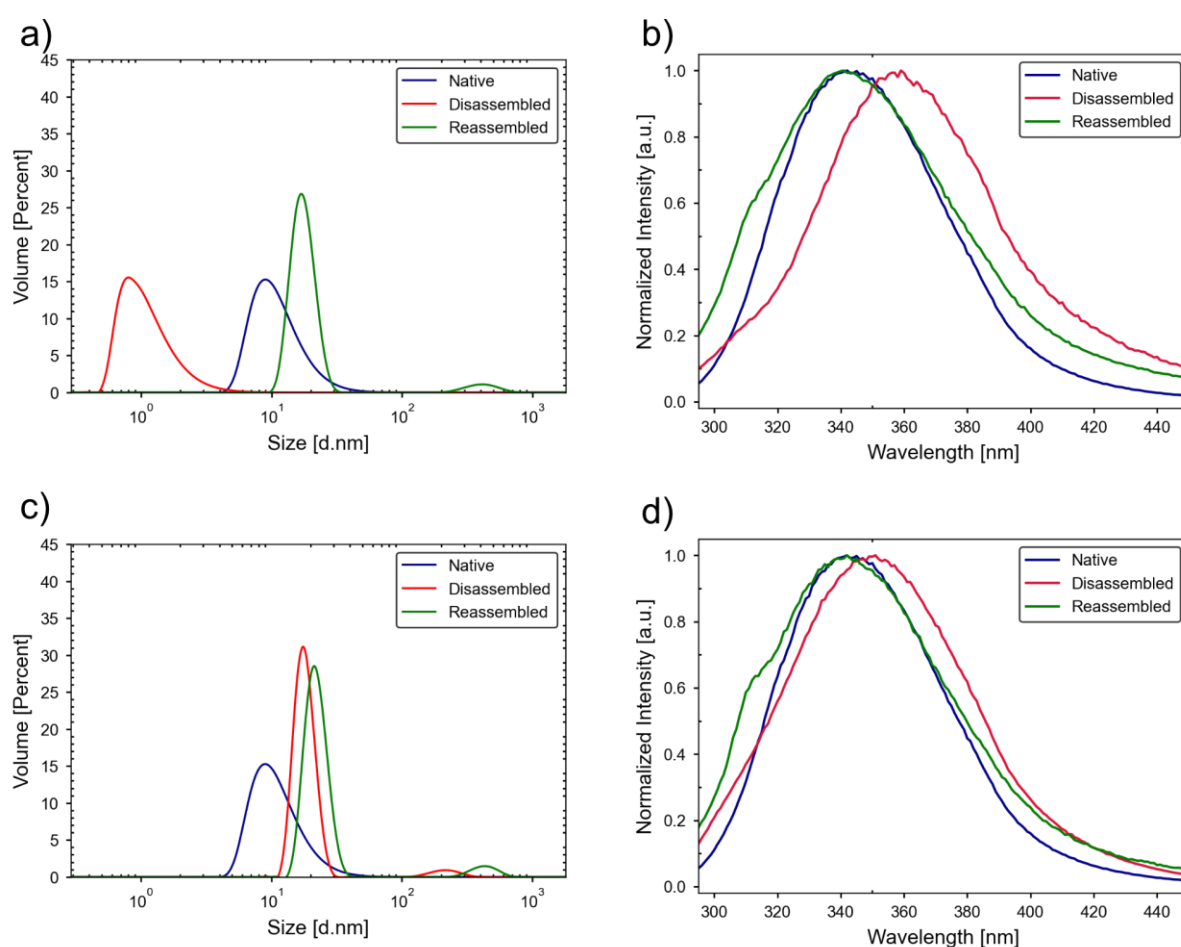


Figure 5.68: Hydrodynamic size distribution and normalized ITF spectra for monitoring for native (blue), disassembled (red) and reassembled (green) T = 1 state of MxEnc. a) Volume-weighted DLS measurements, and b) Normalized ITF spectra upon treatment with 6 M GuHCl treatment and reassembly. c) Volume-weighted DLS measurements, and b) Normalized ITF spectra upon treatment with 8 M urea treatment and reassembly.

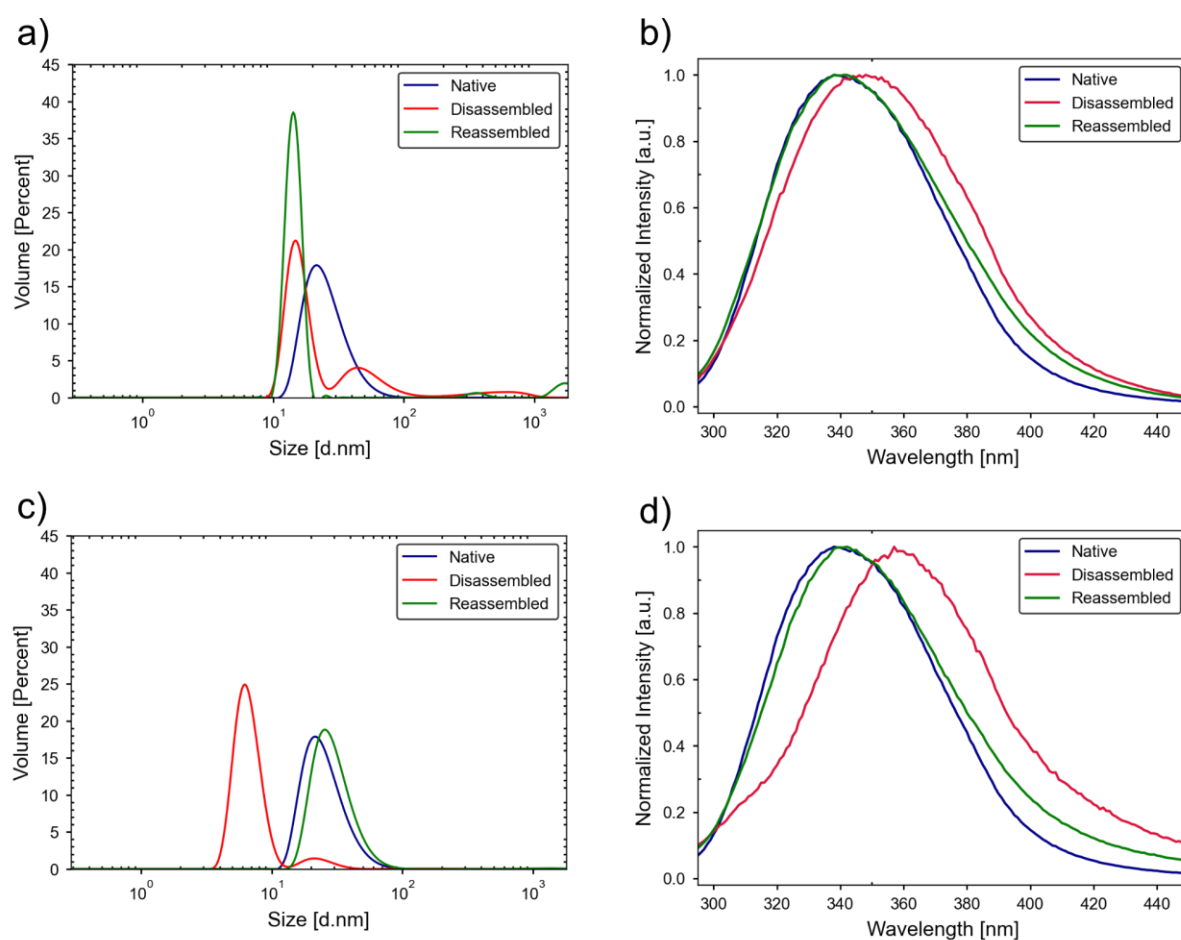


Figure 5.69: Hydrodynamic size distribution and normalized ITF spectra for monitoring for native (blue), disassembled (red) and reassembled (green) T = 3 state of MxEnc. a) Volume-weighted DLS measurements, and b) Normalized ITF spectra upon treatment with 6 M GuHCl treatment and reassembly. c) Volume-weighted DLS measurements, and b) Normalized ITF spectra upon treatment with 8 M urea treatment and reassembly.

Post-reassembly SEC was carried out using a Superose S6 Increase 10/300 GL (see Appendix, Figure 8.16-8.17).

Although the cage peaks were of low intensity for both T = 1 and T = 3 states, reproducible differences were observed. Treatment with 6 M GuHCl favored reassembly of the T = 1 state, producing a weak cage peak. Under the same conditions, the T = 3 state showed poor recovery. In contrast, 8 M urea favored reassembly of the T = 3 state, yielding a weak cage peak, while T = 1 recovery was minimal. These results likely reflect the distinct structural organization of the two states: T = 1 cages are formed exclusively from pentamers, while T = 3 cages contain both pentamers and hexamers. The additional hexameric interfaces may respond differently to denaturants, leading to distinct reassembly preferences.

ITF provided a useful indication of structural changes, showing clear emission shifts even in cases where aggregation was detected by DLS and SEC. These shifts reflect reversible changes in the local environment of tryptophan residues, consistent with their exposure during

disassembly and subsequent reburying upon reassembly. However, ITF alone cannot distinguish between correct cage reformation and misassembly into aggregates. Similar effects have been reported in thermal unfolding studies, where red shifts in tryptophan fluorescence were also influenced by aggregation rather than unfolding alone.^[400] Thus, while ITF is a sensitive local probe of tertiary structural changes, it must be interpreted alongside size-based methods such as SEC and DLS to accurately assess global assembly state.

Incomplete disassembly of T = 3 state was suspected from a residual shoulder near 37 nm in DLS, close to the hydrodynamic size of intact cages (Figure 5.66a,c). To resolve this, many trials were performed varying incubation time, temperature, denaturant concentration, total denaturant volume, and dosing mode. Encapsulins were disassembled with urea after PEG precipitation. Disassembly with 8 M urea at 4 °C and at room temperature was tested for 1 h, 3 h, and 4 h. Overnight disassembly screens at 4 M, 6 M, and 8 M were done. Overnight disassembly using 4 M, 6 M, and 8 M urea at 4 °C was done. Stepwise addition from 4 M to 6 M to 8 M was tested, as well as the reverse sequence from 8 M to 6 M to 4 M. In summary, the best-performing condition in our hands was 8 M urea, prepared in 10mM tris buffer, pH 7.5 with 100 mM NaCl, at a total volume of 1 mL, with incubation for 3 to 4 h on ice. When protein had been stored in the refrigerator for some time, a quick SEC repurification prior to disassembly restored reproducibility. These optimizations clarified how to achieve full disassembly and provided a reliable starting point for subsequent reassembly trials. The dis- and reassembly were monitored using DLS.

Since buffer composition can strongly influence protein folding and cage assembly, especially ionic strength and buffer identity, a set of reassembly buffers was screened. Reassembly was performed using 50 mM tris, pH 7.5, 5 mM DTT, and varying NaCl concentrations: 0 M, 100 mM, 300 mM and 1 M. Post reassembly SEC was done using Superose 6 Increase 10/300 GL column. Generally, the T = 3 state elutes around 9-11 ml and T = 1 state elutes around 13-15 ml.

For the T = 1 state, post reassembly all chromatograms showed a strong peak at ~26 mL, which is beyond the column's separation range (Figure 5.70). By column behavior this would normally correspond to small species such as disassembled subunits or oligomers. However, DLS analysis of this fraction showed very large apparent diameters, indicating the presence of aggregates. This apparent contradiction can be explained by the different sensitivities of the two methods: in SEC, proteins that either interact nonspecifically with the resin or collapse into compact forms may elute later than expected, while in DLS even a small proportion of large aggregates dominates the scattering signal.

The peak corresponding to $T = 1$, eluting at 13 mL, was highest in 0 M NaCl, lowest in 300 mM, and intermediate in 100 mM and 1 M, suggesting that salt concentration influences the balance between cage-like and alternative assemblies. In addition, a small shoulder around 8-10 mL appeared in both the 100 mM and 1 M NaCl conditions, with the feature being more pronounced at 1 M. This shoulder was absent at 0 M NaCl and likely reflects a minor population of $T = 3$ -like species forming under high ionic strength.

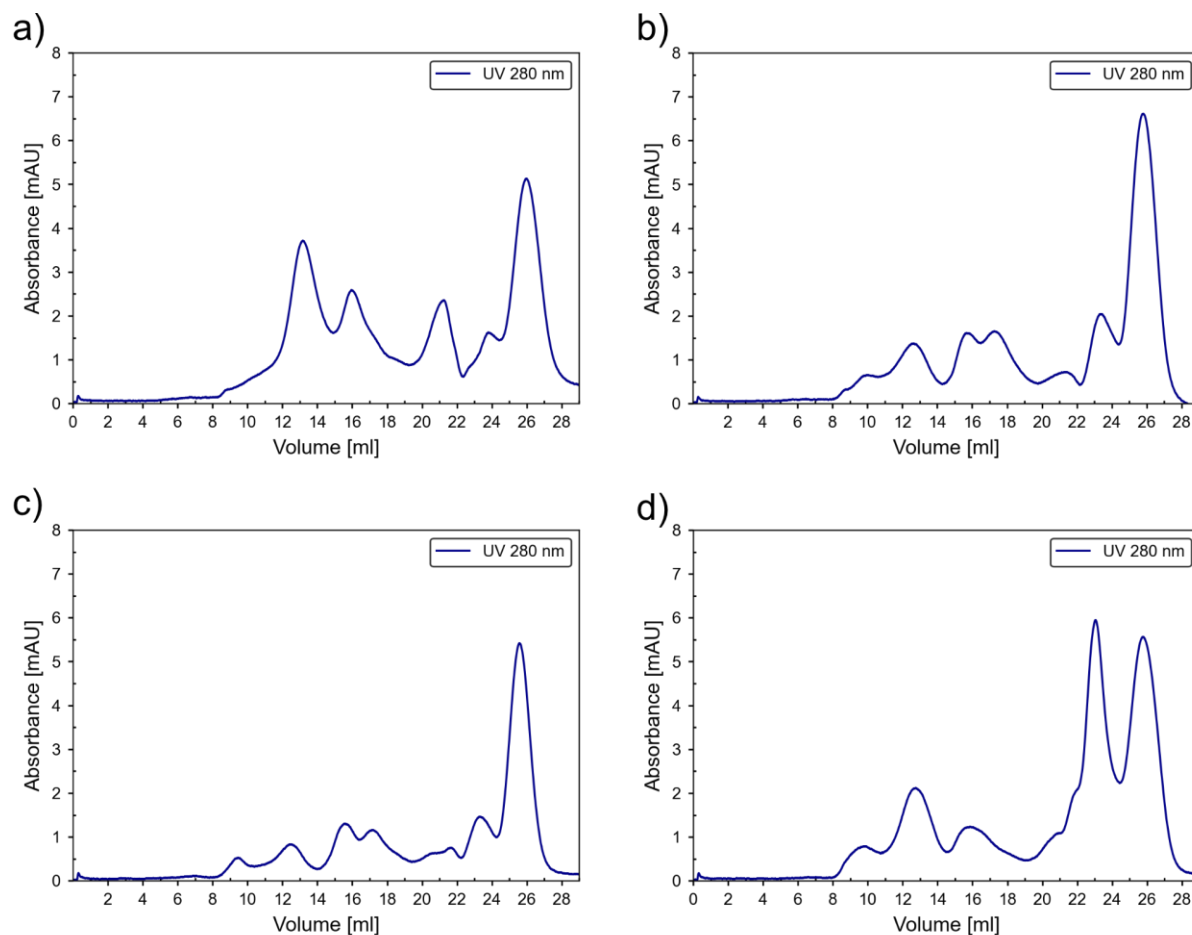


Figure 5.70: Size exclusion chromatograms of $T = 1$ state post reassembly in tris-buffer and 5 mM DTT with different NaCl concentrations. a) 0 M NaCl. b) 100 mM NaCl. c) 300 mM NaCl. d) 1 M NaCl. Absorbance was monitored at 280 nm (blue).

For the $T = 3$ state, post reassembly a prominent peak centered around ~ 13 mL, corresponding to $T = 1$ state, was observed in all chromatograms (Figure 5.71). A strong shoulder appeared at ~ 10 mL, corresponding to intact $T = 3$ cages. This peak was observed under all conditions and was most intense in the 300 mM NaCl buffer, indicating that intermediate salt favored efficient reassembly of $T = 3$ state. At higher elution volumes, only weak signals were observed. The aggregate peak at ~ 26 mL was consistently weak across all conditions.

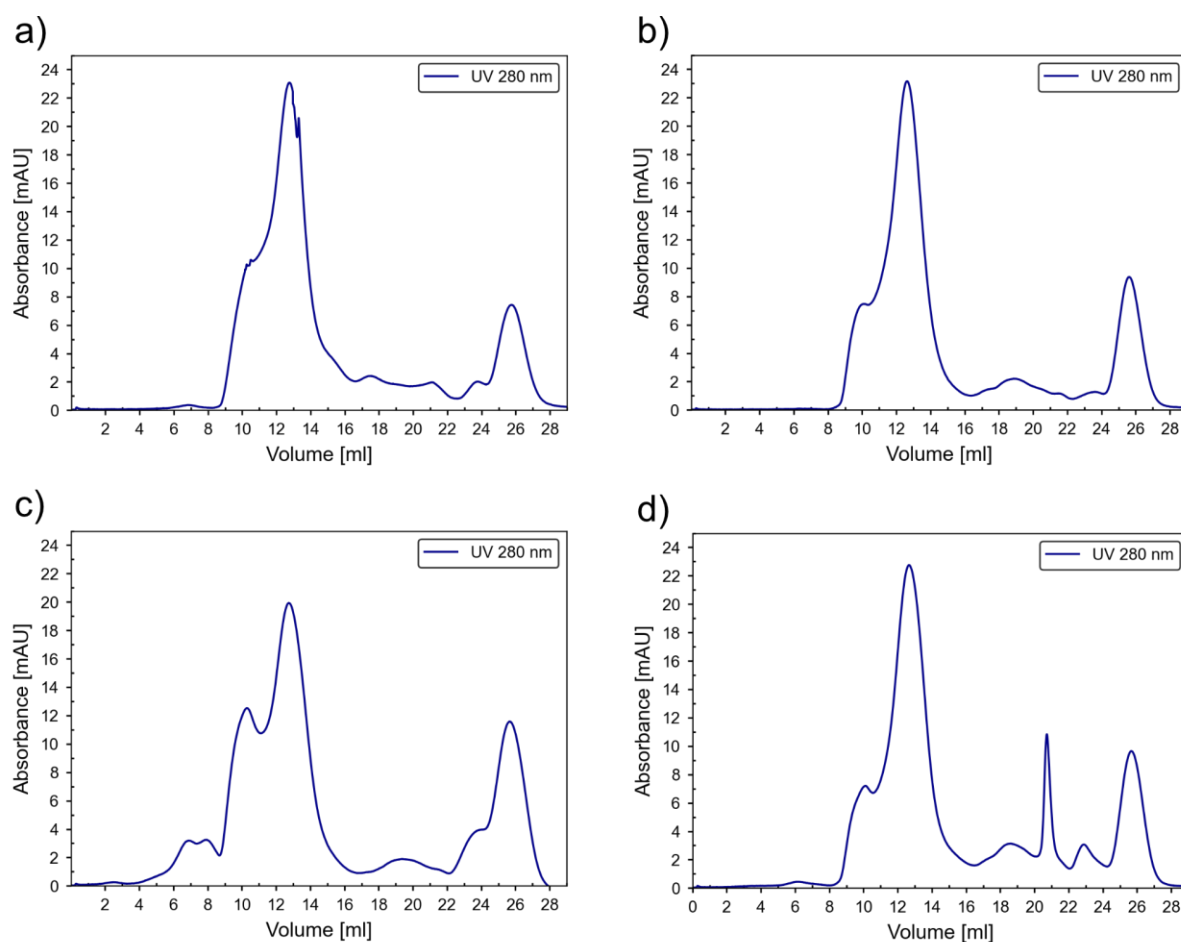


Figure 5.71: Size exclusion chromatograms of T = 3 state post reassembly in tris-buffer and 5 mM DTT with different NaCl concentrations. a) 0 M NaCl. b) 100 mM NaCl. c) 300 mM NaCl. d) 1 M NaCl. Absorbance was monitored at 280 nm (blue).

Together, these experiments demonstrated that T = 1 state reassembled inefficiently, forming aggregates across all conditions. While the T = 3 state reassembled reliably into intact cages, a prominent peak around 13 ml suggested that a substantial fraction reassembled into T = 1 like structures. NaCl concentration influenced the balance between cage formation, misassembly, and aggregation.

Following this, the influence of reducing agent concentration was investigated more systematically. DTT is often included during reassembly to prevent cysteine oxidation by formation of disulfide bonds, but excess reducing conditions can also interfere with disulfide-stabilized folding pathways. To assess this, a titration experiment was performed using T = 1 and T = 3 proteins. Samples were disassembled as before and reassembled in 50 mM tris, 300 mM NaCl, pH 7.5 with either no DTT, a molar equivalent of DTT per subunit (1 \times), or a fivefold molar excess (5 \times). The amount of DTT added was based on the known number of cysteine residues per subunit (calculations shown in table below in Table 5.9) DTT working concentrations were prepared from a 100 mM stock solution.

Table 5.9: Calculations for the amount of DTT used for the reassembly trials.

Sample	T = 1 state	T = 3 state
Amount (mg/ml)	0.8	0.4
Volume (ml)	1	1
Molarity (μM)	24.6	12.3
No. of cysteines	60	180
Molarity of cysteine (nM)	1.4	2.2
DTT (0 times)	9 ml buffer	9 ml buffer
DTT (1 times) (1.4 mM)	8.85 ml buffer + 0.15 ml DTT	8.85 ml buffer + 0.15 ml DTT
DTT (5 times) (7.2 mM)	8.25 ml buffer + 0.75 ml DTT	8.25 ml buffer + 0.75 ml DTT

To enable direct comparison between conditions, SEC chromatograms were normalized to total signal intensity. For the T = 1 state, normalization revealed a clear trend: in the absence of DTT, the cage peak at 13-15 mL dominated, whereas at 1 \times DTT the aggregate peak increased, and at 5 \times DTT the cage peak was barely detectable (Figure 5.72).

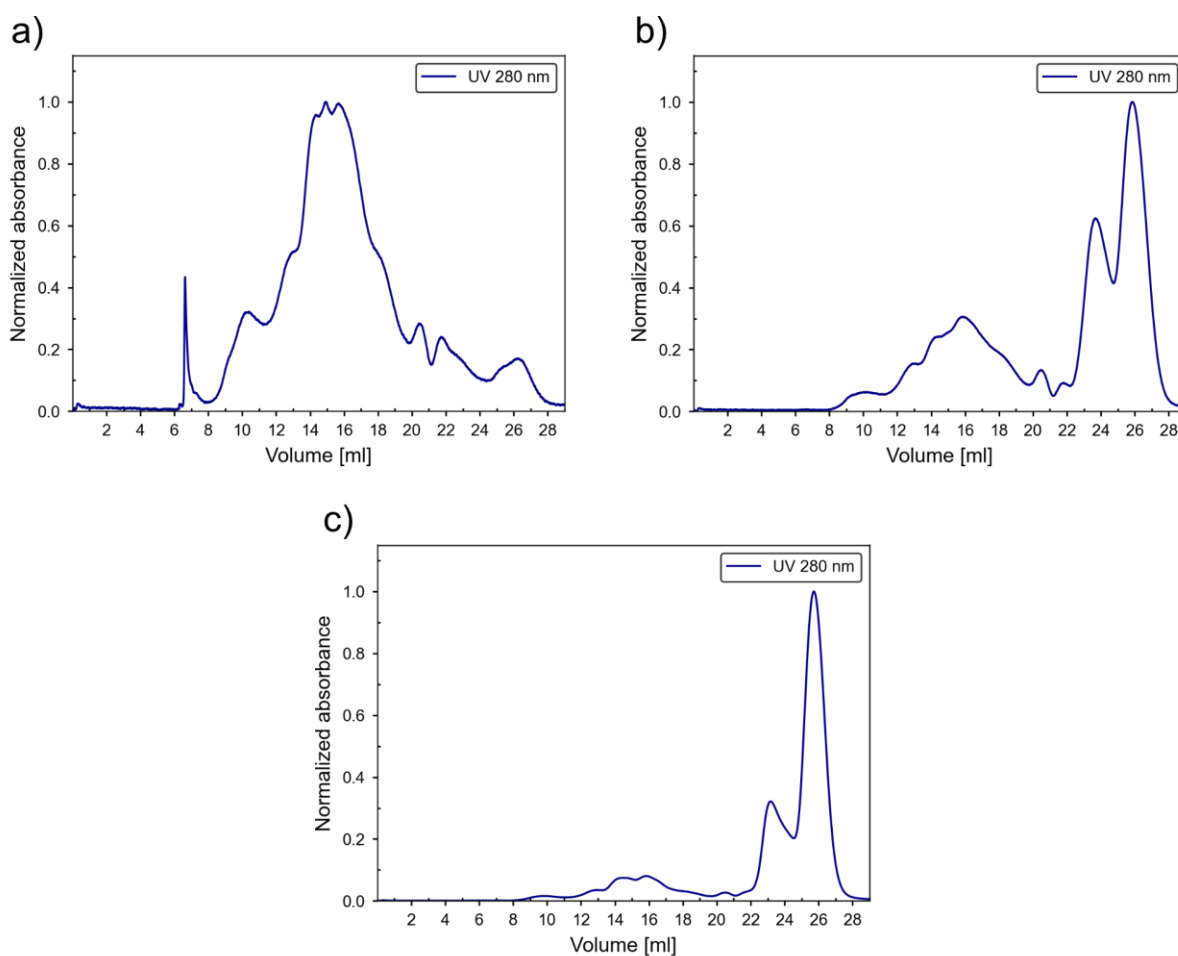


Figure 5.72: Size exclusion chromatograms of T = 1 state post reassembly in tris-buffer with DTT variation. a) 0 times DTT. b) 1 times DTT. c) 5 times DTT. Absorbance was monitored at 280 nm (blue).

These results indicated that reducing conditions should be carefully controlled during reassembly and that omitting DTT altogether produced the highest cage recovery for $T = 1$ under these conditions.

For the $T = 3$ state, reassembly without DTT produced a prominent peak around 10 mL, corresponding to intact $T = 3$ cages. When 1 \times DTT and 5 \times DTT were used, the aggregate peak increased, and the $T = 3$ cage peak diminished in intensity (Figure 5.73).

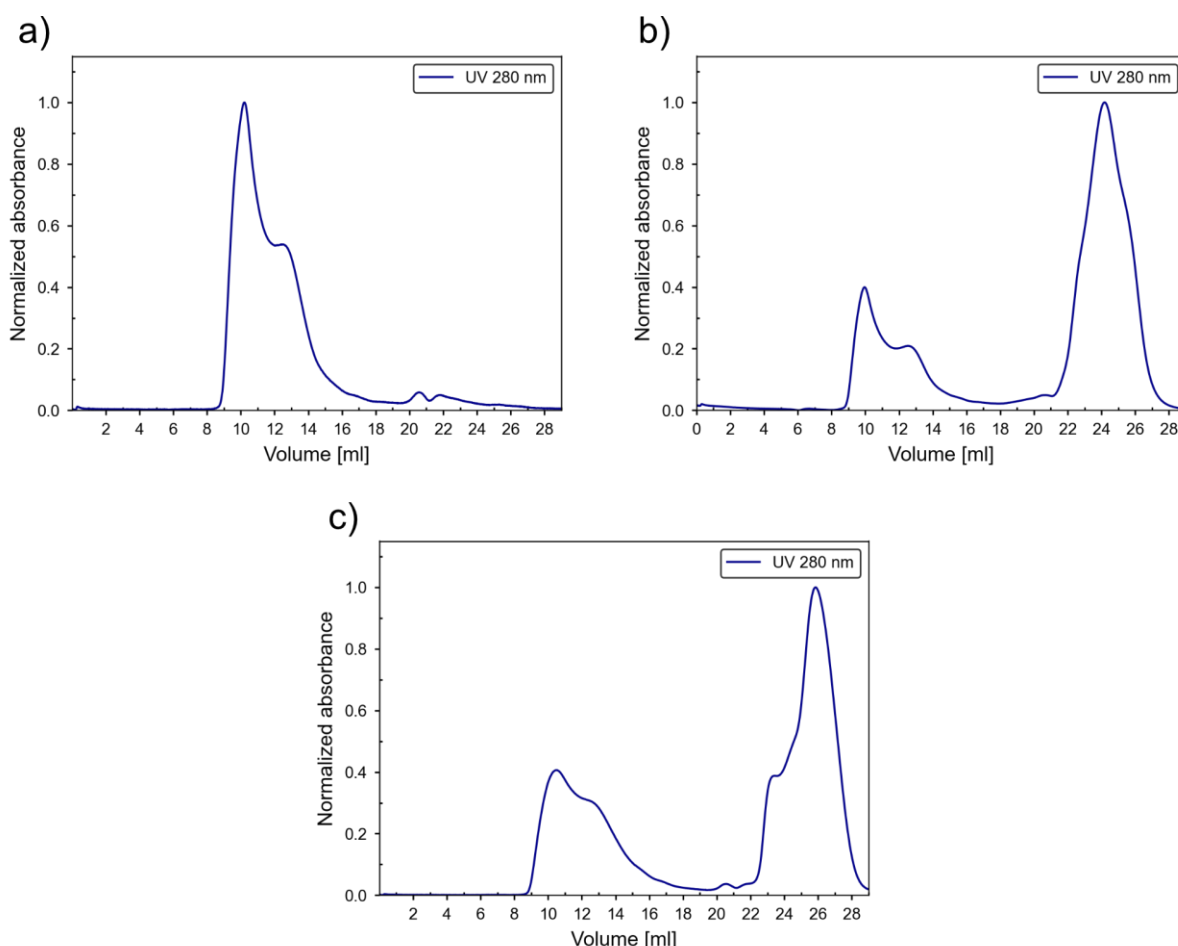


Figure 5.73: Size exclusion chromatograms of $T = 1$ state post reassembly in tris-buffer with DTT variation.

a) 0 times DTT. b) 1 times DTT. c) 5 times DTT. Absorbance was monitored at 280 nm (blue).

These results suggest that $T = 3$ reassembly is less sensitive to DTT concentration than $T = 1$, and that low to moderate DTT levels do not strongly disrupt cage formation.

In summary, extensive optimization was required to achieve reliable disassembly and reassembly of MxEnc. The most consistent outcomes were obtained using PEG precipitation followed by 8 M urea treatment and reassembly in tris buffer, though the efficiency and quality of cage recovery depended strongly on salt concentration. The following section compares these behaviors directly and considers their structural basis.

5.5.2 Comparison of T1 vs. T3 behavior

The systematic disassembly and reassembly trials revealed that the T = 1 and T = 3 states of MxEnc behave in markedly different ways under otherwise identical experimental conditions. While both states could be disrupted using chaotropic agents, their reassembly efficiencies, sensitivity to buffer conditions, and tolerance to redox environments diverged consistently.

A clear distinction was observed in response to denaturant identity. T = 1 state disassembled and reassembled most effectively when GuHCl was used, yielding a distinct cage peak after reassembly, whereas 8 M urea favored aggregation. In contrast, T = 3 reassembly was most successful in urea, producing a strong cage peak, while GuHCl treatment resulted in poor recovery. This suggests that the structural interfaces unique to each geometry respond differently to chaotropes: T = 1 state, composed entirely of pentamers, may be stabilized or destabilized differently compared to the mixed pentamer-hexamer interfaces of T = 3 state.

Buffer composition and ionic strength further emphasized these differences in reassembly behaviour between the two states. For the T = 1 state, a dominant aggregate peak at ~26 mL was observed under all conditions, while the T = 1 state-associated peak at ~13 mL was most pronounced at 0 M NaCl and progressively diminished with increasing salt concentration. A shoulder between 8–10 mL appeared only at 100 mM and 1 M NaCl, suggesting the formation of a minor T = 3-like population under high ionic strength. In contrast, T = 3 state consistently produced a strong shoulder at ~10 mL corresponding to intact cages, most intense at 300 mM NaCl, along with a prominent peak at ~13 mL indicative of T = 1-like structures. These findings highlight that ionic strength differentially modulates the reassembly landscape of the two states, influencing the balance between proper cage formation, misassembly, and aggregation.

The effect of redox conditions also differed between the two states. For T = 1, reassembly was highly sensitive to DTT concentration. In the absence of DTT, the strongest cage peaks were recovered, whereas increasing DTT progressively destabilized the cages and increased the subunit population. For T = 3 state, however, reassembly was less sensitive. A strong T = 3 peak was observed without DTT, and the peak intensity declined with 1x and 5x DTT. This suggests that while disulfide bonds formation may be critical for the T = 1 state, the T = 3 state possesses a comparatively better tolerance to reducing environments.

Overall, these experiments demonstrate that the two states of MxEnc, though structurally related, follow distinct assembly pathways. T = 1 state appears more fragile overall, with efficient reassembly only under carefully tuned conditions and strong sensitivity to reducing agents. T = 3 state, while more robust in terms of chaotrope tolerance and reassembly under intermediate salt, also displays structural heterogeneity, occasionally producing alternative

species not typical of its native state. These differences reflect the underlying architectural divergence between a purely pentameric assembly ($T = 1$ state) and a mixed pentamer-hexamer assembly ($T = 3$ state).

Because reproducible recovery of the $T = 3$ state could not be achieved starting from $T = 1$ state, most encapsulation experiments were carried out using the $T = 3$ state. In addition to its assembly robustness, the $T = 3$ state offers structural advantages due to its combination of pentameric and hexameric facets; the hexamers provide the geometric flexibility necessary to accommodate elongated cargo by enabling lateral expansion and cage elongation. Nevertheless, encapsulation trials were also attempted with $T = 1$ under conditions where partial reassembly was observed, to test whether the presence of cargo could stabilize cage formation.

5.5.3 Encapsulation of Cargo

In all encapsulation experiments, residual urea was removed after disassembly by threefold dilution with water and centrifugal concentration using a 10 kDa cutoff device, ensuring that reassembly proceeded in urea-free buffer compatible with AuNP stability.

The first encapsulation trials were carried out with the $T = 3$ state using MUTAB-coated AuNPs. Prior to encapsulation, the stability of MUTAB-coated AuNPs was assessed in 10 mM phosphate buffer (pH 7.0) with varying NaCl concentrations (0, 0.1, 0.3, and 1 M). The nanoparticles were only stable in 0.1 M NaCl, while precipitation occurred in all other salt conditions (Figure 5.74a). For comparison, CTAC-coated AuNPs were tested under the same buffer conditions, providing a reference for particle behavior under identical ionic environments. Based on this, 10 mM phosphate buffer with 0.1 M NaCl (pH 7.0) was selected for the first encapsulation trials. However, despite this optimization, the sample precipitated rapidly after reassembly, indicating that the combination of MUTAB-coated particles and phosphate buffer did not support stable encapsulation (Figure 5.74b).

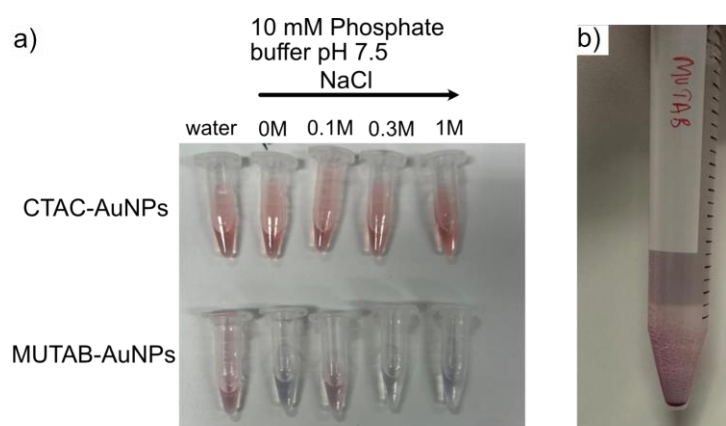


Figure 5.74: Stability of coated AuNPs in phosphate buffer and outcome of an encapsulation attempt. a) CTAC-coated (top row) and MUTAB-coated (bottom row) AuNPs in phosphate buffer at different salt concentrations. b) Encapsulation trial with MUTAB-coated AuNPs showing precipitated (“crashed-out”) particles.

Since MUTAB-coated particles precipitated under the chosen conditions, the next trials were carried out using CLP-functionalized gold nanoparticles. Stability tests in 10 mM phosphate buffer (pH 7.0) with 0.1 M and 0.3 M NaCl showed that CLP-coated particles remained well dispersed under both conditions, with no visible aggregation (Figure 5.75a). This provided a more promising basis for encapsulation. The overall encapsulation workflow is illustrated schematically in Figure 5.75b.

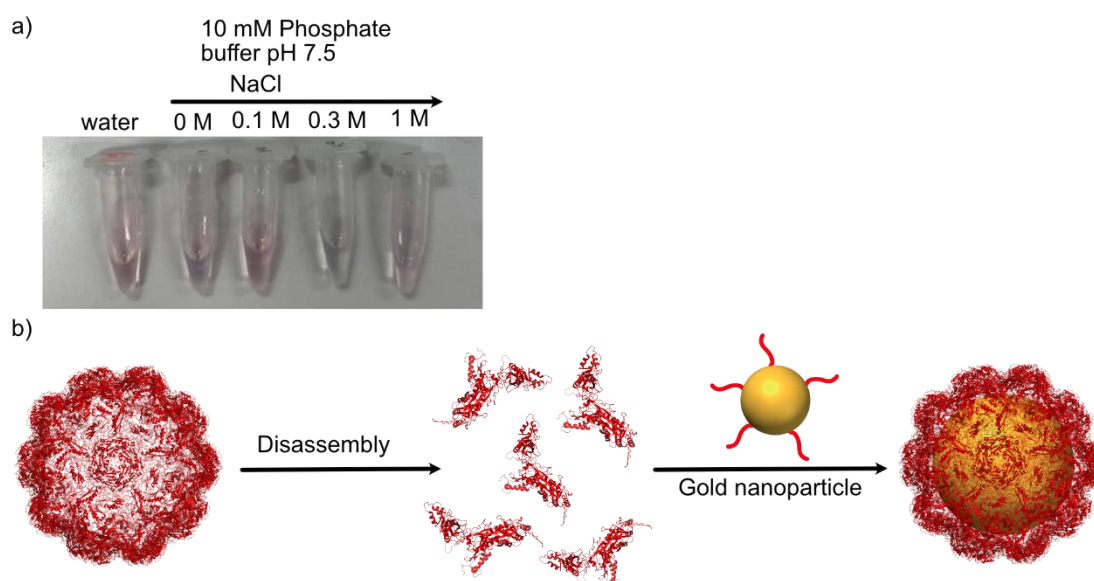


Figure 5.75: Stability of CLP-functionalized AuNPs in phosphate buffer and schematic illustration of encapsulation of gold nanoparticle in *M. xanthus* encapsulin (PDB : 4PT2). a) CLP-functionalized AuNPs in phosphate buffer at different salt concentrations. b) MxEnc is first disassembled and then added to Reassembly buffer containing CLP functionalized gold nanoparticles.

Protein cages were disassembled, freed of urea by dilution and centrifugal concentration, and then reassembled in the presence of CLP-AuNPs. Reassembly reactions were performed in

the same phosphate buffer at 0.1 M and 0.3 M NaCl, and the resulting samples were characterized by IEC and SEC.

IEC chromatograms showed clear absorbance signals at 280 nm (protein), 260 nm (nucleic acids), and 526 nm (AuNPs). All three signals co-eluted at ~46 mS/cm, consistent with the protein fraction, suggesting association of AuNPs with encapsulin (Figure 5.76a,b) Following IEC, the eluted fraction was concentrated and analyzed by SEC. A weak absorbance at 526 nm was observed in the 8-10 mL elution range, corresponding to the T = 3 state (Figure 5.76c,d). This overlap confirmed the presence of AuNPs within or tightly associated with the cages. Notably, the absorbance intensity was higher in the 0.3 M NaCl condition than in 100 mM, suggesting improved encapsulation or enhanced stability at the higher ionic strength.

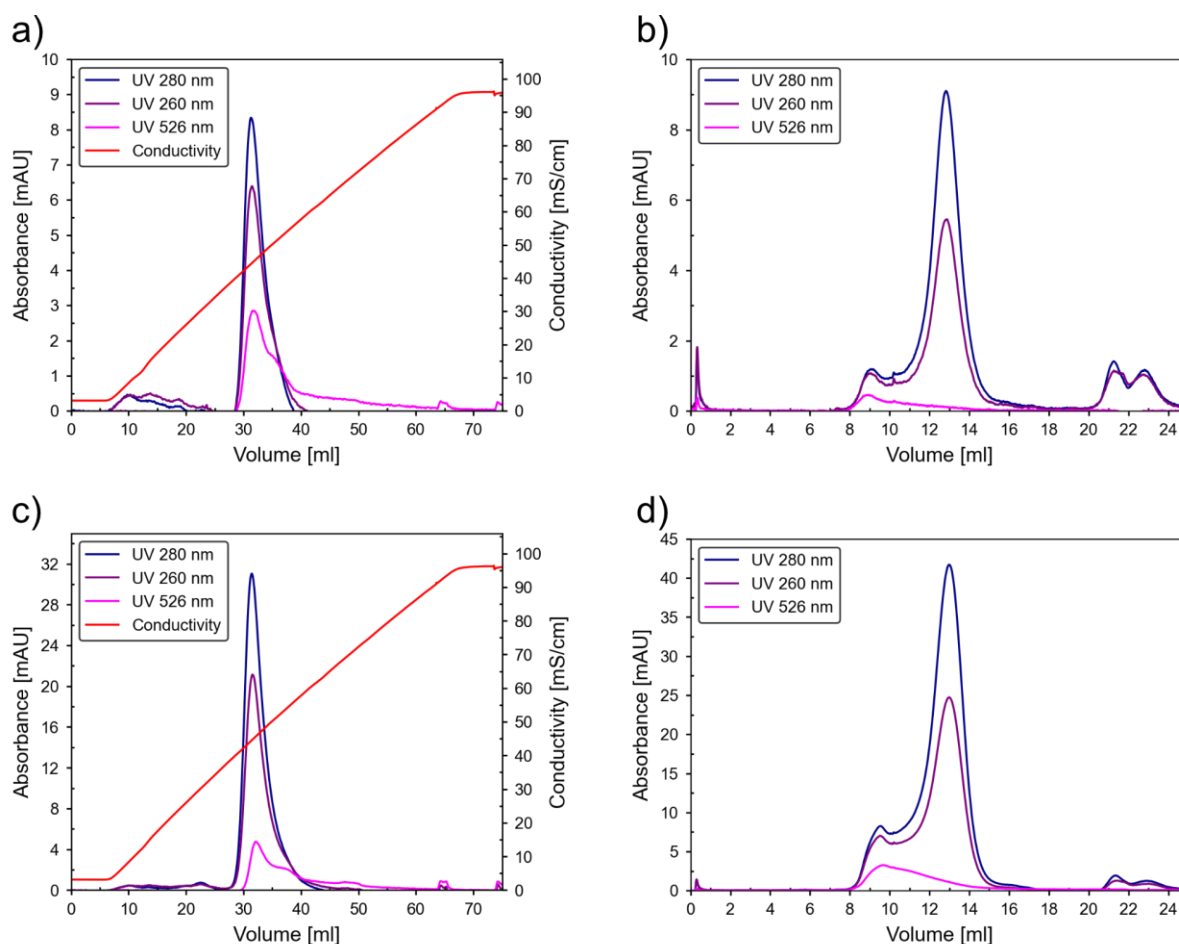


Figure 5.76: Ion-exchange and size-exclusion chromatograms of AuNP-loaded MxEnc in phosphate buffer at two NaCl concentrations. a) IEC, 100 mM NaCl. b) SEC, 100 mM NaCl. c) IEC, 300 mM NaCl. d) SEC, 300 mM NaCl. Absorbance was monitored at 280 nm (blue), 260 nm (purple) and 526 nm (magenta). Conductivity is shown in red.

Post-SEC fractions were concentrated using a 100 kDa cutoff concentrator and subjected to stained TEM analysis (Figure 5.77) Only a few AuNPs were observed within the cages,

indicating that encapsulation efficiency was very low. Most cages appeared empty, suggesting that loading was infrequent under the tested conditions. Increasing the nanoparticle-to-protein ratio was identified as a possible strategy to improve encapsulation, ensuring that an excess of cargo was available during reassembly.

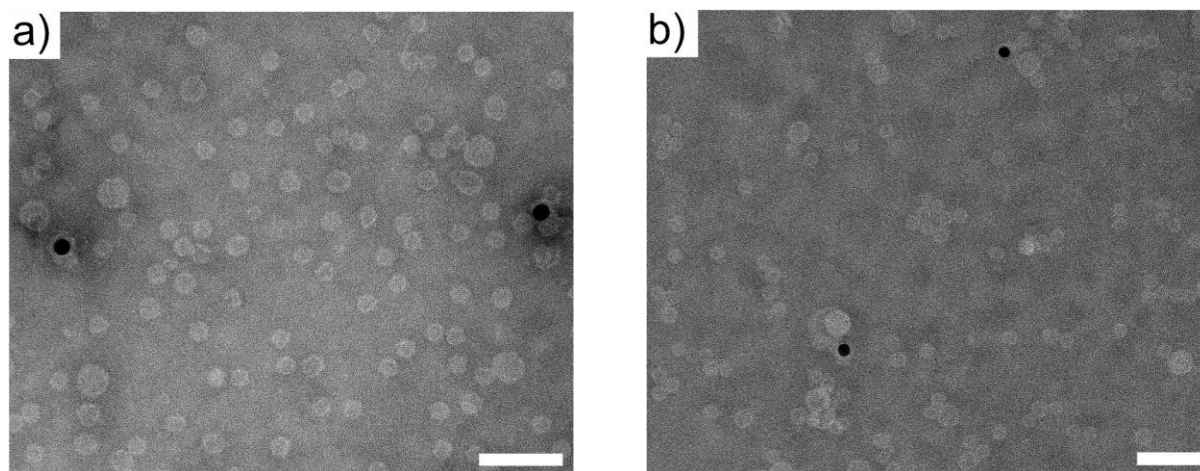


Figure 5.77: Stained TEM images of the sample after SEC. a) 0.1 M salt b) 0.3 M salt

To test reproducibility and improve encapsulation efficiency the experiments were repeated with increased concentration of AuNPs. Because phosphate buffer had shown poor reproducibility and was biased toward $T = 1$ reassembly in earlier trials, subsequent encapsulation experiments were carried out in 20 mM tris buffer, pH 7.5 with 0.1 M NaCl, which had been established as favorable for $T = 3$ recovery. However, the outcomes varied markedly between salt conditions (Figure 5.78). The 0.3 M NaCl condition, which had initially given promising results, failed to reproduce the same outcome upon repetition (Figure 5.78b). Although no visible aggregation was observed, IEC in these trials showed no detectable absorbance at 526 nm at the expected conductivity. Since the 526 nm wavelength is characteristic of the surface plasmon resonance of gold nanoparticles, its absence indicates that the AuNPs were not associated with the protein fraction. This discrepancy was particularly striking given the earlier trial, where a clear 526 nm signal co-eluted with protein, suggesting at least partial encapsulation or strong interaction. The loss of this signal in the repeated experiment points to a failure of encapsulation under otherwise identical conditions. In contrast, the 0.1 M NaCl condition consistently gave better results. IEC showed a sharp peak eluting at the expected conductivity.

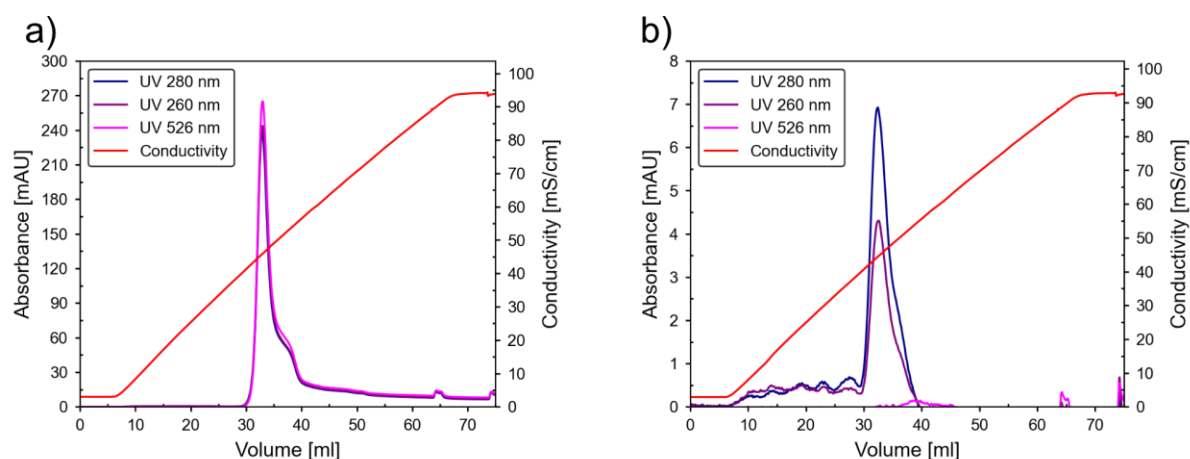


Figure 5.78: Ion exchange chromatograms of AuNP-loaded MxEnc in tris buffer at two NaCl concentrations. a) 0.1 M NaCl. b) 0.3 M NaCl. Absorbance was monitored at 280 nm (blue), 260 nm (purple) and 526 nm (magenta). Conductivity is in red.

Subsequent SEC for the 0.1 M NaCl condition revealed a distinct absorbance at 526 nm in the 8-10 mL elution range, consistent with AuNPs encapsulated in the T = 3 state. However, the peak was broad and extended up to ~16 mL, suggesting incomplete separation between particle-loaded cages and empty cages of other sizes (Figure 5.79). Notably, the absorbance intensity decreased markedly between IEC and SEC, dropping from ~270 mAU in IEC to ~22 mAU in SEC. This reduction likely reflects both sample dilution during fractionation and material loss, as some of the sample was observed to become trapped in the filter during post-IEC concentration. Stained TEM analysis confirmed the presence of AuNPs within T = 3 cages, along with additional protein cages of other sizes (Figure 5.79b).

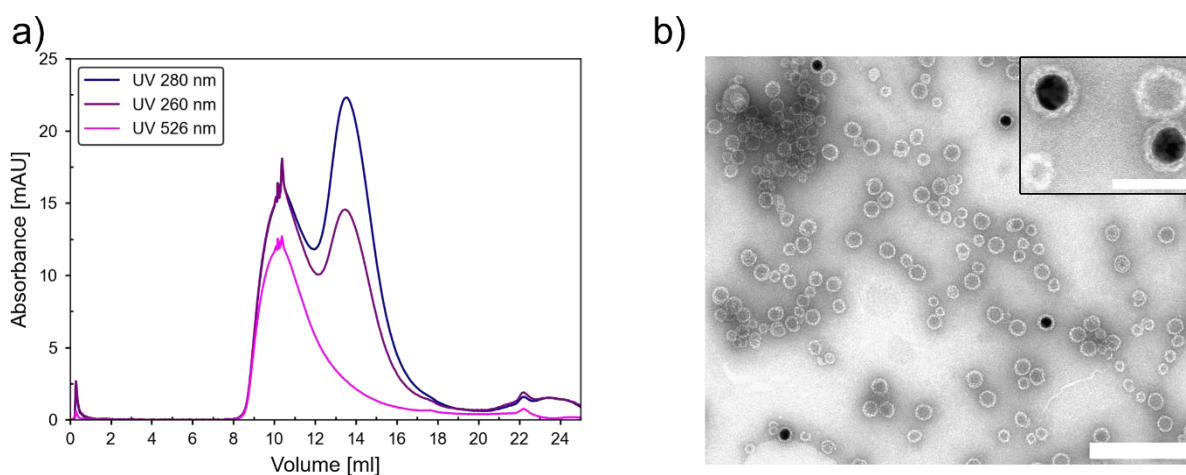


Figure 5.79: Size exclusion chromatogram and stained TEM of AuNP-loaded MxEnc in tris buffer with 0.1 M NaCl. a) SEC. Absorbance was monitored at 280 nm (blue), 260 nm (purple) and 526 nm (magenta). b) Stained TEM images showing encapsulation. Scale bar is 200 nm. Inset showing magnified view. Scale bar is 50 nm.

To further improve separation between encapsulated and empty cages, a second SEC was performed using fractions collected from the first run. The fraction corresponding to the early

eluting peak (~9 mL) was reloaded onto the column. The chromatogram showed a dominant peak at ~9 mL, but with a noticeable tail extending up to 14 mL (Figure 5.80a) The later-eluting fraction (~14 mL) was also re-analyzed by SEC (Figure 5.80b) This sample produced an intense peak centered at 14 mL, but also showed a secondary peak in the 8-10 mL region.

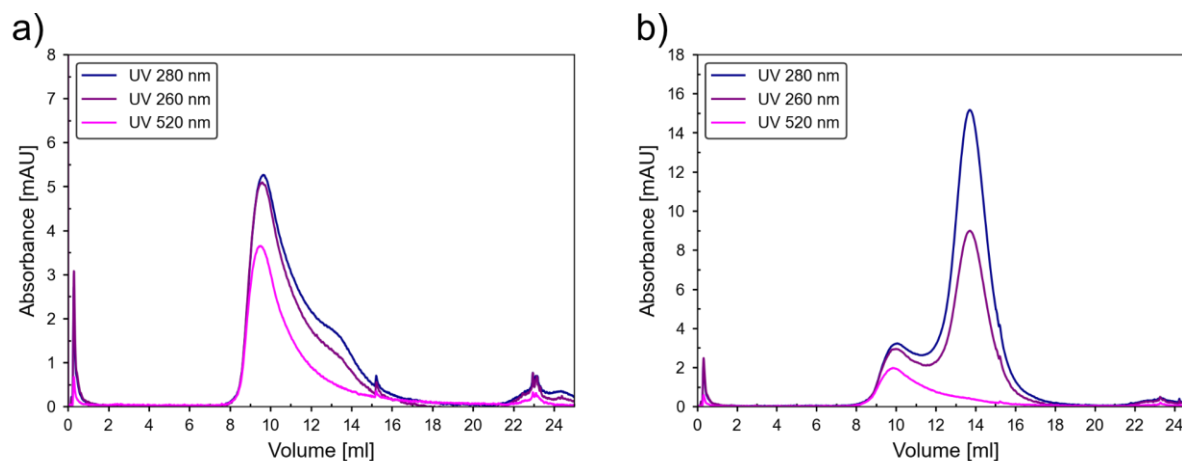


Figure 5.80: Size exclusion chromatograms of AuNP-loaded MxEnc. a) SEC. Absorbance was monitored at 280 nm (blue), 260 nm (purple) and 520 nm (magenta).

Stained TEM, as shown in Figure 5.81, was done on pooled SEC fractions collected as fraction 6 (8-9 mL), fraction 7 (10-11 mL), fraction 8 (12-13 mL), and fraction 9 (14-15 mL). All pools showed a heterogeneous population dominated by $T = 1$ -sized cages with a smaller subset of $T = 3$ cages. The relative proportion of $T = 3$ particles was highest in the earlier fractions (fraction 6-7) and decreased with elution volume, as expected for size-exclusion behavior. A fraction of the $T = 3$ cages contained AuNPs, confirming successful loading (Figure 5.81b). Despite enrichment along the peak, the overlap between $T = 1$ and $T = 3$ populations persisted across adjacent fractions, indicating that under these conditions SEC did not fully resolve the two assembly states.

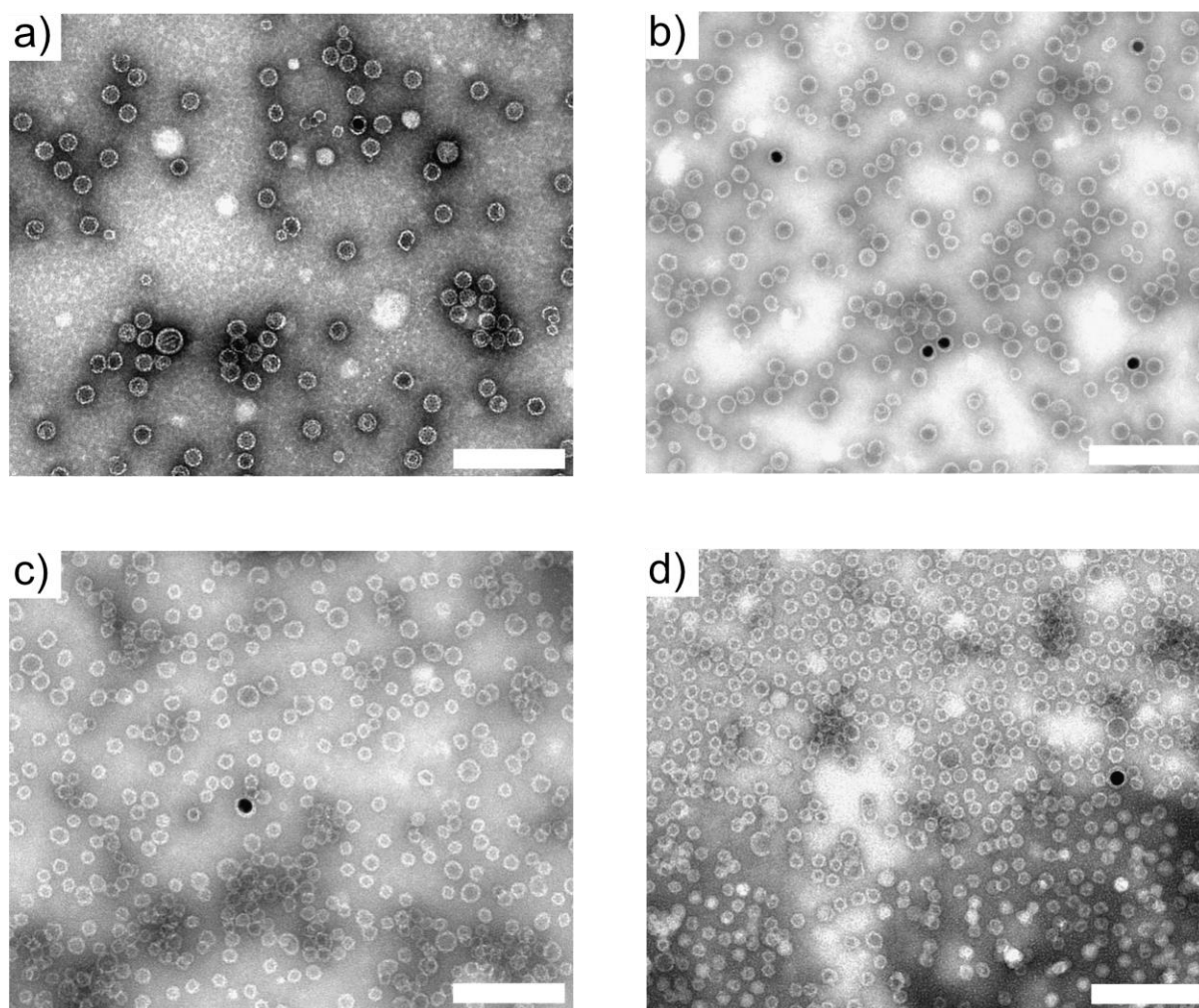


Figure 5.81: Stained TEM images of different fractions collected post second SEC. a) FPLC tube 6 (8-9 mL on the chromatogram). b) tube 7 (10-11 mL). c) tube 8 (12-13 mL). d) tube 9 (14-15 mL). Scale bar is 200 nm.

Overall, these trials demonstrate that while encapsulation of AuNPs within $T = 3$ cages is achievable under carefully selected conditions, the process remains inefficient and poorly reproducible. Phosphate buffer with MUTAB-coated particles did not support encapsulation, while CLP-functionalized particles in phosphate buffer gave only weak and inconsistent signals. Tris buffer with 0.1 M NaCl provided clearer evidence of encapsulation, but SEC and TEM revealed coexisting $T = 1$ and $T = 3$ assemblies, significant sample loss, and low loading efficiency. The persistence of heterogeneous populations and the incomplete resolution of particle-loaded versus empty cages highlight the need for further optimization. Future efforts will require tighter control over buffer composition, salt concentration, and nanoparticle-to-protein ratios to enhance reproducibility and improve encapsulation efficiency. This will be discussed later.

Encapsulation trials with $T = 1$ state

Encapsulation trials were also attempted with the $T = 1$ state using CLP-coated AuNPs in 20 mM tris buffer, pH 7.5 with 100 mM M NaCl (Figure 5.82) The protein-nanoparticle mixture remained stable in solution; however, IEC analysis showed only a very weak absorbance at 526 nm, indicating negligible association of particles with protein and ruling out encapsulation under these conditions. To test whether any $T = 3$ state was present, the sample was analyzed by SEC. The chromatogram showed an intense peak at ~ 17 mL corresponding to smaller species, with only a very weak signal at ~ 14 mL consistent with $T = 1$ particles. Stained TEM analysis was inconclusive and did not provide clear evidence of encapsulation. In contrast, as seen above, under the same buffer conditions, $T = 3$ assemblies supported at least partial encapsulation of CLP-coated AuNPs, highlighting that $T = 3$ cages provide a more favorable scaffold for loading than $T = 1$.

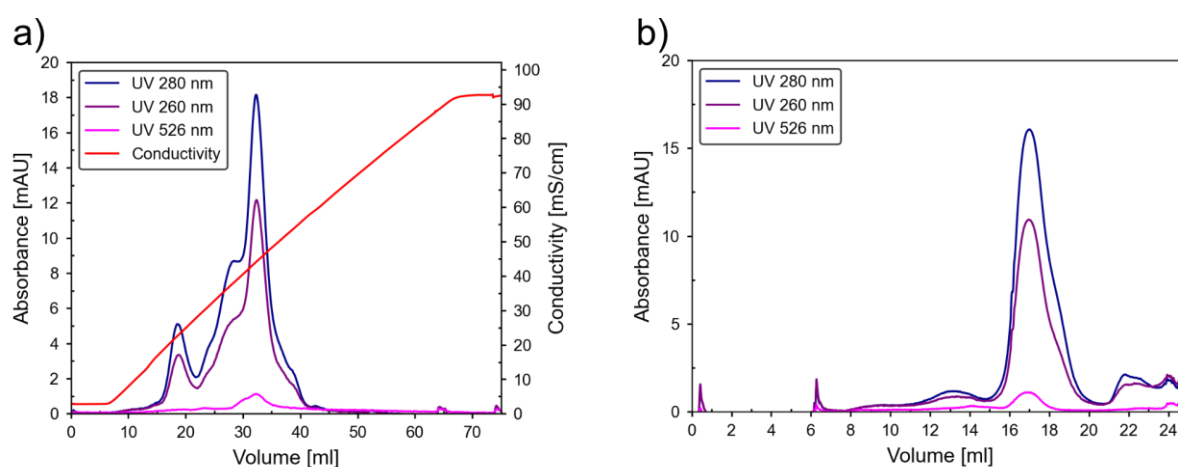


Figure 5.82: Ion-exchange and size-exclusion chromatograms of AuNPs and $T = 1$ state of MxEnc. a) IEC. b) SEC. Absorbance was monitored at 280 nm (blue), 260 nm (purple) and 526 nm (magenta). Conductivity is shown in red.

Encapsulation trials with AuNRs and $T = 3$ state

To explore the encapsulation of anisotropic cargo, AuNRs were also tested. CLP-functionalized AuNRs were incubated with the disassembled $T = 3$ state in 20 mM tris buffer, pH 7.5 with 100 mM NaCl. IEC chromatograms showed an intense peak at 685 nm overlapping with the protein absorbance signal, consistent with initial co-elution of AuNRs and encapsulin (Figure 5.83a). However, subsequent SEC analysis did not show a corresponding 685 nm absorbance in the elution range of cages. Instead, the chromatogram displayed peaks corresponding to $T = 3$ (~ 9 mL) and $T = 1$ (~ 13 mL) assemblies, but without a detectable rod signal in either fraction (Figure 5.83b). Stained TEM analysis confirmed this result: protein cages and aggregates were visible, while AuNRs remained dispersed and stable in solution but unencapsulated (see Appendix, Figure 8.18). Together, these data indicate that although

AuNRs associate with protein during IEC, they are not stably retained within the cages, and instead persist as free rods in the presence of encapsulin. This outcome contrasts with spherical AuNPs, where at least partial encapsulation within $T = 3$ cages was observed under the same buffer conditions, suggesting that article geometry plays a critical role in determining encapsulation efficiency.

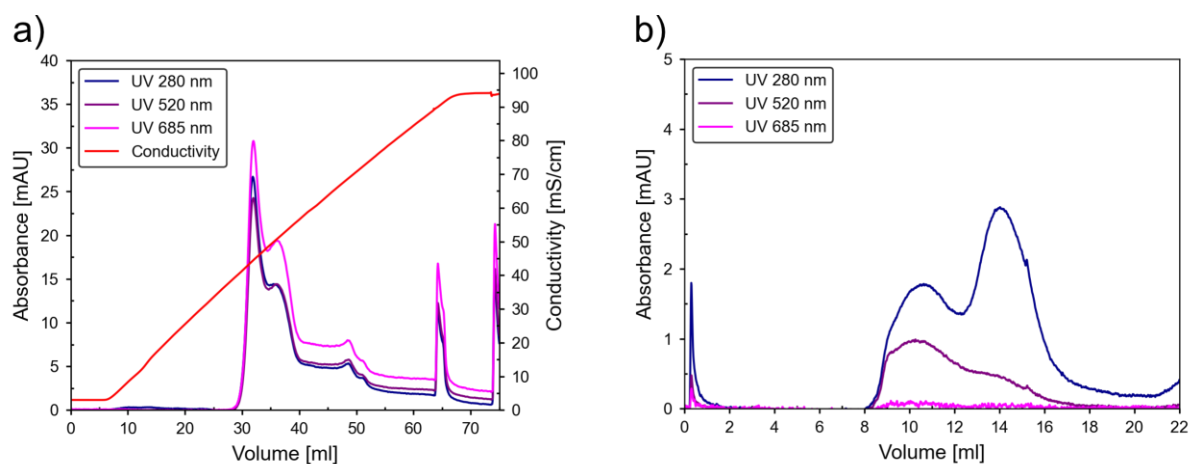


Figure 5.83: Ion-exchange and size-exclusion chromatograms of AuNRs and $T = 3$ state of MxEnc. a) IEC. b) SEC. Absorbance was monitored at 280 nm (blue), 520 nm (purple) and 685 nm (magenta). Conductivity is shown in red.

Role of Cargo in $T = 3$ Reassembly

Finally, to test whether the presence of cargo itself promoted reassembly into the $T = 3$ state, a control experiment was performed under identical conditions but without AuNPs. SEC analysis revealed that compared to the control, the presence of cargo modestly increased the $T = 3$ peak (Figure 5.84a); however, the $T = 1$ peak remained dominant. This observation contrasts with previous reports that cargo promotes preferential formation of the $T = 3$ state.^[13] Instead, the data indicate that additional factors, such as buffer composition, ionic strength, or intrinsic cage stability may play a more decisive role in determining the outcome of reassembly.

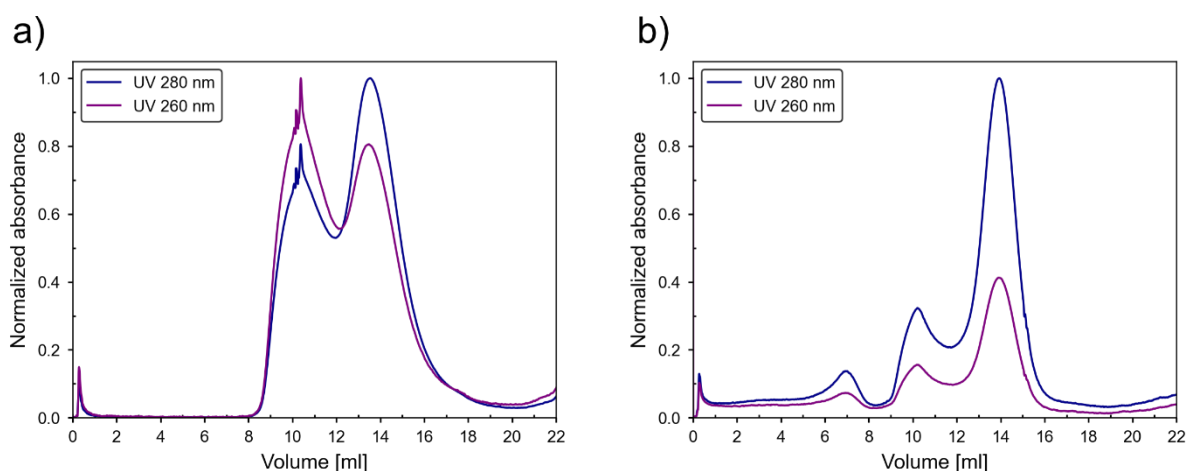


Figure 5.84: Size-exclusion chromatograms of encapsulation and control experiment. a) SEC of encapsulated sample. b) SEC of control sample. Absorbance was monitored at 280 nm (blue), 260 nm (purple).

The outcomes of these experiments highlighted that reassembly into $T = 1$ or $T = 3$ state is not governed by cargo alone. To explore this further, systematic experiments were designed to identify the underlying driving forces that bias reassembly toward either $T = 1$ or $T = 3$. This will be discussed in next section.

5.5.4 Mechanistic Insights into *M. xanthus* Encapsulin Reassembly

The influence of buffer identity, ionic strength, and solution parameters on reassembly of *M. xanthus* was examined. The aim was to clarify the mechanistic basis of encapsulin assembly as well as to identify conditions that could be optimized to enhance encapsulation efficiency. A schematic is shown in Figure 5.85.

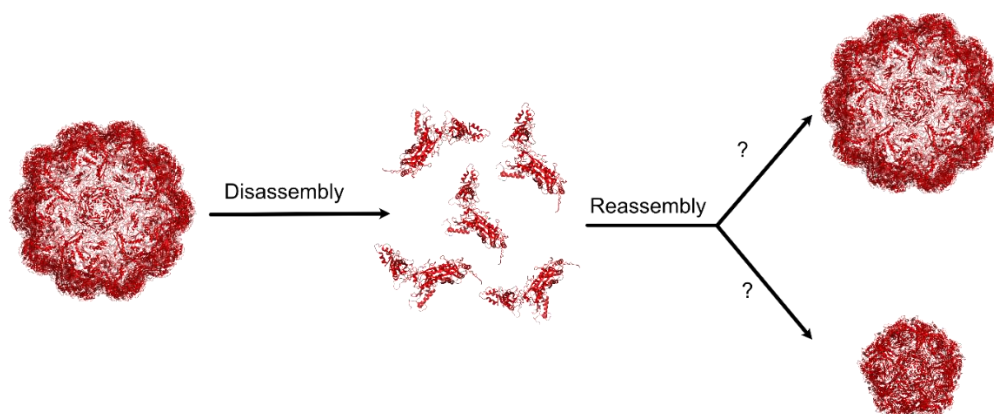


Figure 5.85: Schematic illustration of disassembly of *M. xanthus* encapsulin and reassembly into different states. MxEnc was disassembled and reassembly was triggered by altering buffer conditions, salt concentration and dilution factors (PDB: 4PT2 for $T = 3$; PDB:7S21 for $T = 1$).

Encapsulins were first disassembled by PEG precipitation followed by incubation in 1 mL of 8 M urea for 3 h at 4 °C. DLS confirmed efficient disassembly, showing a dominant peak at

small diameters consistent with subunits (Figure 5.86a). For reassembly, the disassembled protein solution was diluted tenfold with 20 mM tris buffer, pH 7.5 and concentrated back using a 10 kDa cutoff concentrator, thereby removing residual urea. DLS of the concentrated sample revealed a strong peak corresponding to the hydrodynamic diameter of the T = 3 state, indicating successful reassembly (Figure 5.86a). Post-reassembly SEC was carried out using a Superose S6 Increase. SEC chromatogram showed an intense peak at ~9 mL consistent with T = 3 particles, accompanied by a minor shoulder at ~13 mL corresponding to T = 1 (Figure 5.86b). Stained TEM of the reassembled fraction revealed a uniform population of particles with diameters matching the T = 3 state and T = 1 state (Figure 5.86c,d). These images serve as structural benchmarks for subsequent experiments, where direct TEM analysis was not performed.

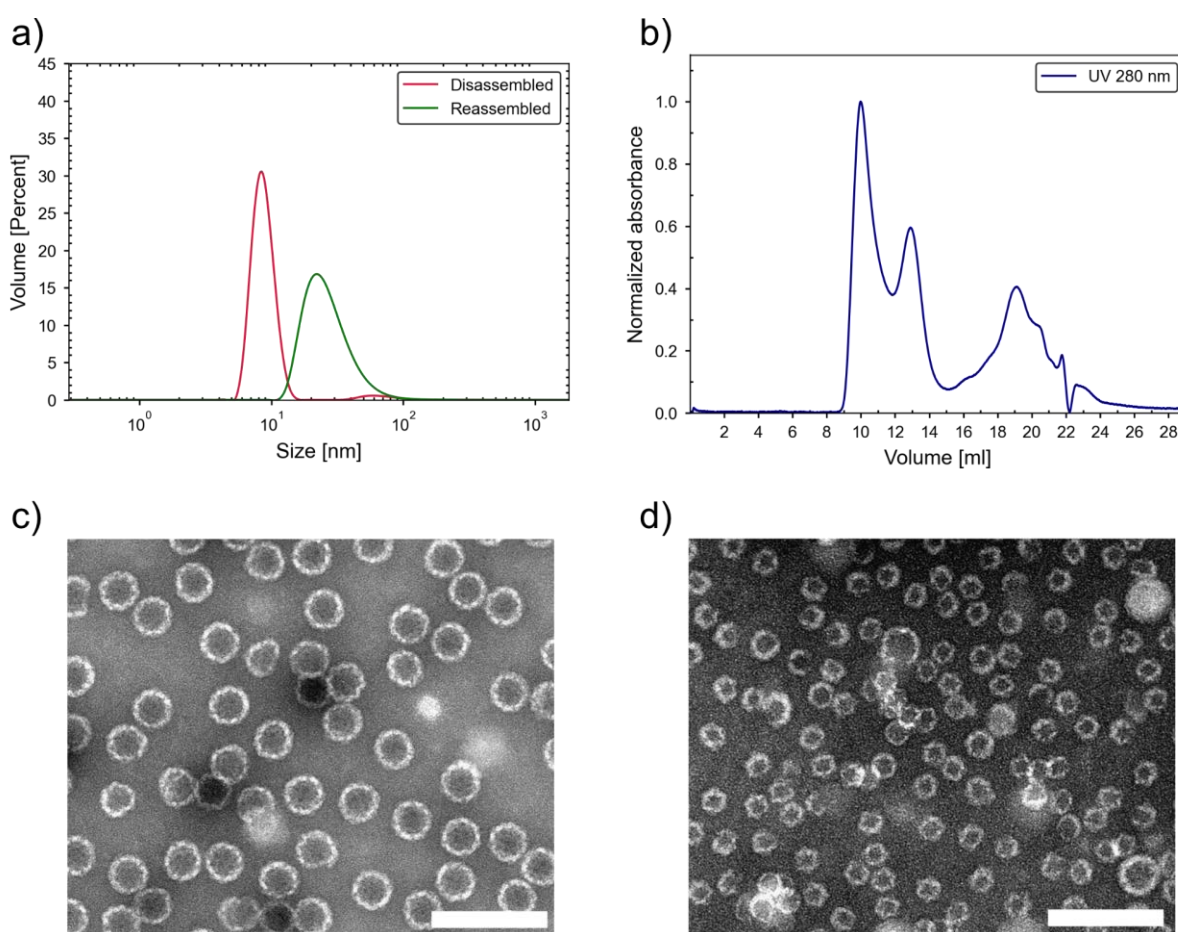


Figure 5.86: Hydrodynamic diameter distributions, normalized size-exclusion chromatogram and stained TEM images of reassembled T = 3 state of MxEnc. Reassembly was performed by a tenfold dilution into reassembly buffer followed by reconcentration to the initial concentration. a) DLS of disassembled (red) and reassembled (green) protein. b) SEC of the reassembled sample. Absorbance was monitored at 280 nm (blue). c) Negative-stain TEM of the ~9 mL peak, showing predominantly intact T = 3 state. d) Negative-stain TEM of the ~13 mL shoulder, enriched in T = 1 assemblies. Scale bars is 100 nm.

When the same protocol was repeated with fivefold dilution into tris buffer, DLS again indicated recovery of the $T = 3$ state. However, SEC showed a different outcome: the profile was dominated by an intense subunit peak at ~ 20 mL, with additional peaks at ~ 9 mL ($T = 3$) and ~ 13 mL ($T = 1$), indicating only partial reassembly into higher-order structures (Figure 5.87).

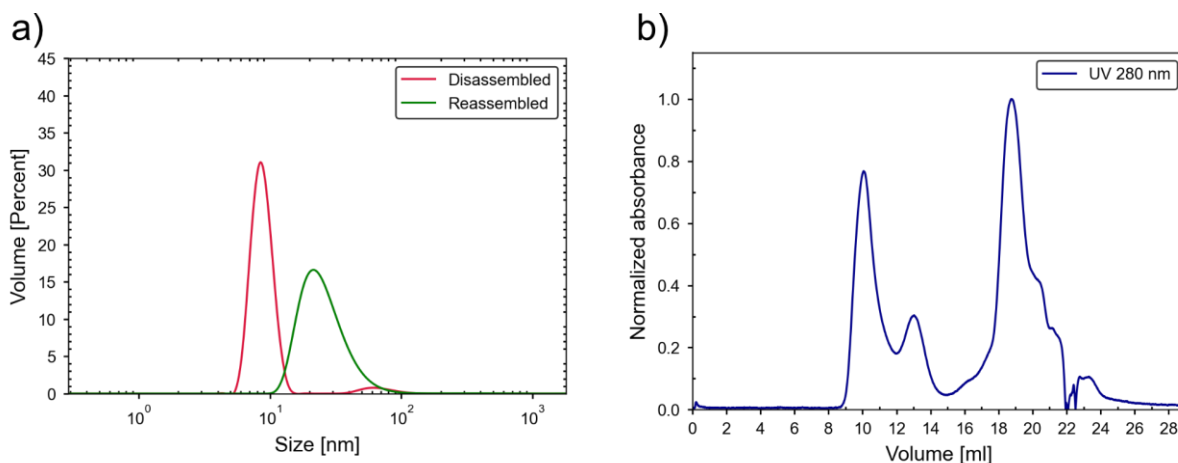


Figure 5.87: Hydrodynamic diameter distributions and normalized size-exclusion chromatogram of reassembled $T = 3$ state of MxEnc. Reassembly was performed by a fivefold dilution into reassembly buffer followed by reconcentration to the initial concentration. a) DLS of disassembled (red) and reassembled (green) protein. b) SEC of the reassembled sample. Absorbance was monitored at 280 nm (blue).

To test whether buffer components were essential for reassembly, the disassembled protein was diluted fivefold into pure water and concentrated using a 10 kDa cutoff concentrator. DLS of the resulting sample showed a dominant peak at small diameters, consistent with subunits (Figure 5.88). Upon subsequent incubation, the DLS profile shifted dramatically, revealing broad peaks at large hydrodynamic diameters consistent with aggregation rather than ordered cage reformation. These results highlight that reassembly into higher-order states does not occur in the absence of buffering ions, and that the destabilized subunits are prone to non-productive aggregation when lacking stabilizing solution components.

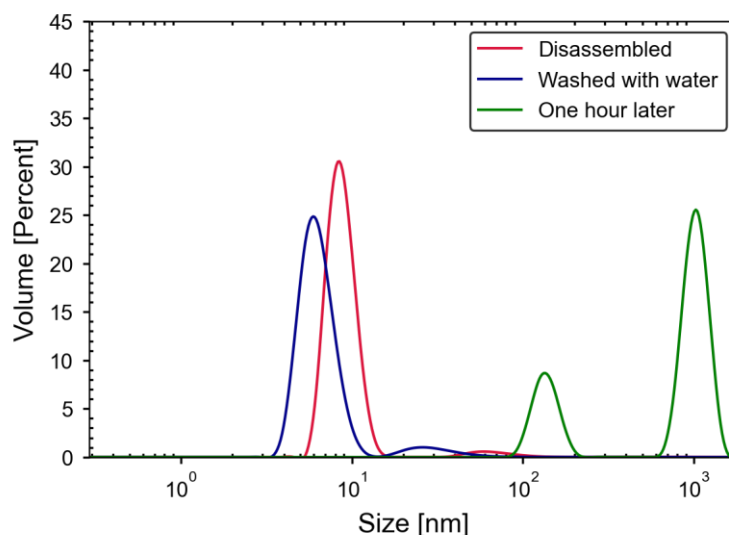


Figure 5.88: Hydrodynamic diameter distributions of the T = 3 state of MxEnc during reassembly by fivefold dilution with water and reconcentration to the initial concentration. DLS of disassembled (red), immediately after fivefold dilution with water followed by reconcentration to the initial concentration (blue), and after 1 h incubation (green).

To systematically examine the effect of buffer identity, two systems were chosen for comparison: 20 mM tris buffer, pH 7.5 with 100 mM NaCl and 20 mM phosphate buffer, pH 7.0 with 100 mM NaCl. Tris was selected because it supported empty-cage reassembly in earlier trials, serving as a benchmark for T = 3 recovery. Phosphate was chosen to reflect encapsulation conditions, enabling direct comparison between mechanistic reassembly and encapsulation performance.

In the first comparison, disassembled protein was diluted fivefold with water, concentrated to 1 mL, and then diluted fivefold with either tris or phosphate buffer before reconcentration. In tris buffer, the primary SEC peak eluted at ~9 mL, consistent with T = 3 particles, though the peak was broad and tailed to ~17 mL. In phosphate buffer, the dominant feature was a subunit peak at ~20 mL, accompanied by a distinct peak at ~13 mL corresponding to T = 1 and broad species eluting between 6-9 mL consistent with aggregates (Figure 5.89).

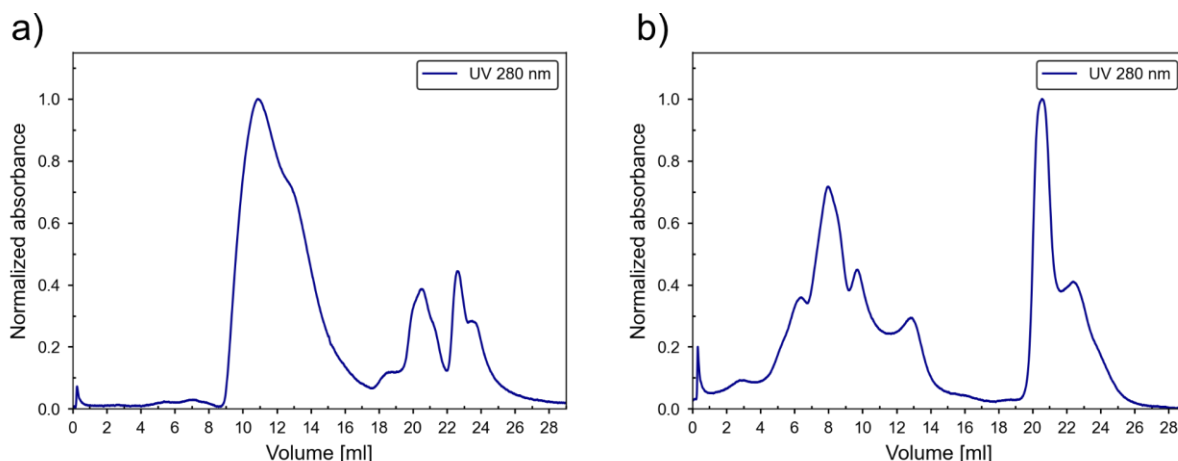


Figure 5.89: Normalized size-exclusion chromatograms of the T = 3 state of MxEnc after urea wash and reassembly by fivefold dilution with buffer followed by reconcentration to the initial concentration. a) Reassembled in tris buffer. b) Reassembled in phosphate buffer. Absorbance was monitored at 280 nm (blue).

To increase buffer exchange, the disassembled protein was diluted 100-fold into either tris or phosphate buffer, incubated overnight, and concentrated the next day using a 100 kDa cutoff concentrator prior to SEC analysis. In tris buffer, the main peak appeared at ~9 mL (T = 3) with a shoulder near 13 mL (T = 1), but the profile also contained a pronounced subunit peak at ~20 mL, indicating incomplete reassembly. In phosphate buffer, the dominant signal was the T = 1 peak centered at ~13 mL with a tail extending to ~16 mL, while only a weak shoulder at ~9 mL suggested partial recovery of T = 3. Here, the subunit contribution was minimal (Figure 5.90).

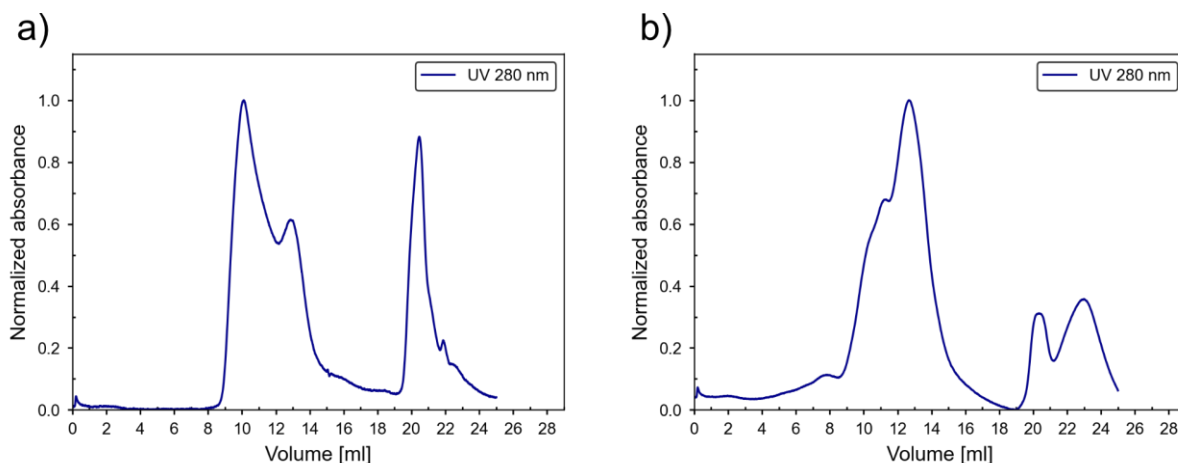


Figure 5.90: Normalized size-exclusion chromatograms of the T = 3 state of MxEnc after 100-fold dilution overnight with buffer followed by reconcentration to the initial concentration. a) Dilution in tris buffer. b) Dilution in phosphate buffer. Absorbance was monitored at 280 nm (blue).

In another experiment, the disassembled protein was diluted tenfold with water, concentrated to 1 mL, and then diluted 50-fold with either tris or phosphate buffer. After overnight incubation, samples were concentrated with a 100 kDa cutoff concentrator. In tris buffer, SEC revealed

an intense ~9 mL peak corresponding to $T = 3$ particles, a smaller peak at ~13 mL ($T = 1$), and a prominent subunit peak at ~20 mL. In phosphate buffer, peaks at ~9 mL, ~13 mL, and ~20 mL were of comparable intensity, indicating no dominant assembly pathway (Figure 5.91).

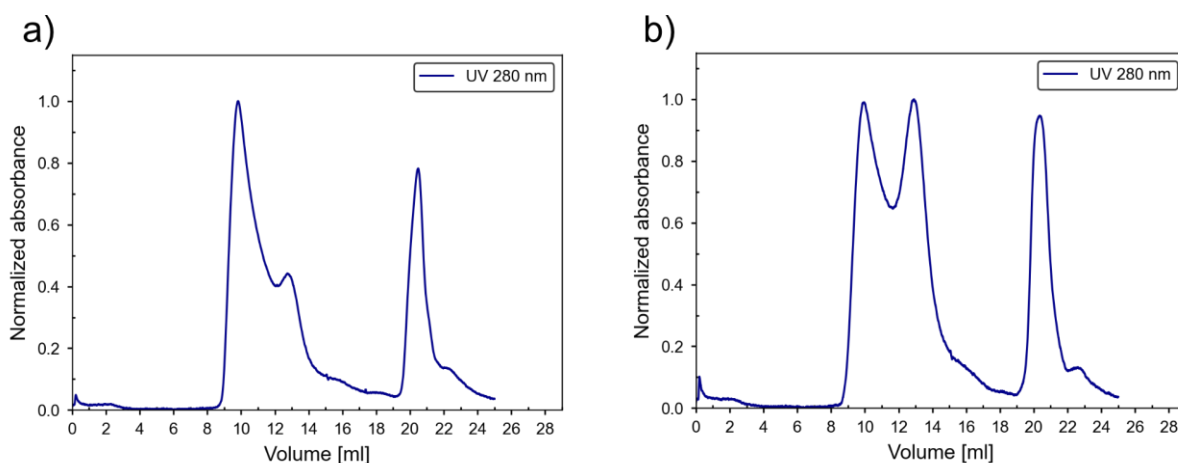


Figure 5.91: Normalized size-exclusion chromatograms of the $T = 3$ state of MxEnc after a water wash, fifty-fold dilution overnight with buffer, and reconcentration to the initial concentration. a) Dilution in tris buffer. b) Dilution in phosphate buffer. Absorbance was monitored at 280 nm (blue).

When the protein was diluted directly 50-fold into buffer without a water wash and processed identically, the outcomes diverged between the two systems. In tris buffer, the ~9 mL peak ($T = 3$) was dominant with a weaker ~13 mL peak ($T = 1$). In phosphate buffer, the opposite trend was observed, with the ~13 mL peak ($T = 1$) most intense and the ~9 mL peak ($T = 3$) reduced (Figure 5.92).

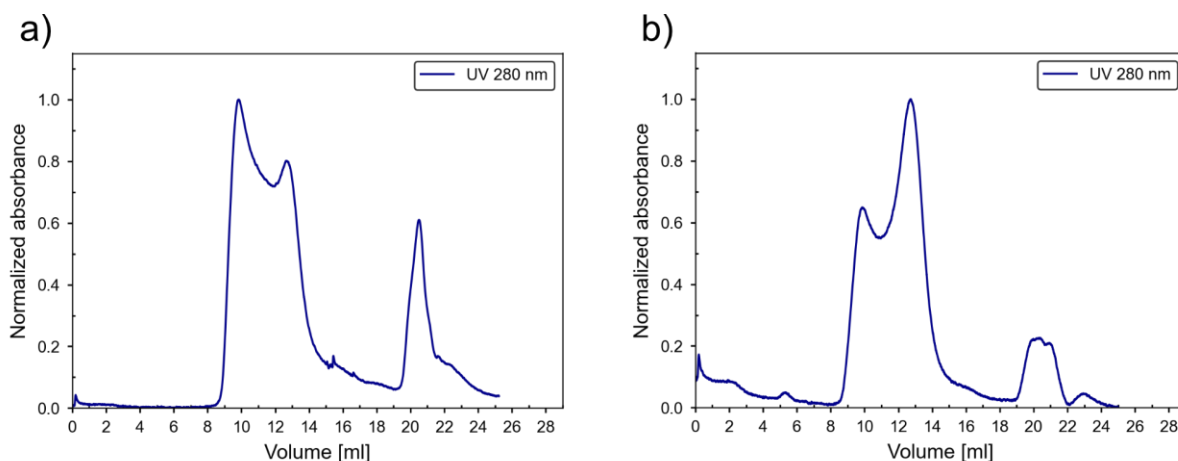


Figure 5.92: Normalized size-exclusion chromatograms of the $T = 3$ state of MxEnc after 50-fold dilution overnight with buffer followed by reconcentration to the initial concentration. a) Dilution in tris buffer. b) Dilution in phosphate buffer. Absorbance was monitored at 280 nm (blue).

Finally, the effect of dilution factor in phosphate buffer alone was examined. At fivefold dilution, three peaks of nearly equal intensity were observed at ~9 mL ($T = 3$), ~13 mL ($T = 1$), and

~20 mL (subunits). At tenfold dilution, the ~13 mL peak ($T = 1$) became dominant, accompanied by a weaker shoulder near 9 mL ($T = 3$) (Figure 5.93).

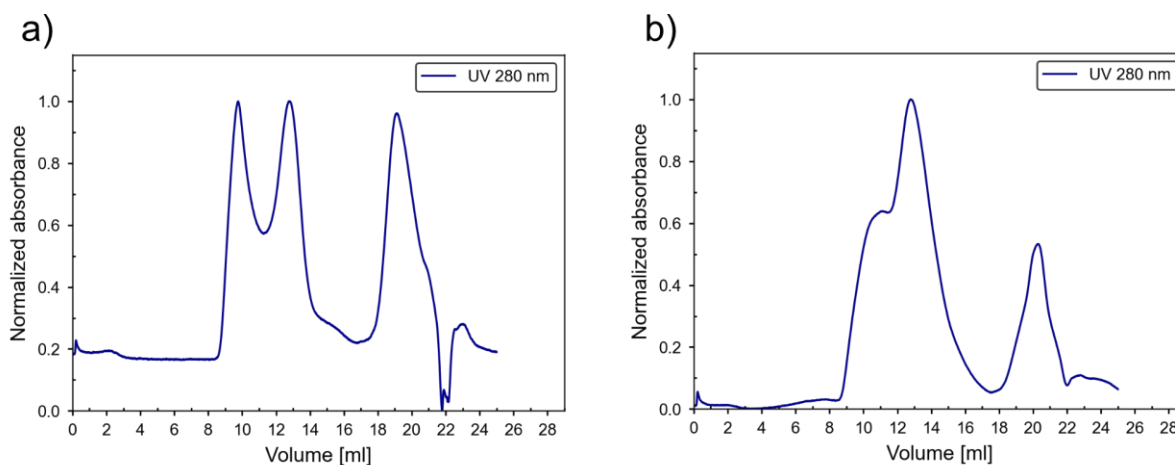


Figure 5.93: Normalized size-exclusion chromatograms of the $T = 3$ state of MxEnc after dilution with phosphate buffer followed by reconcentration to the initial concentration. a) five-fold dilution. b) Ten-fold dilution. Absorbance was monitored at 280 nm (blue).

Taken together, these experiments show that tris consistently favors recovery of the $T = 3$ state, although subunit carryover is common and peak broadening indicates that assembly remains heterogeneous. Phosphate, in contrast, biases reassembly toward the $T = 1$ state, as reflected by the dominant peak at ~13 mL, while subunits and aggregates remain as coexisting species. The relative distribution between $T = 1$, $T = 3$, and subunits depends strongly on the extent of buffer exchange. These findings highlight that effective cage reformation is not triggered by urea removal alone but is governed by buffer identity and exchange protocol, with tris promoting $T = 3$ recovery and phosphate driving the system toward $T = 1$.

To further assess the role of ionic strength, reassembly was tested in tris and phosphate buffers with and without added NaCl. Disassembled protein was diluted fivefold and reconcentrated using a 10 kDa cutoff concentrator in each condition. In 20 mM tris buffer, pH 7.5, the SEC profile was dominated by a $T = 3$ peak at ~9 mL, accompanied by a weaker $T = 1$ peak at ~13 mL and a subunit peak at ~20 mL. In 20 mM tris buffer with 100 mM NaCl, the $T = 3$ signal was reduced and the profile was dominated by subunits, indicating that salt destabilizes cage reassembly under tris conditions (Figure 5.94).

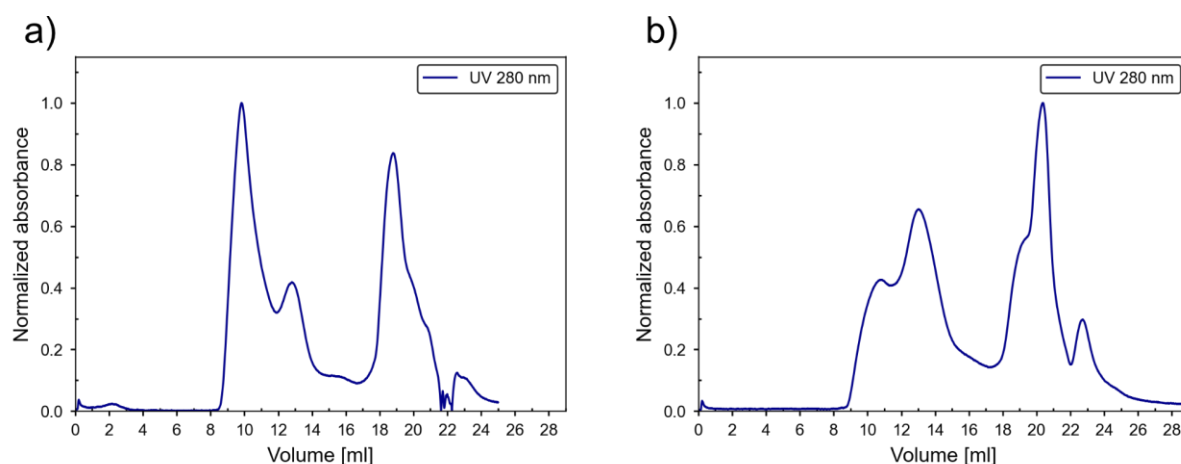


Figure 5.94: Normalized size-exclusion chromatograms of the T = 3 state of MxEnc after dilution with tris buffer with two different NaCl concentrations followed by reconcentration to the initial concentration. a) 0 M NaCl. b) 0.1 M NaCl. Absorbance was monitored at 280 nm (blue).

In phosphate buffer, the outcome was markedly different. At both 0 M and 100 mM NaCl, pH 7.0, the SEC profiles were dominated by the T = 1 peak at ~13 mL, with subunit signal present in both cases. A weak T = 3 peak at ~9 mL was detectable in the 0 M salt condition, but in 0.1 M salt it was reduced to a small shoulder (Figure 5.95). These results indicate that phosphate consistently favors T = 1 reassembly regardless of ionic strength, while tris supports T = 3 formation in the absence of salt but shifts toward subunits when salt is present.

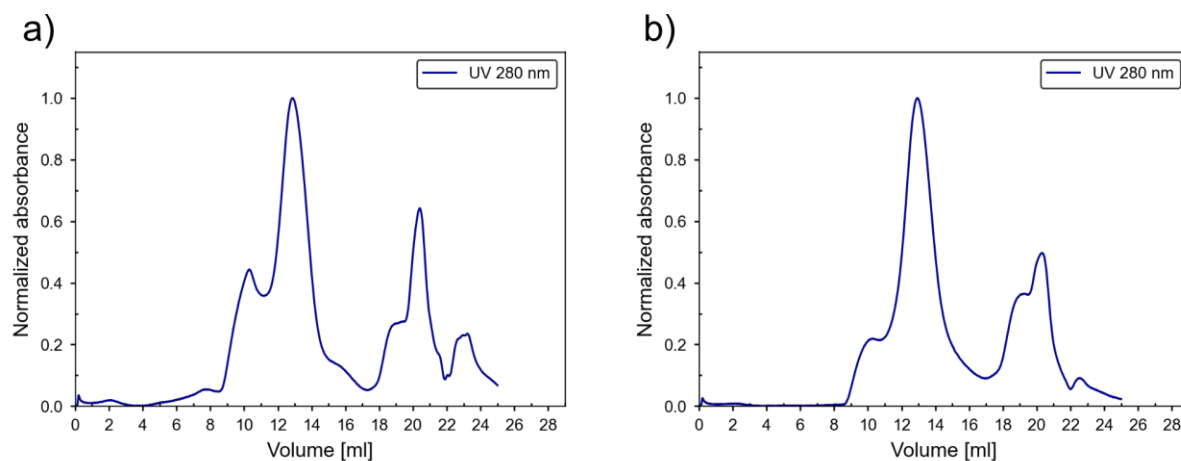


Figure 5.95: Normalized size-exclusion chromatograms of the T = 3 state of MxEnc after dilution with phosphate buffer with two different NaCl concentrations followed by reconcentration to the initial concentration. a) 0 M NaCl. b) 0.1 M NaCl. Absorbance was monitored at 280 nm (blue).

To separate the effect of buffer identity from ionic strength, a systematic salt series was performed in tris buffer. Disassembled protein was diluted fivefold into tris buffers containing 0 M, 100 mM, 500 mM, or 1 M NaCl, pH 7.5 and reconcentrated with a 10 kDa cutoff concentrator prior to SEC analysis. At 0 M NaCl, the profile was dominated by the T = 3 peak at ~9 mL, with only a shoulder at ~13 mL (T = 1) and a weak subunit signal at ~20 mL. At

100 mM NaCl, the outcome shifted: the T = 1 peak at ~13 mL became dominant, while T = 3 was reduced to a smaller shoulder and subunits remained weak. At 500 mM M NaCl, subunits became the most intense signal, though peaks for T = 1 and T = 3 were still detectable, with the T = 3 contribution diminished relative to 100 mM. At 1 M NaCl, the subunit peak dominated the profile, but the T = 1 signal remained strong, while T = 3 was reduced to only a faint trace. (Figure 5.96).

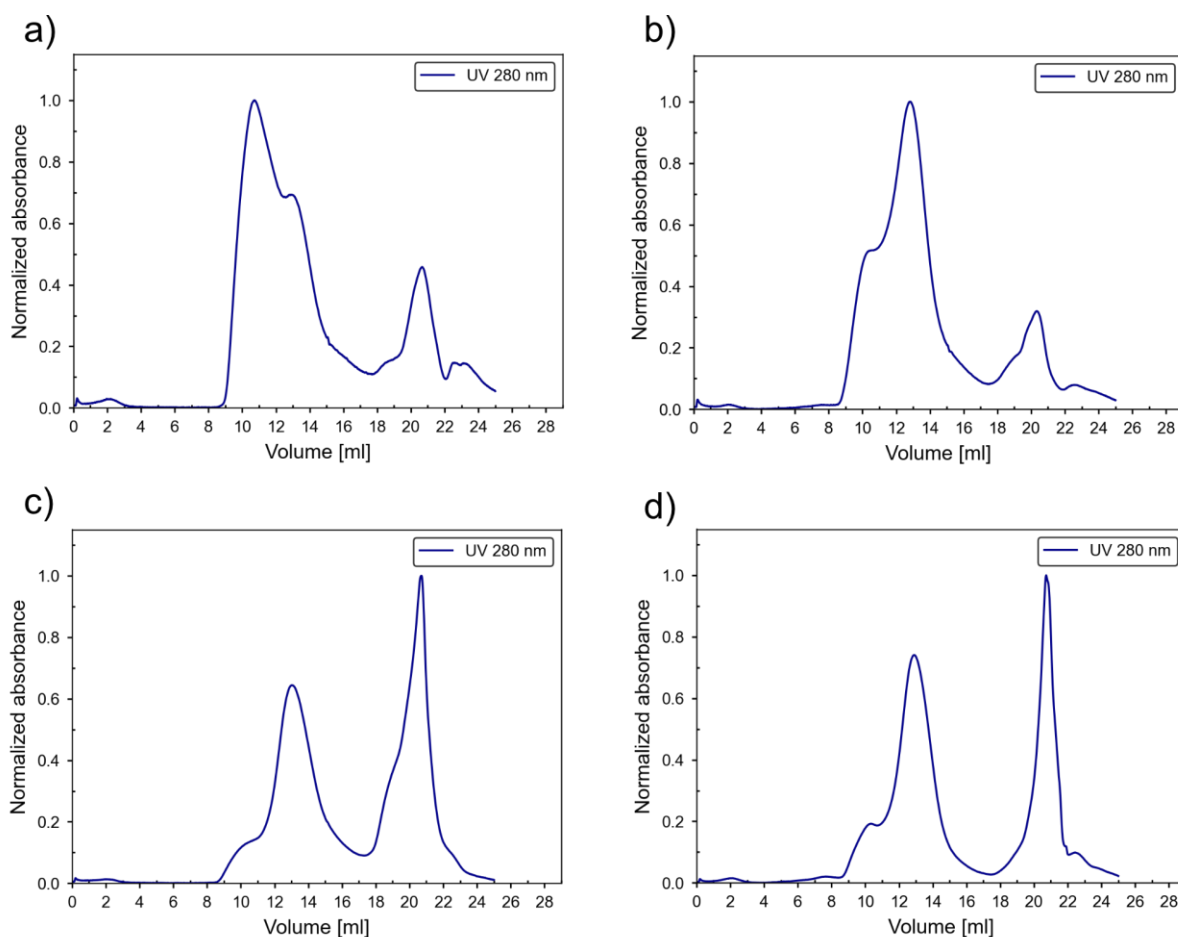


Figure 5.96: Normalized size-exclusion chromatograms of the T = 3 state of MxEnc after dilution with tris buffer with four different NaCl concentrations followed by re-concentration to the initial concentration. a) 0 M NaCl. b) 100 mM NaCl. c) 500 mM NaCl. d) 1 M NaCl. Absorbance was monitored at 280 nm (blue).

These results demonstrate that in tris buffer, T = 3 reassembly is favored only in the absence of salt, while T = 1 becomes increasingly favored as ionic strength is raised, with high salt ultimately destabilizing both states in favor of subunits. This salt-dependent switching can be explained by considering the distinct electrostatic interfaces in the two capsid states.

As shown in Figure 5.97, the T = 1 capsid, the E-loop forms a much larger dimer interface engaging in additional β -sheet contacts, hydrogen bonding, and hydrophobic interactions with the neighboring P-domain. A key feature of this interface is the positioning of threonine residues from adjacent subunits in close proximity, allowing potential polar interactions across

the interface (Figure 5.97b). The distance between the $-OH$ groups of these threonines is consistent with the formation of strong hydrogen bonds. At a low to moderate ionic strength, this conformation is further stabilized, potentially through direct cation coordination that bridges the threonine side chains, effectively creating a salt-stabilized interface.

In contrast, the E-loop in the $T = 3$ state remains in a 180° orientation, resulting in a smaller interface and positioning the corresponding threonines $\sim 5.4 \text{ \AA}$ apart, which is too far for any direct polar interaction (Figure 5.97d). This structural difference likely underlies the salt response: While $T = 1$ benefits from specific salt-stabilized contacts, $T = 3$ is stabilized by more distributed interactions, which are disrupted by ionic screening. Consequently, increasing salt concentration selectively promotes $T = 1$ assembly while simultaneously destabilizing the $T = 3$ state.

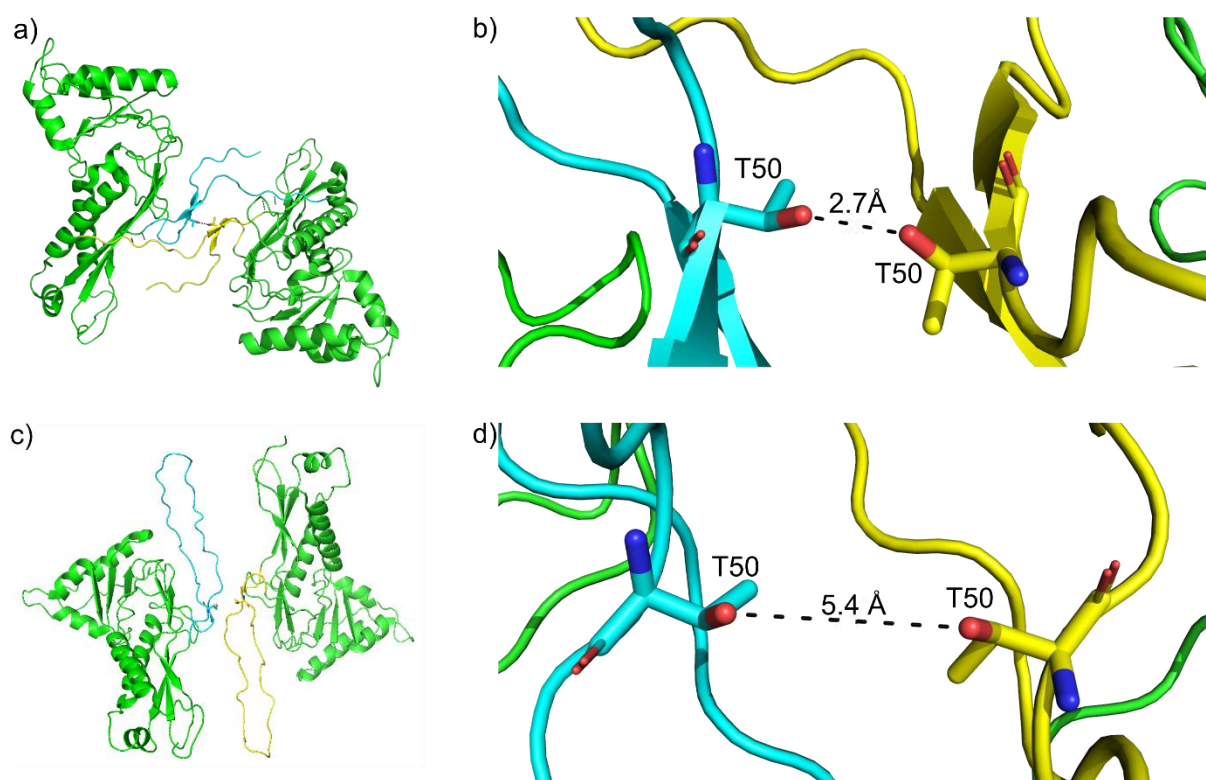


Figure 5.97: Structural comparison of MxEnc arranged in $T = 1$ and $T = 3$ symmetry. a) Arrangement of E-loops between the subunits in $T = 1$ state (PDB : 7S21). b) Close-up view of the interactions, focusing on the polar interactions between $-OH$ groups of threonine. c) Arrangement of E-loops between the subunits in $T = 3$ state (PDB : 4PT2). d) Close-up view of the interactions.

Based on the buffer and ionic strength trials, tris buffer without added salt was identified as the most favorable condition for $T = 3$ reassembly. To test whether these conditions would also improve encapsulation, disassembled protein was washed twice with water by fivefold dilution and concentration using a 10 kDa cutoff concentrator to ensure complete removal of urea. In one trial, the washed protein was diluted 30-fold with 20 mM tris buffer, 0 M NaCl, pH

7.5 and AuNPs were added dropwise. In a second trial, AuNPs were pre-diluted in the same tris buffer and protein was added dropwise. Both reactions were incubated overnight, concentrated the next day with a 100 kDa cutoff concentrator, and analyzed by stained TEM. The two strategies gave markedly different outcomes. When AuNPs were added to protein, TEM revealed aggregated particles without cage structures, indicating that encapsulation had not occurred (Figure 5.98a). In contrast, when protein was added to pre-diluted AuNPs, TEM showed intact T = 3 cages containing electron-dense nanoparticles, confirming successful encapsulation (Figure 5.98b). These results clearly demonstrate that mixing order is critical, with the "protein-into-particle" approach significantly reducing aggregation and promoting successful encapsulation.

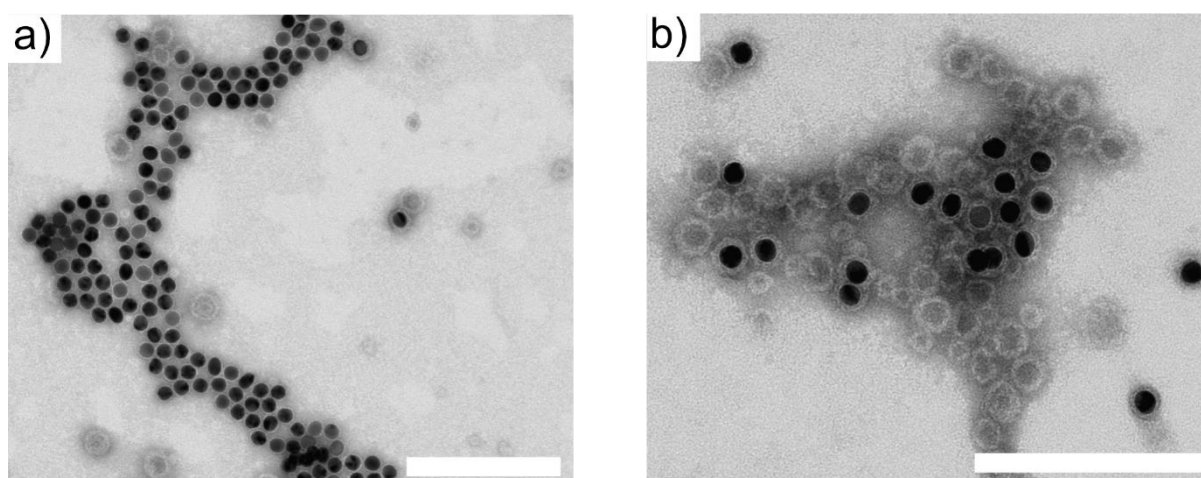


Figure 5.98: Stained TEM images of T = 3 state reassembly and AuNP encapsulation in tris buffer with no salt. a) AuNPs added dropwise to protein after a 30-fold dilution in tris: aggregated particles without cage structures, indicating failed encapsulation. b) Protein added dropwise to AuNPs pre-diluted in tris: intact T = 3 cages containing electron-dense AuNPs, confirming encapsulation. Scale bar is 200 nm.

Stained TEM images confirmed the presence of both empty and cargo-loaded cages. The filled cages appeared more defined and structurally uniform compared to their empty counterparts. This suggests that the presence of encapsulated AuNPs may stabilize the shell or influence its compaction during reassembly. This observation was supported by size measurements. As shown in the Figure 5.99, a consistent shift in apparent cage diameter between the two populations is observed. Empty cages averaged ~32 nm, while filled cages appeared slightly smaller, around ~29 nm. The histograms were compiled from multiple TEM images, as the number of encapsulated particles per field of view was low and a single image did not provide sufficient data for reliable analysis.

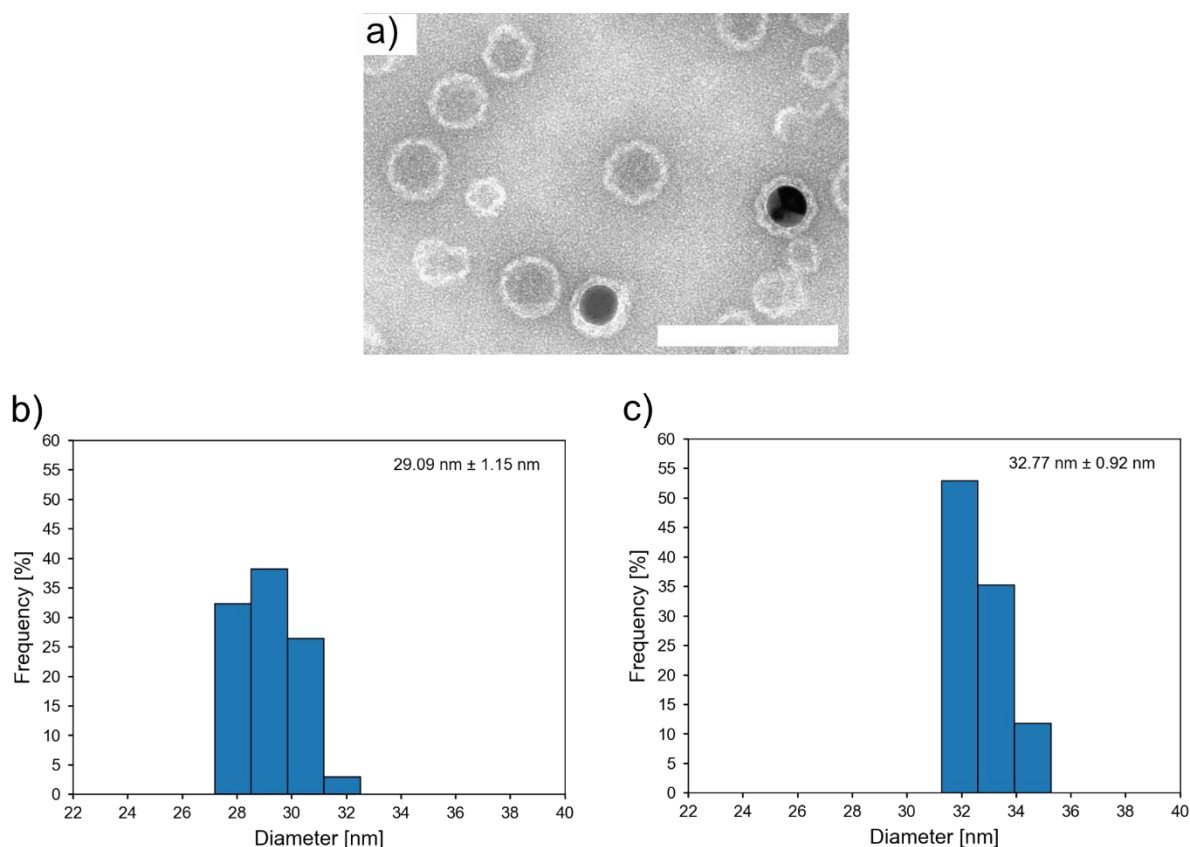


Figure 5.99: Stained TEM and histograms for filled and empty MxEnc cages. a) Stained TEM images showing structural differences between filled and empty cages. b) Histogram and size distribution with standard deviation for filled cages. c) Histogram and size distribution with standard deviation for empty cages. Measurements were pooled from multiple images due to the low number of encapsulated cages per field of view.

Despite this success, overall encapsulation efficiency remained low, suggesting that further optimization is needed. Cargo concentration could all be tuned to enhance loading. Moreover, although this study focused on spherical AuNPs, anisotropic particles such as gold nanorods were not tested in these final reassembly trials due to time constraints. However, given the structural insights gained from the disassembly/reassembly behavior of the $T = 3$ system, particularly under low-salt tris buffer conditions, such trials now appear feasible.

In conclusion, these results highlight the importance of controlling not only buffer identity and ionic strength, but also the mixing strategy and cargo geometry when designing protein-based encapsulation systems. The $T = 3$ scaffold, under appropriate conditions, can accommodate electron-dense nanoparticles and may serve as a promising platform for further exploration with more complex or anisotropic cargo.

6. Summary and Outlook

In conclusion, this thesis established a comprehensive methodological framework for using protein containers as scaffolds for anisotropic nanomaterials. While encapsulation of spherical cargo within protein cages has been demonstrated in several systems, anisotropic particles pose additional challenges arising from elongated shape, aspect ratio, surface chemistry and directional optical properties. The work presented here systematically addressed the significant challenges inherent in moving from the encapsulation of spherical cargo to non-spherical nanoparticles by integrating both metallic and semiconductor anisotropic particles. A dual-scaffold strategy was adopted, utilizing the well-established TmEnc and extensively characterizing the larger MxEnc as a promising alternative for accommodating anisotropic nanoparticles.

The foundation of this work was the synthesis and precise functionalization of a library of anisotropic nanomaterials. Towards this end, CdSe/CdS DiRs were synthesized via a seeded growth method for their high quantum yield and polarized emission. AuNRs were produced using both hydrogen peroxide and CTAB/decanol methods to achieve tunable plasmonic properties. A critical contribution was the development of robust ligand exchange protocols to replace native ligands with biocompatible alternatives. For DiRs, the primary goal was to achieve water solubility, which was accomplished through a multi-tiered strategy. This involved functionalization with AUT, AUT/MUTAB mixtures, and a targeted MUTAB/CLP approach. The success of the CLP conjugation was rigorously confirmed using a fluorophore-labeled CLP, demonstrating successful modification via DTT assay. For AuNRs, the essential goal was to replace the cytotoxic ligand CTAB, which induces protein aggregation, with biocompatible alternatives like MUA and MUTAB. This also served to systematically probe the role of electrostatic interactions in encapsulation.

Encapsulation trials of these functionalized nanoparticles into TmEnc yielded critical insights. Experiments were conducted with DiRs of different sizes (10 x 4 nm and 18.5 x 5.4 nm) using strategies both with and without the CLP. The most promising results were observed for the MUTAB/CLP strategy. Characterization techniques including IEC, SEC, and fluorescence spectroscopy provided strong evidence of successful interaction and incorporation for DiRs. A definitive visualization of an encapsulated anisotropic rod via TEM proved elusive. This highlighted the substantial methodological challenge at the heart of this research and underscored the limitations of TmEnc cavity for larger anisotropic cargo. While it assembles in a $T = 1$ icosahedral symmetry, its rigid cavity is sufficient only for spherical nanoparticles or small guest proteins and is insufficient to accommodate anisotropic cargo without imposing

directional strain. This limitation underscored the need for a more spacious and flexible scaffold, shifting the focus to MxEnc, which assembles into larger $T = 3$ architecture.

Consequently, the research expanded to a detailed exploration of the MxEnc. This involved the optimization of its production and purification. Initial disassembly and reassembly trials were conducted to assess its structural responsiveness. A key finding was the differential susceptibility of its $T = 1$ and $T = 3$ oligomeric states to denaturants, with GuHCl more effective for $T = 1$ state and urea for $T = 3$ state. Reassembly conditions were optimized by varying different parameters such as buffer composition and DTT concentration. It was determined that the presence of DTT lead to formation of more aggregates.

In parallel, AuNPs were synthesized and further functionalized to enable encapsulation. AuNPs were chosen as model system to establish a baseline for encapsulation behavior before progressing to more challenging anisotropic cargo, such as AuNRs, which place greater geometric demands on the cage. The native CTAC ligand was successfully exchanged with MUTAB, enabling a stable and positively charged surface compatible with proteins. CLP loading was performed via electrostatic interaction, and the presence of CLP on the AuNP surface was confirmed using a streptavidin-biotin binding assay. These functionalized AuNPs formed a critical benchmark for spherical cargo encapsulation in MxEnc. Using the standard conditions, encapsulation experiments were carried out and analyzed using IEC, SEC and TEM. However, it was observed that even in the presence of cargo, the $T = 1$ state was predominantly favored over the expected $T = 3$ architecture. This unexpected outcome prompted a more detailed investigation into the factors influencing MxEnc reassembly, particularly how environmental conditions may override cargo-induced structural bias.

To better understand the factors governing MxEnc architecture, a mechanistic study of the reassembly process was conducted. Systematic variation of buffer composition, salt ratios, and dilution factors established a robust toolkit for controlling the final assembly state. It was determined that the presence of salt and the use of phosphate buffer favors the reassembly towards $T = 1$ state, whereas tris buffer favors the reassembly towards $T = 3$ state. Dilution factors on the other hand had no clear influence on the structural outcome. This fundamental knowledge was successfully applied to demonstrate the encapsulation of spherical AuNPs into MxEnc.

This thesis also laid the groundwork for the application through preliminary surface deposition studies, which are described in the experimental section but not discussed in detail in the results. It was found that dip-coating provided more controlled film formation than spin-coating, particularly when using ethanol-based solutions. Additionally, the TmEnc remained stable up to 50% ethanol, defining a practical window for processing.

The findings of this work provide a solid foundation for several specific and promising research directions. The detailed reassembly protocols established for MxEnc can be exploited to perform in-situ encapsulation of isotropic and anisotropic cargo, offering a powerful route to control loading conditions at the point of reassembly. The systematic study of how cargo size and buffer conditions bias during reassembly direct the formation of $T = 1$ versus $T = 3$ assemblies would deepen the understanding of size-selectivity in protein cages and create design rules for tailoring encapsulation outcomes.

Beyond reassembly, nanoparticle synthesis inside the encapsulation shell (mineralization) represents a compelling strategy, leveraging the cage's inherent chemical stability under harsh conditions. Parallel work on engineering encapsulin variants, such as supercharged MxEnc, could allow controlled co-assembly with wild-type cages, enabling binary or higher-order superlattices as modular, hierarchical materials.

The preliminary results on surface deposition point to another important direction. Expanding dip-coating into controlled monolayer and multilayer assemblies, followed by detailed characterization (AFM for nanomechanics, SEM for cargo contrast), would establish encapsulins as practical nanoscale building blocks. Combined with selective cargo loading, these ordered layers could serve as tunable photonic or plasmonic platforms.

Ultimately, the methodological framework developed here, from nanoparticle functionalization to cage reassembly, advances the goal of creating hybrid protein–nanoparticle materials where structure and function can be controlled with molecular precision. Such materials are highly relevant for applications in sensing, catalysis, and nanophotonics, where anisotropic cargo such as DiRs or AuNRs offer unique optical and electronic properties.

7. Experimental Part

7.1 General

All syntheses and buffer preparations were conducted using ultrapure water to minimize the risk of contamination. Ultrapure water was produced with a *Purelab Flex 2* system (resistivity: 18.2 M Ω -cm at 25 °C) from *ELGA LabWater*. Prior to AuNRs/nanoparticle synthesis, all glassware and magnetic stir bars were cleaned using freshly prepared aqua regia and rinsed with ultrapure water to remove residual contaminants. Prepared buffers were filtered through a 0.22 μ m pore size membrane filter (*Carl Roth*). For sample storage and encapsulation experiments, polystyrene tubes (15 mL and 50 mL, *Carl Roth*) and reaction tubes (1.5 mL and 2.0 mL, *Carl Roth*) were used. Centrifugation of 15 mL and 50 mL tubes was performed using an *Eppendorf 5810R* centrifuge, while 1.5 mL and 2.0 mL tubes were centrifuged in a *Heraeus Fresco 21 microcentrifuge* (*Thermo Scientific*). Samples exceeding 50 mL were centrifuged using a *Multifuge X4R Pro* (*Thermo Scientific*). Experiments requiring sterile conditions were conducted in a *Maxisafe 2030i* biosafety cabinet (*Thermo Scientific*). Cryo-cultures and competent cells were stored at -80 °C, while cell pellets containing proteins were stored at -20 °C. Purified protein solutions, as well as loaded protein samples, were stored at 4 °C. Protein concentrations were measured using a NanoDrop One C spectrophotometer (*Thermo Scientific*). Dialysis, including concentration, washing, and buffer exchange, was performed using *Vivaspin® Turbo 15* centrifugal filter units (*Sartorius*) and *Amicon® Ultra-0.5 filters* (*Merck*) with molecular weight cut-offs (MWCO) of 30 kDa or 100 kDa, depending on the molecular weight of the target protein and the desired separation efficiency.

7.2 E. coli strains

Table 7.1: List of used E. coli strains

Strain	Genotype	Supplier
DH5 α	F- Φ 80lacZ Δ M15 Δ (lacZYA-argF) U169 recA1 endA1 hsdR17(rk-, mk+) phoA supE44 thi-1 gyrA96 relA1 λ -	Invitrogen
BL21(DE3)	<i>E. coli</i> B F- dcm ompT hsdS(rB- mB-) gal λ (DE3)	Agilent
C43(DE3)	F- ompT hsdSB (rB- mB-) gal dcm (DE3)	NEB

7.3 Chemicals

All chemicals were purchased from commercial suppliers and used without further purification (chapter)

7.4 Analytical Methods

7.4.1 UV-Vis Spectroscopy

Absorbance spectra were measured using a Cary 60 UV-Vis spectrophotometer (Agilent) with disposable UV microcuvettes (Brand) featuring a 1 cm path length. Ultrapure water or the corresponding buffer served as the reference.

7.4.2 Transmission Electron Microscopy

For transmission electron microscopy (TEM) measurements, carbon-coated copper grids with a 400-mesh size (Ted Pella, 01814-F-X) were generally used. Protein- or nanoparticle-containing samples were analyzed by Stefan Werner (University of Hamburg, Germany) using a JEOL JEM 1011 operating at 100 kV. Unstained samples were prepared by depositing 2 μ L of the sample onto the TEM grid and allowing it to dry. For uranyl acetate-stained samples, a 2% solution was used. The grid was first incubated for 1 minute on a 10 μ L droplet of the sample, followed by three washes in ultrapure water. Subsequently, the grid was washed once and then incubated for 60 seconds on a 2% uranyl acetate droplet. Excess solution was blotted off, and the grid was dried.

Image analysis was conducted using ImageJ software. The size of AuNPs was determined by converting images into binary (black and white) using the threshold function, enabling automated counting and area measurement. At least 200 nanoparticles were analyzed for size determination. Protein cages were measured manually by analyzing 100 particles per sample, with a circular outline drawn around each cage to determine its size.

7.4.3 Dynamic Light Scattering

Dynamic light scattering (DLS) measurements were conducted using a Z-sizer Nano S (Malvern Instruments) equipped with a 633 nm HeNe laser. All measurements were taken at a backscattering angle of 173° and a temperature of 25°C. Protein cage samples were maintained in their respective storage buffers at a concentration of 1 mg/mL, while nanoparticles were measured in ultrapure water. The nanoparticle solution was diluted until

the plasmonic peak intensity was below 0.1 AU. Aqueous solutions were analyzed in disposable cuvettes (Brandt), whereas organic solvents were measured in quartz cuvettes. Before measurement, samples were equilibrated for 120 seconds. Each sample was measured in at least three runs, with the results averaged.

7.4.4 Zeta Potential

ζ -potential measurements were carried out using a Zeta-sizer Nano S (Malvern Instruments) equipped with a 633 nm HeNe laser. Measurements were performed at 25°C using micro ζ -disposable capillary cells (DTS1070, Malvern Instruments). Protein and nanoparticle samples were prepared as described in Chapter 7.4.7. Before measurement, samples were equilibrated for 120 seconds, and at least three measurements were taken and averaged. For data analysis, the Smoluchowski approximation was applied to convert electrophoretic mobility into ζ -potential.

7.4.5 Fluorescence Spectroscopy

Emission spectra were acquired with a Fluoromax 4000 spectrofluorometer (Horiba Jobin Yvon), utilizing the same disposable UV microcuvettes. Ultrapure water or the respective buffer was used as the reference.

7.4.6 SDS Page

For SDS-PAGE, protein samples were denatured at 95°C for 10 minutes in a 1:1 mixture with SDS loading buffer (50 mM tris, pH 6.8, 10% (v/v) glycerol, 0.1% (w/v) bromophenol blue, 2% (w/v) SDS, and 250 mM DTT). The samples were then loaded onto the gel, and electrophoresis was performed at 200 V using 1x tris-Glycine SDS running buffer (25 mM tris, 250 mM glycine, 0.1% (w/v) SDS). Precast tris-Glycine gels (4%-20%) were obtained from Biotrend. After electrophoresis, gels were stained overnight with Coomassie Brilliant Blue stain solution (40% (v/v) methanol, 10% (v/v) acetic acid, and 0.2% (w/v) Coomassie Brilliant Blue R250). Excess stain was removed using a destaining solution composed of 20% (v/v) isopropyl alcohol and 10% (v/v) acetic acid.

7.5 Gold Nanorod Synthesis

For the synthesis of AuNRs, two different syntheses were performed to obtain AuNRs of the desired size. After synthesis, native ligands were removed via ligand exchange reaction. All samples were analyzed by TEM, DLS, ζ -potential and UV-Vis.

7.5.1. H₂O₂ Method

Seed Solution Preparation: Seed solutions were prepared based on a previously reported protocol, with slight modifications.^[199] Specifically, 40.5 μ L of 1% (w/v) HAuCl₄ was added to 4 mL of 0.1 M CTAB solution under gentle stirring. Then, 24 μ L of freshly prepared 0.1 M NaBH₄ was introduced while stirring continuously. Stirring continued for 2 minutes, after which the solution was left undisturbed. The seed solution was aged in a 28 °C water bath for a minimum of 2 hours before use in the nanorod synthesis.

AuNRs Synthesis: AuNRs were synthesized via a seed-mediated growth method. In a typical reaction, 206 μ L of 1% (w/v) HAuCl₄ and 10 μ L of 0.1 M AgNO₃ were added to 10 mL of 0.1 M aqueous CTAB solution. Next, NaOH (1 M) and 6 μ L of 30% H₂O₂ were sequentially added to initiate reduction. The volume of NaOH was varied across trials (37.5 μ L, 45 μ L, 50 μ L, and 100 μ L) to investigate its effect on nanorod growth.

After addition of NaOH and H₂O₂, the solution was stirred for 1 minute until it turned colorless. Then, 30 μ L of the aged seed solution was added, followed by an additional 1 minute of stirring. The reaction mixture was then left undisturbed at 27 °C for 1.5 hours. A wine-purple color developed, indicating successful formation of AuNRs. On colder days, the reaction was conducted in a 27 °C incubator to prevent CTAB crystallization.

Purification and Analysis: The AuNR dispersions were purified using a two-step differential centrifugation protocol to separate particles by size and shape. First, the reaction mixture was centrifuged at 12,000 \times g for 30 minutes at room temperature. The supernatant (Sample A) was collected, while the pellet was redispersed in deionized water and centrifuged again at 15,000 \times g for 30 minutes. This second step yielded a supernatant (Sample B) and a final pellet (Sample C), which was again redispersed in water.

All three fractions, Samples A, B, and C, were characterized independently using UV-Vis spectroscopy to evaluate their optical properties and monitor longitudinal surface plasmon resonance (LSPR) features. Transmission electron microscopy (TEM) was also performed on each sample to assess nanorod morphology, size distribution, and anisotropy.

7.5.2 CTAB-Decanol Method

This procedure was adapted from a previously reported method with slight modifications.^[200]

Preparation of n-Decanol/CTAB Growth Solution : The growth solution was prepared by dissolving 9.111 g of CTAB and 1.068 g of n-decanol in 500 mL of warm deionized water. Both components were weighed directly into a 500 mL Erlenmeyer flask. The solution was stirred at approximately 60 °C for 1 hour or at 30 °C overnight to ensure complete incorporation of n-decanol into the CTAB micelles. Once solubilized, the CTAB/n-decanol micellar solution remained stable at temperatures above 16 °C.

Synthesis of Gold Seeds: To prepare small gold seeds, 200 μ L of 0.05 M HAuCl₄ and 100 μ L of 0.1 M ascorbic acid were added to 20 mL of the prepared CTAB/n-decanol solution (50 mM CTAB, 13.5 mM n-decanol) in a 50 mL glass beaker maintained at 25-27 °C. The resulting solution was initially colorless. After 1-2 minutes, 800 μ L of freshly prepared 0.02 M NaBH₄ was added under vigorous stirring (1000 rpm, using a 30 mm \times 6 mm PTFE-coated magnetic stir bar). This addition led to the formation of a brownish-yellow solution, indicating seed formation. The solution was aged for at least 60 minutes at 25-27 °C to consume excess borohydride and stabilize the seed particles. For the synthesis of standard AuNRs, a seed solution was also prepared using 100 mM CTAB in place of the CTAB/n-decanol mixture.

Synthesis of Small Anisotropic Seeds (21 nm \times 7.5 nm): Small anisotropic seeds were synthesized by combining 2400 μ L of 0.01 M AgNO₃, 21 mL of 1 M HCl, 3000 μ L of 0.05 M HAuCl₄, and 3900 μ L of 0.1 M ascorbic acid with 300 mL of the CTAB/n-decanol solution. The reaction was performed at 25 °C. Once all reactants were fully mixed, 18 mL of the previously prepared seed solution was added under stirring. The mixture was left undisturbed at 25 °C for a minimum of 4 hours, during which the solution color changed from colorless to gray and then to a dark brownish-gray, indicative of nanorod formation. The longitudinal localized surface plasmon resonance (LSPR) of the resulting nanocrystals was expected to be in the range of 725-730 nm.

Purification and Analysis: The anisotropic seed solution was purified by centrifugation at 14,000 \times g for 45-60 minutes, repeated twice. The resulting pellet was redispersed in 10 mM CTAB solution. Samples were characterized using UV-Vis spectroscopy and TEM to assess nanorod morphology, optical response, and uniformity.

7.5.3 Calculation of Gold Nanorod Concentration

For AuNRs synthesized by either method, a ligand exchange procedure was performed following the same general approach used for spherical gold nanoparticles. To calculate the number of AuNRs and determine the required ligand amount, it was assumed that all the gold precursor was fully converted into nanorods. The total amount of gold was calculated from the known concentration and volume of HAuCl_4 used. The volume of gold in the product was then determined using the molar mass and density of elemental gold. The volume of a single nanorod was approximated using the formula for a spherically capped cylinder. The total number of AuNRs was estimated by dividing the total gold volume by the volume of one nanorod and converting moles to particles using Avogadro's number. The surface area of a single AuNR was calculated based on its geometry, and the total surface area was obtained by multiplying by the estimated particle count. From this, the amount of ligand needed was determined using the known grafting density and applying an appropriate excess. The final ligand concentration was calculated based on the total surface area and the footprint of the ligand molecules.

7.6 CdSe/CdS DiR synthesis

This procedure was adopted from a previously reported method.^[70]

Synthesis of CdSe seeds: TOPO (3.0 g), ODPA (280 mg), and CdO (60 mg) were loaded into a 50 mL three-neck flask and heated to ~ 150 °C under vacuum for 1 h to remove residual moisture and oxygen. The flask was then placed under nitrogen and heated above 360 °C until the CdO dissolved completely, yielding a clear, colorless solution. At this stage, 1.8 ml of TOP was injected, and the mixture was allowed to return to the target injection temperature. 0.5 ml of 2 M selenium precursor solution (Se : TOP) was swiftly injected once the desired temperature was reached. The reaction mixture was maintained at that temperature for 5 min before cooling. The nanocrystals were isolated by precipitation with methanol, followed by redissolution in toluene and repeated precipitation with methanol. Samples were analysed with UV/Vis, Fluorescence spectroscopy and TEM. The purified CdSe nanocrystals were finally dispersed in TOP for storage.

Seeded Growth of CdSe/CdS Nanorods: CdO (18 mg), TOPO (3 g), ODPA (65.3 mg), and HPA (18 mg) were combined in a three-neck flask and heated to 150 °C under vacuum for 1 h. The mixture was then heated to 350 °C under nitrogen. 1.8 ml of TOP was injected. After the temperature stabilized, a 1.1 ml of sulfur precursor (S : TOP) and 400 μL of CdSe nanocrystal seeds was rapidly injected. Following injection, the temperature dropped to 300

°C. The nanocrystals were allowed to grow for 8 min, after which the heating mantle was removed.

Purification and analysis: Purification was carried out by precipitation with methanol, redissolution in toluene, and repeated washing. Reaction parameters such as precursor amounts, growth temperature, and reaction duration were systematically varied to control the morphology of the resulting CdSe/CdS DiRs. Samples were analysed with UV/Vis, Fluorescence spectroscopy and TEM.

7.7 AuNPs synthesis:

The synthesis of gold nanoparticles was carried out following a seed-mediated growth method adapted from Schulz *et al.*^[248]

Seed Preparation: 10 ml of 100 mM CTAB aqueous solution was freshly prepared (CTAB dissolves better around 40 °C) The CTAB solution was mixed with 100µL of 25 mM aqueous solution of H₂AuCl₄ in a water bath maintained at 27 °C under stirring at 600 rpm. 1ml of 10 mM NaBH₄ solution (0.01 M) was freshly prepared using ice cold water. 600µL was rapidly injected into the CTAB/H₂AuCl₄ mixture under continuous stirring at 600 rpm. After injection, the stirring rate was reduced to 300 rpm and maintained for 3 min. The reaction mixture was then left undisturbed at 27 °C for 3 h to complete seed formation.

Growth of 20 nm AuNP: To obtain ~20 nm AuNP, 50µL of CTAB-stabilized seeds were combined with 15 ml of 100 mM ascorbic acid and 20 ml of 200 mM CTAC solution at 27 °C under stirring at 600 rpm. A one-shot injection of 20 ml, 0.5 mM H₂AuCl₄ was then carried out. Following injection, the solution was stirred at 300 rpm for 15 min.

Purification: Nanoparticles were purified by centrifugation at 14,000 g for 40 min. The supernatant was discarded, and the pellet was redispersed in ultrapure water, followed by a second centrifugation under the same conditions to remove excess CTAC. Concentration of AuNP suspensions using centrifugal filters was avoided prior to surfactant removal, as excess CTAC damaged filter membranes.

7.9 Ligand Exchange

7.9.1 MUA Stabilized AuNRs

AuNRs synthesized with CTAB were subjected to ligand exchange to replace the CTAB surface coating with MUA. The ligand exchanged was adapted from published work.^[221] Excess CTAB was first removed by two successive centrifugation steps at 21000g for 10

minutes, followed by redispersion in doubly distilled water. After the final wash, OD of the nanorod suspension was measured at 800 nm using a UV-Vis spectrophotometer. The amount of NaBH₄ added was adjusted based on the OD of the sample. For OD = 1, 100 μ L of freshly prepared 50 mM NaBH₄ was added to the nanorod solution. The mixture was gently stirred for 1 hour at room temperature to allow hydride ions to displace CTAB from the gold surface. Immediately following NaBH₄ treatment, 100 μ L of a 10mM ethanolic MUA was added to the solution to facilitate ligand exchange. The thiol groups in MUA rapidly bind to the gold surface, replacing CTAB and forming a stable monolayer. The solution was incubated overnight at room temperature to ensure complete ligand exchange. The following day, excess unbound MUA was removed by centrifugation and redispersion in doubly distilled water. The nanorods were then characterized by DLS and ζ -potential measurements.

7.9.2 MUTAB stabilized AuNRs

The functionalization protocol was adapted from a previously reported method and modified to suit the specific requirements of this study.^[219] The following describes a representative procedure using a 2 mL AuNR suspension, consistent with conditions used during experimental optimization. AuNRs were first purified by two centrifugation steps at 10,000 \times g for 10 minutes each. After each step, the pellet was gently redispersed in Milli-Q water to remove unbound ligands and reaction byproducts. The purified suspension was then diluted up to fivefold with Milli-Q water and reconcentrated to 2 mL using 30 kDa MWCO centrifugal filters. Filtration was performed at 4,000 \times g for 3-5 minutes per cycle. This step served as a gentle washing method to exchange the medium while preserving colloidal stability.

For ligand exchange, the amount of MUTAB was calculated based on the total surface area of AuNRs in the 2 mL suspension. The surface area of a single nanorod was estimated from TEM data, and the total number of rods was determined from previously calculated particle concentrations. Using a MUTAB ligand footprint of 4.8 nm², a 100-fold molar excess of MUTAB relative to the estimated number of surface binding sites was used. The required amount of MUTAB was weighed, dissolved in 500 μ L of ethanol, and mixed with the AuNR suspension under continuous stirring. The mixture was kept in the dark and stirred at room temperature for at least 48 hours (typically over the weekend) to allow complete ligand exchange. Following incubation, excess MUTAB and residual CTAB were removed by centrifugation at 20,000 \times g for 10 minutes. The final pellet was redispersed in Milli-Q water to yield MUTAB-functionalized AuNRs.

CLP loading was then performed. A stock solution of CLP (0.5 mg/mL in *N,N*-Dimethylformamide (DMF)) was prepared, and the AuNR suspension was diluted tenfold with

Milli-Q water. CLP was added in an amount corresponding to 20 peptides per nanorod. The mixture was incubated at room temperature for 16 hours. After incubation, the sample was diluted 1:10 with water and washed five times using centrifugal filtration. The final volume was adjusted to 2 mL in Milli-Q water.

7.9.3 CdSe/CdS DiRs

The ligand exchange of CdSe/CdS DiRs was adapted from a previously reported method using AET, which demonstrated effective transfer of DiRs to the aqueous phase via thiol-mediated surface modification.^[160] Based on this precedent, a structurally similar ligand, AUT was selected for initial experiments. AUT features a thiol group for anchoring to the nanoparticle surface and a terminal primary amine for imparting positive surface charge. The extended aliphatic chain relative to AET was expected to enhance colloidal stability through increased steric hindrance and hydrophobic interactions.

The concentration of DiRs (~0.02 mM) was determined using UV-Vis absorbance and extinction coefficients calculated using established methods.^[379] Based on the known dimensions and concentration of the particles, the total surface area of the sample was estimated, allowing calculation of the ligand excess required for effective coverage. For the initial ligand exchange, 500 μ L of a 0.005 mM DiR solution in toluene was mixed with 1.5 mL of toluene and 2.0 mL of a 0.025 M methanolic AUT solution. The mixture was stirred at 800-1000 rpm for 10 minutes to facilitate ligand exchange on the nanoparticle surface. To transfer the particles to the aqueous phase, 5.0 mL of Milli-Q water was added directly to the reaction mixture, and the solution was stirred overnight (14-16 hours) at room temperature. The following day, the aqueous phase was isolated by centrifugation, washed with isopropanol to remove excess ligands and solvents, and redispersed in Milli-Q water.

While AUT successfully enabled aqueous transfer and initial stabilization, concerns remained regarding its long-term robustness under biologically relevant conditions. Although AUT contains a primary amine, which is generally more stable than secondary amines, primary amines can still engage in protonation-deprotonation equilibria in the presence of H_3O^+ or OH^- ions, which are common in buffered environments. These fluctuations can result in variable surface charge and affect colloidal stability. In contrast, quaternary ammonium ligands such as MUTAB possess a permanent positive charge, making them chemically more stable and better suited for systems exposed to pH variation. To improve stability, a dual-ligand strategy using AUT and MUTAB was tested. Ligand stock solutions were prepared at identical concentrations (0.236 M): AUT (0.0102 g in 180 μ L methanol) and MUTAB (0.0167 g in 180 μ L

ethanol). A diluted DiR solution (100 μ L sample + 100 μ L toluene) was split into four groups, each treated with a different AUT:MUTAB molar ratio.

Each sample was mixed with 1.0 mL Milli-Q water and left to stand overnight at room temperature. The next day, the aqueous phase was separated by centrifugation (max speed, 5 minutes, 2 mL Eppendorf tubes), and the upper organic phase was discarded. The aqueous dispersions were further washed and redispersed in Milli-Q water. Although this mixed-ligand strategy resulted in stable dispersions with moderately positive ζ -potentials, subsequent CLP loading failed. Despite maintaining colloidal stability, the CLP peptide did not effectively bind or associate with the ligand-coated DiRs, likely due to interference from the surface ligands—either through steric hindrance, competitive binding, or disrupted charge accessibility.

To address this, a modified one-step procedure was developed in which MUTAB ligand exchange and CLP loading were performed simultaneously. In this method, a DiR solution in toluene was mixed with a MUTAB solution in ethanol and a CLP stock solution (0.5 mg/mL in DMF). Milli-Q water was then added to initiate aqueous phase transfer, and the mixture was stirred overnight at room temperature. The following day, the aqueous layer was isolated by centrifugation and washed thoroughly with water using centrifugal filters to remove unbound ligand and peptide. The final dispersion volume was adjusted to 1 mL in Milli-Q water. This combined ligand/peptide functionalization approach produced DiRs that were both colloiddally stable and successfully CLP-loaded, overcoming the limitations of the two-step method and enabling use in subsequent encapsulation studies.

7.9.4 Gold Nanoparticles

The ligand exchange protocol was inspired by but adapted to directly replace CTAC with MUTAB, omitting the intermediate CTAB step.^[134] AuNPs were first concentrated and purified by centrifugation at 10,000 \times g for 15 minutes, repeated twice. The resulting pellet was redispersed and diluted to a final volume of 10 mL in Milli-Q water.

MUTAB was added in a calculated 100-fold molar excess relative to the estimated number of surface binding sites on the AuNPs. The required amount of MUTAB was dissolved in 100 μ L of ethanol and added to the AuNP suspension under continuous stirring. The mixture was stirred rigorously at room temperature in the dark and incubated overnight to allow ligand exchange. The next day, the nanoparticles were centrifuged at 10,000 \times g for 15 minutes to remove excess MUTAB and displaced CTAC. The pellet was redispersed in Milli-Q water, and a fresh 100 μ L ethanolic solution of MUTAB was added. This process—overnight stirring followed by centrifugation and redispersion—was repeated for a total of three ligand exchange

cycles to ensure thorough replacement of CTAC with MUTAB. After the final exchange step, the particles were washed one last time and redispersed in Milli-Q water for further use.

CLP loading was then carried out. A CLP stock solution (1 mg/mL in 1:1 DMF/water mixture) was prepared, and the AuNP dispersion was diluted tenfold with Milli-Q water. CLP was added in an amount corresponding to 30 peptides per nanoparticle. The mixture was incubated at room temperature for 16 hours. Following incubation, the sample was diluted 1:10 with water and washed five times using centrifugal filtration. The final volume was adjusted to 1 mL in Milli-Q water.

7.10 Protein Related Protocols

7.10.1 Protein Production and Purification

Protein purification and analysis were performed using either an ÄKTA pure 25 M or an ÄKTA go FPLC system (Cytiva). All buffers were prepared with ultrapure water, filtered, and degassed for at least 30 minutes before use.

7.10.1.1 Negatively Charged *T. maritima* Enc

The expression of Enc^(neg) was based on a previously published protocol with slight modifications.^[14] A starter culture was prepared by inoculating 5 mL of sterile LB medium (supplemented with 150 µg/mL ampicillin) with a cryo stock of *E. coli* C43 cells previously transformed with the Enc^(neg) plasmid (provided by a colleague). The culture was incubated overnight at 37 °C and 250 rpm. The next day, 4 mL of the preculture was added to 400 mL of TB containing ampicillin (150 µg/mL), and the cells were grown at 37 °C and 250 rpm to an OD₆₀₀ of 0.7. Protein expression was induced with 0.5 mM IPTG, and the culture was incubated for 24 hours at 37 °C. Cells were harvested by centrifugation at 4000 × g, and pellets were stored at -20 °C. For purification, cell pellets were resuspended in 20 mL of lysis buffer (50 mM tris, pH 9.0, 0.3 M NaCl) with 30 mg RNase A and 15 mg DNase I. Cells were lysed by sonication on ice using 15 cycles of 1-minute pulses at 60% amplitude, with 1-minute cooling intervals. The lysate was centrifuged at 14,000 × g for 20 minutes. The supernatant was collected, and MgCl₂ (2.5 mM) and CaCl₂ (0.5 mM) were added. The sample was incubated at 37 °C for at least 4 hours, then centrifuged again at 14,000 × g for 15 minutes.

To remove remaining *E. coli* proteins, the supernatant was heated at 65 °C for 15 minutes in a water bath and centrifuged again at 14,000 × g for 15 minutes. The clarified supernatant was subjected to ammonium sulfate precipitation (70% saturation). After centrifugation

(14,000 × g, 20 minutes), the pellet was resuspended in 10 mL of 50 mM tris buffer (pH 9.0), and a second ammonium sulfate precipitation was performed. The resulting pellet was resuspended in 50 mL of 50 mM tris buffer (pH 9.0).

The sample was purified using ion-exchange chromatography on a 5 mL HiTrap™ Q HP column (Cytiva), with a linear NaCl gradient from 0 M to 1 M. Fractions containing Enc^(neg) and nanoparticle-loaded Enc^(neg) were pooled and concentrated to 1.5 mL using a centrifugal filter unit. Further purification was done via size-exclusion chromatography (SEC) using a Superose 6 Increase 10/300 GL column (Cytiva) with SEC buffer (20 mM tris, pH 7.5, 0.3 M NaCl). For crystallization, each sample was run through SEC three times to achieve high purity.

7.10.1.2 *M. xanthus* encapsulin

The MxEnc was expressed in *E. coli* BL21(DE3) cells using a procedure adapted from the Enc^(neg) protocol. Chemically competent *E. coli* BL21(DE3) cells were thawed on ice for 10 minutes along with 5 µL of DpnI-treated plasmid DNA. DNA was gently mixed with 100 µL of competent cells and incubated on ice for 30 minutes. Heat shock was performed at 42 °C for 45 seconds, followed by 2 minutes on ice. Cells were then recovered in 0.9 mL LB or SOB medium and incubated at 37 °C with shaking (225-250 rpm) for 1 hour. After centrifugation at 1000 × g for 1 minute, the supernatant was reduced to ~100 µL. The cells were resuspended in the remaining medium and plated on LB agar containing ampicillin (100 µg/mL). Plates were incubated overnight at 37 °C.

After incubation at 37 °C for 16 h, a preculture is prepared by incubation of single colonies in 5 mL sterile LB medium supplemented with ampicillin (150 µg/mL) at 37 °C and 250 rpm overnight. The next day, 4 mL of the preculture are added to 400 mL terrific broth (TB) containing ampicillin (150 µg/mL). The cells were grown at 37 °C and 250 rpm to an OD₆₀₀ of 0.6. Protein overexpression was induced by adding 160 µL of 0.2 M isopropyl-β-D-1-thiogalactopyranoside (IPTG). Expression was carried out at 18 °C for 36 hours. Cells were harvested via centrifugation at 4000 g. Pellets were stored at -20 °C until further use. Cell pellets were resuspended in lysis buffer (20 mM tris, 200 mM NaCl, pH 8.0) supplemented with DNase I, RNase A, and lysozyme. Cells were lysed by sonication, and lysates were clarified by centrifugation at 14,000 × g for 15 minutes. The supernatant was supplemented with 125 µL of 0.5 M MgCl₂ and 25 µL of 0.5 M CaCl₂ and incubated overnight at 37 °C. After incubation, the sample was centrifuged again at 14,000 × g for 15 minutes.

Remaining soluble contaminants were removed by heat precipitation at 60 °C for 15 minutes. The solution was clarified by centrifugation at 14,000 × g for 15 minutes and proteins were precipitated by ammonium sulfate at 70% saturation. The protein pellet was resuspended in

tris buffer (20 mM tris, pH 8.0) and purified by ion-exchange chromatography (IEC) using a 5 ml HiTrap™ Q HP anion exchange column (Cytiva) with a linear gradient from 0 M to 1 M NaCl. Samples were collected and concentrated with centrifugal filter unit to a final volume of 1.5 mL. Final purification was performed using size-exclusion chromatography (SEC) on a HiPrep™ Sephacryl™ S-500 HR column (Cytiva) in buffer (20 mM tris, 200 mM NaCl, pH 8.0).

7.10.2 Dis and Reassembly

7.10.2.1 *T. maritima* encapsulin

T. maritima encapsulin disassembly was induced by exposure to acidic conditions. Specifically, 1.0 mg of encapsulin (52.2 µL of a 19.2 mg/mL stock in storage buffer: 20 mM tris, pH 7.5, 0.3 M NaCl) was diluted 1:10 with 10 mM phosphate buffer at pH 1.0 and incubated at 4 °C for 1 hour. Reassembly was triggered by a 1:100 dilution into reassembly buffer (20 mM phosphate, pH 7.0) followed by overnight incubation at room temperature. The reassembled sample was then concentrated using a centrifugal filter unit.

7.10.2.2 *M. xanthus* encapsulin

For disassembly of MxEnc, it was first precipitated by adding PEG 8000 and NaCl to final concentrations of 10% and 0.5 M, respectively. The mixture was incubated on ice for 1 hour and centrifuged at 21,000 × g for 45 minutes. The supernatant was removed, and the pellet was gently resuspended in freshly prepared 8 M urea dissolved in 20 mM phosphate, 0.1 M NaCl pH 7.0 buffer. The sample was incubated on ice for 3 hours to allow complete disassembly. Reassembly was initiated by removing urea using a 10,000 MWCO centrifugal concentrator, followed by a 10-fold dilution of the protein in the same phosphate buffer (20 mM phosphate, 0.1 M NaCl, pH 7.0). The sample was incubated at 4 °C overnight to promote reassembly. The reassembled sample was then concentrated using a centrifugal filter unit.

7.10.3 Nanomaterial encapsulation

TmEnc: Cargo encapsulation into *T. maritima* encapsulin was achieved by diluting the disassembled protein in reassembly buffer. Nanomaterials (DiRs dyes or AuNRs) were added dropwise into the protein solution. The relative amounts of protein and cargo were varied systematically. Initial experiments were carried out at a 1:1 protein-to-cargo ratio, which was subsequently adjusted to alternative ratios to improve encapsulation efficiency.

MxEnc: For encapsulation with *M. xanthus* encapsulin, optimal results were obtained when the AuNPs were first diluted in reassembly buffer, followed by the dropwise addition of protein. Encapsulation was tested at a 1:1 protein-to-cargo ratio.

7.11 Surface Deposition

To evaluate conditions suitable for surface deposition, ethanol was introduced into aqueous protein solutions to promote faster evaporation and improved film formation. Since water alone has high surface tension and evaporates slowly, mixtures of water and ethanol were tested. TmEnc was first transferred from tris buffer to pure water using centrifugal filtration. The resulting 1 mg/mL protein solution was mixed with ethanol to final concentrations of 10%, 20%, 30%, 40%, and 50% (v/v). Samples were incubated at room temperature, and DLS measurements were taken after 4 hours and again after 24 hours to monitor changes in size distribution and aggregation. After 24 hours, selected samples were also analyzed by TEM. TEM images showed visible aggregation at higher ethanol concentrations, with proteins clustered together and lacking defined cage morphology. These results indicate that while TmEnc retains stability up to 50% ethanol in solution, structural integrity is compromised over time. Full DLS and TEM data are provided in the Appendix (Figure 8.19-8.20).

8. Appendix

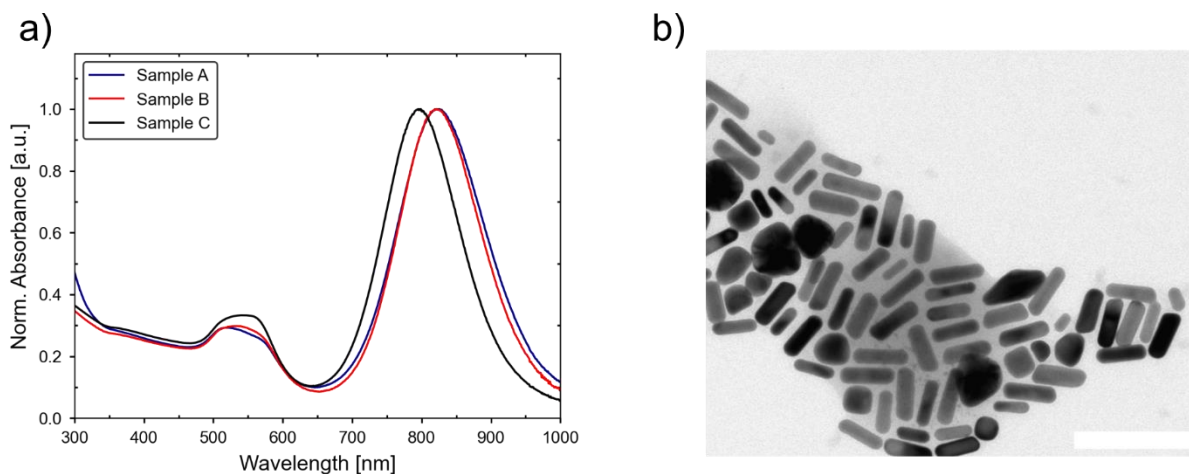


Figure 8.1: Normalized UV-Vis absorption spectra and TEM image of AuNRs synthesized using 37.5 μL NaOH. Scale bar is 100 nm.

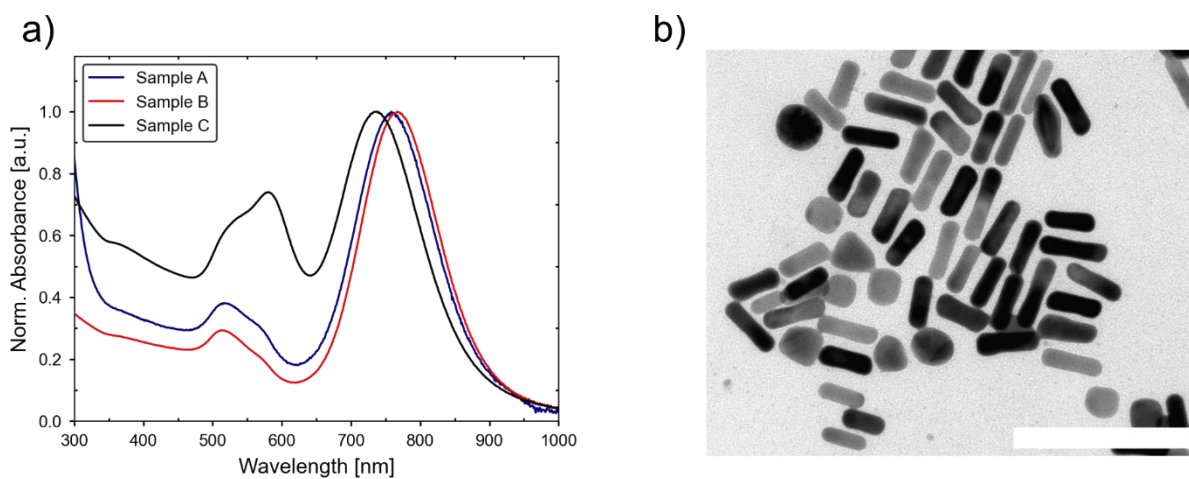


Figure 8.2: Normalized UV-Vis absorption spectra and TEM image of AuNRs synthesized using 45 μL NaOH. Scale bar is 100 nm.

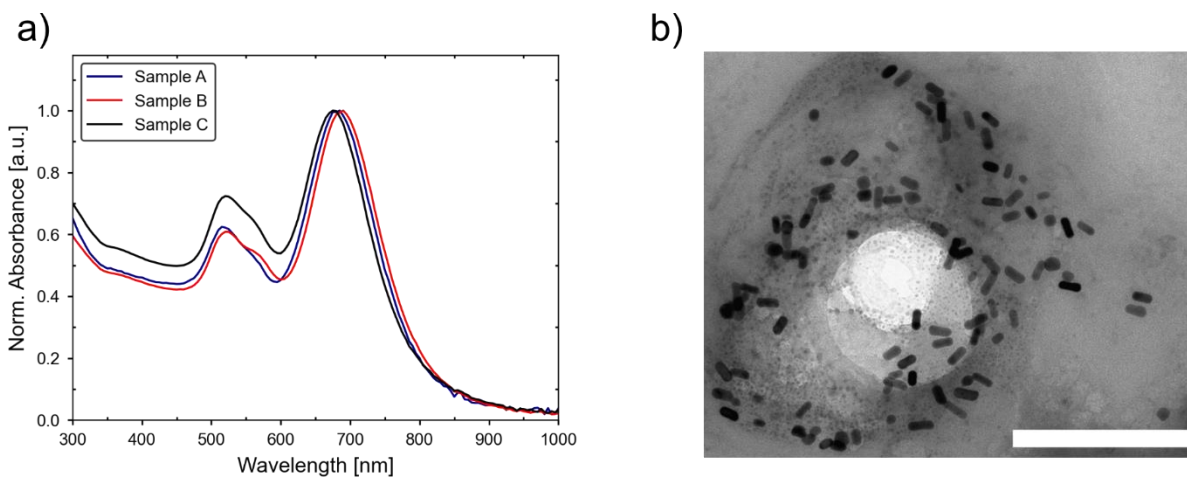


Figure 8.3: Normalized UV-Vis absorption spectra and TEM image of AuNRs synthesized using 100 μ L NaOH. Scale bar is 100 nm.

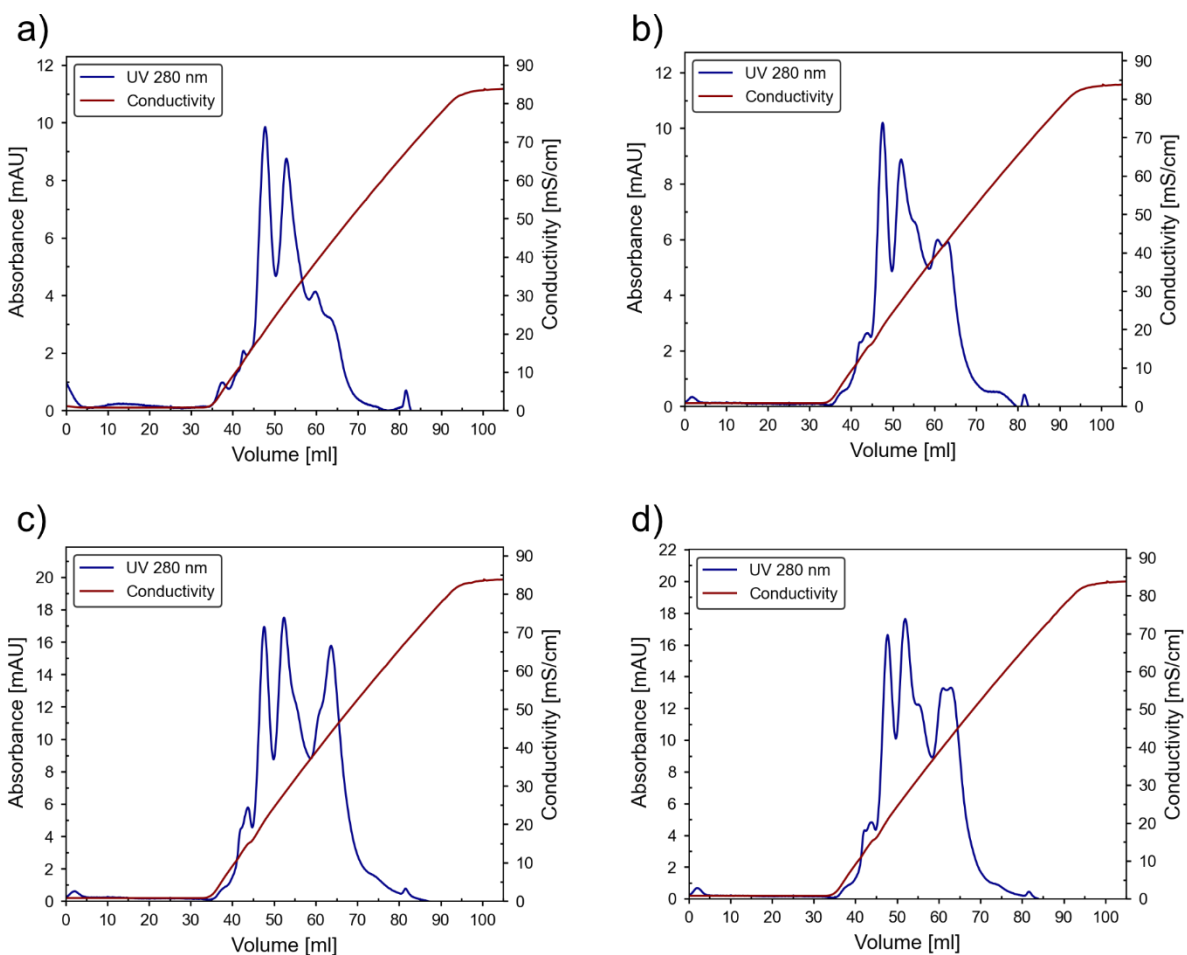


Figure 8.4: Ion exchange chromatograms of MxEnc at different OD₆₀₀. a) 0.2, b) 0.4, c) 0.6, d) 0.75

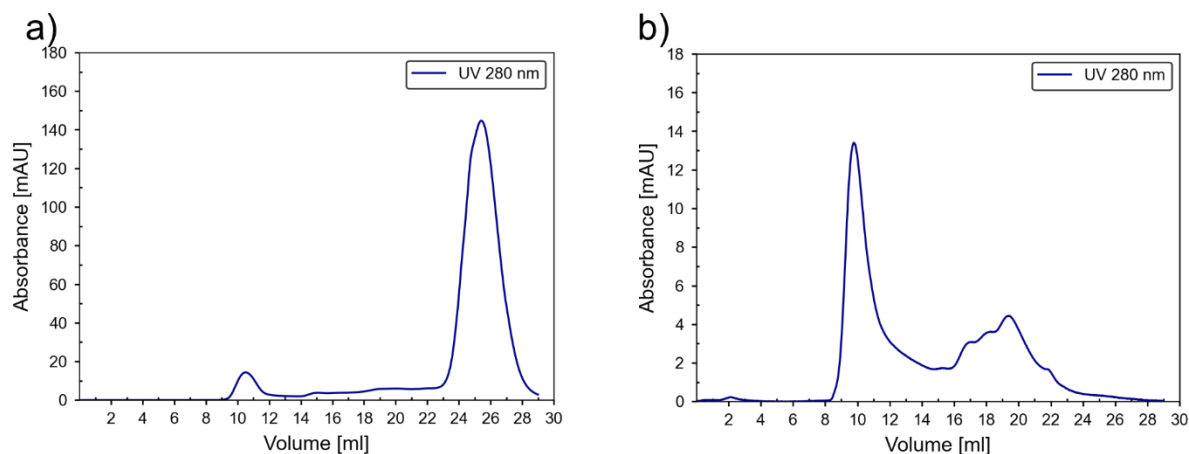


Figure 8.5: Size exclusion chromatograms of MxEnc at two different OD₆₀₀. a) 0.6 and b) 0.75

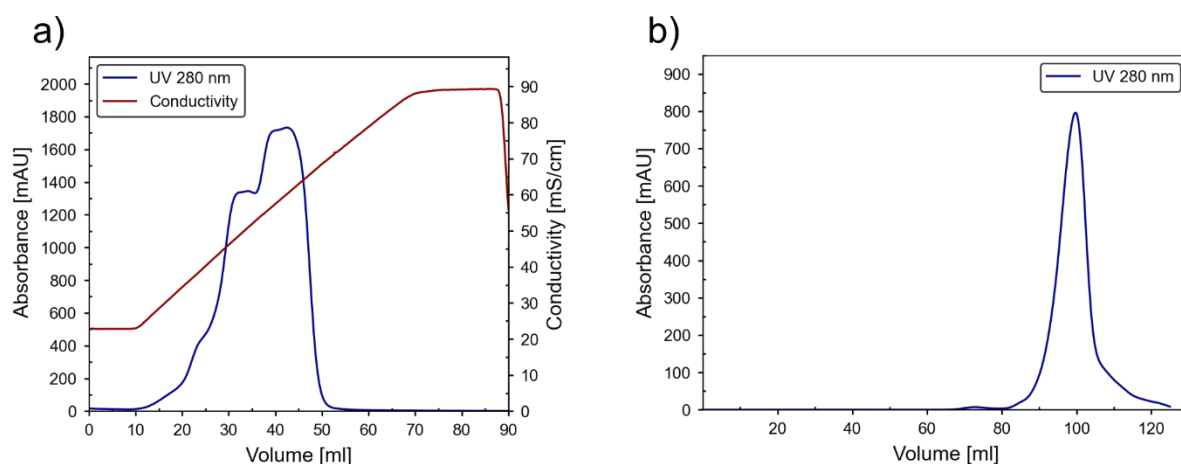


Figure 8.6: Ion exchange and size exclusion chromatograms of MxEnc. Samples were lysed using DNase
 a) IEC chromatogram for MxEnc. Protein elution from 45 mS/cm to 60 mS/cm. b) SEC chromatogram for MxEnc. Protein elution at 100 ml. Absorbance was monitored at 280 nm (blue). Conductivity is shown in red.

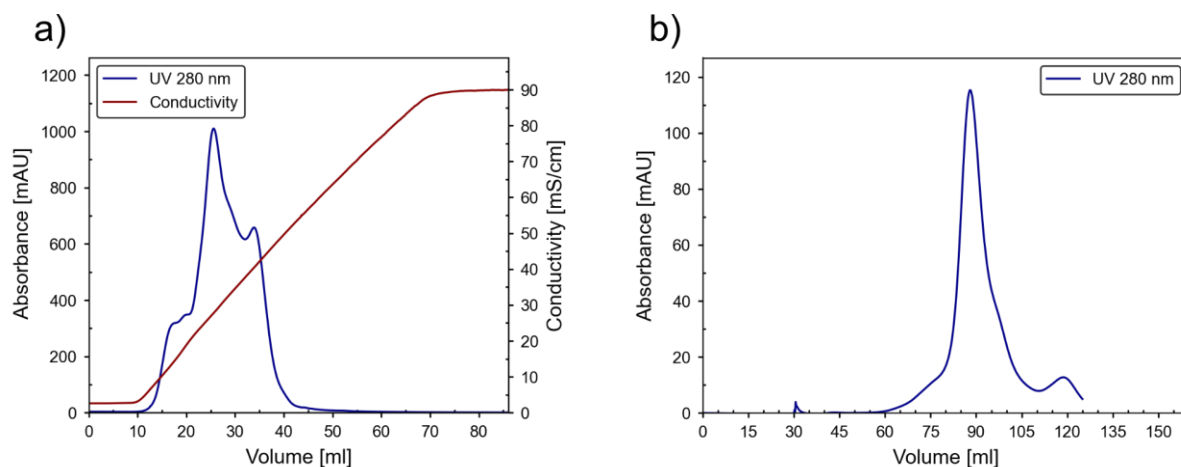


Figure 8.7: : Ion exchange and size exclusion chromatograms of MxEnc. Samples were expressed in LB media for 18h and no heat precipitation. a) IEC chromatogram for MxEnc. Protein elution from 15 mS/cm to 40

mS/cm. b) SEC chromatogram for **MxEnc**. Protein elution at 90 ml. Absorbance was monitored at 280 nm (blue). Conductivity is shown in red.

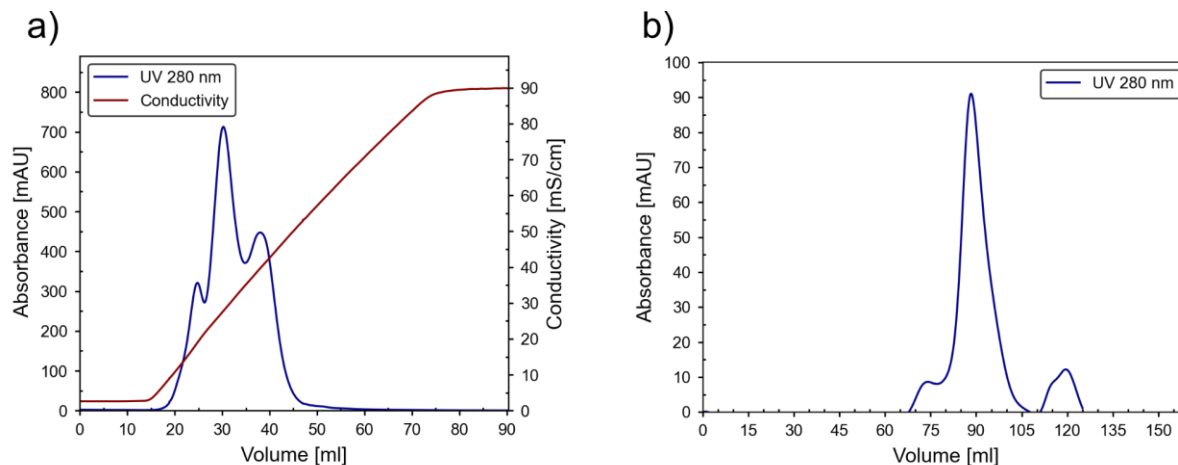


Figure 8.8: Ion exchange and size exclusion chromatograms of MxEnc. Samples were expressed in LB media for 18h and with heat precipitation at 60 °C. a) IEC chromatogram for **MxEnc**. Protein elution from 15 mS/cm to 40 mS/cm. b) SEC chromatogram for **MxEnc**. Protein elution at 90 ml. Absorbance was monitored at 280 nm (blue). Conductivity is shown in red.

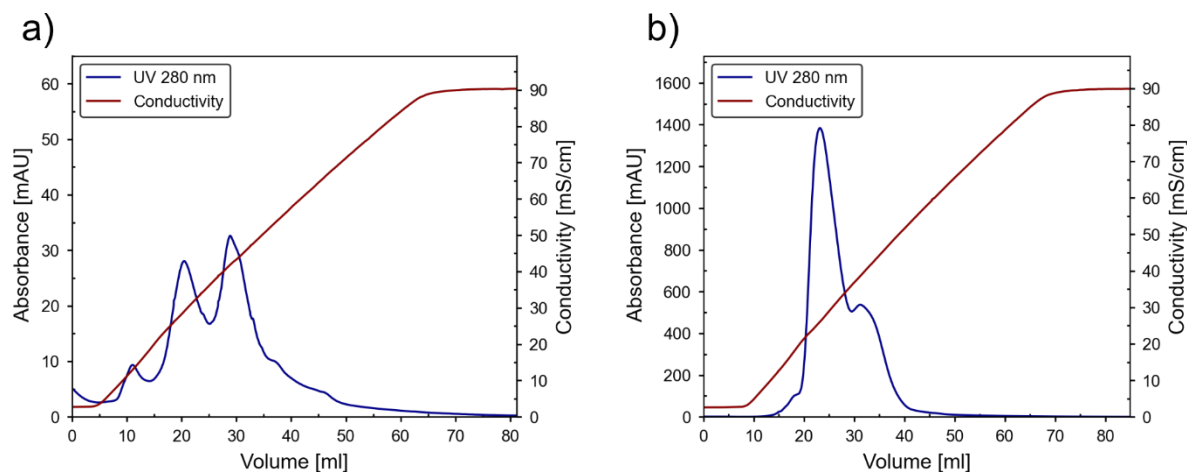


Figure 8.9: Ion exchange chromatograms of MxEnc. Samples were expressed in TB media for 18h and without and with heat precipitation at 60 °C. a) IEC chromatogram for **MxEnc** without heat precipitation. Protein elution from 25 mS/cm to 45 mS/cm. b) IEC chromatogram for **MxEnc** with heat precipitation. Protein elution around 25 mS/cm. Absorbance was monitored at 280 nm (blue). Conductivity is shown in red.

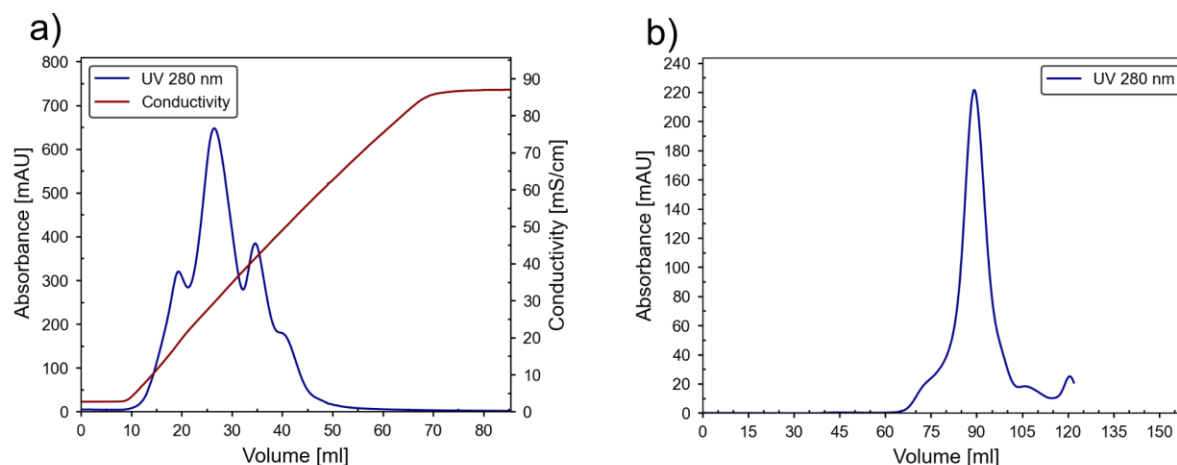


Figure 8.10: Ion exchange and size exclusion chromatograms of MxEnc. Samples were expressed in LB media for 72h and without heat precipitation. a) IEC chromatogram for MxEnc. Protein elution from 20 mS/cm to 40 mS/cm. b) SEC chromatogram for MxEnc. Protein elution at 90 ml. Absorbance was monitored at 280 nm (blue). Conductivity is shown in red.

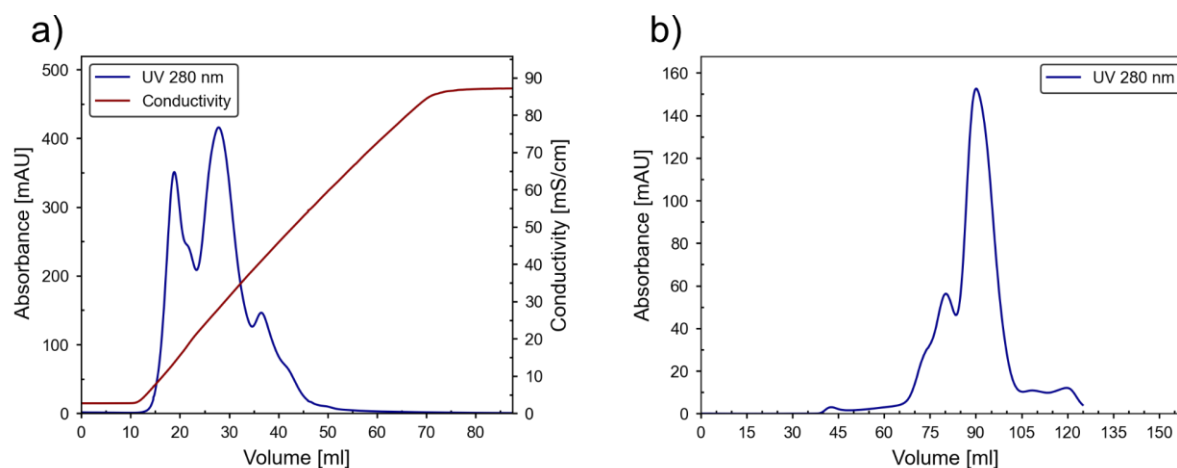


Figure 8.11: Ion exchange and size exclusion chromatograms of MxEnc. Samples were expressed in LB media for 72h and with heat precipitation at 60 °C. a) IEC chromatogram for MxEnc. Protein elution from 15 mS/cm to 30 mS/cm. b) SEC chromatogram for MxEnc. Protein elution around 80 and around 95 ml. Absorbance was monitored at 280 nm (blue). Conductivity is shown in red.

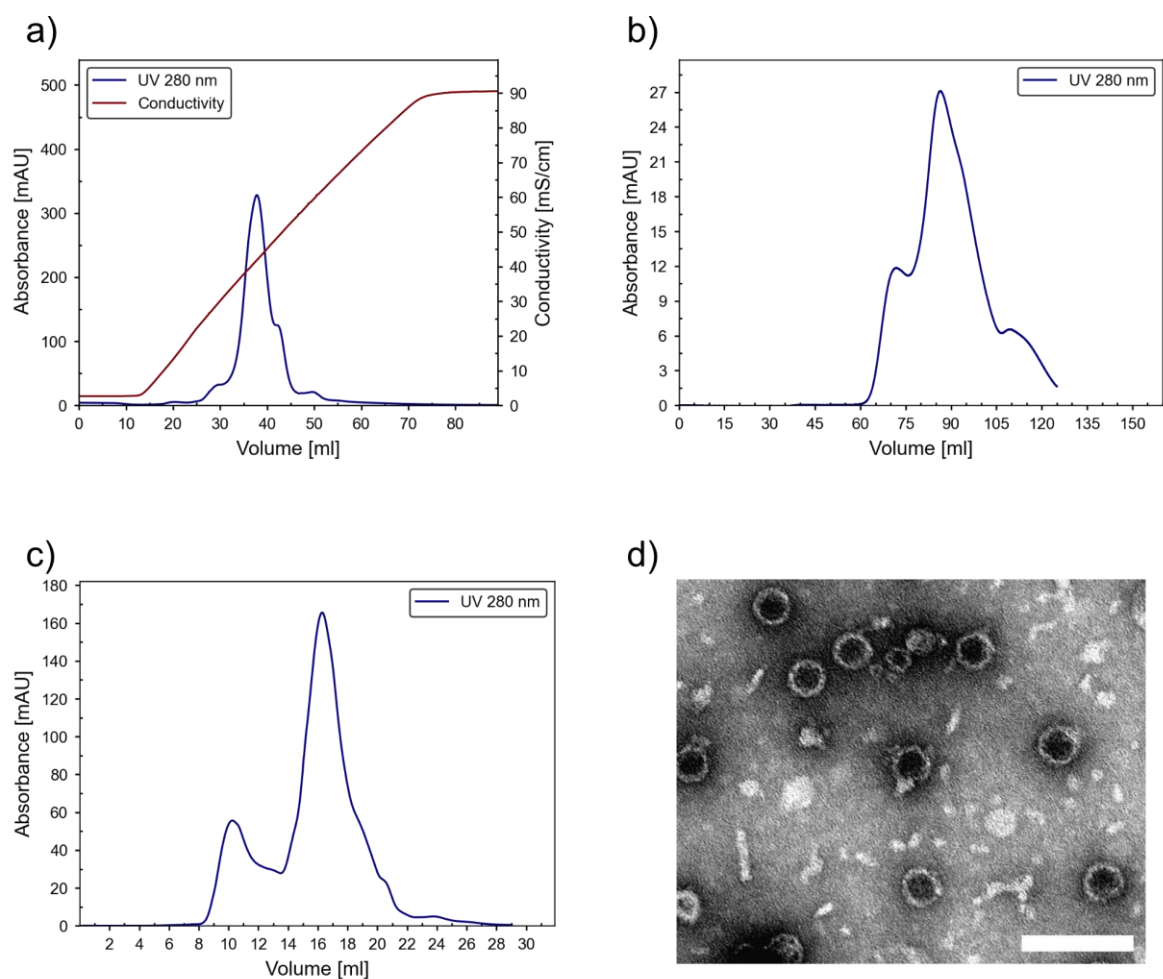


Figure 8.12: Ion exchange, size exclusion chromatograms and stained TEM image of T = 3 state of MxEnc. Samples were expressed in TB media for 72h and with heat precipitation at 60 °C. a) IEC chromatogram of **MxEnc**. Protein elution around 46 mS/cm. b) SEC chromatogram of **MxEnc** on Sephacryl S-500 HR column. Protein elution around 70, corresponding to T = 3 state and around 95 ml, corresponding to T = 1 state. c) SEC chromatogram of **MxEnc** on Superose 6 Increase column. Protein elution around 10 ml and 17 ml Absorbance was monitored at 280 nm (blue). Conductivity is shown in red. d) Stained TEM image of the first peak (T = 3 state).

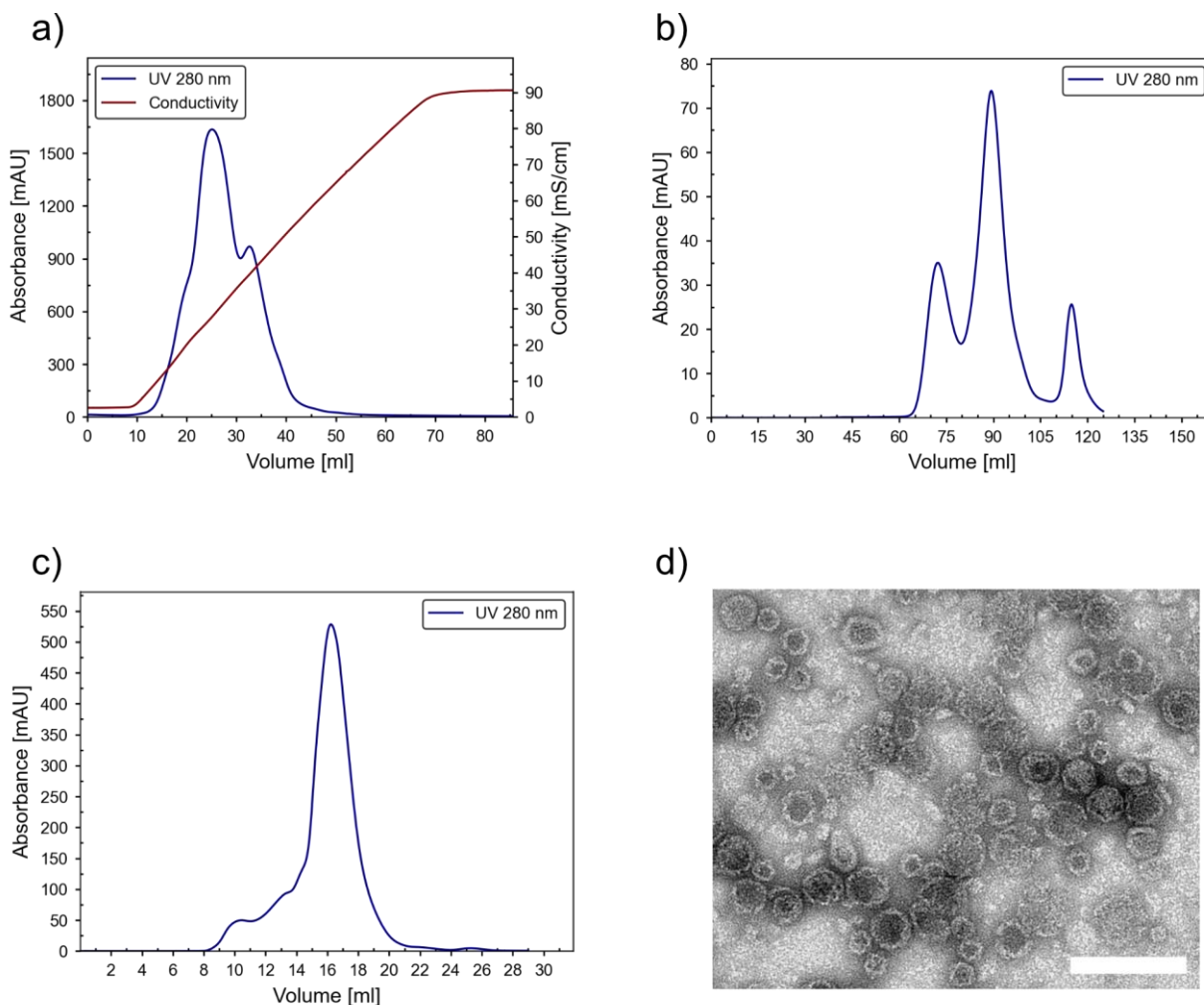


Figure 8.13: Ion exchange, size exclusion chromatograms and stained TEM image of T = 3 state of MxEnc. Samples were expressed in TB media for 72h and without heat precipitation. a) IEC chromatogram of MxEnc. Protein elution around 46 mS/cm. b) SEC chromatogram of MxEnc on Sephacryl S-500 HR column. Protein elution around 75 ml, corresponding to T = 3 state; around 95 ml, corresponding to T = 1 state and around 110 ml, corresponding to subunits or smaller proteins. c) SEC chromatogram of MxEnc on Superose 6 Increase column. Protein elution dominated by peak around 17 ml. Absorbance was monitored at 280 nm (blue). Conductivity is shown in red. d) Stained TEM image of the first peak (T = 3 state)

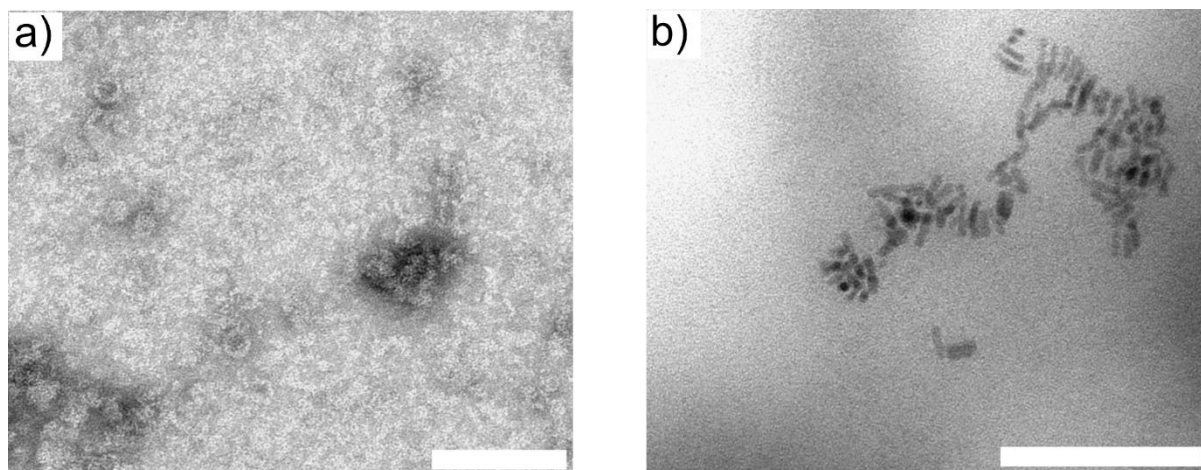


Figure 8.14: TEM images from encapsulation trials using DiRs and *T. maritima* encapsulin in HEPES buffer. a) Stained image showing protein cages. b) unstained image showing DiRs. Scale bar is 100 nm.

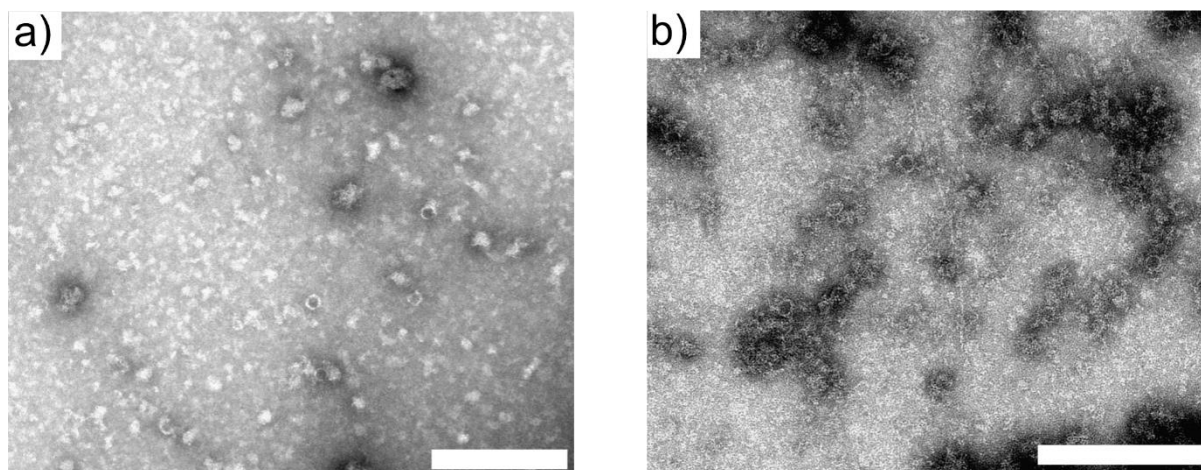


Figure 8.15: Stained TEM images of encapsulation of CdSe/CdS DiRs into *T. maritima* encapsulin at different DiR-to-protein ratios. a) 1:30 ratio. b) 1:40 ratio

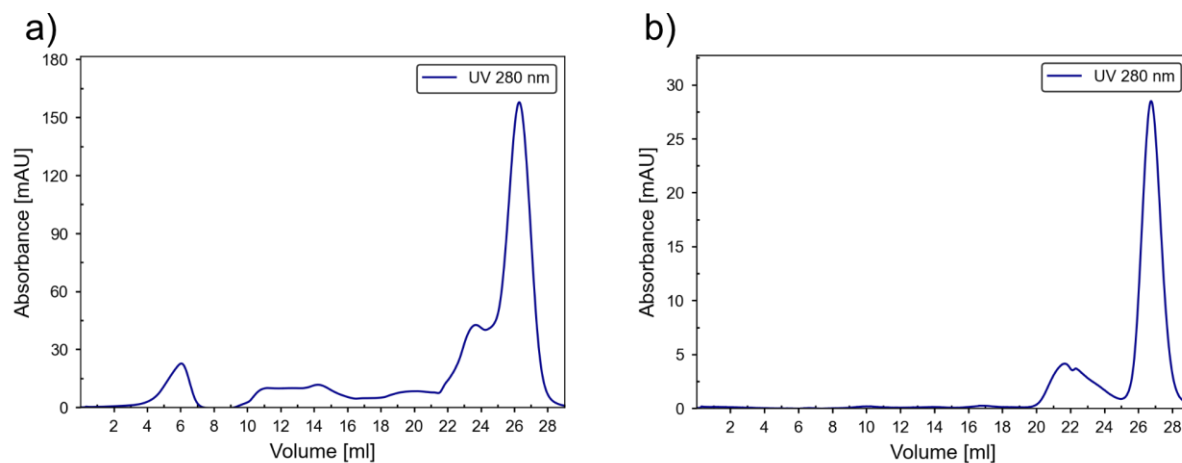


Figure 8.16: Size exclusion chromatograms of T = 1 post reassembly. Disassembly was done using a) 6 M GuHCl, b) 8 M urea. Absorbance was monitored at 280 nm (blue).

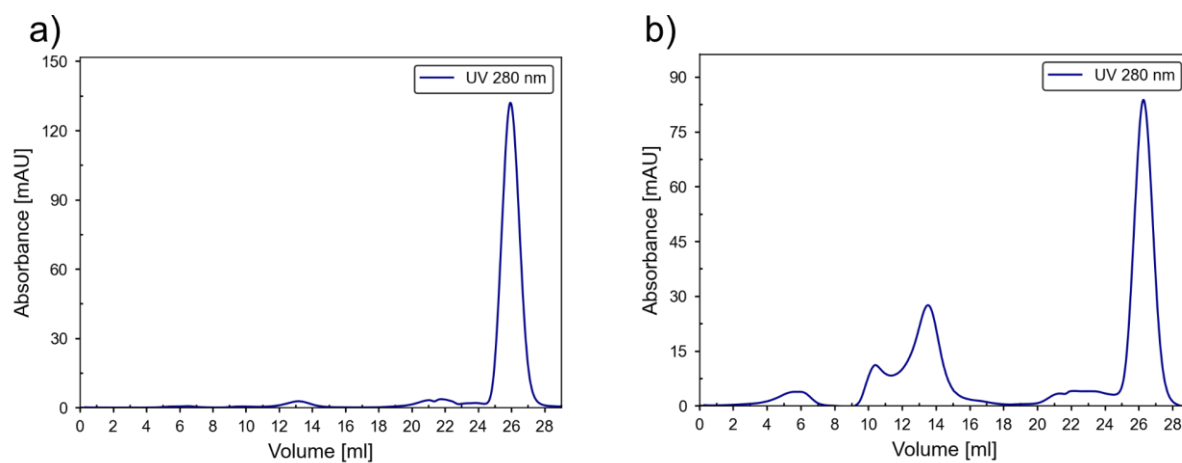


Figure 8.17: Size exclusion chromatograms of T = 3 post reassembly. Disassembly was done using a) 6 M GuHCl, b) 8 M urea. Absorbance was monitored at 280 nm (blue).

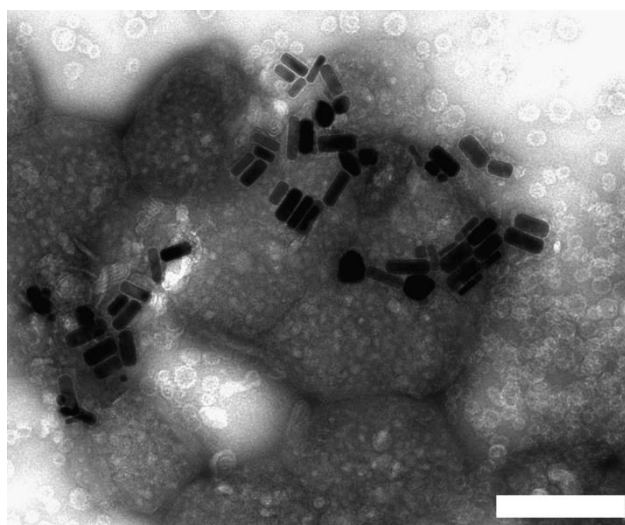


Figure 8.18: Stained TEM image of AuNRs and MxWEnc from the encapsulation trial.

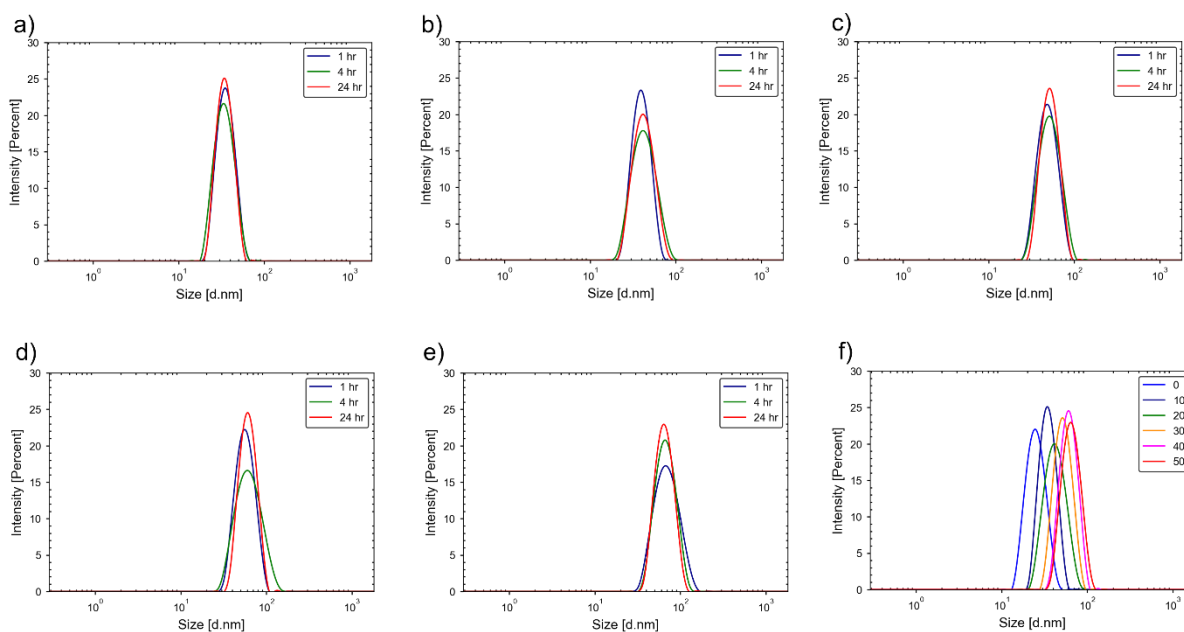


Figure 8.19: Hydrodynamic size distribution of TmEnc in ethanol-water mixture. Intensity weighted size distribution of TmEnc over the duration of 24 hours: a) in 10% ethanol, b) in 20% ethanol, c) in 30% ethanol, d) in 40% ethanol, and e) in 50% ethanol. f) Intensity weighted size distribution of TmEnc after 24 hours in no ethanol, 10%, 20%, 30%, 40% and 50% ethanol.

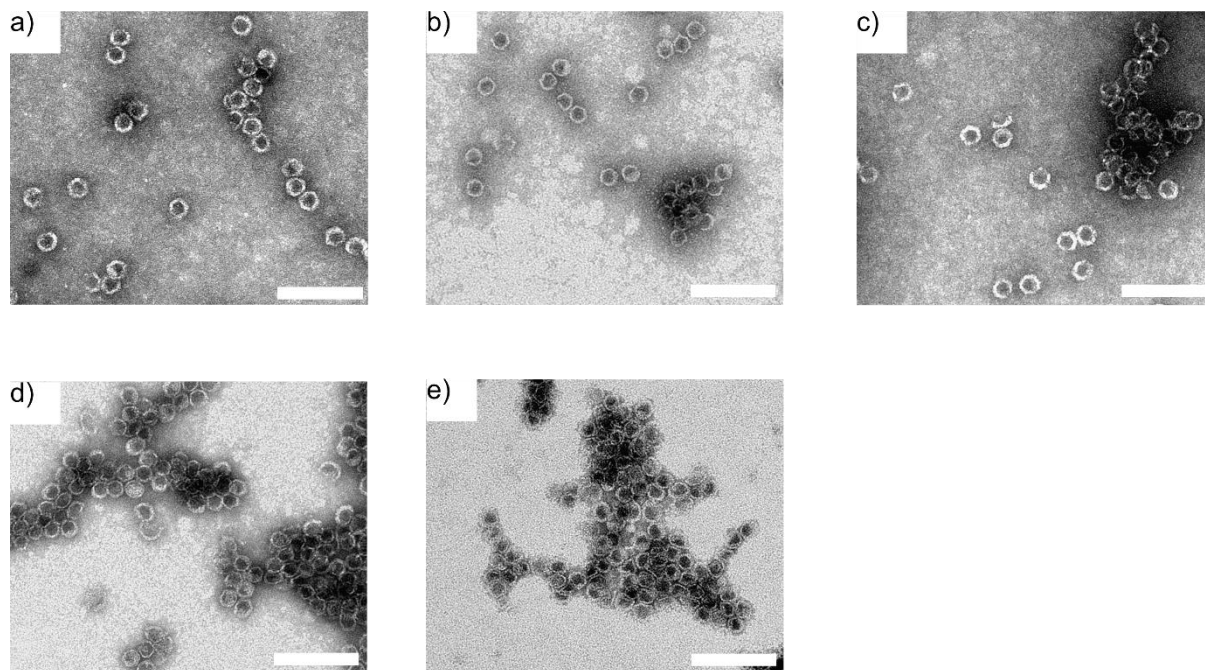


Figure 8.20: Stained TEM images of TmEnc in ethanol-water mixture. a) 10% ethanol, b) 20% ethanol, c) 30% ethanol, d) 40% ethanol, and e) 50% ethanol

9. Bibliography

Uncategorized References

- [1] Z. Guo, J. J. Richardson, B. Kong, K. Liang, *Science Advances* **2020**, *6*, eaaz0330.
- [2] J.-H. Choy, J.-M. Oh, M. Park, K.-M. Sohn, J.-W. Kim, *Advanced Materials* **2004**, *16*, 1181-1184.
- [3] M. Madsen, K. V. Gothelf, *Chemical Reviews* **2019**, *119*, 6384-6458.
- [4] J. Seaberg, H. Montazerian, M. N. Hossen, R. Bhattacharya, A. Khademhosseini, P. Mukherjee, *ACS Nano* **2021**, *15*, 2099-2142.
- [5] E. Ruiz-Hitzky, M. Darder, P. Aranda, K. Ariga, *Advanced Materials* **2010**, *22*, 323-336.
- [6] W. Park, H. Shin, B. Choi, W.-K. Rhim, K. Na, D. Keun Han, *Progress in Materials Science* **2020**, *114*, 100686.
- [7] P.-S. Huang, S. E. Boyken, D. Baker, *Nature* **2016**, *537*, 320-327.
- [8] M. Uchida, M. T. Klem, M. Allen, P. Suci, M. Flenniken, E. Gillitzer, Z. Varpness, L. O. Liepold, M. Young, T. Douglas, *Advanced Materials* **2007**, *19*, 1025-1042.
- [9] T. G. W. Edwardson, M. D. Levasseur, S. Tetter, A. Steinauer, M. Hori, D. Hilvert, *Chemical Reviews* **2022**, *122*, 9145-9197.
- [10] T. W. Giessen, *Annual review of biochemistry* **2022**, *91*, 353-380.
- [11] J. A. Jones, T. W. Giessen, *Biotechnology and bioengineering* **2021**, *118*, 491-505.
- [12] D. Diaz, X. Vidal, A. Sunna, A. Care, *ACS Applied Materials & Interfaces* **2021**, *13*, 7977-7986.
- [13] A. Van de Steen, H. C. Wilkinson, P. A. Dalby, S. Frank, *ACS Appl Bio Mater* **2024**, *7*, 3660-3674.
- [14] M. Kunzle, J. Mangler, M. Lach, T. Beck, *Nanoscale* **2018**, *10*, 22917-22926.
- [15] P. Lohner, M. Zmyslia, J. Thurn, J. K. Pape, R. Gerasimaitė, J. Keller-Findeisen, S. Groer, B. Deuringer, R. Süß, A. Walther, S. W. Hell, G. Lukinavičius, T. Hugel, C. Jessen-Trefzer, *Angewandte Chemie International Edition* **2021**, *60*, 23835-23841.
- [16] M. C. Jenkins, S. Lutz, *ACS Synthetic Biology* **2021**, *10*, 857-869.
- [17] L. H. L. Lua, N. K. Connors, F. Sainsbury, Y. P. Chuan, N. Wibowo, A. P. J. Middelberg, *Biotechnology and Bioengineering* **2014**, *111*, 425-440.
- [18] A. Van de Steen, R. Khalife, N. Colant, H. Mustafa Khan, M. Deveikis, S. Charalambous, C. M. Robinson, R. Dabas, S. Esteban Serna, D. A. Catana, K. Pildish, V. Kalinovskiy, K. Gustafsson, S. Frank, *Synthetic and Systems Biotechnology* **2021**, *6*, 231-241.

- [19] A. N. Gabashvili, N. S. Chmelyuk, V. A. Sarkisova, P. A. Melnikov, A. S. Semkina, A. A. Nikitin, M. A. Abakumov, *International Journal of Molecular Sciences* **2022**, *23*, 15591.
- [20] T. W. Giessen, B. J. Orlando, A. A. Verdegaal, M. G. Chambers, J. Gardener, D. C. Bell, G. Birrane, M. Liao, P. A. Silver, *eLife* **2019**, *8*, e46070.
- [21] J. Zheng, X. Cheng, H. Zhang, X. Bai, R. Ai, L. Shao, J. Wang, *Chemical Reviews* **2021**, *121*, 13342-13453.
- [22] H. Chen, L. Shao, Q. Li, J. Wang, *Chemical Society Reviews* **2013**, *42*, 2679-2724.
- [23] X. Bai, H. Li, Y. Peng, G. Zhang, C. Yang, W. Guo, X. Han, J. Li, R. Chen, C. Qin, *The Journal of Physical Chemistry C* **2022**, *126*, 2699-2707.
- [24] C. She, A. Demortière, E. V. Shevchenko, M. Pelton, *The Journal of Physical Chemistry Letters* **2011**, *2*, 1469-1475.
- [25] R. P. Feynman, *Engineering and Science* **1960**, *23*, 22-36.
- [26] (Eds.: M. Krummenacker, J. Lewis), Wiley, New York, **1995**.
- [27] *Handbook of Nanostructured Materials and Nanotechnology*, Academic Press, New York, **2000**.
- [28] *Nanomaterials: Synthesis, Properties and Applications*, Institute of Physics Publishing Philadelphia, **1996**.
- [29] V. M. Shalaev, *Nano-structured Materials: Clusters, Composites, and Thin Films*, American Chemical Society, Washington, DC, **1997**.
- [30] A. P. Alivisatos, *Science* **1996**, *271*, 933-937.
- [31] M. A. Boles, D. Ling, T. Hyeon, D. V. Talapin, *Nat Mater* **2016**, *15*, 141-153.
- [32] H. Gleiter, *Acta Materialia* **2000**, *48*, 1-29.
- [33] C. B. Murray, C. R. Kagan, M. G. Bawendi, *Annual Review of Materials Science* **2000**, *30*, 545-610.
- [34] G. Schmid, *Chemical Reviews* **2002**, *92*, 1709-1727.
- [35] M. Niederberger, G. Garnweitner, *Chemistry* **2006**, *12*, 7282-7302.
- [36] M. R. Jones, N. C. Seeman, C. A. Mirkin, *Science* **2015**, *347*, 1260901.
- [37] C. Joachim, J. K. Gimzewski, A. Aviram, *Nature* **2000**, *408*, 541-548.
- [38] L. Jacak, P. Hawrylak, A. Wojs, *Quantum Dots*, Springer Berlin Heidelberg, **2013**.
- [39] E. Roduner, *Chem Soc Rev* **2006**, *35*, 583-592.
- [40] C. Zhu, G. Yang, H. Li, D. Du, Y. Lin, *Anal Chem* **2015**, *87*, 230-249.
- [41] J. A. Hubbell, A. Chilkoti, *Science* **2012**, *337*, 303-305.
- [42] J. C. Hsu, Z. Tang, O. E. Eremina, A. M. Sofias, T. Lammers, J. F. Lovell, C. Zavaleta, W. Cai, D. P. Cormode, *Nat Rev Methods Primers* **2023**, *3*.
- [43] X. Peng, L. Peng, C. Wu, Y. Xie, *Chem Soc Rev* **2014**, *43*, 3303-3323.

- [44] G. Chen, J. Seo, C. Yang, P. N. Prasad, *Chem Soc Rev* **2013**, *42*, 8304-8338.
- [45] S. Guo, E. Wang, *Nano Today* **2011**, *6*, 240-264.
- [46] S. Sarkar, N. T. Ponce, A. Banerjee, R. Bandopadhyay, S. Rajendran, E. Lichtfouse, *Environ Chem Lett* **2020**, *18*, 1569-1580.
- [47] J. Chang, L. Zhang, P. Wang, *Environmental Science: Nano* **2018**, *5*, 811-836.
- [48] N. Savage, M. S. Diallo, *Journal of Nanoparticle Research* **2005**, *7*, 331-342.
- [49] Y. Shi, M. Liu, F. Deng, G. Zeng, Q. Wan, X. Zhang, Y. Wei, *J Mater Chem B* **2017**, *5*, 194-206.
- [50] K. D. Patel, R. K. Singh, H.-W. Kim, *Materials Horizons* **2019**, *6*, 434-469.
- [51] T. Traykova, C. Aparicio, M. P. Ginebra, J. A. Planell, *Nanomedicine (Lond)* **2006**, *1*, 91-106.
- [52] K. N. Thakkar, S. S. Mhatre, R. Y. Parikh, *Nanomedicine* **2010**, *6*, 257-262.
- [53] M. A. Bhosale, B. M. Bhanage, *Current Organic Chemistry* **2015**, *19*, 708-727.
- [54] K. Susumu, H. T. Uyeda, I. L. Medintz, T. Pons, J. B. Delehanty, H. Mattoussi, *J Am Chem Soc* **2007**, *129*, 13987-13996.
- [55] M. Yamada, M. Foote, T. W. Prow, *Wiley Interdiscip Rev Nanomed Nanobiotechnol* **2015**, *7*, 428-445.
- [56] G. Pasparakis, *Wiley Interdiscip Rev Nanomed Nanobiotechnol* **2022**, *14*, e1817.
- [57] A. Corma, H. Garcia, *Chem Soc Rev* **2008**, *37*, 2096-2126.
- [58] M. Jeyaraj, S. Gurunathan, M. Qasim, M. H. Kang, J. H. Kim, *Nanomaterials (Basel)* **2019**, *9*.
- [59] L. Zhao, L. Hu, X. Fang, *Advanced Functional Materials* **2012**, *22*, 1551-1566.
- [60] Z. Mamiyev, N. O. Balayeva, *Materials Today Sustainability* **2023**, *21*.
- [61] H. M. Xiong, *Adv Mater* **2013**, *25*, 5329-5335.
- [62] A. Hirsch, *Angewandte Chemie International Edition* **2002**, *41*, 1853-1859.
- [63] S. Iijima, *Nature* **1991**, *354*, 56-58.
- [64] K. S. Novoselov, A. K. Geim, S. V. Morozov, D. Jiang, Y. Zhang, S. V. Dubonos, I. V. Grigorieva, A. A. Firsov, *Science* **2004**, *306*, 666-669.
- [65] A. Biswas, I. S. Bayer, A. S. Biris, T. Wang, E. Dervishi, F. Faupel, *Adv Colloid Interface Sci* **2012**, *170*, 2-27.
- [66] N. Abid, A. M. Khan, S. Shujait, K. Chaudhary, M. Ikram, M. Imran, J. Haider, M. Khan, Q. Khan, M. Maqbool, *Adv Colloid Interface Sci* **2022**, *300*, 102597.
- [67] B. S. Murty, S. Ranganathan, *International Materials Reviews* **2013**, *43*, 101-141.
- [68] R. Janot, D. Guerard, *Progress in Materials Science* **2005**, *50*, 1-92.
- [69] T. Prasad Yadav, R. Manohar Yadav, D. Pratap Singh, *Nanoscience and Nanotechnology* **2012**, *2*, 22-48.

- [70] L. Carbone, C. Nobile, M. De Giorgi, F. D. Sala, G. Morello, P. Pompa, M. Hytch, E. Snoeck, A. Fiore, I. R. Franchini, M. Nadasan, A. F. Silvestre, L. Chiodo, S. Kudera, R. Cingolani, R. Krahn, L. Manna, *Nano Lett* **2007**, *7*, 2942-2950.
- [71] X. Ji, X. Song, J. Li, Y. Bai, W. Yang, X. Peng, *J Am Chem Soc* **2007**, *129*, 13939-13948.
- [72] W. Leng, P. Pati, P. J. Vikesland, *Environmental Science: Nano* **2015**, *2*, 440-453.
- [73] C. B. Whitehead, S. Özkar, R. G. Finke, *Materials Advances* **2021**, *2*, 186-235.
- [74] E. C. Vreeland, J. Watt, G. B. Schober, B. G. Hance, M. J. Austin, A. D. Price, B. D. Fellows, T. C. Monson, N. S. Hudak, L. Maldonado-Camargo, A. C. Bohorquez, C. Rinaldi, D. L. Huber, *Chemistry of Materials* **2015**, *27*, 6059-6066.
- [75] N. T. Thanh, N. Maclean, S. Mahiddine, *Chem Rev* **2014**, *114*, 7610-7630.
- [76] W. Ostwald, *Zeitschrift für Physikalische Chemie* **1900**, *34U*, 495-503.
- [77] Y. Dong, D. Zhang, D. Li, H. Jia, W. Qin, *Science China Materials* **2022**, *66*, 1249-1255.
- [78] P. W. Voorhees, *Journal of Statistical Physics* **1985**, *38*, 231-252.
- [79] A. Kraynov, T. E. Müller, *Concepts for the Stabilization of Metal Nanoparticles in Ionic Liquids, Vol. 7*, **2011**.
- [80] X. Peng, *Advanced Materials* **2003**, *15*, 459-463.
- [81] L. Manna, D. J. Milliron, A. Meisel, E. C. Scher, A. P. Alivisatos, *Nat Mater* **2003**, *2*, 382-385.
- [82] S. Link, C. Burda, B. Nikoobakht, M. A. El-Sayed, *The Journal of Physical Chemistry B* **2000**, *104*, 6152-6163.
- [83] Z. A. Peng, X. Peng, *J Am Chem Soc* **2002**, *124*, 3343-3353.
- [84] C. B. Catherine, S. G. C. Adam, *Journal of Physics D: Applied Physics* **2003**, *36*, R198.
- [85] C. B. Murray, C. R. Kagan, M. G. Bawendi, *Science* **1995**, *270*, 1335-1338.
- [86] B. O. Dabbousi, J. Rodríguez-Viejo, F. V. Mikulec, J. R. Heine, H. Mattoussi, R. Ober, a. K. F. Jensen, M. G. Bawendi, *Journal of Physical Chemistry B* **1997**, *101*, 9463-9475.
- [87] M. L. Steigerwald, A. P. Alivisatos, J. Gibson, T. Harris, R. Kortan, A. Muller, A. Thayer, T. Duncan, D. Douglass, L. E. Brus, *Journal of the American Chemical Society* **1988**, *110*, 3046-3050.
- [88] J. Hierrezuelo, A. Sadeghpour, I. Szilagyi, A. Vaccaro, M. Borkovec, *Langmuir* **2010**, *26*, 15109-15111.
- [89] Z. G. Cui, Y. Z. Cui, C. F. Cui, Z. Chen, B. P. Binks, *Langmuir* **2010**, *26*, 12567-12574.
- [90] F. Loosli, P. Le Coustumer, S. Stoll, *Sci Total Environ* **2015**, *535*, 28-34.
- [91] F. Neville, R. Moreno-Atanasio, *Front Chem* **2018**, *6*, 201.

- [92] A. Housni, M. Ahmed, S. Liu, R. Narain, *The Journal of Physical Chemistry C* **2008**, *112*, 12282-12290.
- [93] W. P. Wuelfing, S. M. Gross, D. T. Miles, R. W. Murray, *Journal of the American Chemical Society* **1998**, *120*, 12696-12697.
- [94] S. Mourdikoudis, L. M. Liz-Marzán, *Chemistry of Materials* **2013**, *25*, 1465-1476.
- [95] S. Zhou, D. Huo, S. Goines, T. H. Yang, Z. Lyu, M. Zhao, K. D. Gilroy, Y. Wu, Z. D. Hood, M. Xie, Y. Xia, *J Am Chem Soc* **2018**, *140*, 11898-11901.
- [96] P. Holmqvist, P. Alexandridis, B. Lindman, *Macromolecules* **1997**, *30*, 6788-6797.
- [97] P. Alexandridis, *Chemical Engineering & Technology* **2010**, *34*, 15-28.
- [98] R. B. Grubbs, *Polymer Reviews* **2007**, *47*, 197-215.
- [99] S. M. Louie, R. D. Tilton, G. V. Lowry, *Environmental Science: Nano* **2016**, *3*, 283-310.
- [100] A. Heuer-Jungemann, N. Feliu, I. Bakaimi, M. Hamaly, A. Alkilany, I. Chakraborty, A. Masood, M. F. Casula, A. Kostopoulou, E. Oh, K. Susumu, M. H. Stewart, I. L. Medintz, E. Stratakis, W. J. Parak, A. G. Kanaras, *Chem Rev* **2019**, *119*, 4819-4880.
- [101] V. Jain, S. Roy, P. Roy, P. P. Pillai, *Chemistry of Materials* **2022**, *34*, 7579-7597.
- [102] P. M. Valencia, M. H. Hanewich-Hollatz, W. Gao, F. Karim, R. Langer, R. Karnik, O. C. Farokhzad, *Biomaterials* **2011**, *32*, 6226-6233.
- [103] M. Green, *Journal of Materials Chemistry* **2010**, *20*.
- [104] K. Mahato, S. Nagpal, M. A. Shah, A. Srivastava, P. K. Maurya, S. Roy, A. Jaiswal, R. Singh, P. Chandra, *3 Biotech* **2019**, *9*, 57.
- [105] P. Thangadurai, S. Balaji, P. T. Manoharan, *Nanotechnology* **2008**, *19*, 435708.
- [106] X. Chen, Y. Lou, A. C. Samia, C. Burda, *Nano Letters* **2003**, *3*, 799-803.
- [107] X. Peng, M. C. Schlamp, A. V. Kadavanich, A. P. Alivisatos, *Journal of the American Chemical Society* **1997**, *119*, 7019-7029.
- [108] J. Hassinen, V. Liljestrom, M. A. Kostianen, R. H. Ras, *Angew Chem Int Ed Engl* **2015**, *54*, 7990-7993.
- [109] R. G. Nuzzo, L. H. Dubois, D. L. Allara, *Journal of the American Chemical Society* **2002**, *112*, 558-569.
- [110] G. Palui, T. Avellini, N. Zhan, F. Pan, D. Gray, I. Alabugin, H. Mattoussi, *J Am Chem Soc* **2012**, *134*, 16370-16378.
- [111] G. T. Wei, Z. Yang, C. Y. Lee, H. Y. Yang, C. R. Wang, *J Am Chem Soc* **2004**, *126*, 5036-5037.
- [112] J. Yang, J. Y. Lee, J. Y. Ying, *Chem Soc Rev* **2011**, *40*, 1672-1696.
- [113] T. K. Sau, A. L. Rogach, *Advanced Materials* **2010**, *22*, 1781-1804.
- [114] Y. Sun, Y. Xia, *Science* **2002**, *298*, 2176-2179.

- [115] R. Sardar, A. M. Funston, P. Mulvaney, R. W. Murray, *Langmuir* **2009**, *25*, 13840-13851.
- [116] Y. Xia, Q. Chen, U. Banin, *Chemical Reviews* **2023**, *123*, 3325-3328.
- [117] N. Li, P. Zhao, D. Astruc, *Angewandte Chemie International Edition* **2014**, *53*, 1756-1789.
- [118] B. T. Diroll, A. Koschitzky, C. B. Murray, *The Journal of Physical Chemistry Letters* **2014**, *5*, 85-91.
- [119] B. Nikoobakht, M. A. El-Sayed, *Chemistry of Materials* **2003**, *15*, 1957-1962.
- [120] B. A. Wacaser, K. A. Dick, J. Johansson, M. T. Borgström, K. Deppert, L. Samuelson, *Advanced Materials* **2009**, *21*, 153-165.
- [121] A. Bouhelier, R. Bachelot, G. Lerondel, S. Kostcheev, P. Royer, G. P. Wiederrecht, *Physical Review Letters* **2005**, *95*, 267405.
- [122] C. X. Shan, Z. Liu, S. K. Hark, *Physical Review B* **2006**, *74*, 153402.
- [123] J. Wang, M. Isshiki, in *Springer Handbooks* (Eds.: S. Kasap, P. Capper), Springer, Cham, **2006**.
- [124] A. W. Achtstein, A. Antanovich, A. Prudnikau, R. Scott, U. Woggon, M. Artemyev, *The Journal of Physical Chemistry C* **2015**, *119*, 20156-20161.
- [125] S. Chen, Z. Fan, D. L. Carroll, *The Journal of Physical Chemistry B* **2002**, *106*, 10777-10781.
- [126] A. Fiore, R. Mastria, M. G. Lupo, G. Lanzani, C. Giannini, E. Carlino, G. Morello, M. De Giorgi, Y. Li, R. Cingolani, L. Manna, *Journal of the American Chemical Society* **2009**, *131*, 2274-2282.
- [127] S.-M. Lee, Y.-w. Jun, S.-N. Cho, J. Cheon, *Journal of the American Chemical Society* **2002**, *124*, 11244-11245.
- [128] P. Reiss, M. Protiere, L. Li, *small* **2009**, *5*, 154-168.
- [129] D. V. Talapin, I. Mekis, S. Götzinger, A. Kornowski, O. Benson, H. Weller, *The Journal of Physical Chemistry B* **2004**, *108*, 18826-18831.
- [130] Z. L. Wang, *Annual Review of Physical Chemistry* **2004**, *55*, 159-196.
- [131] S. E. Skrabalak, L. Au, X. Li, Y. Xia, *Nature protocols* **2007**, *2*, 2182-2190.
- [132] L. R. Hirsch, A. M. Gobin, A. R. Lowery, F. Tam, R. A. Drezek, N. J. Halas, J. L. West, *Annals of biomedical engineering* **2006**, *34*, 15-22.
- [133] P. R. Sajanlal, T. S. Sreeprasad, A. K. Samal, T. Pradeep, *Nano Reviews* **2011**, *2*, 5883.
- [134] C. Kuttner, R. P. M. Holler, M. Quintanilla, M. J. Schnepf, M. Dulle, A. Fery, L. M. Liz-Marzan, *Nanoscale* **2019**, *11*, 17655-17663.
- [135] M. Manceau, Université Pierre et Marie Curie - Paris VI

Università del Salento **2014**.

- [136] K. Rademann, *Berichte der Bunsengesellschaft für physikalische Chemie* **1990**, *94*, 1171-1171.
- [137] A. P. Sutton, *Electronic structure of materials*, Clarendon Press, **1993**.
- [138] W. Y. Liang, *Physics Education* **1970**, *5*, 226.
- [139] R. S. Knox, in *Collective Excitations in Solids* (Ed.: B. Di Bartolo), Springer US, Boston, MA, **1983**, pp. 183-245.
- [140] H. Weller, *Angewandte Chemie International Edition in English* **1993**, *32*, 41-53.
- [141] Y. Kayanuma, *Physical Review B* **1988**, *38*, 9797.
- [142] A. I. Ekimov, A. L. Efros, A. A. Onushchenko, *Solid State Communications* **1985**, *56*, 921-924.
- [143] S. Kargozar, S. J. Hoseini, P. B. Milan, S. Hooshmand, H.-W. Kim, M. Mozafari, *Biotechnology Journal* **2020**, *15*, 2000117.
- [144] A. M. Wagner, J. M. Knipe, G. Orive, N. A. Peppas, *Acta Biomaterialia* **2019**, *94*, 44-63.
- [145] T. Jamieson, R. Bakhshi, D. Petrova, R. Pocock, M. Imani, A. M. Seifalian, *Biomaterials* **2007**, *28*, 4717-4732.
- [146] D. Bera, L. Qian, T.-K. Tseng, P. H. Holloway, *Materials* **2010**, *3*, 2260-2345.
- [147] M. A. Cotta, *ACS Applied Nano Materials* **2020**, *3*, 4920-4924.
- [148] H. Moon, C. Lee, W. Lee, J. Kim, H. Chae, *Advanced Materials* **2019**, *31*, 1804294.
- [149] J. R. McBride, N. Mishra, S. M. Click, N. J. Orfield, F. Wang, K. Acharya, M. F. Chisholm, H. Htoon, S. J. Rosenthal, J. A. Hollingsworth, *The Journal of Chemical Physics* **2020**, *152*.
- [150] W.-S. Chae, T. D. T. Ung, Q. L. Nguyen, *Advances in Natural Sciences: Nanoscience and Nanotechnology* **2013**, *4*.
- [151] A. L. Efros, D. J. Nesbitt, *Nature Nanotechnology* **2016**, *11*, 661-671.
- [152] D. Kim, Y. K. Lee, D. Lee, W. D. Kim, W. K. Bae, D. C. Lee, *ACS Nano* **2017**, *11*, 12461-12472.
- [153] D. V. Talapin, J. H. Nelson, E. V. Shevchenko, S. Aloni, B. Sadler, A. P. Alivisatos, *Nano Letters* **2007**, *7*, 2951-2959.
- [154] I. Coropceanu, A. Rossinelli, J. R. Caram, F. S. Freyria, M. G. Bawendi, *ACS Nano* **2016**, *10*, 3295-3301.
- [155] V. L. Bridewell, R. Alam, C. J. Karwacki, P. V. Kamat, *Chemistry of Materials* **2015**, *27*, 5064-5071.
- [156] Y. Luo, L.-W. Wang, *ACS Nano* **2010**, *4*, 91-98.
- [157] J. R. Lakowicz, *Principles of Fluorescence Spectroscopy*, Plenum Publishers **1999**.

- [158] S. Oszwaldowski, K. P. Roberts, *Mikrochim Acta* **2013**, *180*, 1341-1350.
- [159] H. Zhang, X. Mi, B. Kang, Y. Wu, T. Zhang, P. Liu, X. Sun, Z. Zhang, N. Liu, H. Xu, *ACS Omega* **2023**, *8*, 3762-3767.
- [160] P. Rastogi, F. Palazon, M. Prato, F. Di Stasio, R. Krahné, *ACS Appl Mater Interfaces* **2018**, *10*, 5665-5672.
- [161] T. Kodanek, H. M. Banbela, S. Naskar, P. Adel, N. C. Bigall, D. Dorfs, *Nanoscale* **2015**, *7*, 19300-19309.
- [162] T. He, X. Qiu, J. Li, G. Pang, Z. Wu, J. Cheng, Z. Zhou, J. Hao, H. Liu, Y. Ni, L. Li, X. Lin, W. Hu, K. Wang, R. Chen, *Nanoscale* **2019**, *11*, 15245-15252.
- [163] G. Kalyuzhny, R. W. Murray, *The Journal of Physical Chemistry B* **2005**, *109*, 7012-7021.
- [164] R. R. Knauf, J. C. Lennox, J. L. Dempsey, *Chemistry of Materials* **2016**, *28*, 4762-4770.
- [165] M. Hu, J. Chen, Z.-Y. Li, L. Au, G. V. Hartland, X. Li, M. Marquez, Y. Xia, *Chemical Society Reviews* **2006**, *35*, 1084-1094.
- [166] C. Burda, X. Chen, R. Narayanan, M. A. El-Sayed, *Chemical reviews* **2005**, *105*, 1025-1102.
- [167] X. Huang, S. Neretina, M. A. El-Sayed, *Advanced materials* **2009**, *21*, 4880-4910.
- [168] A. Wijaya, K. Hamad-Schifferli, *Langmuir* **2008**, *24*, 9966-9969.
- [169] E. D. SoRelle, O. Liba, Z. Hussain, M. Gambhir, A. de la Zerda, *Langmuir* **2015**, *31*, 12339-12347.
- [170] L. Tong, Q. Wei, A. Wei, J. X. Cheng, *Photochemistry and photobiology* **2009**, *85*, 21-32.
- [171] P. K. Jain, K. S. Lee, I. H. El-Sayed, M. A. El-Sayed, *The journal of physical chemistry B* **2006**, *110*, 7238-7248.
- [172] M. A. Mackey, M. R. Ali, L. A. Austin, R. D. Near, M. A. El-Sayed, *The Journal of Physical Chemistry B* **2014**, *118*, 1319-1326.
- [173] X. Huang, I. H. El-Sayed, W. Qian, M. A. El-Sayed, *Journal of the American Chemical Society* **2006**, *128*, 2115-2120.
- [174] S. Link, M. A. El-Sayed, *The Journal of Physical Chemistry B* **1999**, *103*, 4212-4217.
- [175] S. Chen, Z. L. Wang, J. Ballato, S. H. Foulger, D. L. Carroll, *Journal of the American Chemical Society* **2003**, *125*, 16186-16187.
- [176] X. Huang, P. K. Jain, I. H. El-Sayed, M. A. El-Sayed, *Lasers in medical science* **2008**, *23*, 217-228.
- [177] R. Kumar, L. Binetti, T. H. Nguyen, L. S. M. Alwis, A. Agrawal, T. Sun, K. T. V. Grattan, *Sci Rep* **2019**, *9*, 17469.

- [178] J. P. Camden, J. A. Dieringer, J. Zhao, R. P. Van Duyne, *Accounts of chemical research* **2008**, *41*, 1653-1661.
- [179] J. Pérez-Juste, I. Pastoriza-Santos, L. M. Liz-Marzán, P. Mulvaney, *Coordination chemistry reviews* **2005**, *249*, 1870-1901.
- [180] N. R. Jana, L. Gearheart, C. J. Murphy, *The Journal of Physical Chemistry B* **2001**, *105*, 4065-4067.
- [181] K. Park, L. F. Drummy, R. C. Wadams, H. Koerner, D. Nepal, L. Fabris, R. A. Vaia, *Chemistry of Materials* **2013**, *25*, 555-563.
- [182] T. K. Sau, C. J. Murphy, *Langmuir* **2004**, *20*, 6414-6420.
- [183] G. Grochola, I. K. Snook, S. P. Russo, *The Journal of chemical physics* **2007**, *127*.
- [184] S. Si, C. Leduc, M.-H. Delville, B. Lounis, *ChemPhysChem* **2012**, *13*, 193-202.
- [185] S. E. Lohse, C. J. Murphy, *Chemistry of Materials* **2013**, *25*, 1250-1261.
- [186] L. Scarabelli, A. Sánchez-Iglesias, J. Pérez-Juste, L. M. Liz-Marzán, *The Journal of Physical Chemistry Letters* **2015**, *6*, 4270-4279.
- [187] M. Reza Hormozi-Nezhad, H. Robotjazi, M. Jalali-Heravi, *Analytica Chimica Acta* **2013**, *779*, 14-21.
- [188] M.-Z. Wei, T.-S. Deng, Q. Zhang, Z. Cheng, S. Li, *ACS Omega* **2021**, *6*, 9188-9195.
- [189] J. Gao, C. M. Bender, C. J. Murphy, *Langmuir* **2003**, *19*, 9065-9070.
- [190] A. Gole, C. J. Murphy, *Chemistry of Materials* **2004**, *16*, 3633-3640.
- [191] S. Jessl, M. Tebbe, L. Guerrini, A. Fery, R. A. Alvarez-Puebla, N. Pazos-Perez, *Small* **2018**, *14*, 1703879.
- [192] M. J. Walsh, S. J. Barrow, W. Tong, A. M. Funston, J. Etheridge, *ACS nano* **2015**, *9*, 715-724.
- [193] L. Gou, C. J. Murphy, *Chemistry of materials* **2005**, *17*, 3668-3672.
- [194] M. G. Méndez-Medrano, E. Kowalska, A. Lehoux, A. Herissan, B. Ohtani, D. Bahena, V. Briois, C. Colbeau-Justin, J. L. Rodríguez-López, H. Remita, *The Journal of Physical Chemistry C* **2016**, *120*, 5143-5154.
- [195] Y. Zheng, X. Zhong, Z. Li, Y. Xia, *Particle & Particle Systems Characterization* **2014**, *31*, 266-273.
- [196] J. E. Millstone, W. Wei, M. R. Jones, H. Yoo, C. A. Mirkin, *Nano Letters* **2008**, *8*, 2526-2529.
- [197] A. Sanchez-Iglesias, K. Jenkinson, S. Bals, L. M. Liz-Marzan, *The Journal of Physical Chemistry C* **2021**, *125*, 23937-23944.
- [198] L. Roach, P. L. Coletta, K. Critchley, S. D. Evans, *The Journal of Physical Chemistry C* **2022**, *126*, 3235-3243.
- [199] D. Xu, J. Mao, Y. He, E. S. Yeung, *Journal of Materials Chemistry C* **2014**, *2*.

- [200] G. Gonzalez-Rubio, V. Kumar, P. Llombart, P. Diaz-Nunez, E. Bladt, T. Altantzis, S. Bals, O. Pena-Rodriguez, E. G. Noya, L. G. MacDowell, A. Guerrero-Martinez, L. M. Liz-Marzan, *ACS Nano* **2019**, *13*, 4424-4435.
- [201] F. Kim, J. H. Song, P. Yang, *Journal of the American Chemical Society* **2002**, *124*, 14316-14317.
- [202] Y.-Y. Yu, S.-S. Chang, C.-L. Lee, C. C. Wang, *The Journal of Physical Chemistry B* **1997**, *101*, 6661-6664.
- [203] V. Sebastián, S.-K. Lee, C. Zhou, M. F. Kraus, J. G. Fujimoto, K. F. Jensen, *Chemical Communications* **2012**, *48*, 6654-6656.
- [204] R. del Caño, J. M. Gisbert-González, J. González-Rodríguez, G. Sánchez-Obrero, R. Madueño, M. Blázquez, T. Pineda, *Nanoscale* **2020**, *12*, 658-668.
- [205] B. C. Rostro-Kohanloo, L. R. Bickford, C. M. Payne, E. S. Day, L. J. Anderson, M. Zhong, S. Lee, K. M. Mayer, T. Zal, L. Adam, C. P. Dinney, R. A. Drezek, J. L. West, J. H. Hafner, *Nanotechnology* **2009**, *20*, 434005.
- [206] S. Lee, L. J. E. Anderson, C. M. Payne, J. H. Hafner, *Langmuir* **2011**, *27*, 14748-14756.
- [207] C. J. Murphy, L. B. Thompson, A. M. Alkilany, P. N. Sisco, S. P. Boulos, S. T. Sivapalan, J. A. Yang, D. J. Chernak, J. Huang, *The Journal of Physical Chemistry Letters* **2010**, *1*, 2867-2875.
- [208] D. Nepal, K. Park, R. A. Vaia, *Small* **2012**, *8*, 1013-1020.
- [209] B. Nikoobakht, M. A. El-Sayed, *Langmuir* **2001**, *17*, 6368-6374.
- [210] B. Nikoobakht, J. Wang, M. A. El-Sayed, *Chemical Physics Letters* **2002**, *366*, 17-23.
- [211] H. Takahashi, Y. Niidome, T. Niidome, K. Kaneko, H. Kawasaki, S. Yamada, *Langmuir* **2006**, *22*, 2-5.
- [212] L. Vigderman, P. Manna, E. R. Zubarev, *Angewandte Chemie International Edition* **2012**, *51*, 636-641.
- [213] A. M. Alkilany, P. K. Nalaria, C. R. Hexel, T. J. Shaw, C. J. Murphy, M. D. Wyatt, *Small* **2009**, *5*, 701-708.
- [214] L. Wang, X. Jiang, Y. Ji, R. Bai, Y. Zhao, X. Wu, C. Chen, *Nanoscale* **2013**, *5*, 8384-8391.
- [215] L. Su, S. Hu, L. Zhang, Z. Wang, W. Gao, J. Yuan, M. Liu, *Small* **2017**, *13*, 1602809.
- [216] A. S. D. Indrasekara, R. C. Wadams, L. Fabris, *Particle & Particle Systems Characterization* **2014**, *31*, 819-838.
- [217] J. G. Mehtala, D. Y. Zemlyanov, J. P. Max, N. Kadasala, S. Zhao, A. Wei, *Langmuir* **2014**, *30*, 13727-13730.
- [218] A. M. Alkilany, P. K. Nalaria, M. D. Wyatt, C. J. Murphy, *Langmuir* **2010**, *26*, 9328-9333.

- [219] V. Wedler, F. Strauss, S. Sudhakar, G. L. Hermsdorf, Y. D. Stierhof, E. Schaffer, *Nanoscale Adv* **2020**, 2, 4003-4010.
- [220] Q. Shou, M. Ebara, J. Wang, Q. Wang, X. Liang, H. Liu, T. Aoyagi, *Applied Surface Science* **2018**, 457, 264-270.
- [221] J. He, S. Unser, I. Bruzas, R. Cary, Z. Shi, R. Mehra, K. Aron, L. Sagle, *Colloids Surf B Biointerfaces* **2018**, 163, 140-145.
- [222] D. Shi, C. Song, Q. Jiang, Z. G. Wang, B. Ding, *Chem Commun (Camb)* **2013**, 49, 2533-2535.
- [223] T. Niidome, M. Yamagata, Y. Okamoto, Y. Akiyama, H. Takahashi, T. Kawano, Y. Katayama, Y. Niidome, *Journal of Controlled Release* **2006**, 114, 343-347.
- [224] F. Schulz, W. Friedrich, K. Hoppe, T. Vossmeier, H. Weller, H. Lange, *Nanoscale* **2016**, 8, 7296-7308.
- [225] Z. Zhang, M. Lin, *RSC Advances* **2014**, 4.
- [226] P.-o. Khunsuk, S. Chawalitpong, P. Sawutdeechaikul, T. Palaga, V. P. Hoven, *Molecular pharmaceuticals* **2018**, 15, 164-174.
- [227] D. F. Moyano, V. M. Rotello, *Langmuir* **2011**, 27, 10376-10385.
- [228] X. Liu, N. Huang, H. Li, H. Wang, Q. Jin, J. Ji, *ACS applied materials & interfaces* **2014**, 6, 5657-5668.
- [229] J. C. Love, L. A. Estroff, J. K. Kriebel, R. G. Nuzzo, G. M. Whitesides, *Chemical reviews* **2005**, 105, 1103-1170.
- [230] G. Li, R. Jin, *Accounts of chemical research* **2013**, 46, 1749-1758.
- [231] H. Qian, M. Zhu, Z. Wu, R. Jin, *Accounts of chemical research* **2012**, 45, 1470-1479.
- [232] J. Xie, Y. Zheng, J. Y. Ying, *Journal of the American Chemical Society* **2009**, 131, 888-889.
- [233] L.-Y. Chen, C.-W. Wang, Z. Yuan, H.-T. Chang, *Analytical chemistry* **2015**, 87, 216-229.
- [234] A. Baral, K. Basu, S. Roy, A. Banerjee, *ACS Sustainable Chemistry & Engineering* **2017**, 5, 1628-1637.
- [235] S.-S. Chang, C.-W. Shih, C.-D. Chen, W.-C. Lai, C. C. Wang, *Langmuir* **1999**, 15, 701-709.
- [236] K. Zheng, M. I. Setyawati, D. T. Leong, J. Xie, *ACS nano* **2017**, 11, 6904-6910.
- [237] M.-C. Daniel, D. Astruc, *Chemical reviews* **2004**, 104, 293-346.
- [238] K. Saha, S. S. Agasti, C. Kim, X. Li, V. M. Rotello, *Chemical reviews* **2012**, 112, 2739-2779.
- [239] A. S. K. Hashmi, G. J. Hutchings, *Angewandte Chemie International Edition* **2006**, 45, 7896-7936.

- [240] D. A. Giljohann, D. S. Seferos, W. L. Daniel, M. D. Massich, P. C. Patel, C. A. Mirkin, *Spherical nucleic acids* **2020**, 55-90.
- [241] R. Herizchi, E. Abbasi, M. Milani, A. Akbarzadeh, *Artificial cells, nanomedicine, and biotechnology* **2016**, *44*, 596-602.
- [242] I. Hammami, N. M. Alabdallah, *Journal of king Saud university-science* **2021**, *33*, 101560.
- [243] J. Turkevich, P. C. Stevenson, J. Hillier, *Discussions of the faraday society* **1951**, *11*, 55-75.
- [244] J. Kimling, M. Maier, B. Okenve, V. Kotaidis, H. Ballot, A. Plech, *The Journal of Physical Chemistry B* **2006**, *110*, 15700-15707.
- [245] G. Frens, *NATURE-PHYSICAL SCIENCE* **1973**, *241*, 20-22.
- [246] F. Schulz, T. Homolka, N. G. Bastus, V. Puentes, H. Weller, T. Vossmeier, *Langmuir* **2014**, *30*, 10779-10784.
- [247] N. R. Jana, L. Gearheart, C. J. Murphy, *Langmuir* **2001**, *17*, 6782-6786.
- [248] F. Schulz, O. Pavelka, F. Lehmkuhler, F. Westermeier, Y. Okamura, N. S. Mueller, S. Reich, H. Lange, *Nat Commun* **2020**, *11*, 3821.
- [249] M. R. Dewi, G. Laufersky, T. Nann, *RSC Advances* **2014**, *4*, 34217-34220.
- [250] C. J. Murphy, T. K. Sau, A. M. Gole, C. J. Orendorff, J. Gao, L. Gou, S. E. Hunyadi, T. Li, *The Journal of Physical Chemistry B* **2005**, *109*, 13857-13870.
- [251] M. Tréguer-Delapierre, J. Majimel, S. Mornet, E. Duguet, S. Ravaine, *Gold Bulletin* **2008**, *41*, 195-207.
- [252] N. R. Jana, L. Gearheart, C. J. Murphy, *Chemistry of Materials* **2001**, *13*, 2313-2322.
- [253] P. Baptista, E. Pereira, P. Eaton, G. Doria, A. Miranda, I. Gomes, P. Quaresma, R. Franco, *Analytical and Bioanalytical Chemistry* **2008**, *391*, 943-950.
- [254] N. M. Schaeublin, L. K. Braydich-Stolle, A. M. Schrand, J. M. Miller, J. Hutchison, J. J. Schlager, S. M. Hussain, *Nanoscale* **2011**, *3*, 410-420.
- [255] A. Gupta, D. F. Moyano, A. Parnsubsakul, A. Papadopoulos, L.-S. Wang, R. F. Landis, R. Das, V. M. Rotello, *ACS Applied Materials & Interfaces* **2016**, *8*, 14096-14101.
- [256] Y. Chen, Y. Xianyu, X. Jiang, *Accounts of Chemical Research* **2017**, *50*, 310-319.
- [257] G. Zhang, Z. Yang, W. Lu, R. Zhang, Q. Huang, M. Tian, L. Li, D. Liang, C. Li, *Biomaterials* **2009**, *30*, 1928-1936.
- [258] Y. Liu, M. K. Shipton, J. Ryan, E. D. Kaufman, S. Franzen, D. L. Feldheim, *Analytical Chemistry* **2007**, *79*, 2221-2229.
- [259] Q. Jin, J. P. Xu, J. Ji, J. C. Shen, *Chem Commun (Camb)* **2008**, 3058-3060.
- [260] W. Zhou, L. Ling, Y. Du, W. He, Q. Xia, C. Yao, X. Li, *Langmuir* **2019**, *35*, 13031-13039.

- [261] W. Zhou, X. Gao, D. Liu, X. Chen, *Chemical Reviews* **2015**, *115*, 10575-10636.
- [262] W. G. Kreyling, A. M. Abdelmonem, Z. Ali, F. Alves, M. Geiser, N. Haberl, R. Hartmann, S. Hirn, D. J. de Aberasturi, K. Kantner, G. Khadem-Saba, J.-M. Montenegro, J. Rejman, T. Rojo, I. R. de Larramendi, R. Ufartes, A. Wenk, W. J. Parak, *Nature Nanotechnology* **2015**, *10*, 619-623.
- [263] A. Kumar, H. Ma, X. Zhang, K. Huang, S. Jin, J. Liu, T. Wei, W. Cao, G. Zou, X.-J. Liang, *Biomaterials* **2012**, *33*, 1180-1189.
- [264] J. Zong, S. L. Cobb, N. R. Cameron, *Biomater Sci* **2017**, *5*, 872-886.
- [265] Z. R. Goddard, M. J. Marin, D. A. Russell, M. Searcey, *Chem Soc Rev* **2020**, *49*, 8774-8789.
- [266] G. Yao, H. Pei, J. Li, Y. Zhao, D. Zhu, Y. Zhang, Y. Lin, Q. Huang, C. Fan, *NPG Asia Materials* **2015**, *7*, e159-e159.
- [267] D. Y. Choi, S. Kim, J.-W. Oh, J.-M. Nam, *Bulletin of the Korean Chemical Society* **2022**, *43*, 1298-1306.
- [268] S. Zeng, K.-T. Yong, I. Roy, X.-Q. Dinh, X. Yu, F. Luan, *Plasmonics* **2011**, *6*, 491-506.
- [269] M. H. Jazayeri, H. Amani, A. A. Pourfatollah, H. Pazoki-Toroudi, B. Sedighimoghaddam, *Sensing and Bio-Sensing Research* **2016**, *9*, 17-22.
- [270] E. Katz, I. Willner, *Angewandte Chemie International Edition* **2004**, *43*, 6042-6108.
- [271] K. M. Kosuda, J. M. Bingham, K. L. Wustholz, R. P. Van Duyne, R. J. Groarke, in *Comprehensive Nanoscience and Nanotechnology (Second Edition)* (Eds.: D. L. Andrews, R. H. Lipson, T. Nann), Academic Press, Oxford, **2016**, pp. 117-152.
- [272] S. Link, M. A. El-Sayed, *Annual Review of Physical Chemistry* **2003**, *54*, 331-366.
- [273] N. J. Halas, S. Lal, W.-S. Chang, S. Link, P. Nordlander, *Chemical Reviews* **2011**, *111*, 3913-3961.
- [274] P. K. Jain, X. Huang, I. H. El-Sayed, M. A. El-Sayed, *Plasmonics* **2007**, *2*, 107-118.
- [275] Z. Yuan, C. C. Hu, H. T. Chang, C. Lu, *Analyst* **2016**, *141*, 1611-1626.
- [276] J. N. Anker, W. P. Hall, O. Lyandres, N. C. Shah, J. Zhao, R. P. Van Duyne, *Nature Materials* **2008**, *7*, 442-453.
- [277] M. Haruta, *Gold Bulletin* **2004**, *37*, 27-36.
- [278] M. Haruta, *The chemical record* **2003**, *3*, 75-87.
- [279] G. C. Bond, C. Louis, D. Thompson, *Catalysis by gold, Vol. 6*, World Scientific, **2006**.
- [280] L. Fabris, *Journal of Optics* **2015**, *17*.
- [281] C. J. Murphy, A. M. Gole, J. W. Stone, P. N. Sisco, A. M. Alkilany, E. C. Goldsmith, S. C. Baxter, *Accounts of chemical research* **2008**, *41*, 1721-1730.
- [282] R. A. Sperling, P. R. Gil, F. Zhang, M. Zanella, W. J. Parak, *Chemical Society Reviews* **2008**, *37*, 1896-1908.

- [283] P. K. Jain, I. H. El-Sayed, M. A. El-Sayed, *Nano Today* **2007**, *2*, 18-29.
- [284] D. Pissuwan, T. Niidome, M. B. Cortie, *Journal of controlled release* **2011**, *149*, 65-71.
- [285] H. Daraee, A. Eatemadi, E. Abbasi, S. Fekri Aval, M. Kouhi, A. Akbarzadeh, *Artificial cells, nanomedicine, and biotechnology* **2016**, *44*, 410-422.
- [286] T. G. Edwardson, M. D. Levasseur, S. Tetter, A. Steinauer, M. Hori, D. Hilvert, *Chemical Reviews* **2022**, *122*, 9145-9197.
- [287] T. W. Giessen, *Current Opinion in Chemical Biology* **2016**, *34*, 1-10.
- [288] M. Sutter, D. Boehringer, S. Gutmann, S. Günther, D. Prangishvili, M. J. Loessner, K. O. Stetter, E. Weber-Ban, N. Ban, *Nature structural & molecular biology* **2008**, *15*, 939-947.
- [289] D. L. Caspar, A. Klug, in *Cold Spring Harbor symposia on quantitative biology, Vol. 27*, Cold Spring Harbor Laboratory Press, **1962**, pp. 1-24.
- [290] D. K. Clare, E. V. Orlova, *J Struct Biol* **2010**, *171*, 303-308.
- [291] A. Korpi, E. Anaya-Plaza, S. Välimäki, M. Kostianen, *WIREs Nanomedicine and Nanobiotechnology* **2020**, *12*, e1578.
- [292] M. L. Baer, F. Houser, L. S. Loesch-Fries, L. Gehrke, *The EMBO Journal* **1994**, *13*, 727-735.
- [293] A. Kumar, V. S. Reddy, V. Yusibov, P. R. Chipman, Y. Hata, I. Fita, K. Fukuyama, M. G. Rossmann, L. S. Loesch-Fries, T. S. Baker, J. E. Johnson, *J Virol* **1997**, *71*, 7911-7916.
- [294] T. Wiryaman, N. Toor, *Journal of Structural Biology: X* **2022**, *6*, 100062.
- [295] Z. Gu, K. Wu, J. Wang, *J Virol* **2024**, *98*, e0006824.
- [296] A. Fokine, P. R. Chipman, P. G. Leiman, V. V. Mesyanzhinov, V. B. Rao, M. G. Rossmann, *Proceedings of the National Academy of Sciences* **2004**, *101*, 6003-6008.
- [297] C. A. Kerfeld, M. R. Sawaya, S. Tanaka, C. V. Nguyen, M. Phillips, M. Beeby, T. O. Yeates, *Science* **2005**, *309*, 936-938.
- [298] C. A. Kerfeld, O. Erbilgin, *Trends in microbiology* **2015**, *23*, 22-34.
- [299] E. C. Theil, *Inorganic chemistry* **2013**, *52*, 12223-12233.
- [300] R. M. Kramer, C. Li, D. C. Carter, M. O. Stone, R. R. Naik, *Journal of the American Chemical Society* **2004**, *126*, 13282-13286.
- [301] G. T. Jennings, M. F. Bachmann, **2008**.
- [302] B. Schwarz, M. Uchida, T. Douglas, *Advances in virus research* **2017**, *97*, 1-60.
- [303] K. Ritsert, R. Huber, D. Turk, R. Ladenstein, K. Schmidt-Bäse, A. Bacher, *Journal of Molecular Biology* **1995**, *253*, 151-167.
- [304] E. Sasaki, D. Böhringer, M. Van de Waterbeemd, M. Leibundgut, R. Zschoche, A. J. Heck, N. Ban, D. Hilvert, *Nature communications* **2017**, *8*, 14663.

- [305] L. S. Adamson, N. Tasneem, M. P. Andreas, W. Close, E. N. Jenner, T. N. Szyszka, R. Young, L. C. Cheah, A. Norman, H. I. MacDermott-Opeskin, *Science Advances* **2022**, 8, eabl7346.
- [306] R. J. Nichols, C. Cassidy-Amstutz, T. Chaijarasphong, D. F. Savage, *Critical reviews in biochemistry and molecular biology* **2017**, 52, 583-594.
- [307] M. Krupovic, E. V. Koonin, *Proceedings of the National Academy of Sciences* **2017**, 114, E2401-E2410.
- [308] N. F. Steinmetz, S. Lim, F. Sainsbury, *Biomaterials Science* **2020**, 8, 2771-2777.
- [309] M. Khoshnejad, H. Parhiz, V. V. Shuvaev, I. J. Dmochowski, V. R. Muzykantov, *Journal of Controlled Release* **2018**, 282, 13-24.
- [310] M. Uchida, M. L. Flenniken, M. Allen, D. A. Willits, B. E. Crowley, S. Brumfield, A. F. Willis, L. Jackiw, M. Jutila, M. J. Young, T. Douglas, *Journal of the American Chemical Society* **2006**, 128, 16626-16633.
- [311] T. Ueno, M. Suzuki, T. Goto, T. Matsumoto, K. Nagayama, Y. Watanabe, *Angewandte Chemie International Edition* **2004**, 43, 2527-2530.
- [312] D. Faivre, D. Schuler, *Chem Rev* **2008**, 108, 4875-4898.
- [313] A. N. Gabashvili, N. S. Chmelyuk, M. V. Efremova, J. A. Malinovskaya, A. S. Semkina, M. A. Abakumov, in *Biomolecules, Vol. 10*, **2020**.
- [314] N. Valdés-Stauber, S. Scherer, *Applied and Environmental Microbiology* **1994**, 60, 3809-3814.
- [315] N. S. Chmelyuk, V. V. Oda, A. N. Gabashvili, M. A. Abakumov, *Biochemistry (Moscow)* **2023**, 88, 35-49.
- [316] F. Akita, K. T. Chong, H. Tanaka, E. Yamashita, N. Miyazaki, Y. Nakaishi, M. Suzuki, K. Namba, Y. Ono, T. Tsukihara, *Journal of molecular biology* **2007**, 368, 1469-1483.
- [317] C. A. McHugh, J. Fontana, D. Nemecek, N. Cheng, A. A. Aksyuk, J. B. Heymann, D. C. Winkler, A. S. Lam, J. S. Wall, A. C. Steven, *The EMBO journal* **2014**, 33, 1896-1911.
- [318] E. M. Williams, S. M. Jung, J. L. Coffman, S. Lutz, *ACS synthetic biology* **2018**, 7, 2514-2517.
- [319] J. Ross, Z. Mclver, T. Lambert, C. Piergentili, J. E. Bird, K. J. Gallagher, F. L. Cruickshank, P. James, E. Zarazúa-Arvizu, L. E. Horsfall, K. J. Waldron, M. D. Wilson, C. L. Mackay, A. Baslé, D. J. Clarke, J. Marles-Wright, *Science Advances* **2022**, 8, eabj4461.
- [320] A. Fazal, T. W. Giessen, *Current Opinion in Microbiology* **2025**, 86, 102629.
- [321] C. Cassidy-Amstutz, L. Oltrogge, C. C. Going, A. Lee, P. Teng, D. Quintanilla, A. East-Seletsky, E. R. Williams, D. F. Savage, *Biochemistry* **2016**, 55, 3461-3468.

- [322] R. Rahmanpour, T. D. Bugg, *The FEBS journal* **2013**, *280*, 2097-2104.
- [323] M. P. Andreas, T. W. Giessen, *Nature Communications* **2021**, *12*, 4748.
- [324] M. Ahmad, J. N. Roberts, E. M. Hardiman, R. Singh, L. D. Eltis, T. D. H. Bugg, *Biochemistry* **2011**, *50*, 5096-5107.
- [325] Y. Sugano, R. Muramatsu, A. Ichianagi, T. Sato, M. Shoda, *Journal of Biological Chemistry* **2007**, *282*, 36652-36658.
- [326] K. A. Lien, K. Dinshaw, R. J. Nichols, C. Cassidy-Amstutz, M. Knight, R. Singh, L. D. Eltis, D. F. Savage, S. A. Stanley, *Elife* **2021**, *10*, e74358.
- [327] H. Moon, J. Lee, J. Min, S. Kang, *Biomacromolecules* **2014**, *15*, 3794-3801.
- [328] F. Sigmund, C. Massner, P. Erdmann, A. Stelzl, H. Rolbieski, M. Desai, S. Bricault, T. P. Worner, J. Snijder, A. Geerlof, H. Fuchs, M. Hrabe de Angelis, A. J. R. Heck, A. Jasanoff, V. Ntziachristos, J. Plitzko, G. G. Westmeyer, *Nat Commun* **2018**, *9*, 1990.
- [329] C. Rennie, C. Sives, I. Boyton, D. Diaz, C. Gorrie, O. Vittorio, L. Collins-Praino, A. Care, *Advanced Therapeutics* **2024**, *7*, 2300360.
- [330] R. Huber, T. A. Langworthy, H. König, M. Thomm, C. R. Woese, U. B. Sleytr, K. O. Stetter, *Archives of Microbiology* **1986**, *144*, 324-333.
- [331] P. M. Hicks, K. D. Rinker, J. R. Baker, R. M. Kelly, *FEBS letters* **1998**, *440*, 393-398.
- [332] R. Jaenicke, G. Böhm, *Current opinion in structural biology* **1998**, *8*, 738-748.
- [333] I. Boyton, S. C. Goodchild, D. Diaz, A. Elbourne, L. E. Collins-Praino, A. Care, *ACS Omega* **2022**, *7*, 823-836.
- [334] T. W. Giessen, P. A. Silver, *ACS Synthetic Biology* **2016**, *5*, 1497-1504.
- [335] D. R. Zusman, A. E. Scott, Z. Yang, J. R. Kirby, *Nature Reviews Microbiology* **2007**, *5*, 862-872.
- [336] C. A. McHugh, J. Fontana, D. Nemecek, N. Cheng, A. A. Aksyuk, J. B. Heymann, D. C. Winkler, A. S. Lam, J. S. Wall, A. C. Steven, E. Hoiczky, *The EMBO Journal* **2014**, *33*, 1896-1911.
- [337] E. Eren, B. Wang, D. C. Winkler, N. R. Watts, A. C. Steven, P. T. Wingfield, *Structure* **2022**, *30*, 551-563 e554.
- [338] T. N. Szyszka, R. Siddiquee, A. Loustau, L. S. R. Adamson, C. Rennie, T. Huang, R. Young, A. Care, Y. H. Lau, *Angewandte Chemie International Edition* **2025**, *64*, e202422459.
- [339] W. J. Altenburg, N. Rollins, P. A. Silver, T. W. Giessen, *Sci Rep* **2021**, *11*, 4951.
- [340] J. A. Jones, R. Benisch, T. W. Giessen, *Journal of Materials Chemistry B* **2023**, *11*, 4377-4388.
- [341] S. Kwon, M. P. Andreas, T. W. Giessen, *Journal of Structural Biology* **2023**, *215*, 108022.

- [342] J. Snijder, M. van de Waterbeemd, E. Damoc, E. Denisov, D. Grinfeld, A. Bennett, M. Agbandje-McKenna, A. Makarov, A. J. R. Heck, *Journal of the American Chemical Society* **2014**, *136*, 7295-7299.
- [343] S. N. Gómez-Barrera, W. Á. Delgado-Tapia, A. E. Hernández-Gutiérrez, M. Cayetano-Cruz, C. Méndez, I. Bustos-Jaimes, *ACS Omega* **2025**, *10*, 7142-7152.
- [344] S. Kwon, M. P. Andreas, T. W. Giessen, *ACS Nano* **2024**, *18*, 25740-25753.
- [345] I. Chakraborty, W. J. Parak, *Advanced Materials Interfaces* **2019**, *6*, 1801407.
- [346] X. Li, Y. Zhang, A. He, Q. Li, S. Wang, J. Shan, S. Li, D. Yang, G. Wu, W. Xiu, Y. Liu, H. Dong, *Coordination Chemistry Reviews* **2025**, *545*, 217003.
- [347] C. Wang, Z. Zhang, J. Wang, Q. Wang, L. Shang, *Materials Today Bio* **2022**, *16*, 100352.
- [348] H. Zhao, Y. Wang, L. Bao, C. Chen, *Accounts of Materials Research* **2022**, *3*, 812-829.
- [349] I. W. Hamley, *Biomacromolecules* **2019**, *20*, 1829-1848.
- [350] L. H. Tan, H. Xing, Y. Lu, *Accounts of chemical research* **2014**, *47*, 1881-1890.
- [351] A. Kuzyk, R. Jungmann, G. P. Acuna, N. Liu, *ACS photonics* **2018**, *5*, 1151-1163.
- [352] Z. Zhao, E. L. Jacovetty, Y. Liu, H. Yan, *Angewandte Chemie* **2011**, *123*, 2089-2092.
- [353] S. Pal, Z. Deng, B. Ding, H. Yan, Y. Liu, *Angewandte Chemie* **2010**, *122*, 2760-2764.
- [354] S. Dey, C. Fan, K. V. Gothelf, J. Li, C. Lin, L. Liu, N. Liu, M. A. Nijenhuis, B. Saccà, F. C. Simmel, *Nature Reviews Methods Primers* **2021**, *1*, 13.
- [355] S. F. van Dongen, H.-P. M. de Hoog, R. J. Peters, M. Nallani, R. J. Nolte, J. C. van Hest, *Chemical reviews* **2009**, *109*, 6212-6274.
- [356] C. M. Niemeyer, *Angewandte Chemie International Edition* **2010**, *49*, 1200-1216.
- [357] M. A. Gauthier, H.-A. Klok, *Polymer chemistry* **2010**, *1*, 1352-1373.
- [358] S. Bhaskar, S. Lim, *NPG Asia materials* **2017**, *9*, e371-e371.
- [359] M. Lach, M. Künzle, T. Beck, *Vol. 58*, ACS Publications, **2018**, pp. 140-141.
- [360] M. Lach, C. Strelow, A. Meyer, A. Mews, T. Beck, *ACS Applied Materials & Interfaces* **2022**, *14*, 10656-10668.
- [361] M. Rütten, L. Lang, H. Wagler, M. Lach, N. Mucke, U. Laugks, C. Seuring, T. F. Keller, A. Stierle, H. M. Ginn, T. Beck, *ACS Nano* **2024**, *18*, 25325-25336.
- [362] Y. Zhou, A. Shaukat, J. Seitsonen, C. Rigoni, J. V. I. Timonen, M. A. Kostianen, *Advanced Science* **2024**, *11*, 2408416.
- [363] M. Künzle, T. Eckert, T. Beck, *Journal of the American Chemical Society* **2016**, *138*, 12731-12734.
- [364] M. Rütten, Staats-und Universitätsbibliothek Hamburg Carl von Ossietzky **2022**.

- [365] K. W. Pulsipher, J. A. Villegas, B. W. Roose, T. L. Hicks, J. Yoon, J. G. Saven, I. J. Dmochowski, *Biochemistry* **2017**, *56*, 3596-3606.
- [366] J. C. Cheung-Lau, D. Liu, K. W. Pulsipher, W. Liu, I. J. Dmochowski, *Journal of Inorganic Biochemistry* **2014**, *130*, 59-68.
- [367] J. Swift, C. A. Butts, J. Cheung-Lau, V. Yerubandi, I. J. Dmochowski, *Langmuir* **2009**, *25*, 5219-5225.
- [368] M. Lach, M. Rütten, T. Beck, *Protein Science* **2024**, *33*, e5153.
- [369] L. Lang, H. Böhler, H. Wagler, T. Beck, *Biomacromolecules* **2024**, *25*, 177-187.
- [370] P. A. Sontz, J. B. Bailey, S. Ahn, F. A. Tezcan, *Journal of the American Chemical Society* **2015**, *137*, 11598-11601.
- [371] A. Liu, M. V. de Ruiter, W. Zhu, S. J. Maassen, L. Yang, J. J. L. M. Cornelissen, *Advanced Functional Materials* **2018**, *28*, 1801574.
- [372] N. O. Junker, A. Lindenau, M. Rütten, M. Lach, A. Nedilko, D. N. Chigrin, G. von Plessen, T. Beck, *Advanced Functional Materials* **2023**, *33*, 2303260.
- [373] H. Böhler, M. Rütten, L. Lang, T. Beck, in *Protein Cages: Design, Structure, and Applications* (Eds.: T. Ueno, S. Lim, K. Xia), Springer US, New York, NY, **2023**, pp. 361-386.
- [374] Aleksandr E. Miklos, C. Kluwe, Bryan S. Der, S. Pai, A. Sircar, Randall A. Hughes, M. Berrondo, J. Xu, V. Codrea, Patricia E. Buckley, Alena M. Calm, Heather S. Welsh, Candice R. Warner, Melody A. Zacharko, James P. Carney, Jeffrey J. Gray, G. Georgiou, B. Kuhlman, Andrew D. Ellington, *Chemistry & Biology* **2012**, *19*, 449-455.
- [375] A. Leaver-Fay, M. Tyka, S. M. Lewis, O. F. Lange, J. Thompson, R. Jacak, K. W. Kaufman, P. D. Renfrew, C. A. Smith, W. Sheffler, I. W. Davis, S. Cooper, A. Treuille, D. J. Mandell, F. Richter, Y.-E. A. Ban, S. J. Fleishman, J. E. Corn, D. E. Kim, S. Lyskov, M. Berrondo, S. Mentzer, Z. Popović, J. J. Havranek, J. Karanicolas, R. Das, J. Meiler, T. Kortemme, J. J. Gray, B. Kuhlman, D. Baker, P. Bradley, in *Methods in Enzymology, Vol. 487* (Eds.: M. L. Johnson, L. Brand), Academic Press, **2011**, pp. 545-574.
- [376] S. Das, L. Zhao, S. N. Crooke, L. Tran, S. Bhattacharya, E. A. Gaucher, M. G. Finn, *Biomacromolecules* **2020**, *21*, 2432-2439.
- [377] Z. S. Mbalaha, P. R. Edwards, D. J. S. Birch, Y. Chen, *ACS Omega* **2019**, *4*, 13740-13746.
- [378] R. Gomes, A. Hassinen, A. Szczygiel, Q. A. Zhao, A. Vantomme, J. C. Martins, Z. Hens, *J Phys Chem Lett* **2011**, *2*, 145-152.
- [379] W. W. Yu, L. Qu, W. Guo, X. Peng, *Chemistry of Materials* **2003**, *15*, 2854-2860.

- [380] J. M. Campiña, A. Martins, F. Silva, *The Journal of Physical Chemistry C* **2007**, *111*, 5351-5362.
- [381] M. M. Rahman, *Natural Science* **2011**, *03*, 208-217.
- [382] C. Soncini, A. Kumar, F. Bondino, E. Magnano, M. Stupar, B. Ressel, G. De Ninno, A. Papadopoulos, E. Serpetzoglou, E. Stratakis, M. Pedio, *Journal of Materials Chemistry C* **2023**, *11*, 10266-10273.
- [383] S. J. Hurst, A. K. R. Lytton-Jean, C. A. Mirkin, *Analytical Chemistry* **2006**, *78*, 8313-8318.
- [384] M. D. Baaske, F. Vollmer, *Nature Photonics* **2016**, *10*, 733-739.
- [385] X. Wang, Y. Li, H. Wang, Q. Fu, J. Peng, Y. Wang, J. Du, Y. Zhou, L. Zhan, *Biosensors and Bioelectronics* **2010**, *26*, 404-410.
- [386] H.-H. Chang, C. J. Murphy, *Chemistry of Materials* **2018**, *30*, 1427-1435.
- [387] W. Haiss, N. T. Thanh, J. Aveyard, D. G. Fernig, *Anal Chem* **2007**, *79*, 4215-4221.
- [388] G. P. Kurzban, G. Gitlin, E. A. Bayer, M. Wilchek, P. M. Horowitz, *Journal of Protein Chemistry* **1990**, *9*, 673-682.
- [389] M. J. Waner, J. M. Hiznay, A. T. Mustovich, W. Patton, C. Ponyik, D. P. Mascotti, *Biochemistry and Biophysics Reports* **2019**, *17*, 127-131.
- [390] S. Rakshit, S. P. Moulik, S. C. Bhattacharya, *Journal of Colloid and Interface Science* **2017**, *491*, 349-357.
- [391] T. L. Jennings, M. P. Singh, G. F. Strouse, *Journal of the American Chemical Society* **2006**, *128*, 5462-5467.
- [392] X. Zhang, C. A. Marocico, M. Lunz, V. A. Gerard, Y. K. Gun'ko, V. Lesnyak, N. Gaponik, A. S. Susa, A. L. Rogach, A. L. Bradley, *ACS Nano* **2012**, *6*, 9283-9290.
- [393] T. Baker, J. Johnson, *Structural biology of viruses* **1997**, 38-79.
- [394] K. N. Parent, J. R. Schrad, G. Cingolani, *Viruses* **2018**, *10*.
- [395] R. Zandi, D. Reguera, R. F. Bruinsma, W. M. Gelbart, J. Rudnick, *Proceedings of the National Academy of Sciences* **2004**, *101*, 15556-15560.
- [396] T. N. Szyszka, M. P. Andreas, F. Lie, L. M. Miller, L. S. R. Adamson, F. Fatehi, R. Twarock, B. E. Draper, M. F. Jarrold, T. W. Giessen, Y. H. Lau, *Proceedings of the National Academy of Sciences* **2024**, *121*, e2321260121.
- [397] C. A. Dutcher, M. P. Andreas, T. W. Giessen, *bioRxiv* **2024**, 2024.2004.2025.591138.
- [398] C. Flinta, B. Persson, H. JÖRnvall, G. v. Heijne, *European Journal of Biochemistry* **1986**, *154*, 193-196.
- [399] R. J. Nichols, B. LaFrance, N. R. Phillips, D. R. Radford, L. M. Oltrogge, L. E. Valentin-Alvarado, A. J. Bischoff, E. Nogales, D. F. Savage, *eLife* **2021**, *10*, e59288.
- [400] C. Duy, J. Fitter, *Biophys J* **2006**, *90*, 3704-3711.

10. Abbreviations

AET	Aminoethanethiol
AFM	Atomic force microscopy
AgBr	Silver bromide
AgNP	Silver nanoparticle
AMV	Alfaalfa mosaic virus
AuNP	Gold nanoparticle
AuNR	Gold nanorod
AUT	Aminoundecanethiol
BDAC	Bisoctyl dimethyl ammonium chloride
BMC	Bacterial microcompartments
CCMV	Cowpea chlorotic mottle virus
CdS	Cadmium sulfide
CdSe	Cadmium selenide
CHES	N-cyclohexyl-2-aminoethanesulfonic acid
CLP	Cargo loading peptide
CTAB	Hexadecyltrimethylammonium bromide
CTAC	Hexadecyltrimethylammonium chloride
Cys	Cysteine
Da	Dalton
DHLA	Dihydrolipoic acid
DiR	Dot-in-rod
DLS	Dynamic light scattering
DMF	<i>N,N</i> -Dimethylformamide
DNA	Deoxyribonucleic acid
EM	Electron Microscopy
Enc	Encapsulin
FLP	Ferritin-like proteins
FPLC	Fast Protein Liquid Chromatography
FRET	Förster resonance energy transfer
FWHM	Full width at half maximum
GuHCl	Guanadine hydrochloride
H ₂ O ₂	Hydrogen Peroxide
HCl	hydrochloride
HAuCl ₄	Gold (III) chloride trihydrate
HEPES	4-(2-Hydroxyethyl)-1-piperazineethanesulfonic acid

Abbreviations

HK97	Hong Kong 97
HPA	Hexylphosphonic acid
IEC	Ion-exchange chromatography
IPTG	Isopropyl- β -D-1-thiogalactopyranoside
LB	Lysogeny broth
LSPR	Localize surface plasmon resonance
<i>M. xanthus</i>	<i>Myxococcus Xanthus</i>
MOF	Metal organic Framework
MPA	Mercaptopropionic acid
MS	Mass spectrometry
MUA	11-Mercaptoundecanoic acid
MUTAB	(11-Mercaptoundecyl)-N,N,N-trimethylammonium bromide
MW	Molecular weight
MWCO	Molecular weight cutoff
MxEnc	<i>Myxococcus Xanthus</i> encapsulin
NaBH ₄	Sodium boronhydride
NaCl	Sodium chloride
NaOH	Sodium hydroxide
NIR	Near Infrared
NMR	Nuclear Magnetic Resonance
ODPA	Octadecylphosphonic acid
PbS	Lead sulfide
PDB	Protein Data Bank
PEG	Polyethylene glycol
PL	Photoluminescence
PLQY	Photoluminescence Quantum Yield
QD	Quantum dot
QY	Quantum yield
RNA	Ribonucleic acid
RT	Room Temperature
SDS-PAGE	Sodium dodecyl sulfate polyacrylamide gel electrophoresis
SEC	Size-exclusion chromatography
SEM	Scanning electron microscopy
SERS	Surface-enhanced Raman Scattering
SOB	Super optimal broth
SPR	Surface Plasmon Resonance

Abbreviations

STM	Scanning Tunneling Microscope
Stp	Streptavidin
T	Triangulation number
<i>T. maritima</i>	<i>Thermotoga maritima</i>
TB	Terrific broth
TEM	Transmission Electron Microscopy
TmEnc	<i>T. maritima</i> wild type encapsulin
TmEnc	<i>Thermotoga maritima</i> encapsulin
TmEnc ^(neg)	Negatively surface charged <i>T. maritima</i> encapsulin
TmEnc ^(pos)	Positively surface charged <i>T. maritima</i> encapsulin
TMV	Tobacco Mosaic Virus
TOP	Trioctylphosphine
TOPO	Trioctylphosphine oxide
tris	tris(hydroxymethyl)aminomethane
UV-Vis	UV visible
VLP	Virus-like particles
VLS	vapor-liquid-solid
ZnO	Zinc oxide

11. List of Figures

Figure 2.1: Lamer model for nanoparticle growth.	4
Figure 2.2: Illustration of the size-dependent optical properties of QDs.	7
Figure 2.3: Schematic of seeded growth mechanism for CdSe/CdS DiRs.	8
Figure 2.4: Schematics of localized plasmon resonance in AuNRs.	11
Figure 2.5: Self-normalized modelled absorption spectra showing the red shift in the Longitudinal Plasmon Resonance	11
Figure 2.6: Schematic diagram of localized plasmon resonance in nanoparticles.	18
Figure 2.7: Schematic overview of major protein cage types.	19
Figure 2.8: Schematic showing the anisotropic containers found in nature.	21
Figure 2.9: Schematic illustration of the three interfaces in a protein cage architecture available for chemical or genetic modification.	23
Figure 2.10: Overview of structural features of encapsulin of the first family.	24
Figure 2.11: Schematic illustration visualizing the peptide-directed encapsulation of gold nanoparticles into <i>T. maritima</i> encapsulin.	27
Figure 2.12: Structural comparison of assembled encapsulin shells from <i>M. xanthus</i>	29
Figure 2.13: Strategy for the encapsulation of gold nanoparticles into the ferritin protein nanocage.	33
Figure 2.14. A general strategy to assemble binary protein-nanoparticle crystals.	35
Figure 2.15: Schematic representation of the formation of heterogeneous binary crystals, composed of AuV and mFt.	36
Figure 3.1: Schematic visualization of encapsulin surface.	38
Figure 3.2: Analytical data for the CLP-mediated encapsulation of gold nanoparticles.	39
Figure 4.1: Schematic overview of the concept.	40
Figure 5.1. Schematic representation of the seeded growth method for synthesizing CdSe/CdS DiRs.	43
Figure 5.2: Characterization of CdSe/CdS DiRs.	44
Figure 5.3: Characterization of CdSe seeds.	45

Figure 5.4: Schematic representation of the seeded growth method for synthesizing gold nanorods.....	46
Figure 5.5: UV-Vis absorption spectra of gold nanorod fractions after two-step centrifugation.	47
Figure 5.6: TEM images and size distribution of gold nanorods from different fractions after two-step centrifugation.	48
Figure 5.7: Schematic representation of the seeded growth method for synthesizing gold nanorods with CTAB/ <i>n</i> -decanol as solvent.....	49
Figure 5.8: UV-Vis absorption spectra of gold nanorods after transfer from CTAB/ <i>n</i> -decanol mixture to CTAB.....	49
Figure 5.9: TEM images and size distribution of gold nanorods from different fractions after two-step centrifugation.	50
Figure 5.10: Schematic representation of the seeded growth method for synthesizing gold nanoparticles.	51
Figure 5.11: Normalized UV-Vis absorption spectra of gold particles of standard and scale up synthesis.....	52
Figure 5.12: TEM images and size distribution of AuNPs.....	53
Figure 5.13: Chemical structures of ligands used for surface modification of CdSe/CdS DiRs.	55
Figure 5.14: Schematic showing ligand exchange strategy for CdSe/CdS DiRs.....	55
Figure 5.15: Normalized emission spectra and TEM images of CdSe/CdS DiRs.....	57
Figure 5.16: Hydrodynamic size distribution of CdSe/CdS DiRs.....	58
Figure 5.17: ζ -potential measurements of CdSe/CdS DiRs capped with AUT:MUTAB mixture.	60
Figure 5.18: Photographs of CdSe/CdS DiRs capped with AUT: MUTAB Mixture.....	61
Figure 5.19: Schematic a of AUT/MUTAB-stabilized CdSe/CdS DiR functionalized with a 16-amino acid long CLP.	61
Figure 5.20: Hydrodynamic size distribution of CdSe/CdS DiRs capped with different AUT: MUTAB ratios and CLP.....	62
Figure 5.21: TEM images of CdSe/CdS DiRs capped with different AUT: MUTAB ratios and CLP.....	63

Figure 5.22: Schematic a of MUTAB-stabilized CdSe/CdS DiR functionalized with a 16-amino acid long CLP.....	64
Figure 5.23: Volume weighted hydrodynamic size distribution and TEM images of MUTAB/CLP capped CdSe/CdS DiRs.	64
Figure 5.24: Normalized emission spectra of CdSe/CdS DiRs.	65
Figure 5.25: Emission spectra of CdSe/CdS DiRs and CLP-FAM conjugates under 450 nm and 495 excitation.....	67
Figure 5.26: Chemical structures of ligands used for surface modification of AuNRs.	68
Figure 5.27: Schematic showing removal of CTAB from the nanorod surface and replacement with MUA.	69
Figure 5.28: UV-Vis characterization of CTAB removal and MUA replacement.	70
Figure 5.29: ζ -potential and hydrodynamic size distribution of CTAB and MUA-coated AuNRs.	70
Figure 5.30: Schematic illustration showing the replacement of CTAB with MUTAB.	71
Figure 5.31: Normalized UV-Vis absorption spectra of AuNRs.....	72
Figure 5.32: ζ -potential, hydrodynamic size distribution and stained TEM images of CTAB and MUTAB coated AuNRs.	73
Figure 5.33: Normalized absorption spectra, hydrodynamic size distributions and ζ -potential for CLP functionalzation of MUTAB coated AuNRs.	74
Figure 5.34: Normalized UV-Vis absorption spectra of NaBH ₄ and MUTAB treated AuNRs.76	
Figure 5.35: Emission spectra of NaBH ₄ and MUTAB (ethanol) treated AuNRs.	76
Figure 5.36: Ligand Exchange of AuNPs from CTAC to MUTAB.....	79
Figure 5.37: Stained TEM images of AuNPs.	80
Figure 5.38: Schematic a of MUTAB-stabilized AuNP functionalized with a 16-amino acid long CLP.....	81
Figure 5.39: CLP-loading of MUTAB coated AuNPs.....	82
Figure 5.40: Schematic illustration of the detection strategy used to confirm CLP and Streptavidin-Biotin binding highlighting amino acids and hydrogen bonds.....	83
Figure 5.41: UV-Vis absorption spectra of AuNPs to confirm presence of CLP using Biotin-Streptavidin binding.	84

Figure 5.42: Emission spectra of AuNPs to confirm presence of CLP using Biotin-Streptavidin binding.	85
Figure 5.43: Ion-exchange and size-exclusion chromatograms of negatively surface charged TmEnc ^(neg) encapsulin.....	86
Figure 5.44: : TEM images of TmEnc ^(neg) and corresponding histogram with size distribution.	87
Figure 5.45: : Ion-exchange and size-exclusion chromatograms of MxEnc.	88
Figure 5.46: Hydrodynamic size distribution of T = 1 and T = 3 state of MxEnc.....	88
Figure 5.47: Stained TEM images of T = 3 and T = 1 state of MxEnc and corresponding histogram with size distribution.	90
Figure 5.48: Ion-exchange and size-exclusion chromatograms of MxEnc. Samples were purified without ammonium sulfate.	91
Figure 5.49: Ion-exchange and size-exclusion chromatograms of MxEnc. Samples were purified with ammonium sulfate.....	92
Figure 5.50: Ion-exchange and size-exclusion chromatograms of MxEnc. Samples were lysed using DNase and lysosyme.	93
Figure 5.51: Ion-exchange and size-exclusion chromatograms of MxEnc.	95
Figure 5.52: Size-exclusion chromatogram and stained TEM of MxEnc.....	96
Figure 5.53. ESI-MS spectrum of MxEnc.	97
Figure 5.54: Ion-exchange and size-exclusion chromatograms of MxEnc.	98
Figure 5.55: TEM images of MxEnc and corresponding histogram with size distribution.	99
Figure 5.56: Encapsulation of DiRs into the negatively charged encapsulin cage.	101
Figure 5.57: Size-exclusion chromatograms and corresponding PL spectra of the DiRs and TmEnc ^(neg) in CHES buffer.....	104
Figure 5.58: TEM images of DiRs and TmEnc ^(neg) in CHES buffer without salt.	105
Figure 5.59: TEM images of DiRs and TmEnc ^(neg) in CHES buffer with salt.....	106
Figure 5.60: Encapsulation of DiRs into the negatively charged encapsulin cage.	106
Figure 5.61: Stained TEM images of encapsulation of CdSe/CdS DiRs into <i>T. maritima</i> encapsulin at different DiR-to-protein ratios.	108

Figure 5.62: Stained TEM images of encapsulation of CdSe/CdS DiRs into <i>T. maritima</i> encapsulin at 1:15 DiR-to-protein ratio.	108
Figure 5.63: Ion-exchange and size-exclusion chromatograms of DiR-loaded TmEnc ^(neg) encapsulin.....	109
Figure 5.64: Normalized emission spectra of TmEnc ^(neg) and CdSe/CdS DiRs sample.....	110
Figure 5.65: Stained TEM images of the sample post ion exchange and size exclusion chromatography.....	111
Figure 5.66: Ion-exchange and size-exclusion chromatograms of DiR-loaded TmEnc ^(neg) encapsulin.....	112
Figure 5.67: Stained and unstained TEM images of the AuNR-TmEnc ^(neg) sample post encapsulation reaction.	114
Figure 5.68: Hydrodynamic size distribution and normalized ITF spectra for monitoring for native(blue), disassembled (red) and reassembled (green) T = 1 state of MxEnc.	117
Figure 5.69: Hydrodynamic size distribution and normalized ITF spectra for monitoring for native (blue), disassembled (red) and reassembled (green) T = 3 state of MxEnc.	118
Figure 5.70: Size exclusion chromatograms of T = 1 state post reassembly in tris-buffer and 5 mM DTT with different NaCl concentrations.	120
Figure 5.71: Size exclusion chromatograms of T = 3 state post reassembly in tris-buffer and 5 mM DTT with different NaCl concentrations.	121
Figure 5.72: Size exclusion chromatograms of T = 1 state post reassembly in tris-buffer with DTT variation.	122
Figure 5.73: Size exclusion chromatograms of T = 1 state post reassembly in tris-buffer with DTT variation.	123
Figure 5.74: Stability of coated AuNPs in phosphate buffer and outcome of an encapsulation attempt.....	126
Figure 5.75: Stability of CLP-functionalized AuNPs in phosphate buffer and schematic illustration of encapsulation of gold nanoparticle in <i>M. xanthus</i> encapsulin (PDB : 4PT2).	126
Figure 5.76: Ion-exchange and size-exclusion chromatograms of AuNP-loaded MxEnc in phosphate buffer at two NaCl concentrations.....	127
Figure 5.77: Stained TEM images of the sample after SEC.....	128

Figure 5.78: Ion exchange chromatograms of AuNP-loaded MxEnc in tris buffer at two NaCl concentrations.....	129
Figure 5.79: Size exclusion chromatogram and stained TEM of AuNP-loaded MxEnc in tris buffer with 0.1 M NaCl.....	129
Figure 5.80: Size exclusion chromatograms of AuNP-loaded MxEnc.	130
Figure 5.81: Stained TEM images of different fractions collected post second SEC.....	131
Figure 5.82: Ion-exchange and size-exclusion chromatograms of AuNPs and T = 1 state of MxEnc.....	132
Figure 5.83: Ion-exchange and size-exclusion chromatograms of AuNRs and T = 3 state of MxEnc.....	133
Figure 5.84: Size-exclusion chromatograms of encapsulation and control experiment.	134
Figure 5.85: Schematic illustration of disassembly of <i>M. xanthus</i> encapsulin and reassembly into different states.....	134
Figure 5.86: Hydrodynamic diameter distributions, normalized size-exclusion chromatogram and stained TEM images of reassembled T = 3 state of MxEnc.	135
Figure 5.87: Hydrodynamic diameter distributions and normalized size-exclusion chromatogram of reassembled T = 3 state of MxEnc.	136
Figure 5.88: Hydrodynamic diameter distributions of the T = 3 state of MxEnc during reassembly by fivefold dilution with water and reconcentration to the initial concentration.	137
Figure 5.89: Normalized size-exclusion chromatograms of the T = 3 state of MxEnc after urea wash and reassembly by fivefold dilution with buffer followed by reconcentration to the initial concentration.	138
Figure 5.90: Normalized size-exclusion chromatograms of the T = 3 state of MxEnc after 100-fold dilution overnight with buffer followed by reconcentration to the initial concentration. .	138
Figure 5.91: Normalized size-exclusion chromatograms of the T = 3 state of MxEnc after a water wash, fifty-fold dilution overnight with buffer, and reconcentration to the initial concentration.	139
Figure 5.92: Normalized size-exclusion chromatograms of the T = 3 state of MxEnc after 50-fold dilution overnight with buffer followed by reconcentration to the initial concentration. .	139
Figure 5.93: Normalized size-exclusion chromatograms of the T = 3 state of MxEnc after dilution with phosphate buffer followed by reconcentration to the initial concentration.....	140

Figure 5.94: Normalized size-exclusion chromatograms of the T = 3 state of MxEnc after dilution with tris buffer with two different NaCl concentrations followed by reconcentration to the initial concentration. 141

Figure 5.95: Normalized size-exclusion chromatograms of the T = 3 state of MxEnc after dilution with phosphate buffer with two different NaCl concentrations followed by reconcentration to the initial concentration. 141

Figure 5.96: Normalized size-exclusion chromatograms of the T = 3 state of MxEnc after dilution with tris buffer with four different NaCl concentrations followed by reconcentration to the initial concentration. 142

Figure 5.97: Structural comparison of MxEnc arranged in T = 1 and T = 3 symmetry..... 143

Figure 5.98: Stained TEM images of T = 3 state reassembly and AuNP encapsulation in tris buffer with no salt..... 144

Figure 5.99: Stained TEM and histograms for filled and empty MxEnc cages. 145

Figure 8.1: Normalized UV-Vis absorption spectra and TEM image of AuNRs synthesized using 37.5? μ L NaOH. 163

Figure 8.2: Normalized UV-Vis absorption spectra and TEM image of AuNRs synthesized using 45 μ L NaOH. 163

Figure 8.3: Normalized UV-Vis absorption spectra and TEM image of AuNRs synthesized using 100 μ L NaOH. 164

Figure 8.4: Ion exchange chromatograms of MxEnc at different OD₆₀₀..... 164

Figure 8.5: Size exclusion chromatograms of MxEnc at two different OD₆₀₀..... 165

Figure 8.6: Ion exchange and size exclusion chromatograms of MxEnc. Samples were lysed using DNase..... 165

Figure 8.7: : Ion exchange and size exclusion chromatograms of MxEnc. Samples were expressed in LB media for 18h and no heat precipitation. 165

Figure 8.8: Ion exchange and size exclusion chromatograms of MxEnc. Samples were expressed in LB media for 18h and with heat precipitation at 60 °C..... 166

Figure 8.9: Ion exchange chromatograms of MxEnc. Samples were expressed in TB media for 18h and without and with heat precipitation at 60 °C..... 166

Figure 8.10: Ion exchange and size exclusion chromatograms of MxEnc. Samples were expressed in LB media for 72h and without heat precipitation..... 167

Figure 8.11: Ion exchange and size exclusion chromatograms of MxEnc. Samples were expressed in LB media for 72h and with heat precipitation at 60 °C. 167

Figure 8.12: Ion exchange, size exclusion chromatograms and stained TEM image of T = 3 state of MxEnc. Samples were expressed in TB media for 72h and with heat precipitation at 60 °C. 168

Figure 8.13: Ion exchange, size exclusion chromatograms and stained TEM image of T = 3 state of MxEnc. Samples were expressed in TB media for 72h and without heat precipitation. 169

Figure 8.14: TEM images from encapsulation trials using DiRs and *T. maritima* encapsulin in HEPES buffer. 170

Figure 8.15: Stained TEM images of encapsulation of CdSe/CdS DiRs into *T. maritima* encapsulin at different DiR-to-protein ratios. 170

Figure 8.16: : Size exclusion chromatograms of T = 1 post reassembly. 171

Figure 8.17: Size exclusion chromatograms of T = 3 post reassembly. 171

Figure 8.18: Stained TEM image of AuNRs and MxWEnc from the encapsulation trial. 172

Figure 8.19: Hydrodynamic size distribution of TmEnc in ethanol-water mixture. 172

Figure 8.20: Stained TEM images of TmEnc in ethanol-water mixture. 173

12. List of Tables

Table 5.1: Molar ratios of AUT:MUTAB	59
Table 5.2: AuNRs samples with washing steps and MUTAB solvent.....	75
Table 5.3: Screening conditions for optimizing the production of MxEnc.	94
Table 5.4: Molecular mass determined via ESI MS for MxEnc.	97
Table 5.5: Stability of DiRs in different buffer solutions.....	102
Table 5.6: Structure of different buffers and their pH range.....	102
Table 5.7: Encapsulation trials in different reassembly buffers.	103
Table 5.8: Stability of MUTAB/CLP functionalized DiRs in different buffer solutions.	107
Table 5.9: Calculations for the amount of DTT used for the reassembly trials.	122
Table 7.1: List of used E. coli strains.....	149

13. List of Chemicals

Chemical	Supplier	H- and P- Statements	GHS Symbols
Acetic acid	VWR	H: 226-314 P: 210-243-280- 301+330+331-304+340- 308+310	GHS02; GHS05
Aminoundecanethiol	Sigma Aldrich	H: 315-319-335 P: 261-264-271-280- 302+352-305+351+338	GHS07
Ammonium sulfate	AppliChem	H: 302-315-319-335-411 P: 261-264-270-271-273- 280-301+312-302+352- 304+340-305+351+338- 312-321-330-332+313- 337+313-362-391- 403+233-405-501	-
Ampicillin sodium salt	AppliChem	H: 317-334 P: 261-272-280-284-321- 302+352-304+341- 333+313-342+311- 362+364-501	GHS08
Ascorbic Acid	Sigma Aldrich	-	-
Cadmium oxide	Fisher Scientific	H: 330-341-350-361fd-372- 410 P: 273-280-304+340-310	GHS06, GHS08, GHS09
Calcium chloride dihydrate	Sigma Aldrich	H: 319 P: 264-280-305+351+338- 337+313	GHS07
CHES	Sigma Aldrich	H: 302-317-319-410 P: 264-280-305+338+351- 313+337	GHS07, GHS09
Decanol	Sigma Aldrich	H: 319-412 P: 264-273-280- 305+351+338-337+313- 501	GHS07
di-Potassium hydrogen phosphate trihydrate	Roth	-	-
Dithiothreitol	Sigma Aldrich	H: 302-315-319-335 P: 280-302+352- 305+351+338-308+311	GHS07
Ethanol	VWR	H: 225-319 P: 210-240-305+351+338- 403+233	GHS02
Glycerol	VWR	-	-
Gold (III) chloride trihydrate	Sigma Aldrich	H: 314-317 P: 280-305+351+338-310	GHS01, GHS07
Guanidine hydrochloride	Sigma Aldrich	H: 302+332-315-319 P: 261-280-301+312-330- 304+340+312- 305+351+338-337+313	GHS07

List of Chemicals

HEPES	Roth	H 315-319-335 P: 261-264-270-271-280-301+312-302+352-304+312-304+340-305+351+338-312-321-322-330-332+313-337+313-362-363-403+233-405-501	-
Hexadecyltrimethylammonium bromide	Sigma Aldrich	H: 302-315-318-335-373-400-410 P: 273-280-301+312-305+351+338-314	GHS08, GHS05, GHS07, GHS09
Hexadecyltrimethylammonium chloride	Sigma Aldrich	H: 302-311-314-410 P: 260-273-280-301+312-303+361+353-305+351+338	
Hexylphosphonic acid	Thermo Fischer	H: 315-319-335 P: 280-302+352-304+340-312-332+313-337+313	GHS07
Hydrochloric acid (37%)	VWR	H: 290-314-335 P: 260-280-303+361+353-304+340+310-305+351+338	GHS05
Hydrogen Peroxide	Roth	H: 302+332-318 P: 280-302+352-305+351+338-310	GHS05, GHS07
IPTG	Roth	H: 319-335-315 P: 280-302+352-304+340-305+351+338-312	GHS08, GHS07
LB-Medium	Roth	-	-
Magnesium chloride	Roth	-	-
MES monohydrate	AppliChem	H: 315-319-335 P: 261-305+351+338	GHS07
(11-Mercaptoundecyl)- <i>N,N,N</i> -trimethylammoniumbromid	Sigma Aldrich	-	-
11-Mercaptoundecanoic acid	Sigma Aldrich	H: 315-319-335 P: 261-264-271-280-302+352-305+351+338	GHS07
Methanol	VWR	H: 225-331-311-301-370 P: 210-233-280-302+352-304+340-308+310-403+235	GHS06, GHS02
<i>N,N</i> -Dimethylformamide	VWR	H: 226-312-332-319-350-360 P: 201-210-233-271-308+313-363-370+378-305+351+338-403+235-405-501	
Octadecylphosphonic acid	abcr	H315, H319, H335 P: 280-261-304+340-305+351+338-337+313	GHS07
Potassium dihydrogen phosphate	Roth	-	-

List of Chemicals

2-Propanol	VWR	H: 225-319-336 P: 210-280-305+351+338	GHS02, GHS07
Selenium	Sigma Aldrich	H: 301+331-373-413 P: 260-264-273-301+310-304+340+311-314	GHS06, GHS08
Silver nitrate	Sigma Aldrich	H: 272-290-314-360D-410 P: 210-260-280-303+361+353-304+340+310-305+351+338	GHS03, GHS08, GHS05, GHS09
SOB medium	Roth	-	-
Sodium borohydride	Sigma Aldrich	H: 260-301-314-360fd P: 231+232-260-280-303+361+353-304+340+310-305+351+338	GHS02, GHS06, GHS08, GHS05
Sodium chloride	Roth	-	-
Sodium hydroxide	Grussing	H: 290-314 P: 280-301+330+331-305+351+338-308+310	GHS05
Sulphur	Sigma Aldrich	H: 315 P: 264-280+302+352-332+313-362+364	GHS07
TB medium	Roth	-	-
Toluene	Fisher Scientific	H: 225-304-315-336-361d-373 P: 210-240-301+310+330-302+352-314-403+233	GHS08, GHS02, GHS07
Trioctylphosphine	Sigma Aldrich	H: 314 P: 280-303+361+353-304+340+310-305+351+338-363-405	GHS05
Trioctylphosphinoxide	Sigma Aldrich	H: 315-318-412 P: P264-273-280-302+352-305+351+338 -332+313	GHS05
TRIS	Roth	-	-
tris-Hydrochloride	Roth	-	-
Uranyl acetate	Science Services	H: 300+330-373-411 P: 260-264-270-271-273-284-301+310-304+340-310-314-320-321-330-391-403+233-405-501	GHS06, GHS08, GHS09
Urea	VWR	-	-

Acknowledgement

It is quite difficult to sum up the support I've received over the years from everyone who helped make this thesis possible. This journey has been shaped by the guidance, generosity, and encouragement of many people, and I am deeply grateful to each of them.

First and foremost, I would like to thank my supervisor, Prof. Tobias Beck for his invaluable guidance, scientific insight, and, above all, his understanding and empathetic nature. His ability to recognize when to challenge and when to support made all the difference. Whether it was through helpful feedback, patient listening, or the occasional well-timed joke, his guidance was steady throughout. And of course, true to his self-appointed title (and Wi-Fi hotspot), he always lived up to being *Gandalf*—arriving precisely when he meant to, with the right advice at the right moment. I will do my best to do justice to his mentorship. I hope to be as rigorous, precise, ambitious, and committed as he is, in my next scientific steps.

I would like to sincerely thank Prof. Volker Abetz for kindly agreeing to review this thesis. I am also grateful to Prof. Wolfgang Maison and Dr. Tobias Vossmeier for serving on my defense committee and for their time and valuable feedback.

I would also like to thank the GRK 2536 “Nanohybrid” Research Training Group for providing an inspiring and interdisciplinary research environment. I am thankful to my supervisory team, Prof. Alf Mews and Prof. Carmen Hermann, within the GRK for their guidance and constructive feedback throughout the course of my PhD. I acknowledge and deeply appreciate the financial support provided by the graduate school, which made this work possible.

Additionally, I would like to acknowledge the following staff and service departments at the Institute of Physical Chemistry in Hamburg for their assistance with measurements: Stefan Werner (TEM), Robert Schön (SEM), and the Mass Spectrometry teams (ESI, MALDI).

I would like to thank Dr. Vincent Mittag for his support with the synthesis of CdSe/CdS DiRs and for generously providing materials essential to this work. I am also thankful to Julian Schattschneider for his assistance in providing the DiRs.

I would also like to thank my undergraduate student Fredryk Marti, my research student Heddy Rust, as well as my master's student Marfa Wulf, whose contributions, whether direct or indirect, supported the success of this dissertation.

I would like to thank Dr. Hendrik Böhler, Dr. Michael Rütten, and Dr. Laurin Lang for patiently answering all my (often naïve) questions when I first joined the lab. Your guidance helped me find my footing, and I learned a great deal just by watching how you approached science and handled chaos. I would like to thank my colleagues Niklas Mucke, Tobias Katenkamp, Maximilian Ruffer, Henrike Wagler, Dr. Lars Klemeyer, Dr. Rafiga Masmaliyeva, Dr. Markus

Perbandt, Dr. Skadi Kull, Petra Belda and Sofia Boja for the friendly working atmosphere and the scientific exchange and support. Thank you for the everyday moments, jokes, and shared challenges that made the lab feel like a safe space. As this chapter comes to a close, I already feel a sense of anticipatory nostalgia—knowing I will miss working alongside you all. Beyond the experiments and deadlines, I'm deeply thankful for the everyday moments that made this journey feel lighter. The coffee breaks that turned into therapy sessions, lunch discussions, board game evenings, and all the laughter that echoed louder than the centrifuge. These were the moments that brought balance.

I would like to thank Dr. Michael Rütten, Niklas Mucke, Tobias Katenkamp and Maximillian Ruffer for being brave enough to endure the first draft of this thesis. Your patience, feedback, and sense of humor were greatly appreciated.

I would like to thank my friends, both here and back home, for the wonderful times shared outside PhD. It provided the much-needed joy and balance. A special thanks goes to my imaginary friends from the books I've read. For keeping me company through long nights, for offering escapes when reality got too heavy, and for reminding me that there's always another world waiting, just a page away. :D

I would like to thank Didi, who was the first one to tell me about the opportunities in Germany. Her encouragement set everything in motion and opened a path I wouldn't have found on my own. I would like to thank Arushi, whom I first met in a professional setting but over the years, became a trusted presence and a true friend. Your kindness, clarity, and perspective have helped me more than words can express, and I'm incredibly grateful for the space you held for me through it all.

A very special thank you goes to someone who has been by my side since the very beginning, right from the days of writing applications, reading and editing countless cover letters, and gently correcting every careless mistake. You believed in me even when I wanted to give up, and your quiet motivation carried me through more than you know. Your support made this possible.

Finally, my deepest thanks go to my family, especially my parents for their unwavering support and belief in me. For making education a priority for us from the beginning. For supporting me even though you didn't know the path I was on or when I insisted on taking the road less traveled (which was often). Their quiet strength, sacrifices, and belief in me laid the foundation for everything I've achieved. This thesis is as much theirs as it is mine.

I am especially thankful to my siblings, who have always been there for me with unconditional love, unwavering support, and laughter. *You are, therefore I am.*

Statutory Declaration

I hereby declare and affirm that this doctoral dissertation is my own work and that I have not used any aids and sources other than those indicated. If electronic resources based on generative artificial intelligence (gAI) were used in the course of writing this dissertation, I confirm that my own work was the main and value-adding contribution and that complete documentation of all resources used is available in accordance with good scientific practice. I am responsible for any erroneous or distorted content, incorrect references, violations of data protection and copyright law or plagiarism that may have been generated by the gAI.

09.10.2025

V. Gadav

Curriculum Vitae

Personal

Name	Varnika Yadav
Date of Birth	26 October 1995
Place of Birth	Jhajjar
Nationality	Indian

Education & Work

09/2021 - Present	Doctoral Studies Institute of Physical Chemistry University of Hamburg
03/2018-02/2021	Teaching Faculty Meritnation (now Aakash)
09/2018-02/2019	Project Research Associate IIT Mandi
06/2018-08/2018	Intern IIT Mandi
07/2016-06/2018	Master of Science in Chemistry IIT Mandi
07/2012-06/2015	Bachelor of Science in Chemistry (honours) Mirada House University of Delhi
04/2005-05/2012	Senior Secondary Education RED School, Chhuchhakwas, Jhajjar
04/2000-03/2005	Primary School HR Green Field, Jhajjar

Self-five. Varnika out!